Assessing Interactions of Future Climate Change, Wildfires, and Terrestrial Biogeochemical Feedbacks

A Dissertation Presented for the
Doctor of Philosophy
Degree
The University of Tennessee, Knoxville

Cheng-En Yang
December 2019

Copyright © 2019 by Cheng-En Yang
All rights reserved.

DEDICATION

I dedicate this work first to my beloved family for their endless support and encouragement; and second to those people and places that have inspired me to explore more ways in which I could become involved in science.

ACKNOWLEDGEMENTS

First, I am indebted to my advisor, Dr. Joshua Fu, for his help and support in my study since 2012. His outstanding teaching skills guided me to learn new knowledge and to develop essential skills for conducting scientific research independently. His superior outreach network also provided me with numerous opportunities to meet and work with talented researchers from universities, national laboratories, and governmental agencies. I would like to thank the rest of my dissertation committee members (Dr. Forrest Hoffman, Professor Chris Cox, Dr. John Drake, Dr. Katherine Evans, and Dr. Daniel Ricciuto) for their great support and invaluable advice. I am grateful to Dr. Hoffman who supported me and shared with me not only his knowledge in science but also his invaluable life experiences which made my graduate life more colorful and cheerful. I am deeply appreciative of Professor Chris Cox for his support and comments to shape my fundamental knowledge in civil and environmental engineering and final dissertation. I am also grateful to Dr. Drake for his insightful comments and for teaching me his programming techniques in climate modeling. I am obliged to Dr. Evans for agreeing to serve on my dissertation committee on such a short notice. Dr. Evans has a very tight schedule as the Division Director of Computational Sciences and Engineering Division at Oak Ridge National Laboratory. Yet she spared time and provided me with detailed comments about my dissertation. I am thankful to Dr. Ricciuto for his crucial comments and suggestions of terrestrial carbon cycle and land processes in the Earth system modeling. I would also like to thank all the members of our research group for their friendship and great support. I also extend my gratitude to the staff members in the Department of Civil and Environmental Engineering at The University of Tennessee, especially Lisa Smith for her support and help during the past years. Last but not least, I would like to express my deepest gratitude to my family. This dissertation would not have been possible without their support, encouragement, patience, and unwavering love.

ABSTRACT

Rising anthropogenic emissions of radiatively active greenhouse gases and particulate matter (PM) are altering Earth's climate, increasing human and ecosystem health risks, and inducing feedbacks from terrestrial and marine ecosystems on future atmospheric carbon dioxide (CO_2) levels and PM concentrations. Process-based Earth system models (ESMs) and regional climate and chemistry transport models offer the best approach for quantifying these feedbacks and their uncertainties, projecting future atmospheric CO_2 levels and resulting temperature increases and wildfire risks, predicting hazardous PM concentrations and human health risks, and understanding the impacts of potential mitigation efforts. In this dissertation, I address these globally significant environmental issues through three studies designed to highlight biases in global ESM vegetation distributions, investigate terrestrial carbon cycle feedbacks from solar radiation management (SRM) climate change mitigation, and explore impacts of future regional wildfire emissions on ozone (O_3) and fine (≤2.5 micrometers) particulate matter ($PM_{2.5}$) due to unmitigated climate change.

In the first study, I analyzed CO_2 mole fraction-driven simulations of ESMs from the fifth phase of the Coupled Model Intercomparison Project (CMIP5) and found that ESMs exhibited large biases in forest distribution, fraction, and biomass in leaves, wood, and roots. These biases induced an uncertainty of −20 Pg C to 135 Pg C in forest total biomass estimates over northern extratropical regions in ESMs, influencing estimates of carbon cycle feedbacks, fuel loads and distributions, and, thus, wildfire risk. In the second study, I found terrestrial ecosystems became a stronger carbon sink, adding 79 Pg C stored on land, under a SRM strategy designed to maintain global surface temperature at 2020 levels for the remainder of the twenty-first century. While fuel loads were increased, wildfire risks were reduced by mitigating increases in global temperature. In the third study, I found, by employing global climate and chemistry-transport model output to force the Community Multiscale Air Quality model, increased fire intensity between contemporary (2003–2010) and future years (2050–2059) had little effect on atmospheric O_3 concentrations in the Western United States, but projected $PM_{2.5}$ concentrations induced by fire could be as much as 21 times higher in future years in this region.

TABLE OF CONTENTS

CHAPTER 1 Introduction 1
Wildfires and terrestrial ecosystem responses in a changing climate 1
Climate intervention 2
Challenges in assessing climate-wildfires-terrestrial ecosystem interactions 2
Motivations and overview of this work 5
CHAPTER 2 Uncertainty Quantification of Extratropical Forest Biomass in CMIP5 Models over The Northern Hemisphere 8
Abstract 9
Introduction 10
Results 12
Spatial differences of forest fractions and total carbon mass *12*
Magnitude of forest biomass uncertainty *25*
Carbon allocation to forest compartments *36*
Spatial covariation of forest total biomass and climatic conditions *36*
Spin-up impacts *45*
Discussion 45
Conclusion 54
Methods 55
Model outputs *55*
Observation-based data sets *56*
Common–grid land mask *56*
Land cover types and forest fractions *57*
Spatial correlations and skill scores *57*
Relative error *58*
Spin-up effects *59*
CHAPTER 3 Interactions and Biogeochemical Feedbacks in The Climate-Wildfire-Terrestrial Ecosystem under Geoengineering 60
Abstract 61
Main 62
Results 64

Global climate change *64*
Global terrestrial biogeochemical responses *67*
Carbon sink strength and atmospheric CO_2 trajectory adjustments *77*
Implications of terrestrial biogeochemical responses to geoengineering *83*
Biomass in individual compartments and fuel loads *86*
Methods 96
Stratospheric Aerosol Geoengineering Large Ensemble (GLENS) dataset *96*
Ecoregions *98*
Carbon sink strength *98*
Adjusted atmospheric CO_2 and surface temperature trajectory *99*
CHAPTER 4 Impacts of Wildfires on Air Quality Changes in The Western United States 101
Abstract 102
Introduction 102
Methods 104
Model descriptions *104*
Meteorological and initial and boundary inputs for CMAQ *106*
Emission inputs for present year CMAQ simulations *106*
Emission inputs for future year CMAQ simulations *112*
Experimental design *114*
Model performance metrics *117*
Results 118
Evaluations of CMAQ model performance *118*
Wildfire-induced ozone and $PM_{2.5}$ changes in present years *122*
Projections of wildfire-induced ozone and $PM_{2.5}$ changes *130*
Conclusion 143
CHAPTER 5 Conclusion and Future Studies 147
REFERENCES 149
VITA 169

LIST OF TABLES

Table 2-1. Summary of eight CMIP5 earth system models used in this study. Modeling centers include (A) GCESS, (B) MOHC, (C) IPSL, and (D) MIROC. 13
Table 2-2. Global land cover classification for the year 2000 from Global Land Cover 2000 (GLC2000) (Joint Research Centre, 2003) and CMIP5 models. Modeling centers (A)–(D) are the same as shown in Table 2-1. 17
Table 2-3. Global total carbon mass (Pg C) of forest compartments across 30°N–80°N for CMIP5 models (*Model*) and upscaled observations (*Obs.*) at $F_f = 0$ during the contemporary period (Modern) and the pre-industrial (PI) periods. "Wood+Root" is the sum of biomass in wood and in roots. Modeling centers are the same as shown in Table 2-1. Model outputs are from (1) BNU-ESM, (2) HadGEM2-CC, (3) HadGEM2-ES, (3_{PFT}) HadGEM2-ES with detailed grid-level biomass for each PFT, (4) IPSL-CM5A-LR, (5) IPSL-CM5A-MR, (6) IPSL-CM5B-LR, (7) MIROC-ESM, and (8) MIROC-ESM-CHEM. Each modeling center (B), (C), and (D) has "Mean" values from the averages of all available model outputs within an institute. The "Multi-Model Mean" values are the averages of all model outputs ($n = 9$) whereas the "Institutional Mean" are the averages of the four modeling centers' mean values ($n = 4$). Note that in each model resolution a common grid mask is applied to both *Model* and *Obs*. 31
Table 2-4. Grid cell-level relative errors of all compartments ($ER_{grid,total}$), leaves ($ER_{grid,leaf}$), wood ($ER_{grid,wood}$), roots ($ER_{grid,root}$), and wood plus roots ($ER_{grid,wood+root}$) for each model during the contemporary period at $F_f = 0$. Numbers represent global mean and one standard deviation of ER_{grid} values for all available grid cells after masks applied. Model numbers are the same as shown in Figure 2-3. 37
Table 2-5. Forest type definitions for Whittaker diagrams. Modeling centers (A) – (D) are the same as shown in Table 2-1. Numbers represent the PFT classes defined in Table 2-2. Forest types include broadleaf evergreen trees (BET), needleleaf evergreen trees (NET), broadleaf deciduous trees (BDT), and needleleaf deciduous trees (NDT). Note that MOHC models only have broadleaf trees (BT) and deciduous trees (DT). 42
Table 2-6. Definitions of forest types in GLC2000 and each modeling center. Modeling centers (A) – (D) are the same as shown in Table 2-1. Numbers represent the classes defined in Table 2-2. Unavailable land types are denoted by *N/A*. The GLC2000 forest definition is adopted from Thurner et al. (2014). 46
Table 3-1. Accumulated global climate change over various time periods. Numbers represent the mean and cross-ensemble standard deviation of the first three ensemble members for the *BASE*, *CTRL*, and *GEOENG* (abbreviated as *GEOG*). *PRECIP* and *ET* are precipitation and evapotranspiration (unit: mm/day), respectively, and the other variable annotations (unit: Pg C) are the same as shown in the Methods section. Positive values for *GPP*, *NPP*, *NEP*, and *NBP* indicate carbon gains in ecosystems while negative values represent carbon losses to the atmosphere; the opposite applies to R_a and R_h. Symbol "Δ" denotes the differences of *GEOENG−CTRL*. The asterisk sign indicates 2011–2019 cumulative sum of *NBP*.80

Table 3-2. Accumulated net biome production (*NBP*) of individual ecoregions over different time periods. Numbers represent the mean and cross-ensemble standard deviation of the first three ensemble members in the *BASE*, *RCP85*, and *GEOENG* cases (abbreviated as *GEOG*). "Δ" symbol denotes the difference of *NBP* between *GEOENG* and *RCP85*. Positive values indicate carbon gains in land. 81
Table 3-3. Same as Table 3-2 except for the carbon amount in total vegetation (Pg C). . 92
Table 4-1. Updated mapping table for gas-phase pollutant emissions (mole/s) based on Gao et al. (2013). XYL represents xylene. 107
Table 4-2. Species mapping between CMAQ CB05 and FINN MOZART4. 109
Table 4-3. Hourly buoyant efficiency. 111
Table 4-4. Parameters as a function of fire size classes based on burned area. 111
Table 4-5. Mapping of emission sectors from IIASA RCP8.5 to U.S. EPA. 113
Table 4-6. Species mapping between CMAQ CB05 and IIASA RCP8.5 database. 115
Table 4-7. Emission factors (g/kg) for various species from fires. NMOC denotes non-methane volatile organic compounds and nNMOC is unidentified NMOC. Other abbreviated species names can be found in Table 4-2. 115
Table 4-8. Model performance of seasonal O_3 and $PM_{2.5}$ based on the monthly MFE and MFB values. 121
Table 4-9. Land use categories used in CMAQ v5.0 (USGS 20 land use categories) and CMAQ v5.2 (USGS 24 land use categories). 123

LIST OF FIGURES

Figure 1-1. A schematic diagram of the climate-wildfires-ecosystem feedbacks (adopted from United Nations Environment Programme (2011)). Red arrows show positive feedbacks between wildfires and phenomena induced by increased atmospheric CO_2 mole fraction while green arrows represent the reduction of atmospheric CO_2 mole fraction by ecosystems. Golden arrows indicate disturbances due to human activities. 3
Figure 1-2. Current climate intervention proposals (adopted from Lawrence et al. (2018)). 4
Figure 2-1. Forest fractions in the northern extratropical regions during the contemporary period for upscaled observations (top row), CMIP5 models (center row), and the differences (bottom row, model−observation). Different resolutions according to model setup are shown (left to right): BNU-ESM, HadGEM2-ES, IPSL-CM5A-MR, and MIROC-ESM. Each model output and its corresponding upscaled observation data are masked by a common-grid land mask. Missing data is presented in light gray color. 14
Figure 2-2. Same as Figure 2-1 except for forest total carbon mass (10^{-2} Pg C). 15
Figure 2-3. Same as Figure 2-1 except for all ESMs (column-wise, left to right): BNU-ESM, HadGEM2-CC, HadGEM2-ES, and IPSL-CM5A-LR. Dominant PFT in each model. PFT types are listed in Table 2-2. Models include (1) BNU-ESM, (2) HadGEM2-CC, (3) HadGEM2-ES, (4) IPSL-CM5A-LR, (5) IPSL-CM5A-MR, (6) IPSL-CM5B-LR, (7) MIROC-ESM, and (8) MIROC-ESM-CHEM. 16
Figure 2-4. Same as Figure 2-1 except for all ESMs (column-wise, left to right): BNU-ESM, HadGEM2-CC, HadGEM2-ES, and IPSL-CM5A-LR..... 20
Figure 2-5. Same as Figure 2-2 except for all ESMs (column-wise, left to right): BNU-ESM, HadGEM2-CC, HadGEM2-ES, and IPSL-CM5A-LR..... 22
Figure 2-6. (Top) Effective forest area of forest total carbon mass at default forest threshold ($F_f = 0$) from model outputs (red) and from upscaled observations (black) during the contemporary period. A common-grid mask in both observed and modeled values is applied. (Bottom) The ratios of effective forest area at various forest fraction thresholds to that at $F_f = 0$. Models (1) – (8) are the same as shown in Figure 2-3.. 24
Figure 2-7. Taylor diagrams of (a) all model results and (b) model results of standardized deviations smaller than 2.5 for the northern extratropical forest carbon mass at various forest fraction thresholds (F_f) ranging from 0.0 to 0.9. Model numbers represent the CMIP5 models. Models (1) – (8) are the same as shown in Figure 2-3. 26
Figure 2-8. Skill scores for modeled global forest carbon mass in different forest fraction thresholds during the contemporary period. Models (1) – (8) are the same as shown in Figure 2-3..... 27
Figure 2-9. Global extratropical forest total carbon mass (Pg C) in the Northern Hemisphere for individual forest compartments: (a) all compartments, (b) wood and roots, (c) leaves, (d) wood, and (e) roots during the contemporary period at $F_f = 0$. Columns in light gray are the masked observations at each model resolution with

error bars showing the uncertainty. The colored columns represent modeled results from BNU-ESM (1, red), HadGEM2-CC (2, green), HadGEM2-ES (3, blue), HadGEM2-ES with detailed PFT information (3_{PFT}, orange), IPSL-CM5A-LR (4, magenta), IPSL-CM5A-MR (5, light green), IPSL-CM5B-LR (6, violet), MIROC-ESM (7, light blue), and MIROC-ESM-CHEM (8, dark brown). The mean value (yellow) is the average of all model results. (a,b) and (d) use the same vertical scale while (c) and (e) use different vertical scales. 28
Figure 2-10. Relative errors for (a) global forest total carbon mass and (b) averaged forest total carbon mass at grid cell level during the contemporary period. Each sub-panel (top to bottom) represents all compartments (Total), wood and roots (Wood+Root), leaves, wood, and roots at $F_f = 0$. Model numbers are the same as used in Figure 2-9. 34
Figure 2-11. Institutional averaged (a) relative errors and (b) relative errors at grid cell level for individual forest compartments (top to bottom) during the contemporary period: all compartments, wood and roots, leaves, wood, and roots. Letters for modeling centers are the same as used in Table 2-1. "Mean" represents the average of all four modeling centers' outputs. 35
Figure 2-12. Allocations of global forest total carbon mass in (a) wood and roots, (b) leaves, (c) wood, and (d) roots during the contemporary period at $F_f = 0$. Model numbers and colors are the same as used in Figure 2-9. (a) and (c) use the same vertical scale while (b) and (d) use different vertical scales 38
Figure 2-13. Global correlation maps of observation (top row), model outputs during the contemporary period (middle row), and model outputs at pre-industrial period (bottom row) for each model resolution. Missing data on land is shown in gray color. The color table represents the magnitude of correlations between forest total carbon mass and precipitation (horizontal) and between forest total carbon mass and surface temperature (vertical). Grid resolutions include (left to right): BNU-ESM, HadGEM2-ES, IPSL-CM5A-MR, and MIROC-ESM. 40
Figure 2-14. Same as Figure 2-13 except for all ESM resolutions (left to right, columnwise): BNU-ESM, HadGEM2-CC, HadGEM2-ES, IPSL-CM5A-LR, IPSL-CM5A-MR, IPSL-CM5B-LR, MIROC-ESM, and MIROC-ESM-CHEM. 41
Figure 2-15. Whittaker diagrams of various forest types ($F_f = 0.2$) for upscaled observations (top row), models (center row), and observed biomass in modeled climate space for BNU-ESM (left) and HadGEM2-ES (right) during the contemporary period. Colors represent different PFT categories defined in Table 2-3 43
Figure 2-16. Ratios for global mean relative errors of masked carbon mass at grid cell level during the pre-industrial period to that during the contemporary period at $F_f = 0$. Forest compartments include (a) all compartments, (b) leaves, (c) wood, and (d) roots. The colors and model numbers are the same as used in Figure 2-9. Forest types in each sub-panel (top to bottom): lumped, broadleaf, needleleaf, evergreen, and deciduous trees. Dashed lines represent $SR = 1$. 47
Figure 2-17. Mask and unmasked (checkered columns) forest total carbon mass (Pg C) for ESM outputs (blue) and upscaled observational data sets (red) in (a) total biomass, (b) wood and roots, (c) leaves, (d) wood, and (e) roots during the

contemporary period. ESM numbers are the same as used in Table 2-5. “Mean” represents the average of all ESM outputs. 50
Figure 3-1. Changes of spatial distributions between *CTRL* and *BASE* (top row), between *GEOENG* and *BASE* (middle row), and between *GEOENG* and *CTRL* (bottom row) for surface temperature (K, (a)–(c)), precipitation (mm/day, (d)–(f)), total downward direct solar radiation (W/m^2, (g)–(i)), and total downward diffuse solar radiation (W/m^2, (j)–(l)). The spatial distribution of *CTRL* is from the 2020–2097 time-averaged results without geoengineering while that of *GEOENG* is from the 2020–2097 time-averaged results with geoengineering applied. The spatial distribution of *BASE* is from the 2010–2019 time-average results. 65
Figure 3-2. Ecoregions defined in this study. 66
Figure 3-3. Same as Figure 3-1 except for photosynthesis rates ($\mu mol\ m^{-2}\ s^{-1}$, (a)–(c)), gross primary production ($kg\ C\ m^{-2}\ yr^{-1}$, (d)–(f)), net primary production ($kg\ C\ m^{-2}\ yr^{-1}$, (g)–(i)), and net biome production ($kg\ C\ m^{-2}\ yr^{-1}$, (j)–(l)). 68
Figure 3-4. Spatial distributions of soil moisture (kg/m^2). Left column shows the averaged values for *BASE* (2010–2019, top), *CTRL* (2020–2097, middle), and *GEOENG* (2020–2097, bottom). Right column shows the differences of *CTRL*−*BASE* (top), *GEOENG*−*BASE* (middle), and *GEOENG*−*CTRL* (bottom). 70
Figure 3-5. Same as Figure 3-4 except for net nitrogen mineralization rate ($kg\ N\ m^{-2}\ yr^{-1}$). 71
Figure 3-6. Same as Figure 3-4 except for autotrophic respiration ($kg\ C\ m^{-2}\ yr^{-1}$). 72
Figure 3-7. Same as Figure 3-4 except for carbon loss from litters ($kg\ C\ m^{-2}\ yr^{-1}$). 73
Figure 3-8. Same as Figure 3-4 except for heterotrophic respiration ($kg\ C\ m^{-2}\ yr^{-1}$). 74
Figure 3-9. Same as Figure 3-4 except for evapotranspiration (mm/day). 75
Figure 3-10. Same as Figure 3-4 except for net ecosystem production ($kg\ C\ m^{-2}\ yr^{-1}$) 76
Figure 3-11. Same as Figure 3-4 except for burned area fractions by fires in each grid cell ($\times 10^{-9}$, unitless). 78
Figure 3-12. Same as Figure 3-4 except for column-level non-peatland carbon loss by fires ($kg\ C\ m^{-2}\ yr^{-1}$). 79
Figure 3-13. Percentages of ensemble mean of accumulated *NBP* for each ecoregion with respect to the accumulated global *NBP* from 2020 to 2097. Ecoregion labels are the same as those defined in Figure 3-2. Colored columns denote the cases *CTRL* (red), *GEOENG* (blue), and *GEOENG*−*CTRL* (Δ, green). The numbers above each column represent the percentages. 84
Figure 3-14. The trajectories of (a) accumulated global carbon sink strength changes (Pg C) due to geoengineering, (b) the atmospheric CO_2 mole fraction (ppm) during 2010–2097 for *CTRL* (Meinshausen et al., 2011) (black line) and the adjusted atmospheric CO_2 mole fraction due to the terrestrial BGC feedbacks (blue line), (c) surface temperature responses due to atmospheric CO_2 mole fraction adjustments, and (d) sulfur injection rates in GLENS (red) and adjusted injection rates due to terrestrial BGC feedbacks (blue). Shaded area in (a) represents the range of changes for the first three ensemble members between *GEOENG* and *CTRL*; solid green line is the ensemble mean. Adjusted values shown in (b) – (d) are calculated based on the ensemble mean values from (a). 85
Figure 3-15. Same as Figure 3-4 except for biomass in vegetation ($kg\ C\ m^{-2}$). 87

Figure 3-16. Same as Figure 3-4 except for biomass in wood (kg C m^{-2}). 89
Figure 3-17. Same as Figure 3-4 except for biomass in leaves (kg C m^{-2}). 90
Figure 3-18. Same as Figure 3-4 except for biomass in fine roots (kg C m^{-2}) 91
Figure 3-19. Accumulated global biomass changes (*GEOENG−CTRL*) in individual compartments and carbon pools (Pg C). (a) Carbon in total vegetation (green), (b) carbon in leaves (blue), (c) carbon in wood (light brown), (d) carbon in roots (orange), (e) litter carbon loss (red), and (f) carbon in soil (black). Solid lines represent the ensemble mean of the three ensemble members with the shaded area showing the standard deviation. Numbers in each panel along with the curves denote the starting and ending values of biomass change between *GEOENG* and *CTRL*. .. 94
Figure 3-20. Annual global carbon allocation in individual compartments (%) for *CTRL* (red) and *GEOENG* (blue). (a) carbon allocation in leaves, (b) carbon allocation in wood, (c) carbon allocation in roots. Solid lines represent the ensemble mean of the three ensemble members with the shaded area showing the standard deviation. Values are computed based on accumulated biomass in each compartment. 95
Figure 3-21. Same as Figure 3-4 except for carbon in fuel loads (kg C m^{-2}). 97
Figure 4-1. The simulation domain used in this study. 107
Figure 4-2. A schematic diagram of the experimental design in this study. 116
Figure 4-3. Model performance of monthly O_3 concentration (ppbv) in WUS. The vertical axis denotes the range of MFE (%) while the horizontal axis represents the fire months. Black markers within the shaded area denote the simulated O_3 values meet the model performance goal (dark gray) or the model performance criteria (light gray). 119
Figure 4-4. Same as Figure 4-3 except for MFB (%). 119
Figure 4-5. Model performance of monthly $PM_{2.5}$ concentration (μg/m^3) in WUS. The vertical axis denotes the range of MFE (%) while the horizontal axis represents the fire months. Black markers within the shaded area denote the simulated $PM_{2.5}$ values meet the model performance goal (dark gray) or the model performance criteria (light gray). 120
Figure 4-6. Same as Figure 4-5 except for MFB (%). 120
Figure 4-7. Simulated monthly O_3 domain mean concentration (ppb) and the maximum change (%) at grid-cell level during 2003–2010. Solid lines represent the domain averaged O_3 concentration for *BASE* (green) and *NoFireP* (black) while the dashed line denotes the maximum change (*(BASE−NoFireP)/NoFireP×100%*) at grid-cell level within the WUS domain. Months are (a) April, (b) May, (c) June, (d) July, (e) August, (f) September, (g) October, and (h) November. 124
Figure 4-8. Decadal average of (a) monthly and (b) seasonal O_3 changes (ppb) due to fires during 2003–2010. Curves represent the domain mean (red) and the maximum within the domain (blue). Shaded area is the one standard deviation range. The "All" in seasonal O_3 changes represents all fire months during 2003–2010. 126
Figure 4-9. Same as Figure 4-7 except for $PM_{2.5}$ (μg/m^3). 127
Figure 4-10. Same as Figure 4-8 except for $PM_{2.5}$ (μg/m^3). 129
Figure 4-11. Simulated monthly O_3 domain mean concentration (ppb) and the maximum change (%) at grid-cell level during 2050–2059. Solid lines represent the domain averaged O_3 concentration for *IIASA* (red), *USFS* (blue), and *NoFireF* (black) while

the dashed line denotes the maximum changes for *IIASA* (red, *(IIASA−NoFireP)/NoFireP×100%*) and *USFS* (blue, *(USFS−NoFireP)/NoFireP×100%*) at grid-cell level. Months are (a) April, (b) May, (c) June, (d) July, (e) August, (f) September, (g) October, and (h) November. 131
Figure 4-12. Decadal average of (a) monthly and (b) seasonal O_3 changes (ppb) between *IIASA* and *NoFireF* due to fires during 2050–2059. Curves represent the domain mean (red) and the maximum within the domain (blue). Shaded area is the one standard deviation range. 133
Figure 4-13. Same as Figure 4-12 except for the changes between *USFS* and *NoFireF*. Note that missing values are due to the values with monthly O_3 changes smaller than 0.1 ppb..... 134
Figure 4-14. Same as Figure 4-11 except for $PM_{2.5}$ (μg/m^3). 136
Figure 4-14 (*continued*). 137
Figure 4-15. Same as Figure 4-12 except for $PM_{2.5}$ (μg/m^3). 138
Figure 4-16. Same as Figure 4-13 except for $PM_{2.5}$ (μg/m^3). 140
Figure 4-17. Projected $PM_{2.5}$ emission rates (g/s/grid) due to wildfires on August 2, 2050 used in *IIASA* (top) and in *USFS* (bottom) experiments. 141
Figure 4-18. Same as Figure 4-18 except on April 13, 2056. 142
Figure 4-19. Simulated monthly domain mean (red) and domain maximum (blue) changes for $PM_{2.5}$ (μg/m^3). Solid lines show the *IIASA* results during 2050–2059. Dashed lines are the 2005 domain mean and domain maximum changes. Months are (a) April, (b) May, (c) June, (d) July, (e) August, (f) September, (g) October, and (h) November. 144
Figure 4-20. Same as Figure 4-15 with the dashed lines represent the 2005 domain mean and domain maximum $PM_{2.5}$ changes..... 146

CHAPTER 1
INTRODUCTION

Wildfires and terrestrial ecosystem responses in a changing climate

Rising temperatures and the increasing frequency of droughts are driving up wildfire intensity and fire-associated hazardous air pollutants, posing threats not only to property and infrastructure, but also to human health and the functioning of entire ecosystems. Intensified wildfire activities characterized by the frequency of occurrence, the burning durations, and burned areas have been observed in recent decades (Littell et al., 2009; Y. Liu et al., 2013; Marlon et al., 2012; Miller et al., 2009; Westerling et al., 2006; Wiedinmyer & Neff, 2007). Changing climate conditions are believed to be the major cause of increasing wildfire activities. With rising temperatures and reduced precipitation and soil moisture projected in the future (Cayan et al., 2010; Chylek et al., 2017; A. Dai et al., 2004; Gao et al., 2014; Pachauri & Meyer, 2014), climate conditions will be more conducive for wildfire disturbances in the future.

As elevated anthropogenic emissions are responsible for climate change, ecosystems also play an important role in altering the climate through biogeochemical (BGC) feedbacks (Bonan, 2008; Bonan & Doney, 2018; Heimann & Reichstein, 2008; Jolly et al., 2015; Shaver et al., 2000; Stevens-Rumann et al., 2018; Tian et al., 2016; Turner, 2010). With sufficient water and sunlight provided, increasing atmospheric carbon dioxide (CO_2) concentration induces higher photosynthesis rates and productivity for plants (Enoch, 1984; Lloyd, 1999; Ziska & Bunce, 1997), known as the CO_2 fertilization effect. Such increases in plant productivity induce a strong carbon sink and additional carbon sequestered in ecosystems from the atmosphere, hence reducing the atmospheric CO_2 mole fraction. This negative feedback on climate change weakens radiative forcing, which in turn induces smaller temperature increases caused by CO_2, resulting in lower wildfire risks. Nevertheless, terrestrial ecosystems in arid and semi-arid regions, where plants have high moisture stress, could encounter more wildfire events during dry seasons in a changing climate. Higher temperatures increase evapotranspiration rates that drain

water from soils to the atmosphere. Plants on drier lands are more vulnerable to wildfires because more dry biomass and litterfall from withered plants and necromass (dead wood and roots), are accumulated on land. If there were wildfires, the larger amount of accumulated dry matters could release more CO_2 through biomass burning and hence enhance the temperature warming. This positive feedback on climate change would exacerbate water deficits, which make the plants in arid and semi-arid regions more vulnerable to wildfires. The complicated responses and feedbacks between climate, wildfires, and ecosystem are illustrated in Figure 1-1.

Climate intervention

To counteract the global warming temperatures caused by growing anthropogenic emissions, multiple climate engineering strategies (also known as "climate geoengineering") have been proposed to mitigate projected warming (Shepherd, 2009), which plays an important role in triggering wildfires. Figure 1-2 summarizes these strategies proposed to date (Lawrence et al., 2018). Solar dimming by aerosol injections into the lower stratosphere is one such strategy (Crutzen, 2006). This strategy is suggested to be an inexpensive and efficient way to keep the surface temperature constant at a targeted level (Keller et al., 2014; Russell et al., 2012), even though anthropogenic CO_2 emission still increases over time. However, simulations from Earth system models (ESMs) demonstrated that while future global temperature could be controlled at its 2020 level, there could be substantial side effects such as ocean acidification and rapid temperature warming if aerosol injections stopped (Robock, 2008). Responses and BGC feedbacks of ecosystems to the geoengineered climate may also influence fire risks because biomass and available fuel loads are expected to be higher in a cooler climate compared to an unmitigated climate with high greenhouse gas emissions.

Challenges in assessing climate-wildfires-terrestrial ecosystem interactions

Wildfire activities are associated with the fuel loads from biomass as well as climate change. Although the ensemble mean of ESMs is able to capture fairly well the amount of

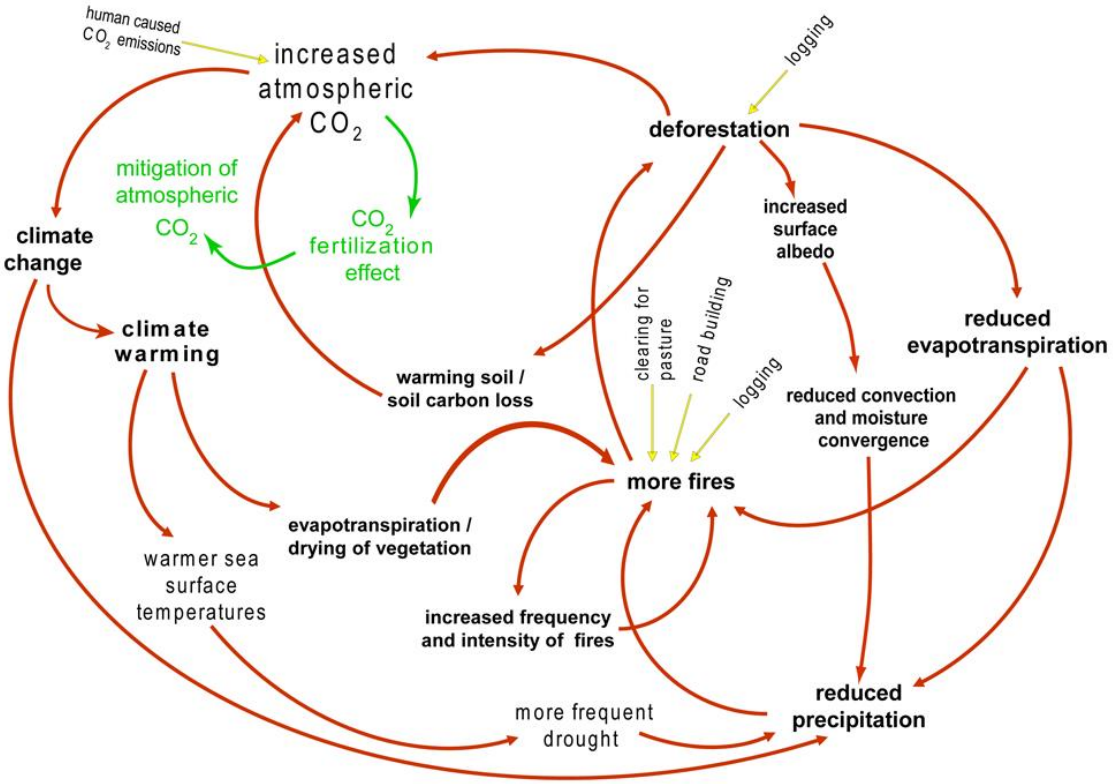


Figure 1-1. A schematic diagram of the climate-wildfires-ecosystem feedbacks (adopted from United Nations Environment Programme (2011)). Red arrows show positive feedbacks between wildfires and phenomena induced by increased atmospheric CO_2 mole fraction while green arrows represent the reduction of atmospheric CO_2 mole fraction by ecosystems. Golden arrows indicate disturbances due to human activities.

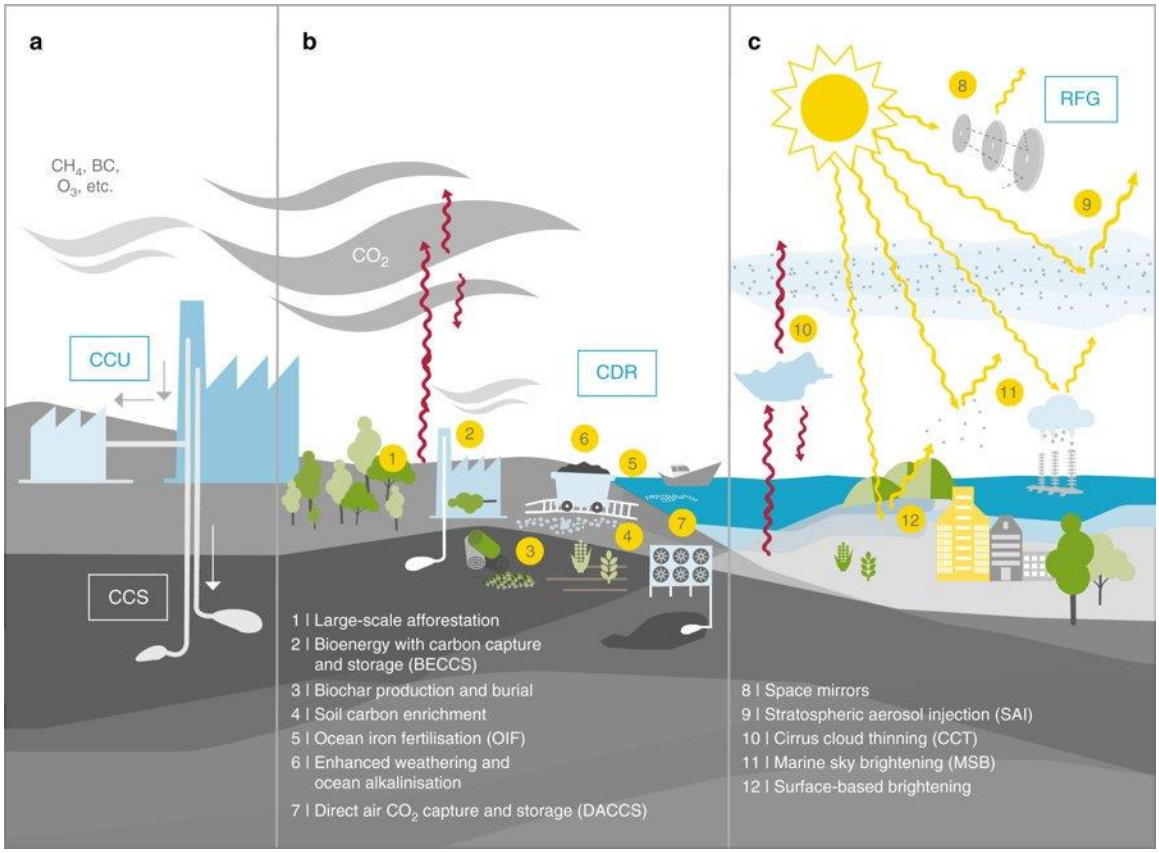


Figure 1-2. Current climate intervention proposals (adopted from Lawrence et al. (2018)).

global terrestrial total live biomass found in observations, substantial variations in ESM simulated forest biomass (Jiang et al., 2015) and in observational data sets (Gibbs et al., 2006; Watson et al., 2000) remains large. While Negrón-Juárez et al. (2015) demonstrated the uncertainty of tropical forest biomass estimates in ESMs, the uncertainty in extratropical (boreal and temperate) forests has not been fully examined. Despite the relative smaller carbon stock stored in the boreal and temperate forests compared to that stored in tropical forests (Pan et al., 2011), reducing the uncertainty of extratropical forest biomass estimates are also important due to the increasing water stress in the extratropical regions.

Impacts of geoengineering on climate change have been largely discussed with respect to atmospheric and hydrological properties (Irvine et al., 2016; Kravitz et al., 2009, 2013; Tilmes et al., 2013; Xia et al., 2016). There are few studies using idealized or simplified ESMs to simulate the responses and feedbacks of ecosystems to geoengineering (Cao, 2018; Cao & Jiang, 2017; Tjiputra et al., 2016; Xia et al., 2016). Results from high-resolution fully-coupled ESMs are required to improve the understanding of the interactions between climate and ecosystems, which influence future fire events as a result of changes in biomass and atmospheric CO_2 mole fractions.

Future climate without mitigations is likely to induce increased fire intensities, which will emit various air toxics. Studies have shown increasing importance of wildfire contributions to regional $PM_{2.5}$ concentration during the contemporary period (D. Jaffe et al., 2008; J. C. Liu et al., 2016; O'Dell et al., 2019; Spracklen et al., 2009). However, it remains uncertain whether wildfires will still be an important source of regional $PM_{2.5}$ concentration given more anthropogenic emissions in the future compared to the present time. In addition, large uncertainty exist in projected wildfire emissions depending on the metrics, such as meteorology and socio-economic activities (Riahi et al., 2011; Urbanski, 2014), used to derive the fire emissions.

Motivations and overview of this work

This work is dedicated to the investigation of the interactions and feedbacks in the climate-wildfire-terrestrial ecosystem in a changing world. Different future climate

scenarios and a geoengineering technique that increases planetary albedo are simulated by models to project future wildfire activities, air quality, and ecosystem responses. Previous studies have suggested increasing human health risks associated with wildfire smoke $PM_{2.5}$ (J. C. Liu et al., 2017; Moore et al., 2006; Stowell et al., 2019). Evaluating future wildfires in a changing climate are important for health impact assessments and for policy-making strategies in environmental management. Because changes in fuel loads from biomass as well as climate change are key to future wildfire projections. I conducted a series of studies incorporating data analysis and model simulations to evaluate interactions between climate change, ecosystems, and wildfires.

The first part of this work, presented in Chapter 2 investigated the causes of uncertainty in biomass estimates from multiple ESM outputs in the fifth phase of the Coupled Model Intercomparison Project (CMIP5) (Taylor et al., 2012). I evaluated extratropical forest biomass data from ESMs and compared it to a recent observation-based data set across the northern extratropical region (30° N–80° N) (Thurner et al., 2014). I also compared ESM data containing detailed information on forest biomass of individual plant functional types and the grid-cell level data reported to CMIP5 to investigate the biomass uncertainty simulated by ESMs. In addition, I adopted the concept from Exbrayat et al. (2014) to investigate if uncertainty of biomass estimates during the spin-up period persists in current and future years. Small relative errors between current and future years with respect to the observations imply parametric or structural model configurations are a large source of uncertainty in biomass estimates in ESMs.

The second part of this work shown in Chapter 3 examined a recent dataset simulated by a high-resolution fully-coupled ESM. I compared the differences between the climate with the Representative Concentration Pathway 8.5 (RCP8.5) high greenhouse gas emissions scenario to the scenario with RCP8.5 geoengineered by stratospheric aerosol injections. I analyzed the dataset in terms of climate change, the responses of terrestrial ecosystems, biomass changes, and fire activities (burned area) between the two climate scenarios. The interactions between climate change and terrestrial ecosystems were determined by the carbon sink strength, which represents changes in net biome production. Fire activities were evaluated by the burned area and fuel loads from the model output.

Chapter 4 described the third part of this work regarding the impacts of wildfires on air quality in the future. Since most parts of the western United States (WUS) are classified as a semi-arid climate zone (Kottek et al., 2006), it is expected to experience more wildfire events since ESMs predict much drier climate conditions in the future (Y. Liu et al., 2013). Therefore, I conducted two sets of model simulations, including climate and chemistry-transport models at global and regional scales, to evaluate the changes in air quality due to climate and wildfires in both present and future years in WUS. I particularly focused on the changes of fine particulate matter (diameter $\leq$ 2.5 μm) ($PM_{2.5}$) and ozone (O_3), which are two criteria air pollutants defined by U.S. Environmental Protection Agency (EPA). I also compared two sets of wildfire emissions projected from different models to examine the uncertainty of the impacts on $PM_{2.5}$ and O_3 concentration due to wildfires. The information provided in this work can be beneficial for future research and policy-making strategies regarding climate change, wildfires, and environmental management.

CHAPTER 2
UNCERTAINTY QUANTIFICATION OF EXTRATROPICAL FOREST BIOMASS IN CMIP5 MODELS OVER THE NORTHERN HEMISPHERE

A version of this chapter was originally published by Cheng-En Yang, Jiafu Mao, Forrest M. Hoffman, Daniel M. Ricciuto, Joshua S. Fu, Chris D. Jones, and Martin Thurner:

Cheng-En Yang, Jiafu Mao, Forrest M. Hoffman, Daniel M. Ricciuto, Joshua S. Fu, Chris D. Jones & Martin Thurner (2018). Uncertainty Quantification of Extratropical Forest Biomass in CMIP5 Models over the Northern Hemisphere. *Scientific Reports*, *8*(1), 10962. https://doi.org/10.1038/s41598-018-29227-7.

Tables and figures are renumbered, and their captions are adjusted accordingly. Jiafu Mao conceived the study. Jiafu Mao and Forrest M. Hoffman recommended analytical and graphical methods. Cheng-En Yang performed the analysis, generated graphical results, and prepared the manuscript in consultation with Jiafu Mao, Daniel M. Ricciuto., Forrest M. Hoffman, and Joshua S. Fu. Martin Thurner prepared the observational data. Chris D. Jones prepared the detailed PFT-level biomass data from the HadGEM2-ES model. All authors reviewed and edited the manuscript.

Abstract

Simplified representations of processes influencing forest biomass in Earth system models (ESMs) contribute to large uncertainty in projections. We evaluate forest biomass from eight ESMs outputs archived in the Coupled Model Intercomparison Project Phase 5 (CMIP5) using the biomass data synthesized from radar remote sensing and ground-based observations across northern extratropical latitudes. ESMs exhibit large biases in the forest distribution, forest fraction, and mass of carbon pools that contribute to uncertainty in forest total biomass (biases range from −20 Pg C to 135 Pg C). Forest total biomass is primarily positively correlated with precipitation variations, with surface temperature becoming equally important at higher latitudes, in both simulations and observations. Relatively small differences in forest biomass between the pre-industrial period and the contemporary period indicate uncertainties in forest biomass were introduced in the pre-industrial model equilibration (spin-up), suggesting parametric or structural model differences are a larger source of uncertainty than differences in transient responses. Our findings emphasize the importance of improved (1) models of carbon allocation to biomass compartments, (2)

distribution of vegetation types in models, and (3) reproduction of pre-industrial vegetation conditions, in order to reduce the uncertainty in forest biomass simulated by ESMs.

Introduction

The amount of carbon stored in vegetation biomass in terrestrial ecosystems plays an important role in influencing Earth's climate. Variations in productivity, respiration, carbon turnover and in carbon allocation to biomass compartments in response to anthropogenic and natural climate change influence the magnitude, spatial distribution and allocation of vegetation carbon stocks. At present, the land biosphere is a carbon sink since atmospheric carbon dioxide (CO_2) is increasingly sequestered in terrestrial ecosystems (Friedlingstein et al., 1999; Friend et al., 2014; Pan et al., 2011; Le Quéré et al., 2016; Sitch et al., 2008). The largest pools of terrestrial carbon are within soils and the live biomass of forests (Jobbágy & Jackson, 2000; Malhi et al., 2002; Sedjo & Sohngen, 2012; Watson et al., 2000). Previous studies found that forests presently store 47% of total global carbon on land around the world (Pan et al., 2011), and land absorbs approximately one-third of global anthropogenic CO_2 emissions each year (Le Quéré et al., 2016). A recent report showed that 11.5% of total greenhouse gas emissions over the contiguous United States in 2014 were offset by land use, land-use change, and forestry (U.S. EPA, 2016). Therefore, investigations of forest biomass magnitude and carbon allocation are critical to reduce the uncertainty of future global and regional carbon stock estimates in the Earth system models (ESMs).

Differences in parametric and structural representations of vegetation and soil processes in ESMs, as well as uncertainties in simulated climate drivers, result in a wide range of carbon stock estimates. As we will show, biases induced by such parametric and structural differences in the initial state of vegetation biomass (i.e., during the pre-industrial (PI) period following model spin-up) often persist into future biomass predictions. In addition, poor representations of carbon allocation processes (Franklin et al., 2012; De Kauwe et al., 2014; Litton et al., 2007), inconsistent definitions of biomass in wood and in roots across ESMs (Negrón-Juárez et al., 2015), and uncertainties in allocation trade-offs in a changing climate (Doughty et al., 2014, 2015) also enlarge uncertainties of projected

carbon allocation in the terrestrial biosphere, increasing the range of carbon–climate feedback estimates. Another challenge to minimize uncertainties in ESMs is accurately representing the types and fractional coverage of global forests (Saatchi et al., 2007, 2011; Schimel et al., 2015). Despite the creation of several observationally constrained estimates of biomass in above- and below-ground vegetation compartments over the past few decades (Baccini et al., 2012; Bradley et al., 2006; Hurtt et al., 2010; Jackson et al., 2002; Pan et al., 2011; Saatchi et al., 2011; Thurner et al., 2014), the uncertainties of observation-based forest biomass due to different retrieval techniques (Bradshaw & Warkentin, 2015; Pacala et al., 2001; Shvidenko et al., 2010) and upscaling procedures in regions with sparse data availability (Boudreau et al., 2008; Houghton et al., 2008) remain large and poorly quantified. Confidence in the feedback of the vegetation carbon cycle in forest ecosystems to climate change thus requires accurate representation of carbon stocks, forest distribution, and allometric relationships between biomass compartments and the responses of underlying processes to environmental conditions in coupled ESMs.

In this study, we quantify the uncertainty of forest biomass, in terms of its magnitude and carbon allocation among vegetation components, from ESM outputs archived in the Coupled Model Intercomparison Project Phase 5 (CMIP5) (Taylor et al., 2012) by comparing the simulated results to a recent observation-based data set across the northern extratropical region (30°N–80°N) (Thurner et al., 2014). Spatial correlations of forest biomass and climatic conditions over this region are also assessed. Some of the ESMs analyzed here allowed for prognostic vegetation distributions using a Dynamic Global Vegetation Model (DGVM) and some did not. In addition, we compare the differences between area-weighted forest biomass at grid cell level and detailed information on forest biomass of individual plant functional types (PFTs) for each model realization. The former provides only the mean carbon density of all PFTs within a grid cell but no carbon density for individual PFTs, while the latter retains different carbon densities for each PFT within a grid cell. Moreover, we analyze the differences of biases in ESMs during the contemporary period and the PI period to investigate the uncertainty caused by parametric or structural model configurations. Hence, taking into account the uncertainty in observations, this study indicates sources of uncertainty for the magnitude

and carbon allocation of extratropical forest biomass estimates that may facilitate improved representation of land processes in ESMs that will impact carbon–climate simulations such as those for the Coupled Model Intercomparison Project Phase 6 (CMIP6).

Results

Spatial differences of forest fractions and total carbon mass

Four ESMs outputs, one per modeling center, from the eight selected ESM realizations (Table 2-1) demonstrate substantial differences of spatial forest fractions and forest total biomass compared to observations (Figures 2-1 and 2-2). BNU-ESM overestimates forest fractions and total biomass at midlatitudes over Europe, the United States, and China while it underestimates forest fractions in Siberia. These discrepancies of forest fractions (*min* = −0.92; *max* = 0.95) and total carbon mass (*min* = −0.39 Pg C; *max* = 1.63 Pg C) at grid cell level are mainly due to broadleaf deciduous temperate trees in the regions of overestimated forest fractions and C_3 arctic grass in the regions of underestimated forest fractions (Figure 2-3). HadGEM2-ES, one of the two configurations from the Met Office Hadley Centre, noticeably underestimates forest fractions and biomass over Russia and Northern Canada with a magnitude up to 0.98 (*min* = −0.98; *max* = 0.96) and 0.14 Pg C (*min* = −0.14 Pg C; *max* = 0.14 Pg C), respectively. The uncertainty originates from the model identifying these regions as shrub-dominant (Figure 2-3) whereas large portions of needleleaf forest are present in the observations. IPSL-CM5A-MR, one of the three ESM configurations from the Institut Pierre Simon Laplace (IPSL), shows biases in forest total biomass ranging from −0.19 Pg C to 0.41 Pg C with relatively lower biases in forest fractions (*min* = −0.58; *max* = 0.78) compared to the other three centers' ESMs; nevertheless, they generally exhibit positive biases in forest fractions across northern high latitudes, especially between 45°N–60°N. This is a consequence of excessively large fractions of boreal needleleaf evergreen trees and boreal needleleaf summergreen trees apportioned in the three IPSL ESMs (Figure 2-3). MIROC-ESM, one of the two model configurations from the Model for Interdisciplinary Research on Climate (MIROC), demonstrates that the simulated forest fractions deviate from the observations by −0.68 to 0.97 with overpredicted forest fractions in Northern Canada and Eurasia north

Table 2-1. Summary of eight CMIP5 earth system models used in this study. Modeling centers include (A) GCESS, (B) MOHC, (C) IPSL, and (D) MIROC.

Modeling center	Model	Resolution*	Grid cells	Land carbon cycle component	Dynamic vegetation	Land cover change	References
(A)	BNU-ESM	2.8125° × 2.8125°	64 × 128	CoLM3 and BNU-DGVM	Yes	Yes†	(Y. Dai et al., 2003, 2004; Ji et al., 2014)
(B)	HadGEM2-CC HadGEM2-ES	1.25° × 1.25°	145 × 192	JULES and TRIFFID	Yes	Yes	(Bellouin et al., 2011; Collins et al., 2011; Cox, 2001; Cox et al., 1999; Essery et al., 2003; Jones et al., 2011)
(C)	IPSL-CM5A-LR IPSL-CM5A-MR IPSL-CM5B-LR	1.9° × 3.75° 1.25° × 1.25° 1.9° × 3.75°	96 × 96 143 × 144 96 × 96	ORCHIDEE	No	Yes‡	(Dufresne et al., 2013; Krinner et al., 2005)
(D)	MIROC-ESM MIROC-ESM-CHEM	2.8125° × 2.8125°	64 × 128	MATSIRO and SEIB–DGVM	Yes	Yes	(Sato et al., 2007; Watanabe et al., 2011)

*: latitude × longitude; †: no land cover change due to anthropogenic land use change; ‡: no prognostic land cover change.

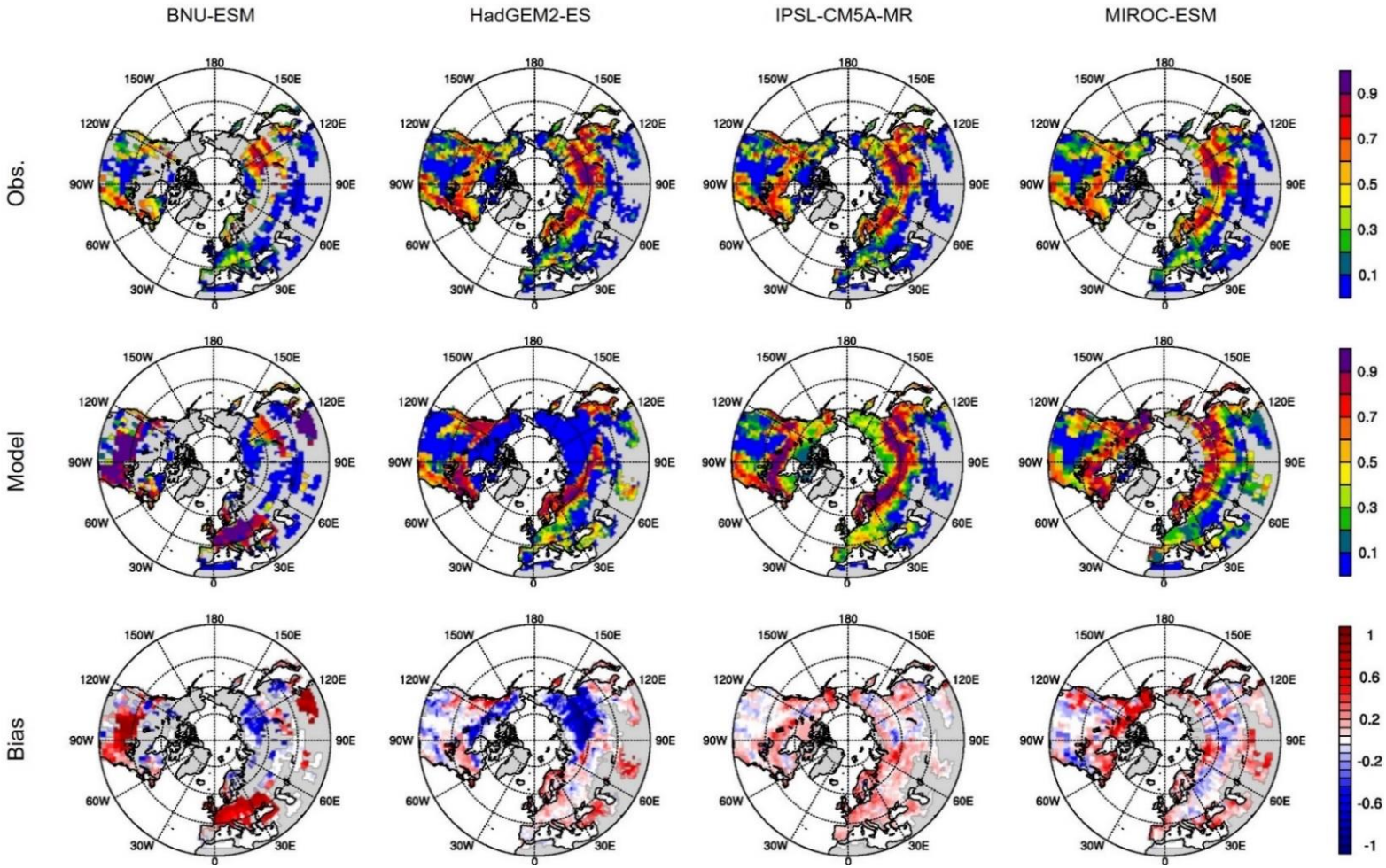


Figure 2-1. Forest fractions in the northern extratropical regions during the contemporary period for upscaled observations (top row), CMIP5 models (center row), and the differences (bottom row, model−observation). Different resolutions according to model setup are shown (left to right): BNU-ESM, HadGEM2-ES, IPSL-CM5A-MR, and MIROC-ESM. Each model output and its corresponding upscaled observation data are masked by a common-grid land mask. Missing data is presented in light gray color.

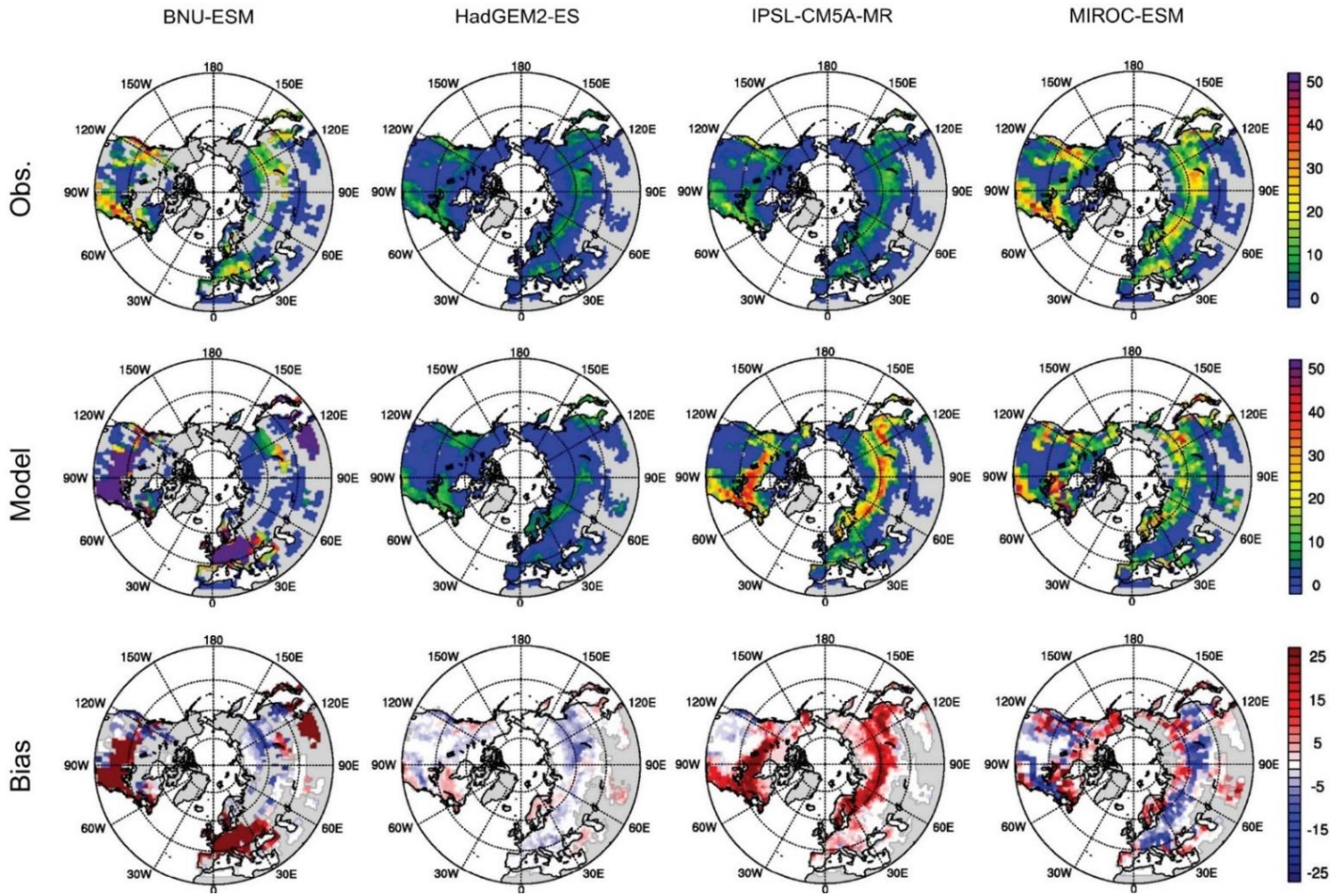


Figure 2-2. Same as Figure 2-1 except for forest total carbon mass (10^{-2} Pg C).

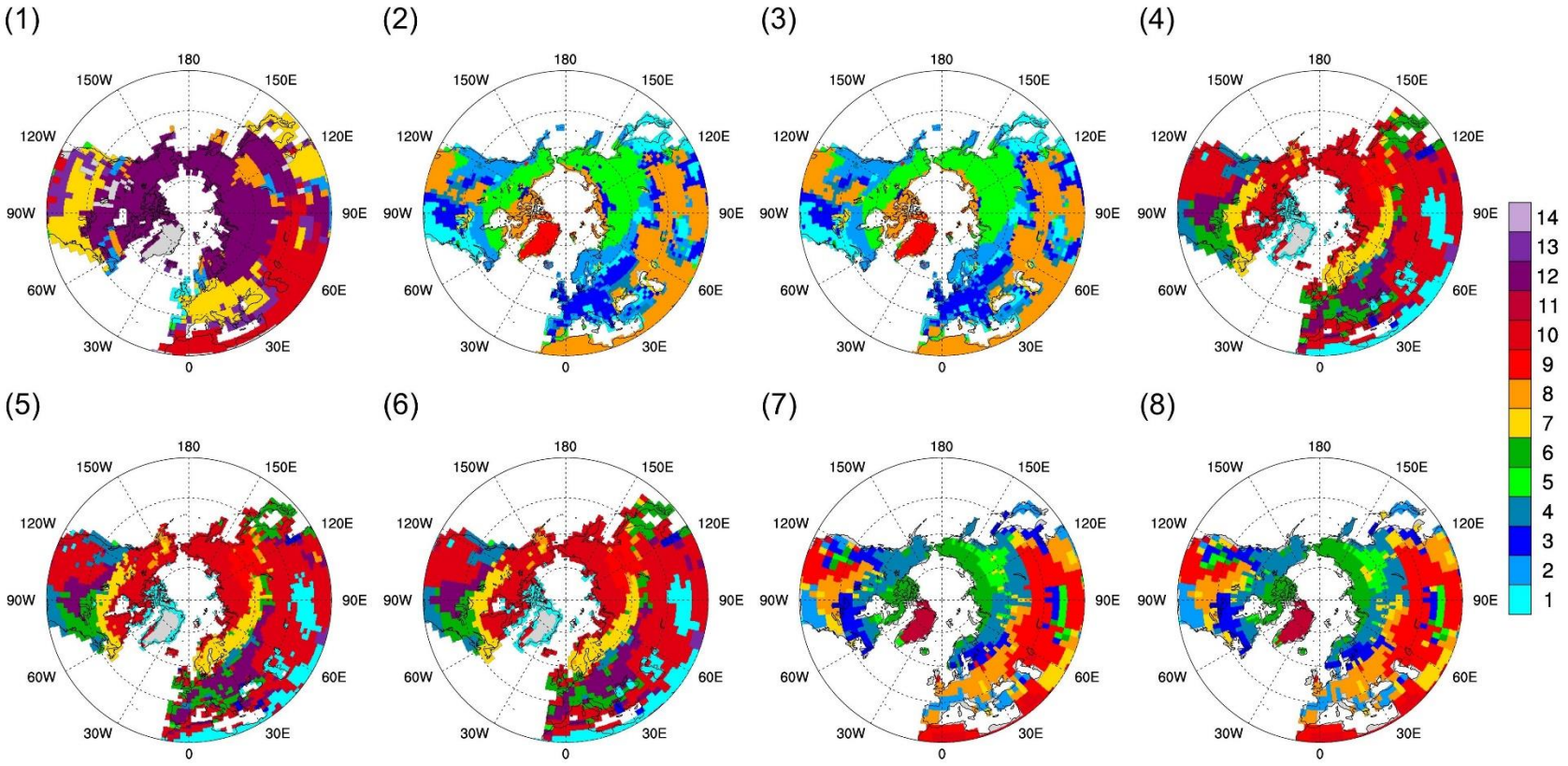


Figure 2-3. Same as Figure 2-1 except for all ESMs (column-wise, left to right): BNU-ESM, HadGEM2-CC, HadGEM2-ES, and IPSL-CM5A-LR. Dominant PFT in each model. PFT types are listed in Table 2-2. Models include (1) BNU-ESM, (2) HadGEM2-CC, (3) HadGEM2-ES, (4) IPSL-CM5A-LR, (5) IPSL-CM5A-MR, (6) IPSL-CM5B-LR, (7) MIROC-ESM, and (8) MIROC-ESM-CHEM.

Table 2-2. Global land cover classification for the year 2000 from Global Land Cover 2000 (GLC2000) (Joint Research Centre, 2003) and CMIP5 models. Modeling centers (A)–(D) are the same as shown in Table 2-1.

Class	GLC2000	(A)	(B)	(C)	(D)
1	Tree Cover, broadleaf, evergreen	Needleleaf evergreen temperate tree	Broadleaf trees	Bare soil	Tropical forest
2	Tree Cover, broadleaf, deciduous, closed	Needleleaf evergreen boreal tree	Needleleaf trees	Tropical broadleaf evergreen trees	Temperate evergreen
3	Tree Cover, broadleaf, deciduous, open	Needleleaf deciduous boreal tree	C_3 (temperate) grass	Tropical broadleaf raingreen trees	Temperate deciduous
4	Tree Cover, needleleaf, evergreen	Broadleaf evergreen tropical tree	C_4 (tropical) grass	Temperate needleleaf evergreen trees	Boreal evergreen
5	Tree Cover, needleleaf, deciduous	Broadleaf evergreen temperate tree	Shrubs	Temperate broadleaf evergreen trees	Boreal deciduous
6	Tree Cover, mixed leaf type	Broadleaf deciduous tropical tree	Urban	Temperate broadleaf summergreen trees	C_3 grass
7	Tree Cover, regularly flooded, fresh water	Broadleaf deciduous temperate tree	Inland water	Boreal needleleaf evergreen trees	C_4 grass
8	Tree Cover, regularly flooded, saline water	Broadleaf deciduous boreal tree	Bare soil	Boreal broadleaf summergreen trees	Crop
9	Mosaic: Tree cover / Other natural vegetation	Broadleaf evergreen shrub	Ice	Boreal needleleaf summergreen trees	Pasture
10	Tree Cover, burnt	Broadleaf deciduous temperate shrub	Natural C_3 grass	Bare ground	
11	Shrub Cover, closed-open, evergreen	Broadleaf deciduous boreal shrub	Natural C_4 grass	Residual	

Table 2-2 (*continued*).

Class	GLC2000	(A)	(B)	(C)	(D)
12	Shrub Cover, closed-open, deciduous	C_3 arctic grass		Agricultural C_3 grass	
13	Herbaceous Cover, closed-open	C_3 non-arctic grass		Agricultural C_4 grass	
14	Sparse Herbaceous or sparse Shrub Cover	C_4 grass			
15	Regularly flooded Shrub and/or Herbaceous Cover				
16	Cultivated and managed areas				
17	Mosaic: Cropland / Tree Cover / Other natural vegetation				
18	Mosaic: Cropland / Shrub or Grass Cover				
19	Bare areas				
20	Water Bodies				
21	Snow and Ice				
22	Artificial surfaces and associated areas				

of 60°N (boreal forests) but with underestimated forest fractions over the northeast coast of North America (dominated by C_4 grasses) and over Eurasia south of 60°N (dominated by crops) (Figure 2-3). The differences of global forest total biomass range from −0.37 Pg C to 0.62 Pg C. Spatial differences of forest fractions and total biomass of all eight ESMs are illustrated in Figures 2-4 and 2-5.

Differences between the observed and modeled forest area also increase the uncertainty of forest biomass estimates when converting the carbon density retrieved from the CMIP5 archive and from the observations to carbon mass. We apply a common-grid land mask (see Methods in this chapter) to each grid cell for each ESM output and its corresponding upscaled observations (obsESMs) based on the Global Land Cover 2000 (GLC2000) data (Joint Research Centre, 2003). Different ESMs have different masks depending on the forest fraction and biomass availability in grid cells for an ESM and its obsESM. Masked forest area ("effective forest area" hereafter in this chapter) and thus forest total biomass can exhibit substantial variations within ESMs and within obsESMs. For example, smaller effective forest area is found in the upscaled observation for the BNU-ESM (obsBNU-ESM) compared to that for the other obsESMs. This is because the mask applied to obsBNU-ESM excludes grid cells where BNU-ESM considers little or no forest existence in the model. With the common-grid land mask applied, the effective forest area for ESMs is $(1.2–2.0) \times 10^9$ ha, whereas that for obsESMs is $(0.8–1.6) \times 10^9$ ha (Figure 2-6). Modeled effective forest area is underestimated in both HadGEM2 ESMs (−24% for HadGEM2-CC and −19% for HadGEM2-ES) while overestimated effective forest area is found in BNU-ESM (47%) as well as in the IPSL ESMs and the MIROC ESMs (29–36%). This uncertainty is mainly attributable to the lack of the ESMs representing the observed land cover types shown in GLC2000. For instance, BNU-ESM allocates C_3 arctic grass rather than any forest type in most regions north of 50°N. Another example can be found from the HadGEM2 ESMs in which the majority of land over Asian Russia and northwest North America is covered by shrubs, resulting in low proportions of forest types being allocated in the models. Due to large uncertainties between ESMs and obsESMs caused by different land cover definitions, we apply various thresholds of the forest fraction (F_f) to examine how uncertainty varies with F_f. It is expected that higher F_f

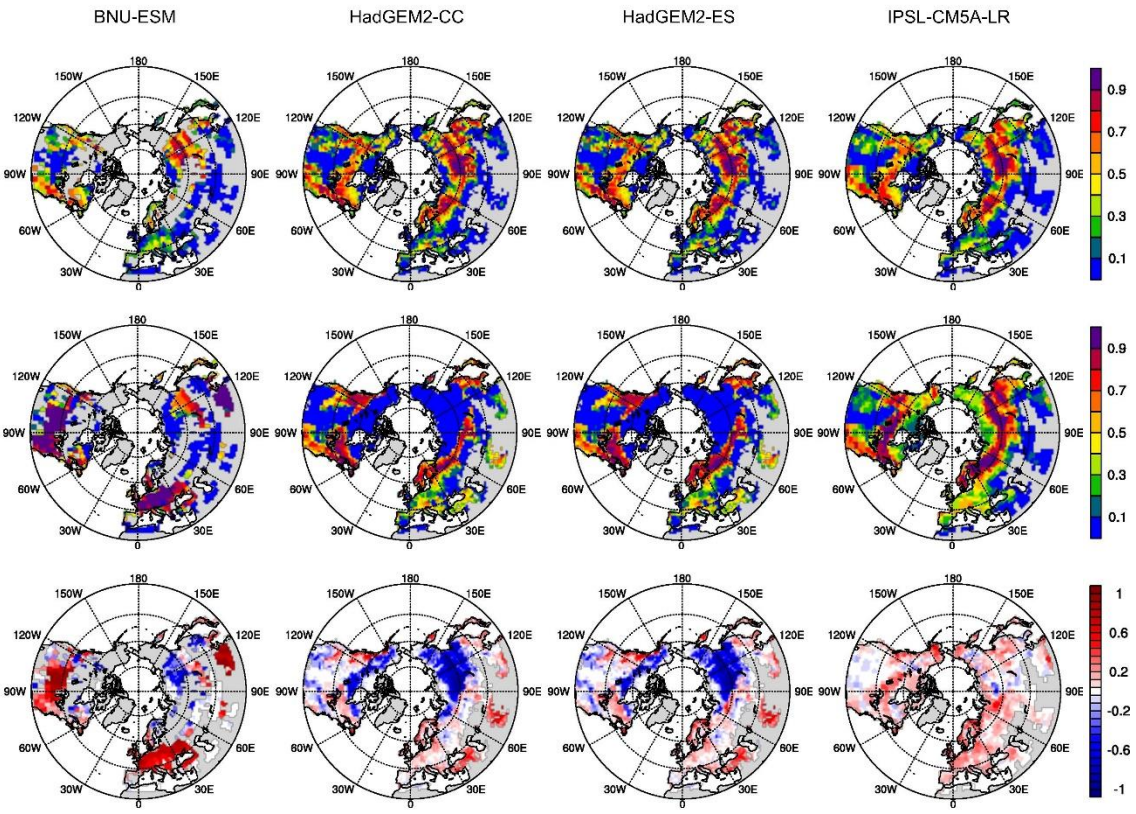


Figure 2-4. Same as Figure 2-1 except for all ESMs (column-wise, left to right): BNU-ESM, HadGEM2-CC, HadGEM2-ES, and IPSL-CM5A-LR.

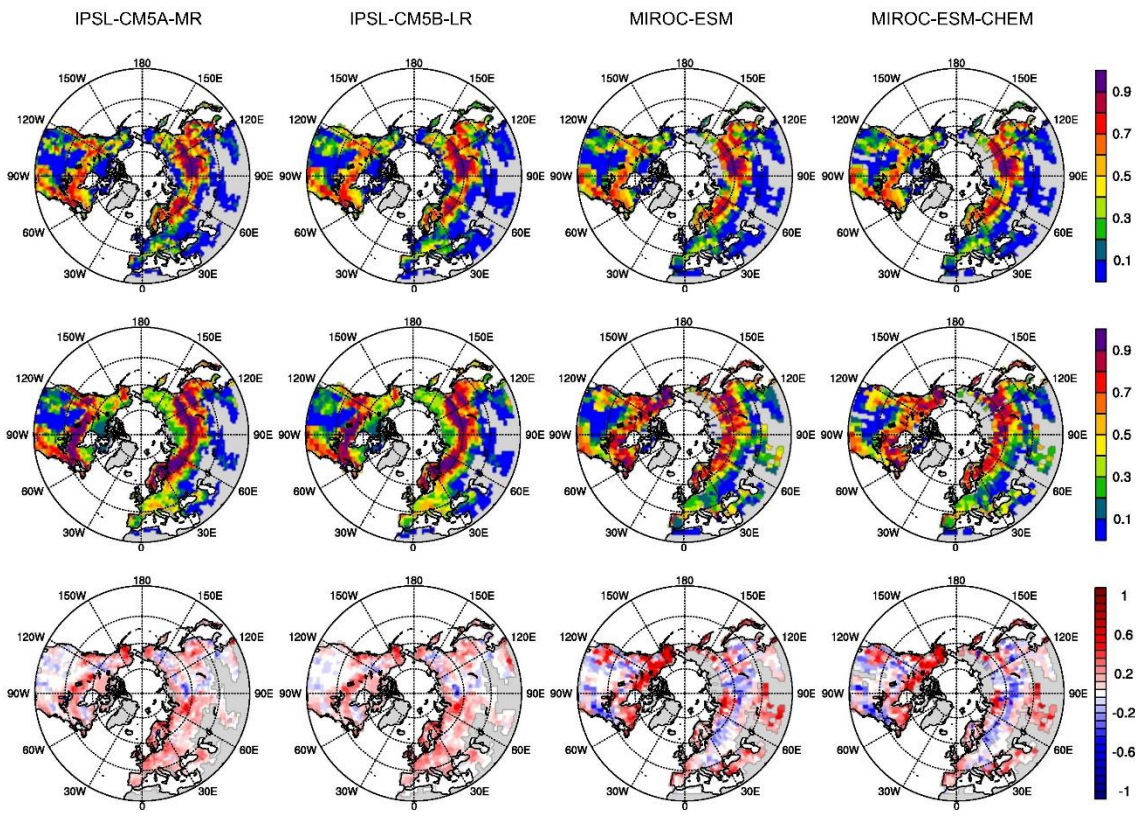


Figure 2-4 (*continued*). Same as Figure 2-1 except for all ESMs (column-wise, left to right): IPSL-CM5A-MR, IPSL-CM5B-LR, MIROC-ESM, and MIROC-ESM-CHEM.

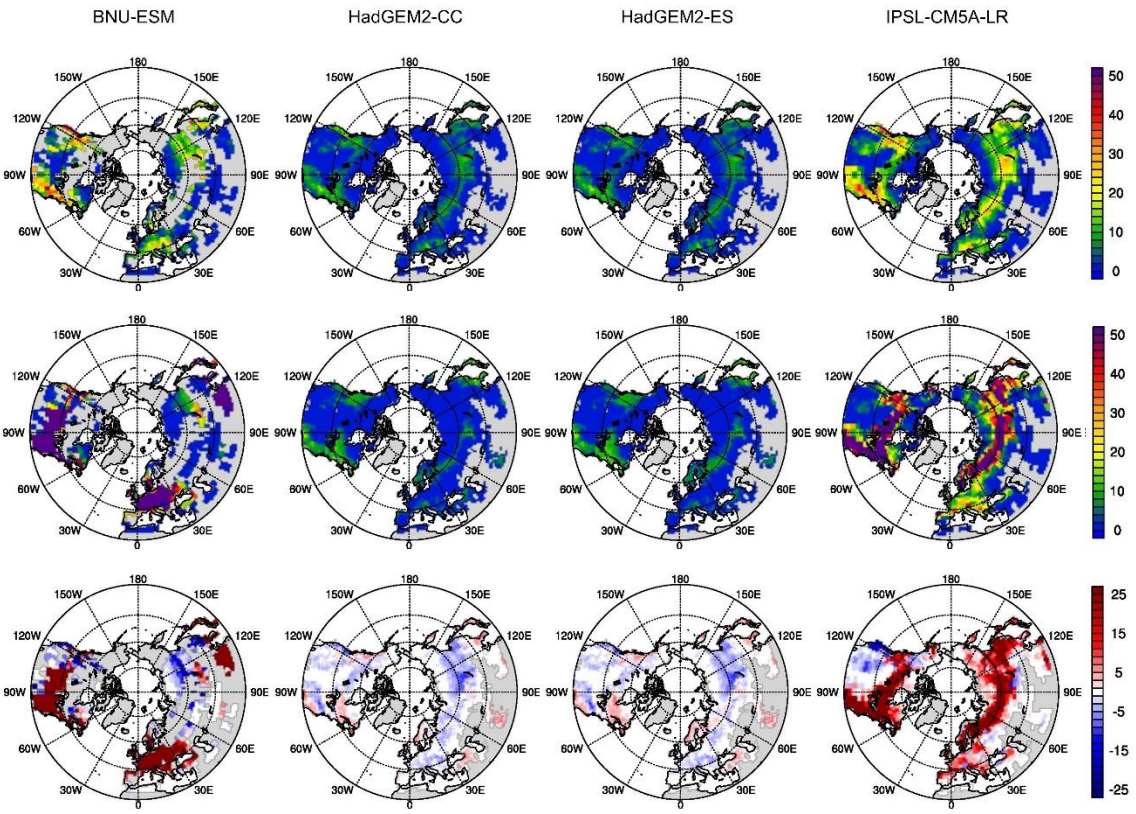


Figure 2-5. Same as Figure 2-2 except for all ESMs (column-wise, left to right): BNU-ESM, HadGEM2-CC, HadGEM2-ES, and IPSL-CM5A-LR.

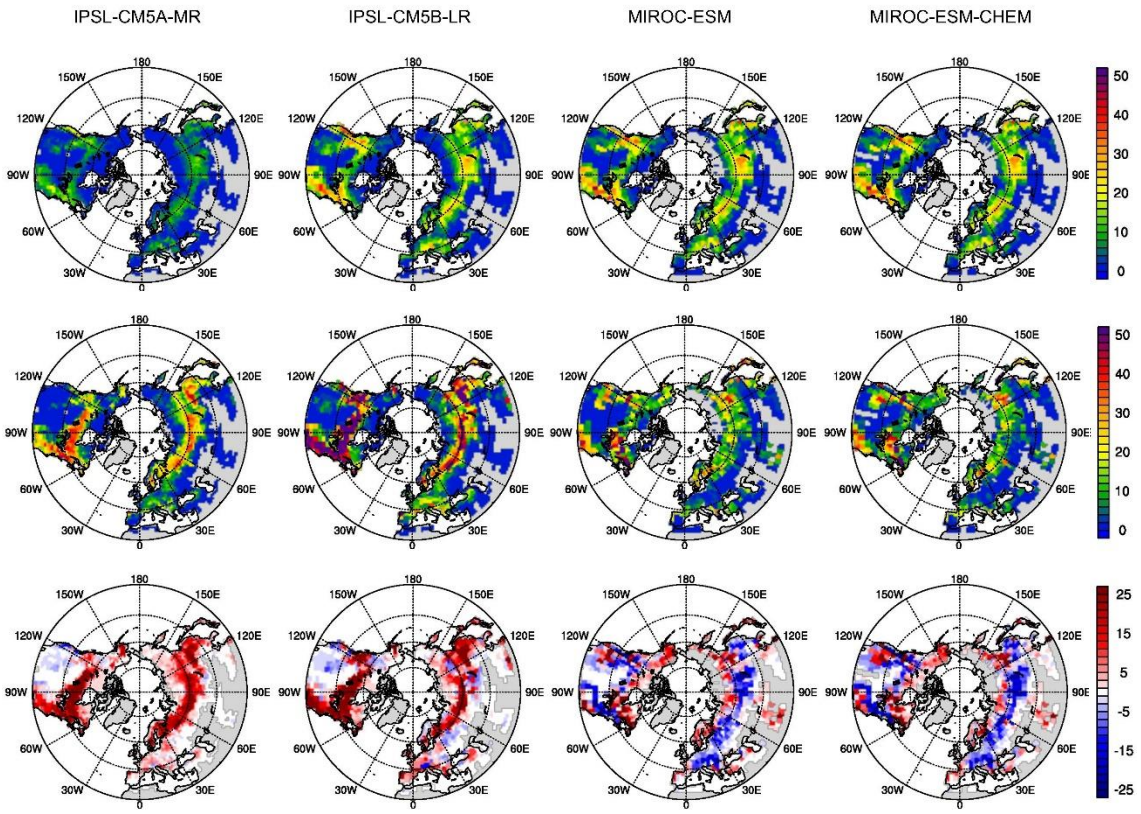


Figure 2-5 (*continued*). Same as Figure 2-2 except for all ESMs (column-wise, left to right): IPSL-CM5A-MR, IPSL-CM5B-LR, MIROC-ESM, and MIROC-ESM-CHEM.

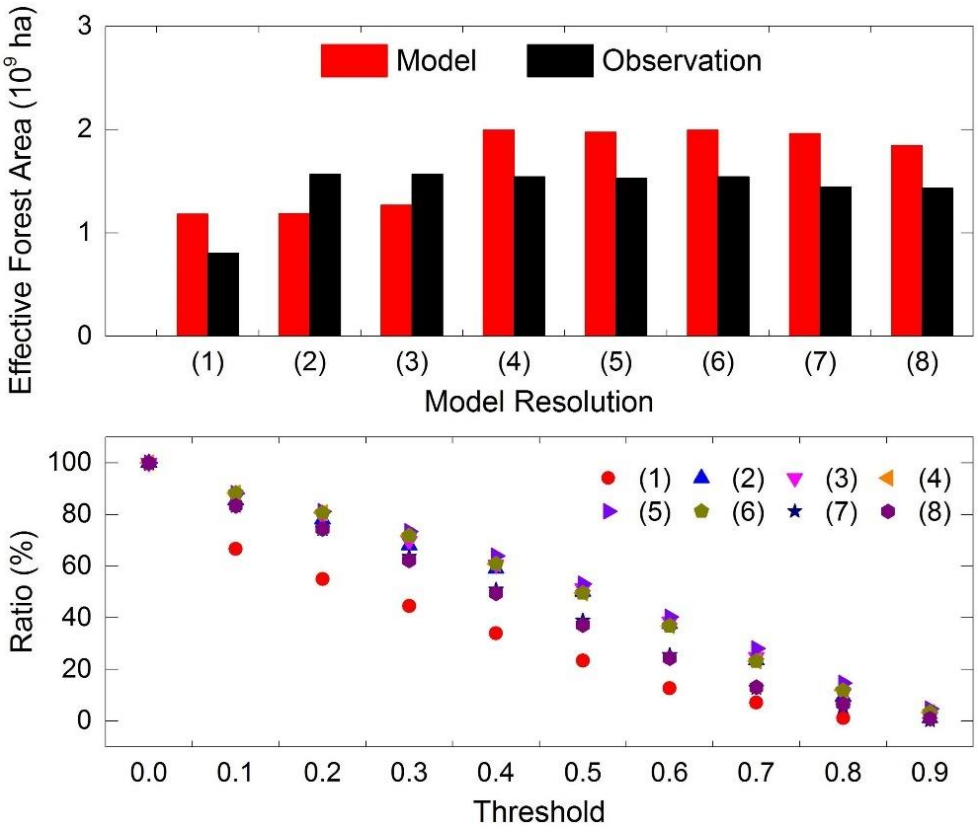


Figure 2-6. (Top) Effective forest area of forest total carbon mass at default forest threshold ($F_f = 0$) from model outputs (red) and from upscaled observations (black) during the contemporary period. A common-grid mask in both observed and modeled values is applied. (Bottom) The ratios of effective forest area at various forest fraction thresholds to that at $F_f = 0$. Models (1) – (8) are the same as shown in Figure 2-3.

levels produce grid cells more dominated by homogeneous forest types and thus minimize the inconsistencies of PFT definitions between ESMs and obsESMs. However, higher F_f thresholds result in less data availability. For example, by increasing F_f from 0 to 0.1, the effective forest area significantly reduces to two-thirds of its value at $F_f = 0$ for BNU-ESM and to 83–88% for the other ESMs (Figure 2-6). Therefore, this study applies $F_f = 0$ to avoid utilizing forest biomass data from only a few grid cells to represent all extratropical forest biomass over the Northern Hemisphere.

A further investigation on the similarity of the spatial patterns of forest biomass between ESMs and obsESMs is illustrated by Taylor diagrams (Figure 2-7). The ESMs, while able to capture the spatial distributions of forest biomass at high F_f levels, have huge variations in terms of carbon mass magnitude owing to different land cover types and forest fractions (Figure 2-7a). Correlations between the spatial patterns of simulated and observed forest carbon mass increase with F_f for all ESMs, while the variances of modeled forest biomass are generally greater than that of observed values since the normalized deviations are greater than one (except for MIROC-ESM at $F_f = 0.8$ and MIROC-ESM-CHEM at $F_f = 0.9$) (Figure 2-7b). BNU-ESM exhibits the lowest skill scores (see Equation (2.1) in Methods in this chapter) (0.006 ± 0.005) because it has the largest variance among all ESMs at all F_f levels (Figure 2-7a; Figure 2-8). The IPSL ESMs perform slightly better than BNU-ESM, but their large variances cause low skill scores (0.11 ± 0.04) as well (Figure 2-7a; Figure 2-8). Higher skill scores are found for the HadGEM2 ESMs (0.85 ± 0.10) and the MIROC ESMs (0.64 ± 0.14) (Figure 2-7b; Figure 2-8).

Magnitude of forest biomass uncertainty

The biases of masked global forest total carbon mass in each biomass compartment, including the lumped total biomass from all forest compartments and the biomass in leaves, in wood, and in roots, are investigated along with the combined wood and roots ("Wood + Root") to avoid inconsistent definitions of root biomass between ESMs (Negrón-Juárez et al., 2015). Results demonstrate that the biases of modeled global forest total carbon mass at $F_f = 0$ ranges from −20.3 Pg C in HadGEM2-CC to 134.7 Pg C in IPSL-CM5A-MR (Figure 2-9a). In terms of individual forest compartments, the combined

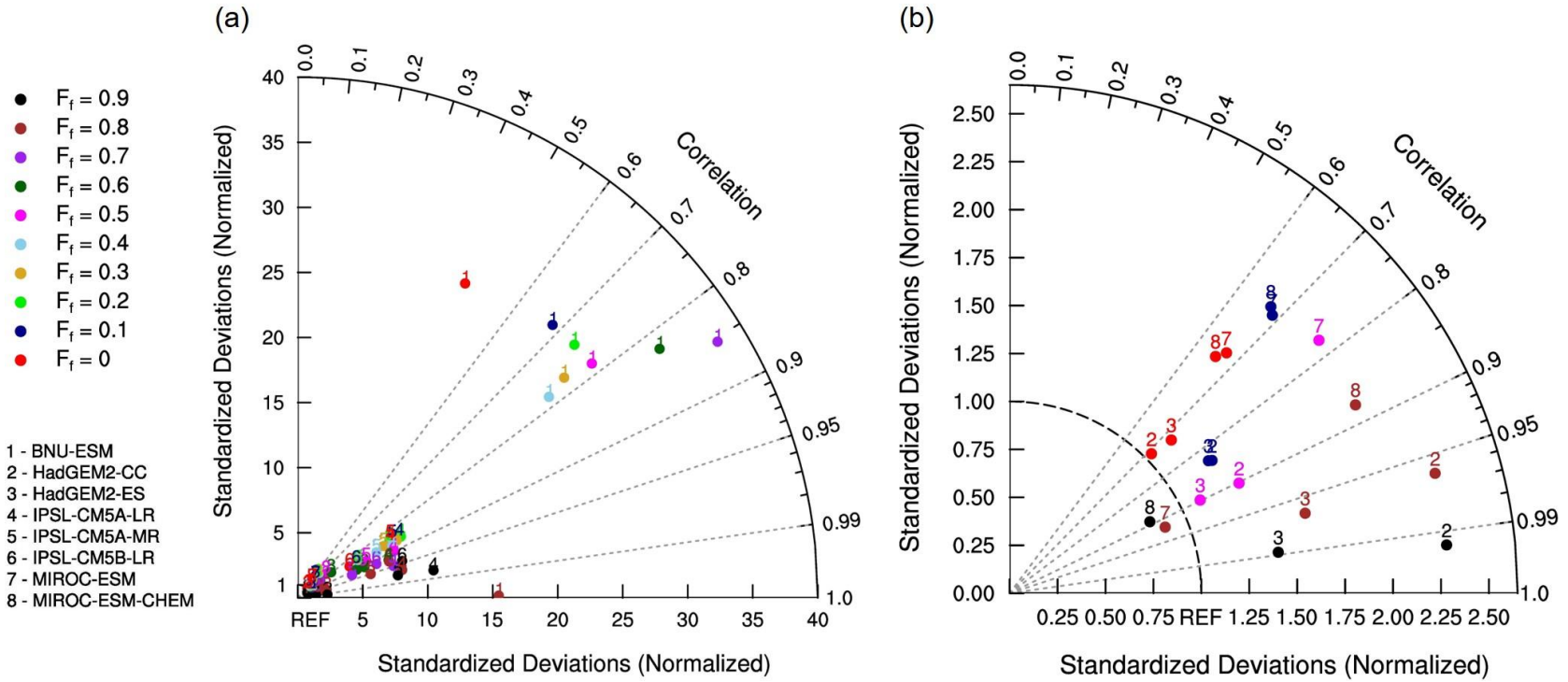


Figure 2-7. Taylor diagrams of (a) all model results and (b) model results of standardized deviations smaller than 2.5 for the northern extratropical forest carbon mass at various forest fraction thresholds (F_f) ranging from 0.0 to 0.9. Model numbers represent the CMIP5 models. Models (1) – (8) are the same as shown in Figure 2-3.

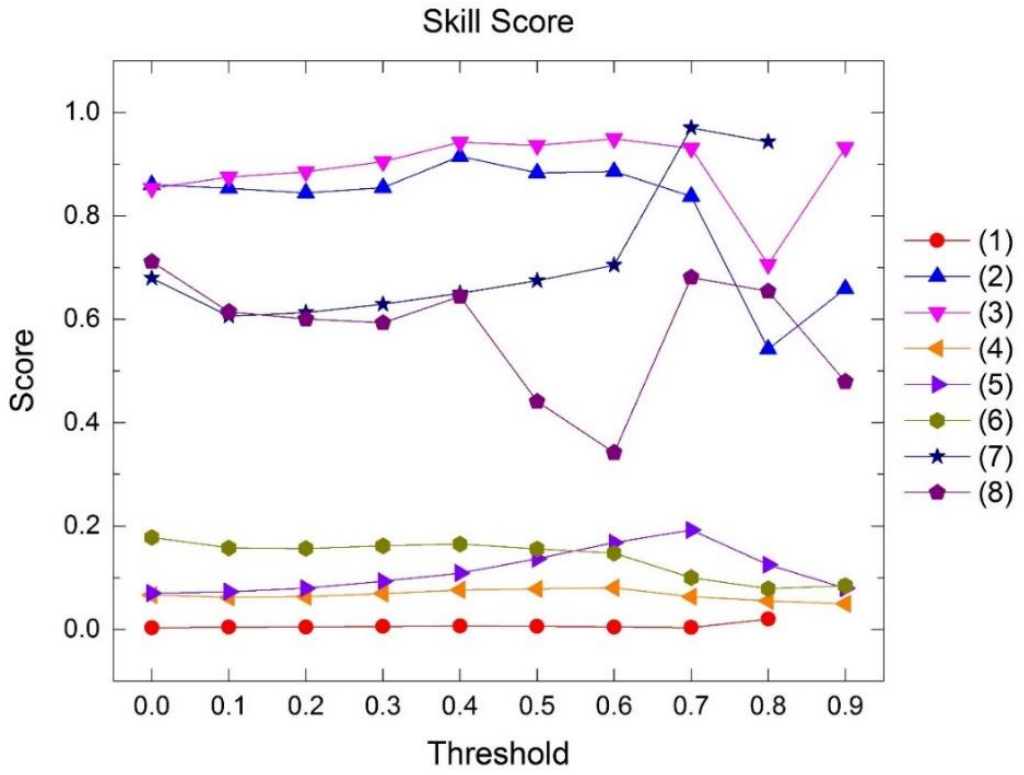


Figure 2-8. Skill scores for modeled global forest carbon mass in different forest fraction thresholds during the contemporary period. Models (1) – (8) are the same as shown in Figure 2-3.

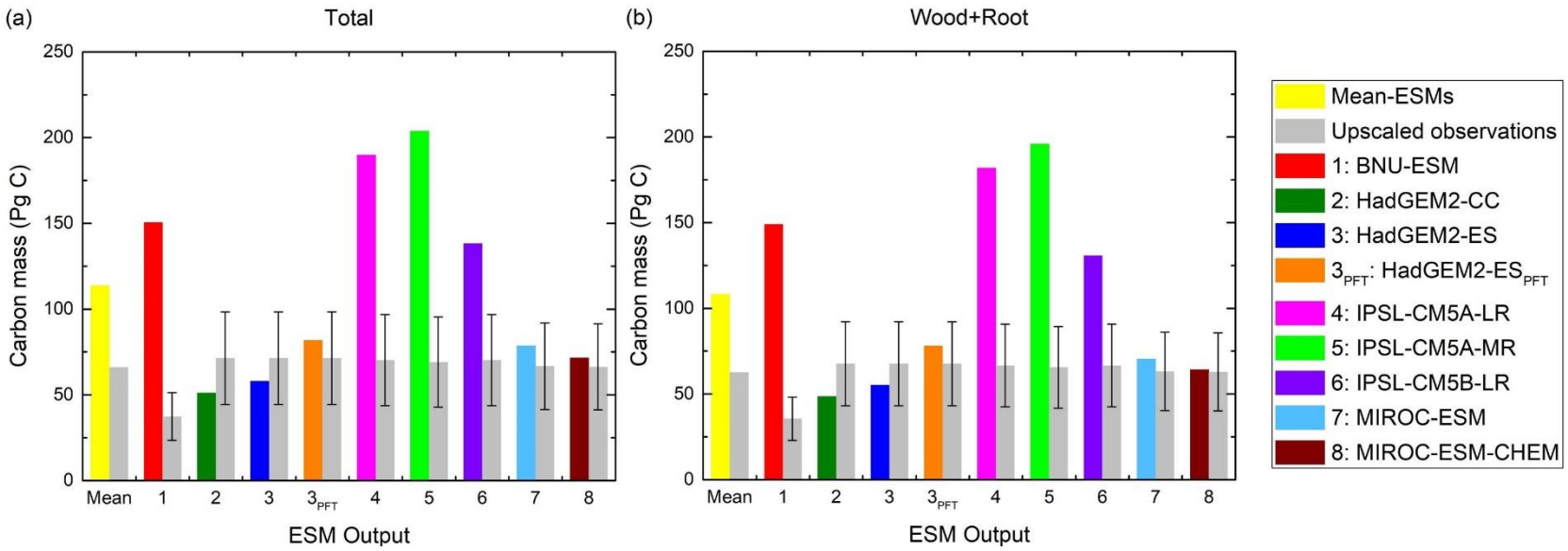


Figure 2-9. Global extratropical forest total carbon mass (Pg C) in the Northern Hemisphere for individual forest compartments: (a) all compartments, (b) wood and roots, (c) leaves, (d) wood, and (e) roots during the contemporary period at $F_f = 0$. Columns in light gray are the masked observations at each model resolution with error bars showing the uncertainty. The colored columns represent modeled results from BNU-ESM (1, red), HadGEM2-CC (2, green), HadGEM2-ES (3, blue), HadGEM2-ES with detailed PFT information (3_{PFT}, orange), IPSL-CM5A-LR (4, magenta), IPSL-CM5A-MR (5, light green), IPSL-CM5B-LR (6, violet), MIROC-ESM (7, light blue), and MIROC-ESM-CHEM (8, dark brown). The mean value (yellow) is the average of all model results. (a,b) and (d) use the same vertical scale while (c) and (e) use different vertical scales.

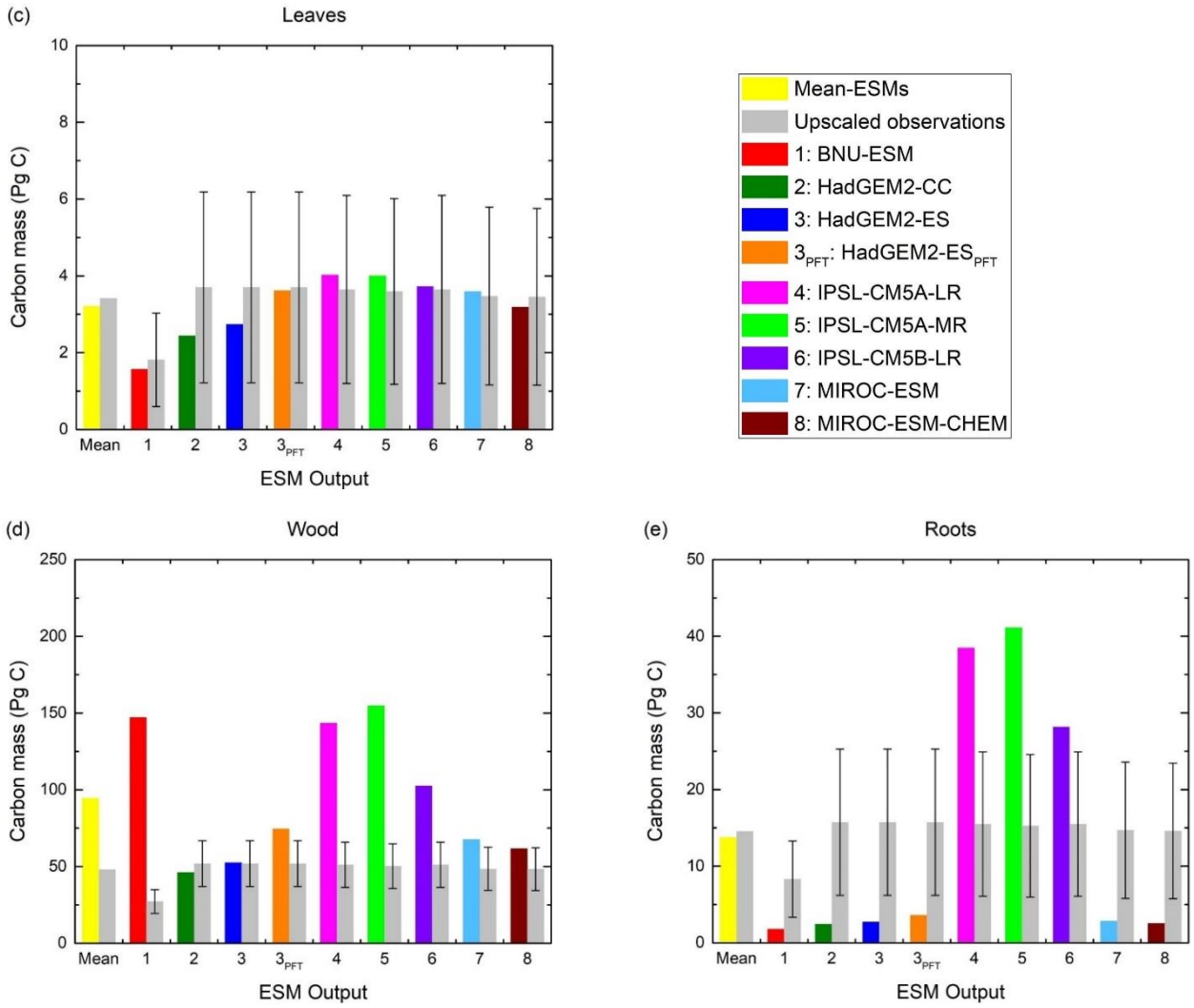


Figure 2-9 (*continued*).

Wood + Root biomass has biases ranging from −19.0 Pg C in HadGEM2-CC to 130.4 Pg C in IPSL-CM5A-MR (Figure 2-9b); the biases of biomass in leaves ranges from −1.3 Pg C in HadGEM2-CC to 0.4 Pg C in IPSL-CM5A-MR (Figure 2-9c); the biases of biomass in wood ranges from −5.7 Pg C in HadGEM2-CC to 120.0 Pg C in BNU-ESM (Figure 2-9d); the biases of biomass in roots ranges from −13.3 Pg C in HadGEM2-CC to 25.8 Pg C in IPSL-CM5A-MR (Figure 2-9e). A further examination on utilizing detailed biomass data at grid cell level rather than the grid area-weighted level from the HadGEM2-ES model results illustrates relatively smaller biases, though the bias of forest total biomass changes from negative (−13.4 Pg C) by utilizing grid area-averaged biomass data to positive (10.5 Pg C) by utilizing detailed biomass data at the grid cell level (Table 2-3). Compared to the mean value of forest total biomass from all obsESMs, that from all ESMs is overpredicted by 47.8 Pg C; for individual forest compartments, the mean value from all ESMs shows overpredicted forest biomass in Wood + Root by 43.4 Pg C, in wood by 41.5 Pg C, and in roots by 1.9 Pg C, while the biomass in leaves is underpredicted by 0.2 Pg C. Note that all ESMs predict the biomass in leaves within the uncertainty range of obsESMs, while BNU-ESM and the IPSL ESMs predict too much forest total biomass and biomass in Wood + Root due to overestimated biomass in wood (Figure 2-9d). The institutional mean values of forest biomass for each modeling center show enlarged magnitude of bias in total mass (7.7 Pg C) and biomass in Wood + Root (10.2 Pg C) compared to multi-model mean values. The increased bias of biomass in wood (14.8 Pg C) is the major cause of the increasing discrepancies, even though the institutional mean biomass in roots is reduced (−4.57 Pg C). Details of extratropical forest carbon mass across 30° N–80° N for each ESM and for each modeling center is shown in Table 2-3.

According to the masked forest biomass in ESMs and obsESMs, the magnitude of biases varies over a wide range. To minimize the influences of various masks applied to ESMs, we evaluate the model uncertainty in terms of relative errors (*ER*, see Equation (2.2) in Methods in this chapter) so that underestimates or overestimates in model results can be quantified in a standardized way. The multi-model *ER* average from the *ER*s of all ESMs shows that ESMs simulate excess forest total biomass (ER_{total} = 0.84), biomass in wood (ER_{wood} = 1.15), and biomass in Wood + Root ($ER_{wood+root}$ = 0.86), whereas

Table 2-3. Global total carbon mass (Pg C) of forest compartments across 30°N–80°N for CMIP5 models (*Model*) and upscaled observations (*Obs.*) at F_f = 0 during the contemporary period (Modern) and the pre-industrial (PI) periods. "Wood+Root" is the sum of biomass in wood and in roots. Modeling centers are the same as shown in Table 2-1. Model outputs are from (1) BNU-ESM, (2) HadGEM2-CC, (3) HadGEM2-ES, (3_{PFT}) HadGEM2-ES with detailed grid-level biomass for each PFT, (4) IPSL-CM5A-LR, (5) IPSL-CM5A-MR, (6) IPSL-CM5B-LR, (7) MIROC-ESM, and (8) MIROC-ESM-CHEM. Each modeling center (B), (C), and (D) has "Mean" values from the averages of all available model outputs within an institute. The "Multi-Model Mean" values are the averages of all model outputs (n = 9) whereas the "Institutional Mean" are the averages of the four modeling centers' mean values (n = 4). Note that in each model resolution a common grid mask is applied to both *Model* and *Obs.*

Modeling center	Model	Type	Total		Leaf		Wood		Root		Wood+Root	
			Modern	PI	Modern	PI	Modern	PI	Modern	PI	Modern	PI
(A)	(1)	*Obs.*	37.35	—	1.81	—	27.23	—	8.30	—	35.53	—
		Model	150.59	141.20	1.57	1.37	147.21	138.26	1.81	1.57	149.02	139.83
(B)	(2)	*Obs.*	71.36	—	3.70	—	51.93	—	15.73	—	67.66	—
		Model	51.11	68.15	2.44	3.31	46.23	61.52	2.44	3.31	48.67	64.83
	(3)	*Obs.*	71.36	—	3.70	—	51.93	—	15.73	—	67.66	—
		Model	58.01	74.16	2.74	3.61	52.54	66.95	2.74	3.61	55.27	70.55
	(3_{PFT})	*Obs.*	71.36	—	3.70	—	51.93	—	15.73	—	67.66	—
		Model	81.81	—	3.62	—	74.57	—	3.62	—	78.19	—
	Mean	*Obs.*	71.36	—	3.70	—	51.93	—	15.73	—	67.66	—
		Model	63.64	71.16	2.93	3.46	57.78	64.24	2.93	3.46	60.71	67.69

Table 2-3 (*continued*).

Modeling center	Model	Type	Total		Leaf		Wood		Root		Wood+Root	
			Modern	PI	Modern	PI	Modern	PI	Modern	PI	Modern	PI
(C)	(4)	*Obs.*	70.24	—	3.65	—	51.10	—	15.49	—	66.59	—
		Model	189.86	201.53	4.02	4.16	143.44	152.36	38.48	40.73	181.91	193.09
	(5)	*Obs.*	69.11	—	3.59	—	50.24	—	15.27	—	65.51	—
		Model	203.80	213.54	4.00	4.16	154.83	162.20	41.10	42.97	195.93	205.16
	(6)	*Obs.*	70.24	—	3.65	—	51.10	—	15.49	—	66.59	—
		Model	138.26	140.91	3.73	3.55	102.66	104.76	28.16	28.65	130.82	133.41
	Mean	*Obs.*	69.86	—	3.63	—	50.81	—	15.42	—	66.23	—
		Model	177.31	185.33	3.92	3.96	133.64	139.77	35.91	37.45	169.55	177.22
(D)	(7)	*Obs.*	66.70	—	3.47	—	48.53	—	14.69	—	63.22	—
		Model	78.73	110.38	3.59	4.51	67.73	96.51	2.85	3.64	70.58	100.14
	(8)	*Obs.*	66.33	—	3.46	—	48.28	—	14.60	—	62.88	—
		Model	71.64	118.55	3.19	4.77	61.78	104.06	2.58	3.77	64.36	107.83
	Mean	*Obs.*	66.52	—	3.47	—	48.41	—	14.65	—	63.05	—
		Model	75.19	114.47	3.39	4.64	64.76	100.29	2.72	3.71	67.47	103.99
Multi-Model Mean (n = 9)		*Obs.*	66.01	—	3.41	—	50.55	—	13.21	—	63.76	—
		Model	113.76	133.55	3.21	3.68	92.04	110.83	15.10	16.03	107.14	126.86
Institutional Mean (n = 4)		*Obs.*	61.27	—	3.15	—	44.59	—	13.52	—	58.12	—
		Model	116.68	128.04	2.95	3.36	100.85	110.64	10.84	11.55	111.69	122.18

underestimated biomass in leaves (ER_{leaf} = −0.06) and biomass in roots (ER_{root} = −0.10) are found at F_f = 0 (Figure 2-10; institutional-averaged results are shown in Figure 2-11). The overestimation of global forest total carbon mass is mainly a result of overestimated biomass in wood. All IPSL ESMs significantly overestimate forest biomass in all compartments (ER_{total} = 0.97–1.95, ER_{leaf} = 0.02–0.11, ER_{wood} = 1.01–2.08, ER_{root} = 0.82–1.69, and $ER_{wood+root}$ = 0.96–1.99), while HadGEM2-CC simulates too little forest biomass in all compartments (ER_{total} = −0.28, ER_{leaf} = −0.34, ER_{wood} = −0.11, ER_{root} = −0.84, and $ER_{wood+root}$ = −0.28). BNU-ESM exhibits the largest overestimates in forest total carbon amount by more than three times the observational estimate (ER_{total} = 3.03) due to extremely overestimated biomass mass in wood (ER_{wood} = 4.41). For individual forest compartments, MIROC-ESM-CHEM has the smallest deviation from observations for forest total biomass (ER_{total} = 0.08) and for biomass in Wood + Root ($ER_{wodd+root}$ = 0.02); IPSL-CM5B-LR shows the smallest deviation for biomass in leaves (ER_{leaf} = 0.02); HadGEM2-ES shows the smallest deviation for biomass in wood (ER_{wood} = 0.01); BNU-ESM shows the smallest deviation for biomass in roots (ER_{root} = 0.04). Similar to the magnitude of forest carbon mass, utilizing detailed PFT-level biomass data from HadGEM2-ES results in better model performance with smaller absolute ER magnitude (except for biomass in wood) compared to using grid area-weighted biomass products (Figure 2-10a). The *ER* value changes from −0.19 to 0.15 for forest total biomass, from −0.18 to 0.16 for biomass in Wood + Root, from −0.26 to −0.02 for biomass in leaves, from 0.01 to 0.44 for biomass in wood, and from −0.83 to −0.77 for biomass in roots.

All ESMs exhibit positive global-averaged relative errors at grid cell level (ER_{grid}, see Equation (2.3) in Methods in this chapter) in all compartments at F_f = 0 (Figure 2-10b; institutional-averaged results are shown in Figure 2-11), indicating all ESMs overestimate forest biomass. The magnitude of absolute ER_{grid} values can be two to three orders of magnitude larger than *ER*. The largest relative errors for forest total biomass ($ER_{grid,total}$) and for individual forest compartments ($ER_{grid,leaf}$, $ER_{grid,wood}$, $ER_{grid,root}$, and $ER_{grid,wood+root}$) at grid cell level are found in IPSL-CM5A-LR ($ER_{grid,total}$ = 281.0, $ER_{grid,leaf}$ = 55.4, $ER_{grid,wood}$ = 327.3, $ER_{grid,root}$ = 207.7, $ER_{grid,wood+root}$ = 287.3). BNU-ESM has the smallest relative error for biomass in leaves ($ER_{grid,leaf}$ = 20.6) and in roots ($ER_{grid,root}$ = 10.1),

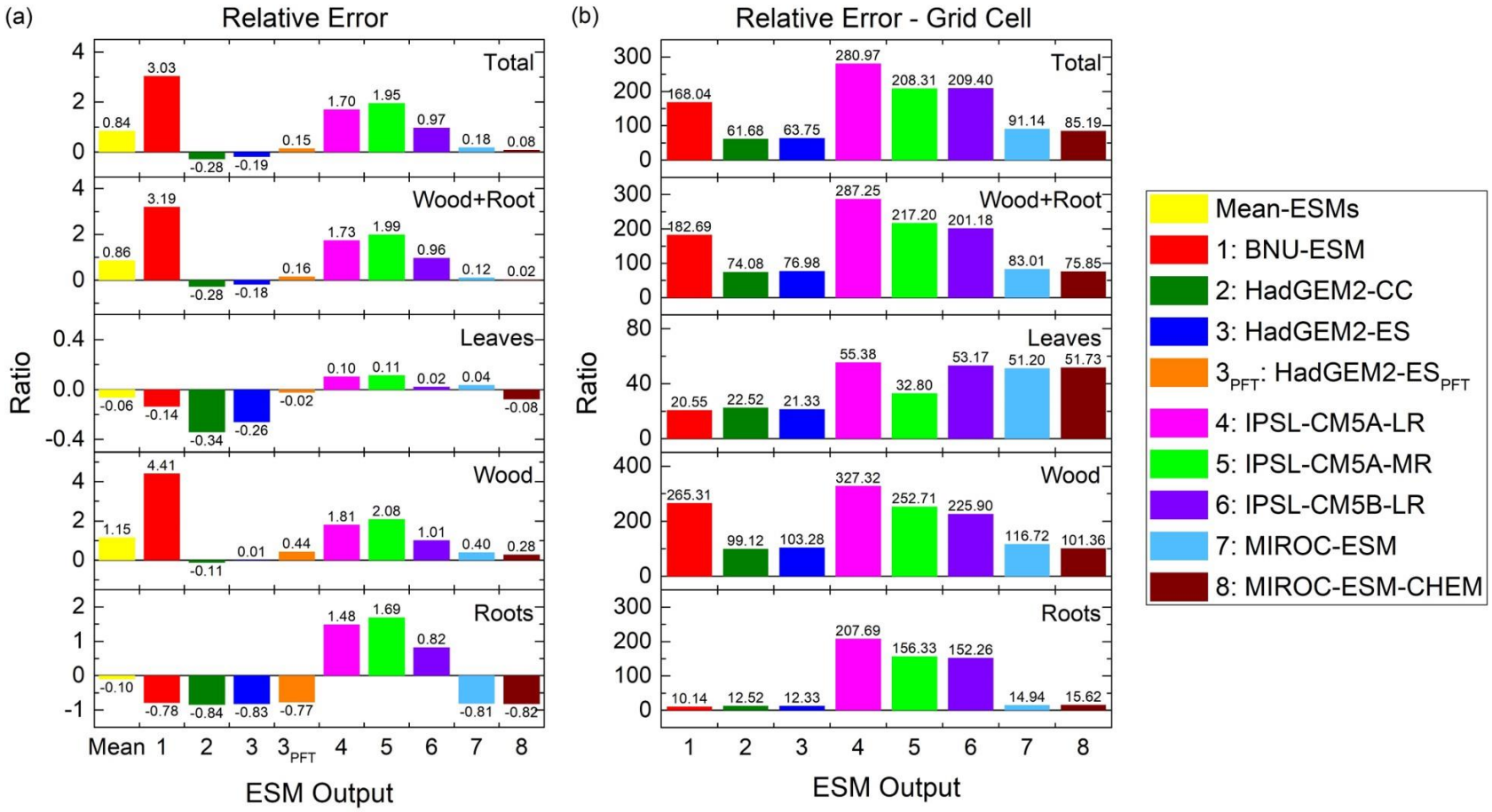


Figure 2-10. Relative errors for (a) global forest total carbon mass and (b) averaged forest total carbon mass at grid cell level during the contemporary period. Each sub-panel (top to bottom) represents all compartments (Total), wood and roots (Wood+Root), leaves, wood, and roots at $F_f = 0$. Model numbers are the same as used in Figure 2-9.

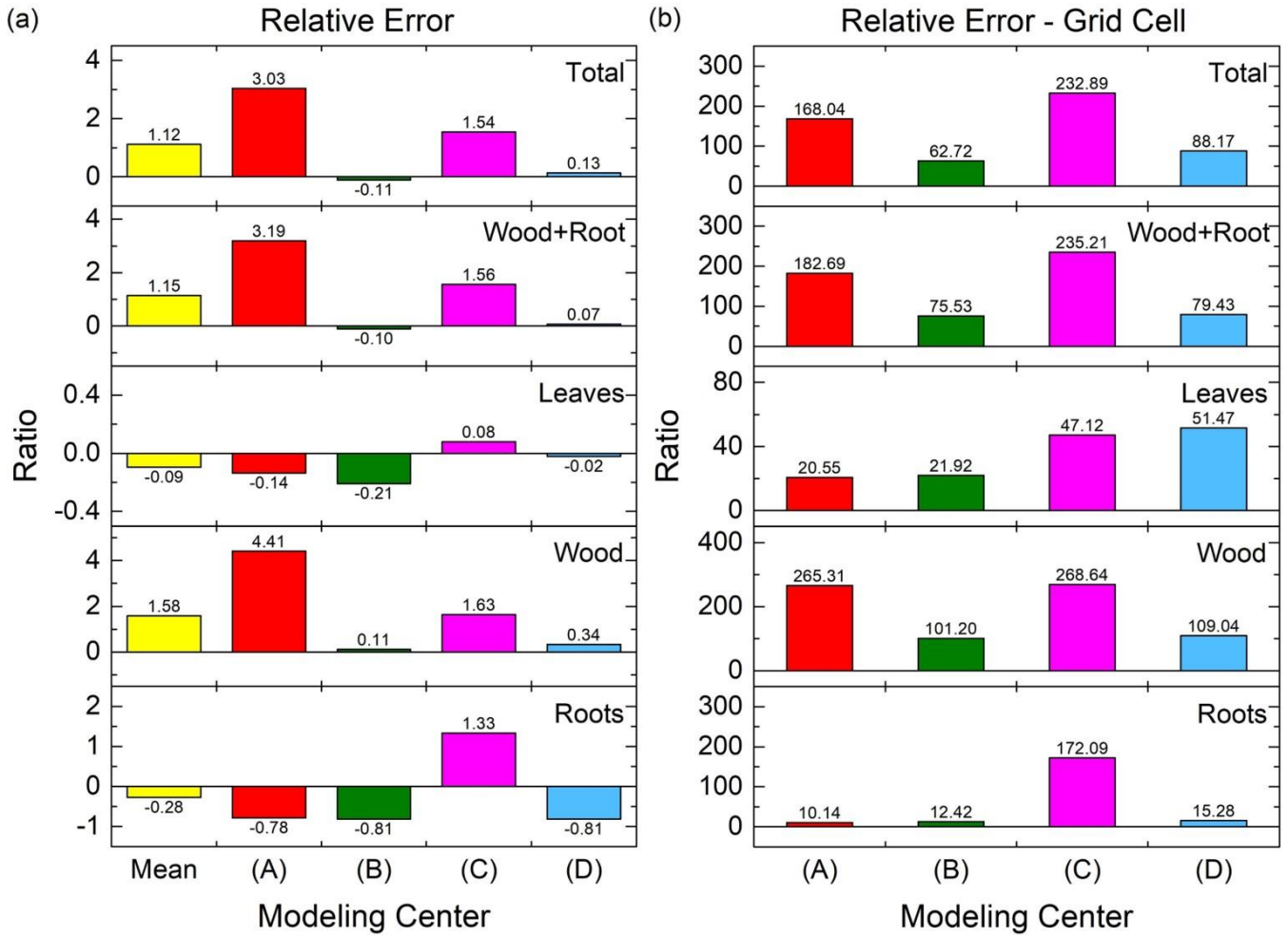


Figure 2-11. Institutional averaged (a) relative errors and (b) relative errors at grid cell level for individual forest compartments (top to bottom) during the contemporary period: all compartments, wood and roots, leaves, wood, and roots. Letters for modeling centers are the same as used in Table 2-1. "Mean" represents the average of all four modeling centers' outputs.

whereas HadGEM2-CC has the smallest relative errors for forest total biomass ($ER_{grid,total}$ = 61.68) and biomass in wood ($ER_{grid,wood}$ = 99.12) and in Wood + Root ($ER_{grid,wood+root}$ = 74.08) at grid cell level. These huge relative errors at grid cell level imply that ESMs exhibit substantial overestimates at certain grid cells in which observed forest biomass is very small and thus large variations of forest biomass at grid cell level are expected for all ESMs (Table 2-4).

Carbon allocation to forest compartments

Global carbon mass allocated in forest biomass compartments for all but the IPSL ESMs is consistently over-apportioned to wood but under-apportioned to leaves and roots (Figure 2-12). The carbon allocation to forest compartments for all obsESMs ranges from 93.7–97.4% in Wood + Root, 2.6–6.3% in leaves, 67.9–83.3% in wood, and 13.9–25.9% in roots, while the mean values of all obsESMs with one standard deviation are 96.5% ± 1.5%, 3.5% ± 1.5%, 87.1% ± 7.9%, and 9.4% ± 8.5%, respectively. All IPSL ESMs apportion carbon mass to wood and to roots, with an institutional average of 76.96% ± 0.59% for the former and 20.73% ± 0.19% for the latter, the closest to the observed values. The institutional averages from the two MIROC ESMs and from the two HadGEM2 ESMs are found to allocate the carbon mass in Wood + Root (95.25% ± 0.04% for HadGEM2 ESMs and 95.22% ± 0.09% for MIROC ESMs) and in leaves (4.75% ± 0.04% for HadGEM2 ESMs and 4.78% ± 0.09% for MIROC ESMs) the closest to the observations. These results suggest that the HadGEM2 ESMs and the MIROC ESMs combine the biomass of coarse roots into the woody biomass pool, so that too much carbon is apportioned to wood and too little is apportioned to roots; on the contrary, the IPSL ESMs likely define the carbon mass in roots as the sum of coarse and fine root carbon mass since the carbon allocations are closer to the observed values.

Spatial covariation of forest total biomass and climatic conditions

The spatial correlations of forest total biomass and climatic conditions are generally consistent in ESMs and obsESMs in terms of the high positive correlations between biomass and precipitation (PR) at midlatitudes (30°N–60°N), while surface temperature

Table 2-4. Grid cell-level relative errors of all compartments ($ER_{grid,total}$), leaves ($ER_{grid,leaf}$), wood ($ER_{grid,wood}$), roots ($ER_{grid,root}$), and wood plus roots ($ER_{grid,wood+root}$) for each model during the contemporary period at $F_f = 0$. Numbers represent global mean and one standard deviation of ER_{grid} values for all available grid cells after masks applied. Model numbers are the same as shown in Figure 2-3.

Model	$ER_{grid,total}$	$ER_{grid,leaf}$	$ER_{grid,wood}$	$ER_{grid,root}$	$ER_{grid,wood+root}$
(1)	168.0±1702.5	20.6±202.6	265.3±2811.7	10.1±151.4	182.7±1853.9
(2)	61.7±1665.8	22.5±332.5	99.1±2839.9	12.5±296.6	74.1±2093.3
(3)	63.8±1792.9	21.3±339.5	103.3±3061.8	12.3±307.5	77.0±2253.7
(4)	281.0±2876.4	55.4±502.1	327.3±3628.5	207.7±2116.5	287.3±3126.4
(5)	208.3±2009.3	32.8±284.8	252.7±2551.8	156.3±1535.6	217.2±2115.1
(6)	209.4±2234.3	53.2±480.4	225.9±2722.1	152.3±1622.1	200.9±2355.7
(7)	91.1±893.0	51.2±574.4	116.7±1206.0	14.9±167.0	83.0±841.8
(8)	85.2±886.0	51.7±531.8	101.4±1114.7	15.6±168.6	75.9±844.5

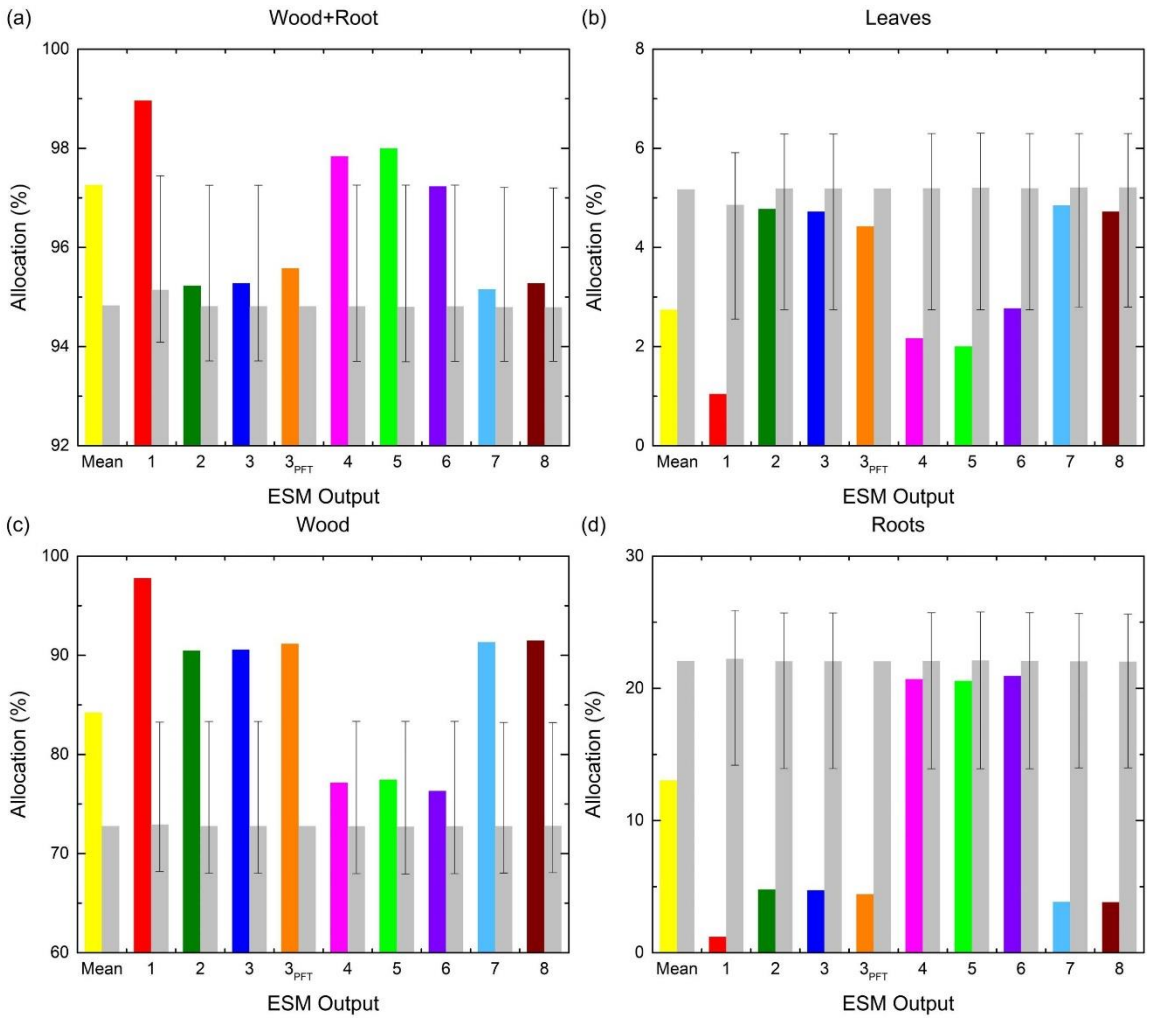


Figure 2-12. Allocations of global forest total carbon mass in (a) wood and roots, (b) leaves, (c) wood, and (d) roots during the contemporary period at $F_f = 0$. Model numbers and colors are the same as used in Figure 2-9. (a) and (c) use the same vertical scale while (b) and (d) use different vertical scales

(TAS) becomes as important as PR at high latitudes (60°N–75°N) (Figure 2-13). Due to the data aggregation process at different grid resolutions, some minor discrepancies exist between obsESMs, even the ones from the same modeling center (Figure 2-14). The three major inconsistent signals between ESMs and obsESMs are located in Alaska, northern China, and Scandinavia. In Alaska, the observations show positive correlations of forest total biomass with only TAS while both HadGEM2 ESMs show positive correlations of forest total biomass with both PR and TAS; IPSL-CM5A-MR and the MIROC ESMs capture the responses of forest total biomass to PR and TAS relatively better than the other ESMs. In northern China, models with higher resolutions (HadGEM2 ESMs and IPSL-CM5A-MR) exhibit weak positive correlations between forest total biomass and TAS, whereas the variations of forest total biomass are weakly negatively correlated with PR. These signals are not seen in either observations or ESMs at lower resolutions. In Scandinavia, the observed forest carbon mass at different model resolutions shows negative forest biomass responses to both PR and TAS changes. All IPSL and MIROC ESMs demonstrate similar results except that MIROC-ESM-CHEM shows a positive correlation between observed forest total biomass and PR in western Russia, while a negative correlation is found in the model (Figure 2-14). In contrast, forest total biomass is positively correlated to changes of PR and TAS in BNU-ESM and the HadGEM2 ESMs. Overall, the correlations of spatial variations in forest total biomass to that in PR and in TAS for IPSL-CM5A-MR are closer to the observations. A further analysis of the forest biomass in climatic PR–TAS space on a Whittaker diagram (Whittaker, 1975) highlights the spatial distributions of forest biomes in ESMs as compared with obsESMs. For this analysis, we combined all model forest PFTs into four biome categories—broadleaf evergreen tree, needleleaf evergreen tree, broadleaf deciduous tree, and needleleaf deciduous tree—except for the HadGEM2 ESMs, which were grouped into broadleaf tree and needleleaf tree only because of its simplified PFT representation (Tables 2-2 and 2-5). We found that ESMs roughly capture the spread of forest biomes in the Northern Hemisphere extratropics, except that ESMs have very few grid cells representing forests below −10 °C (Figure 2-15). The masked observational biomass in the modeled PR–TAS space, compared to that in the observed PR–TAS space, also shows fewer grid cells

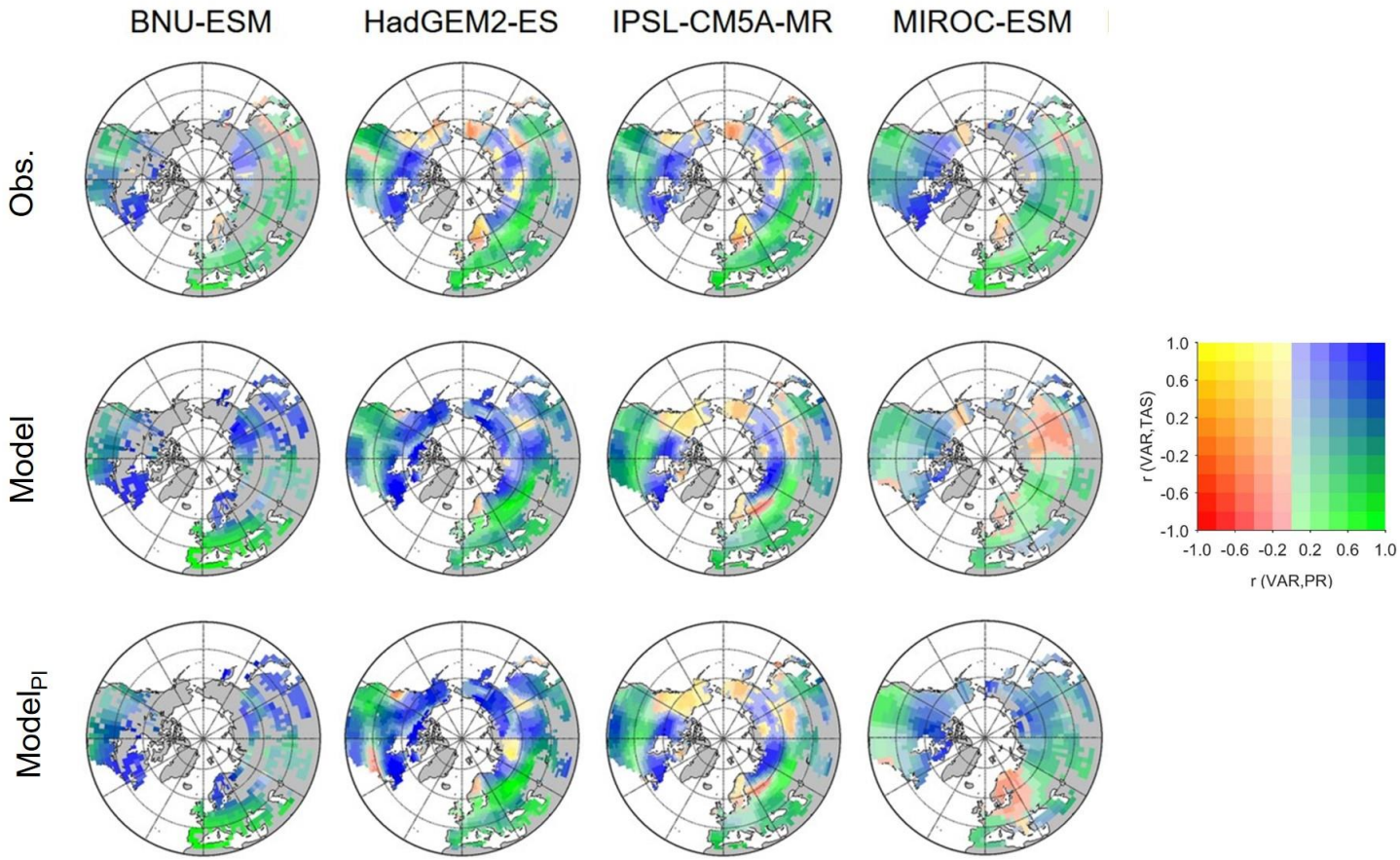


Figure 2-13. Global correlation maps of observation (top row), model outputs during the contemporary period (middle row), and model outputs at pre-industrial period (bottom row) for each model resolution. Missing data on land is shown in gray color. The color table represents the magnitude of correlations between forest total carbon mass and precipitation (horizontal) and between forest total carbon mass and surface temperature (vertical). Grid resolutions include (left to right): BNU-ESM, HadGEM2-ES, IPSL-CM5A-MR, and MIROC-ESM.

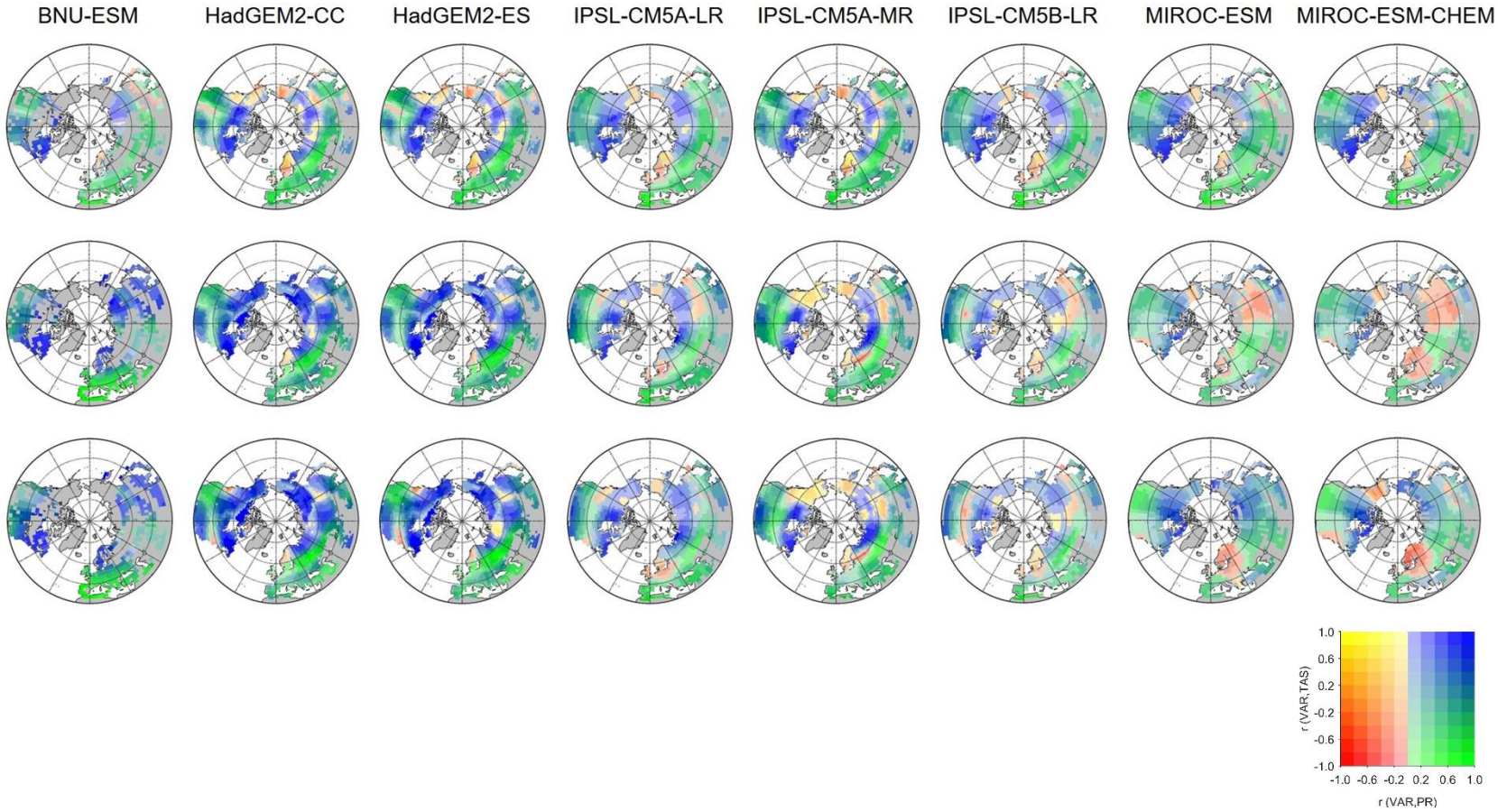


Figure 2-14. Same as Figure 2-13 except for all ESM resolutions (left to right, columnwise): BNU-ESM, HadGEM2-CC, HadGEM2-ES, IPSL-CM5A-LR, IPSL-CM5A-MR, IPSL-CM5B-LR, MIROC-ESM, and MIROC-ESM-CHEM.

Table 2-5. Forest type definitions for Whittaker diagrams. Modeling centers (A) – (D) are the same as shown in Table 2-1. Numbers represent the PFT classes defined in Table 2-2. Forest types include broadleaf evergreen trees (BET), needleleaf evergreen trees (NET), broadleaf deciduous trees (BDT), and needleleaf deciduous trees (NDT). Note that MOHC models only have broadleaf trees (BT) and deciduous trees (DT).

Dataset	BET	NET	BDT	NDT	BT	NT
GLC2000	1	4	2, 3	5	1, 2, 3	4, 5
(A)	4, 5	1, 2	6, 7, 8	3	—	—
(B)	—	—	—	—	1	2
(C)	2, 5	4, 7	3, 6, 8	9	—	—
(D)	1	2, 4	3	5	—	—

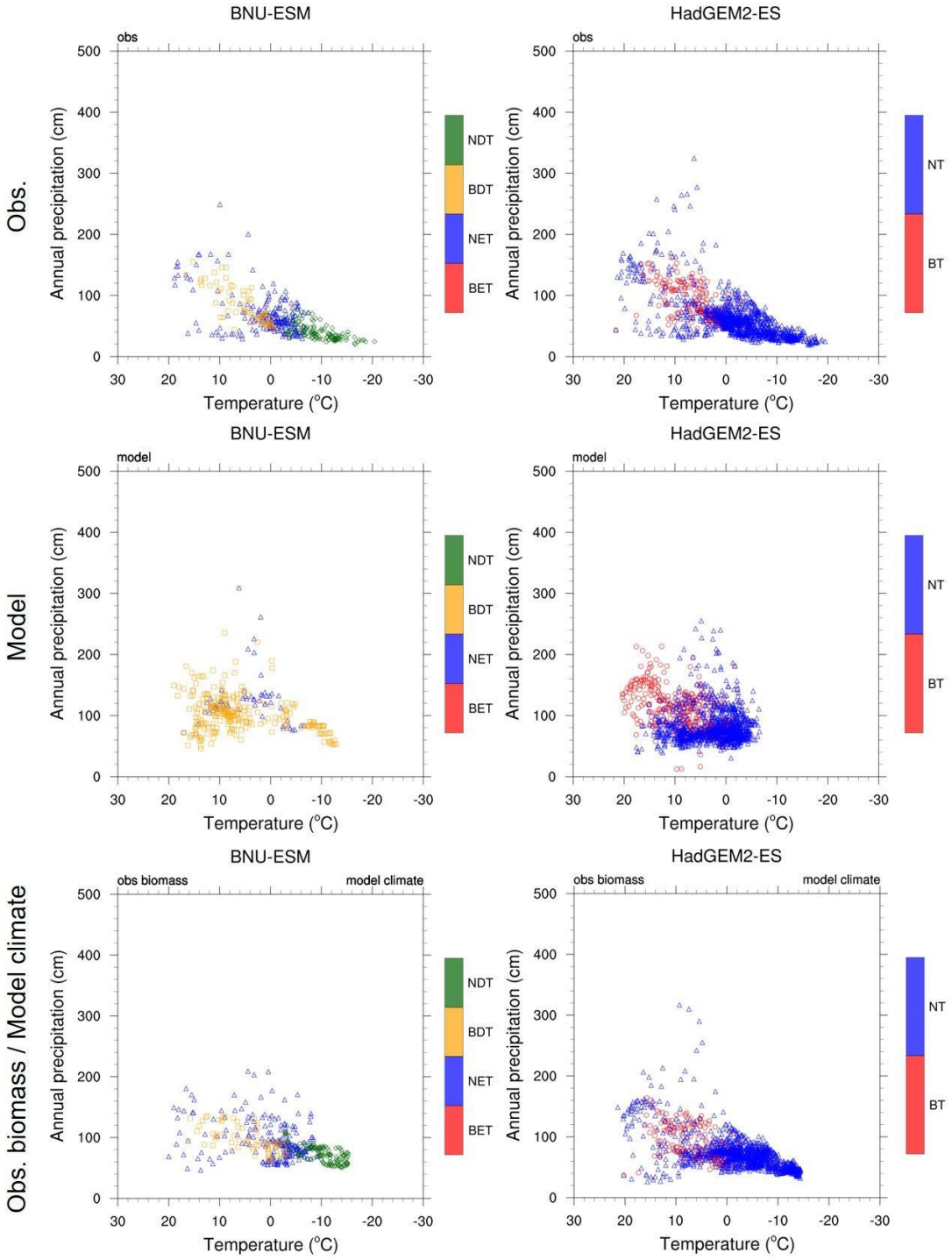


Figure 2-15. Whittaker diagrams of various forest types (F_f = 0.2) for upscaled observations (top row), models (center row), and observed biomass in modeled climate space for BNU-ESM (left) and HadGEM2-ES (right) during the contemporary period. Colors represent different PFT categories defined in Table 2-3.

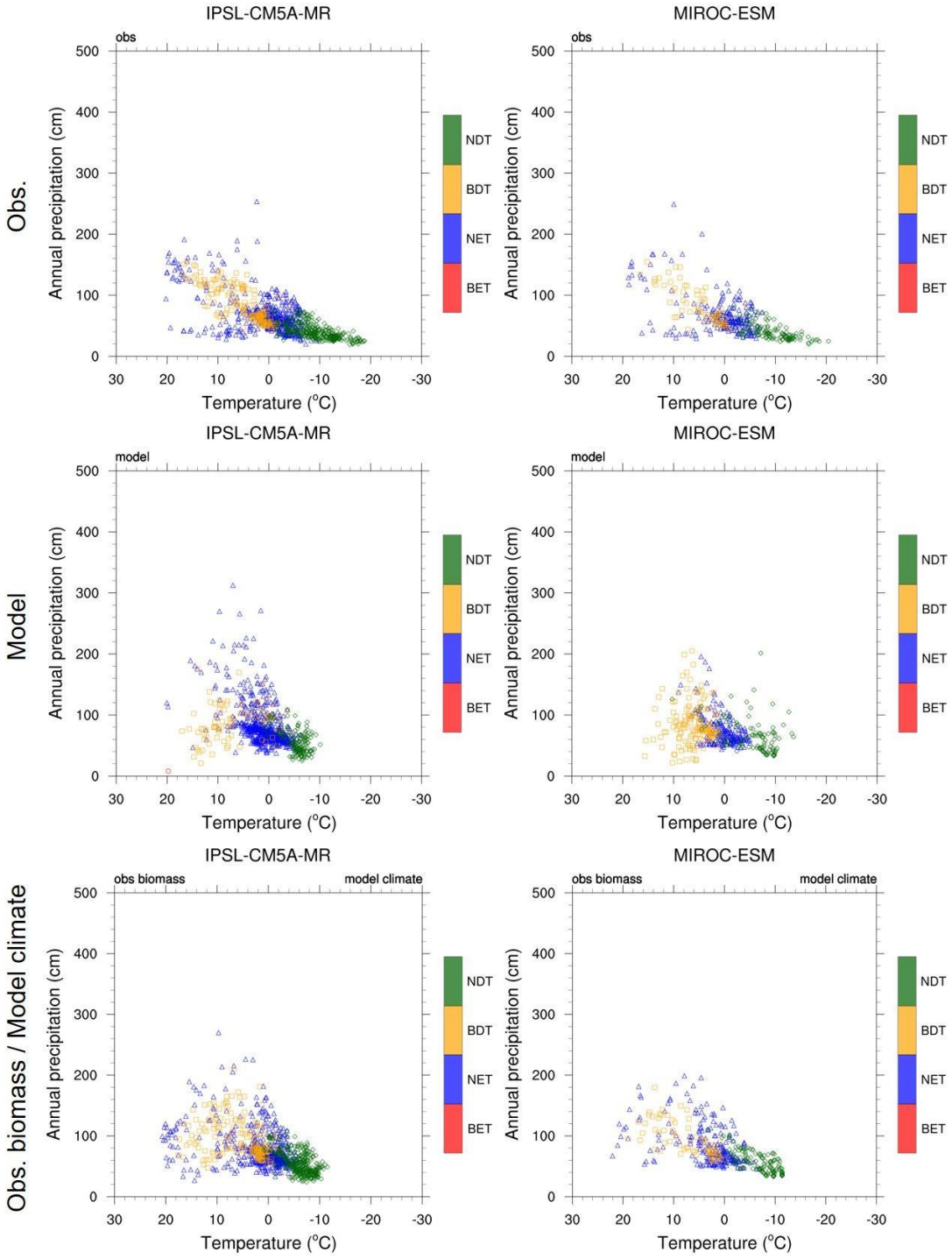


Figure 2-15 (*continued*). Whittaker diagrams of various forest types (F_f = 0.2) for upscaled observations (top row), models (center row), and observed biomass in modeled climate space for IPSL-CM5A-MR (left) and MIROC-ESM (right) during the contemporary period: Colors represent different PFT categories defined in Table 2-3.

representing forests below −15 °C implying biases in modeled climatic conditions. Among the ESMs, only BNU-ESM shows broadleaf deciduous forests spanning a wide range in TAS, from −10 °C to 20 °C, while the observations indicate a narrower range for these forests.

Spin-up impacts

The ratios of ER_{grid} for four forest types (Table 2-6) during the PI period over that during the contemporary period are calculated as an index (*SR*, see Equation (2.4) in Methods in this chapter) for evaluating the uncertainty caused by the spin-up processes. For individual forest compartments at $F_f = 0$, BNU-ESM shows that *SR* values are close to unity in forest total biomass ($SR_{total} = 1.02$) and biomass in leaves ($SR_{leaf} = 0.76$), in wood ($SR_{wood} = 1.03$), and in roots ($SR_{root} = 0.51$). Similar to BNU-ESM, the mean *SR* values of all forest compartments simulated by the IPSL ESMs are also close to unity (SR_{total} = 0.95±0.05, SR_{leaf} = 1.08±0.06, SR_{wood} = 0.94±0.06, SR_{root} = 0.95±0.05) (Figure 2-16). These results imply the uncertainty may have been introduced at the beginning of the simulations in the ESMs due to the initial conditions derived from spin-up output. Similar unity *SR* values are also found in individual forest types, especially for the broadleaf and for the deciduous forests for the ESMs from these two modeling centers. On the contrary, moderate to substantial differences of ER_{grid} values for the HadGEM2 ESMs (SR_{total} = 1.92±0.43, SR_{leaf} = 2.49±0.21, SR_{wood} = 1.85±0.45, SR_{root} = 2.17±0.23) and the MIROC ESMs (SR_{total} = 5.18±0.82, SR_{leaf} = 3.91±0.43, SR_{wood} = 6.42±1.66, SR_{root} = 4.94±0.42), especially MIROC-ESM-CHEM ($SR_{total} = 5.76$, $SR_{leaf} = 4.21$, $SR_{wood} = 7.60$, $SR_{root} = 5.23$), suggest uncertainty carried from the spin-up outputs due to vegetation parameterizations are minimized in these ESMs.

Discussion

The present study evaluates the uncertainty of forest biomass across northern extratropical latitudes from eight coupled ESM simulations. Instead of regridding all ESM outputs and a recent observation-based data to a common grid resolution that induces additional uncertainty, we aggregate the fine-resolution observational data to the same grid

Table 2-6. Definitions of forest types in GLC2000 and each modeling center. Modeling centers (A) – (D) are the same as shown in Table 2-1. Numbers represent the classes defined in Table 2-2. Unavailable land types are denoted by *N/A*. The GLC2000 forest definition is adopted from Thurner et al. (2014).

Forest Type	GLC2000	(A)	(B)	(C)	(D)
Broadleaf	1–3	5, 7, 8	1	5, 6, 8	*N/A*
Needleleaf	4, 5	1, 2, 3	2	4, 7, 9	*N/A*
Evergreen	1, 4	1, 2, 5	*N/A*	4, 5, 7	2, 4
Deciduous	2, 3, 5	3, 7, 8	*N/A*	6, 8, 9	3, 5
Lumped	1–10	1–3, 5, 7, 8	1, 2	4–9	2–5

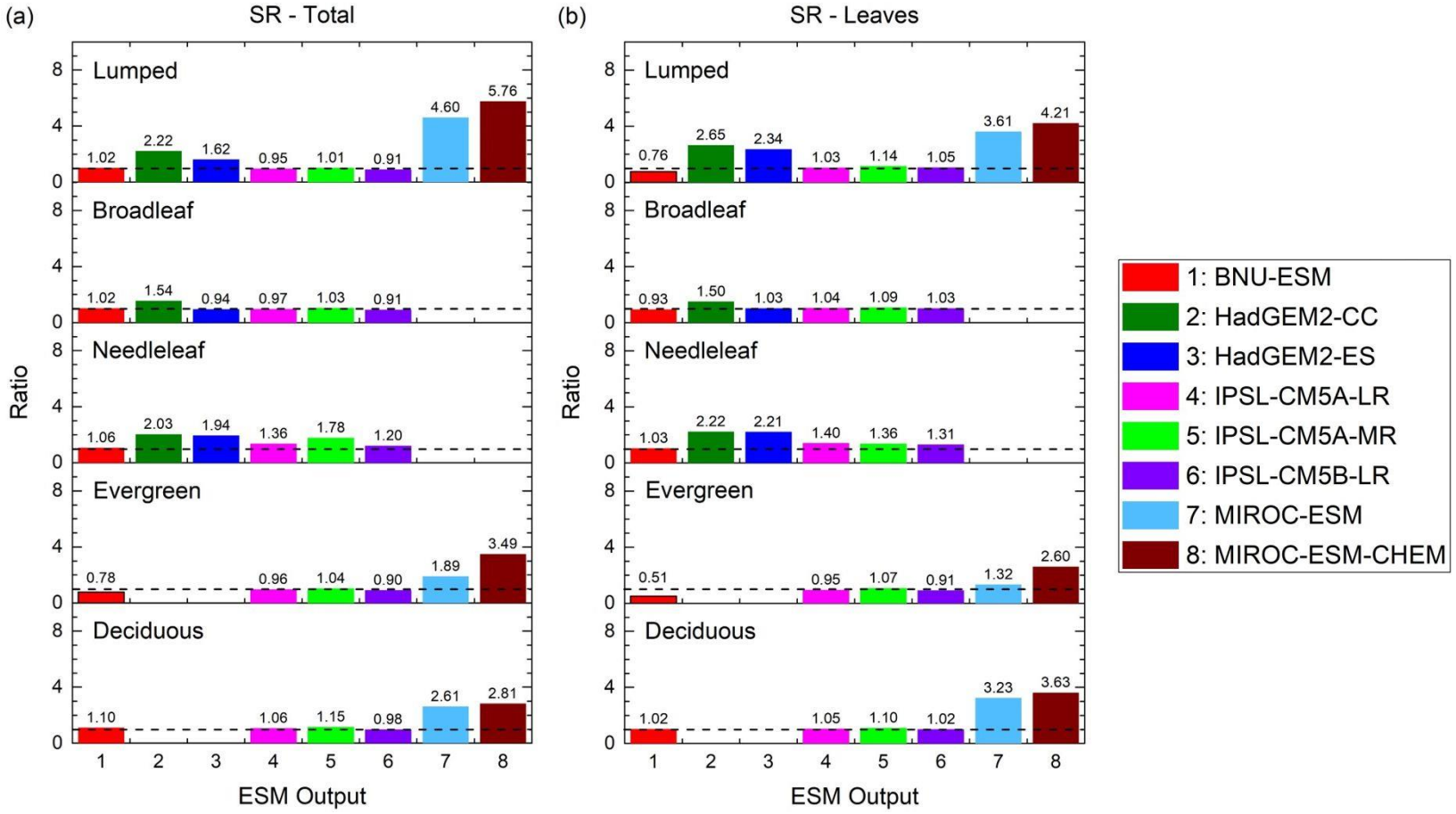


Figure 2-16. Ratios for global mean relative errors of masked carbon mass at grid cell level during the pre-industrial period to that during the contemporary period at $F_f = 0$. Forest compartments include (a) all compartments, (b) leaves, (c) wood, and (d) roots. The colors and model numbers are the same as used in Figure 2-9. Forest types in each sub-panel (top to bottom): lumped, broadleaf, needleleaf, evergreen, and deciduous trees. Dashed lines represent $SR = 1$.

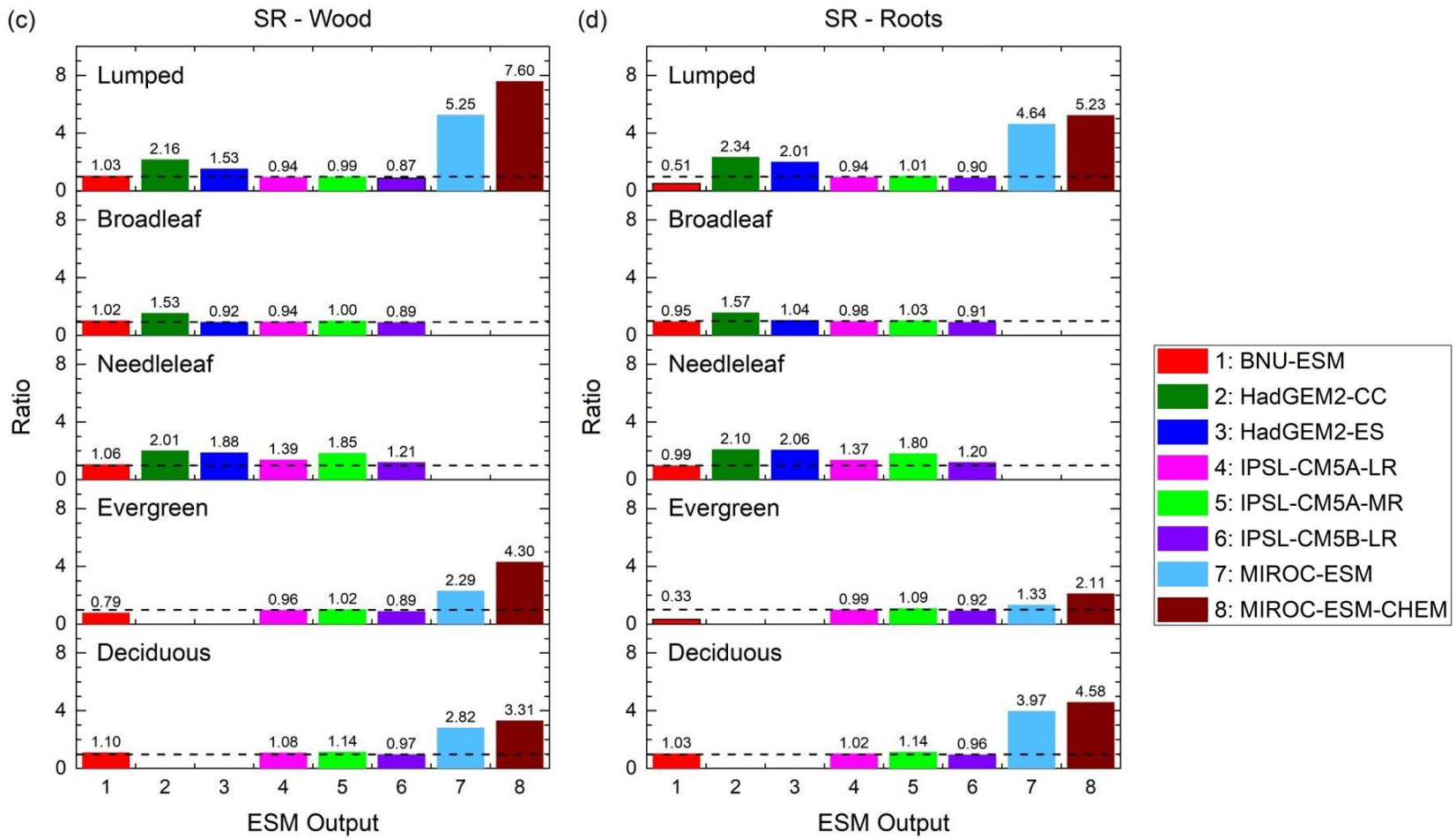


Figure 2-16 (*continued*).

resolution of each ESM so that each ESM output can be compared fairly to the aggregated observations. We examine the sources of uncertainty of forest biomass estimates through the forest fractions, the magnitude of carbon mass differences, the carbon mass allocations in forest compartments, and the biases carried from the spin-up results. Inconsistent definitions of PFTs between ESMs and observations contribute to the uncertainty of forest spatial distributions and thus large variations of forest fractions and biomass in each grid cell are found in ESMs (Poulter et al., 2011). After masks are applied, such inconsistencies cause significant differences in effective forest area among ESMs and among obsESMs. We also find that the unmasked total carbon mass in each aggregated observation data set for different ESM grid resolutions is the same but becomes smaller after forest-only masks are applied to grid cells (Figure 2-17). The magnitude of discrepancy in modeled forest fraction and total biomass can be up to 0.98 and up to 1.63 Pg C, respectively, compared to the aggregated observations at the grid cell level. The bias of masked forest total biomass estimates in the northern extratropical region ranges from −20.3 Pg C to 134.7 Pg C and is mainly attributed to the bias in the wood compartment (−5.7 Pg C to 120.0 Pg C). In addition, CMIP5 models typically do not output the varying carbon density for all available PFTs within a grid cell. Some of the forest biomass uncertainty results from aggregation of PFT-level carbon pools to the grid cell level for purposes of reporting. This causes the loss of carbon density heterogeneity at the grid cell level and tends to lead to larger biases in carbon mass estimates. Analysis of HadGEM2-ES outputs with detailed PFT-level carbon pools demonstrates a reduction in modeled forest total carbon mass bias of 2.9 Pg C compared to the grid cell-level data reported in the CMIP5 archive. Hence, we suggest adding detailed PFT-level output of carbon stock and flux variables in CMIP6 simulations so that the uncertainty in future carbon mass estimates reported to the Sixth Assessment Report of the Intergovernmental Panel on Climate Change can be attributed to ecosystem processes for each PFT. While causes of individual variations among model estimates of biomass are difficult to ascertain, multiple sources of uncertainty, as described below, contribute, including prognostic vegetation dynamics, land use and land cover change, and carbon allocation.

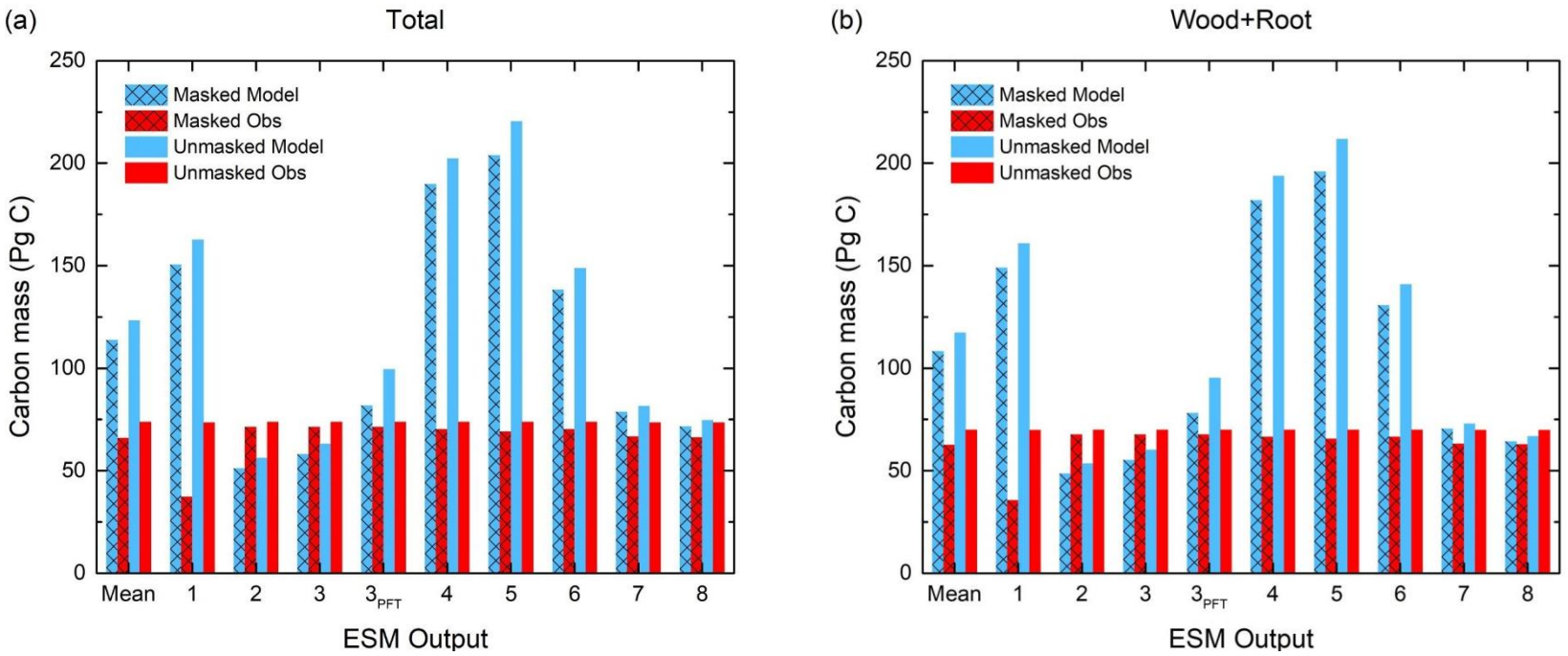


Figure 2-17. Mask and unmasked (checkered columns) forest total carbon mass (Pg C) for ESM outputs (blue) and upscaled observational data sets (red) in (a) total biomass, (b) wood and roots, (c) leaves, (d) wood, and (e) roots during the contemporary period. ESM numbers are the same as used in Table 2-5. "Mean" represents the average of all ESM outputs.

For the uncertainty of forest total carbon mass, our analyses show that four of the ESM simulations, if observational uncertainty is considered, overestimate the total carbon mass mainly due to overestimated biomass in wood. Since all ESMs consider carbon cycle feedbacks and land use change, the overestimates are possibly associated with biases in PFT structures and parameters in the DGVM and the land cover change setup in the ESMs. Traditionally, climate models use a prescribed coverage of land surface types, based on present-day observed land cover, but increasingly, ESMs are simulating the vegetation coverage internally using process-based DGVMs embedded within their land-surface scheme. This means that the models may incur biases and errors in the coverage of vegetated lands (e.g. trees, grasses, etc.), but such DGVMs offer the advantage that changes in vegetation cover in response to climate and CO_2 can be simulated interactively. It has been shown that future changes in land cover induced by climate change can be just as big as changes induced by anthropogenic land-use change, and so such schemes are vital to fully capture changes in the terrestrial carbon cycle (Davies-Barnard et al., 2015). In our results, BNU-ESM used a DGVM to provide prognostic, climate-driven land cover change, but did not consider anthropogenic land use change; the three IPSL ESMs simulated the forest biomass with prescribed land use change but without prognostic land cover change; the two MIROC ESMs and the two HadGEM2 ESMs employed DGVMs for prognostic land cover change and incorporated prescribed land use change impacts (Table 2-1). Our analyses show that BNU-ESM and the IPSL ESMs exhibit large uncertainty in forest biomass estimates (institutional mean $ER_{total} = 3.03$ and 1.54, respectively), while relatively smaller biases are found in the HadGEM2 ESMs and in the MIROC ESMs (institutional mean $ER_{total} = -0.11$ and 0.13, respectively). Furthermore, Northern Hemisphere extratropical forest distributions in Whittaker climate space are mostly consistent with aggregated observations, except that BNU-ESM shows broadleaf deciduous trees below −10 °C, where needleleaf deciduous trees are found in the observations (Figure 2-15). According to the Whittaker diagrams, vegetation models from all modeling centers, except BNU-ESM, capture biome distributions reasonably well; however, too little forest biomass was simulated by ESMs in low temperature zones, i.e., needleleaf or needleleaf deciduous trees were underrepresented in the ESMs. For BNU-

ESM, forest biomass was underestimated over northern Asia because too much carbon was allocated to C_3 arctic grass instead of to needleleaf forests. Biases in modeled climatic conditions also induce uncertainty in forest biomass estimates. The Whittaker diagrams of observed biomass in modeled climate space show a bias towards warmer temperatures over land in regions where needleleaf deciduous trees are located in the observations. These results suggest that (1) better PFT representations in the DGVM, (2) land use change, and (3) reducing biases in climatic conditions that affect plant productivity should all be considered in simulations to reduce the uncertainty of future forest carbon pool estimates. Further simulations for each model can help improve the understanding of the impact on biomass uncertainty due individually to the DGVM, land use changes, and climatic conditions.

In addition to the DGVM and land cover changes, the allometric equations of forest carbon mass also contribute to the simulated forest biomass uncertainty in ESMs. For example, the simulations from the HadGEM2 ESMs indiscriminately allocate exactly the same carbon mass in roots and in leaves (Table 2-3), which induces uncertainty in forest biomass estimates in these two simulations. Better representations of the dynamic carbon allocation schemes apportioning the carbon mass in leaves and roots should reduce the uncertainty of forest biomass estimates in ESMs (De Kauwe et al., 2014; Mao et al., 2016). Furthermore, all simulations except those from the IPSL ESMs consistently allocate too much carbon mass to wood but too little to leaves and roots. Although the proportions of carbon mass in wood and in roots simulated by the IPSL ESMs are within the observational uncertainty (Figure 2-12c,d), the HadGEM2 ESMs and the MIROC ESMs have better carbon allocations for combined wood and root biomass (Figure 2-12a). This result, which has also been shown in Negrón-Juárez et al. (2015), suggests the HadGEM2 ESMs and the MIROC ESMs include the coarse roots in the wood pool, while the IPSL ESMs report the coarse roots biomass as a part of root biomass. Therefore, it is more appropriate to compare the combined biomass in wood and in roots when estimating the uncertainty between ESMs, for individual models and the aggregated observations. Overestimation of wood and total biomass may also be attributable to positive biases in net primary productivity, poor parameterization of fire frequency and intensity (Hantson et al., 2016), lack of insect and

disease processes in ESMs (Hicke et al., 2012), simplified characterization of canopy structure, overestimation of recruitment, and underestimation of tree mortality. As terrestrial ecosystem models evolve to simulate vegetation dynamics and demography (Fisher et al., 2015, 2018; Medvigy et al., 2009; Moorcroft et al., 2001), development of improved and explicit representations of stand-level processes–including recruitment, succession, growth, mortality, and various kinds of disturbance–must be informed by systematic evaluation and benchmarking (Forrest M Hoffman et al., 2017; Luo et al., 2012; Randerson et al., 2009), using *in situ* and remotely sensed observational data for burned area (Giglio et al., 2013), forest inventories (O'Connell et al., 2014), primary production (Running et al., 2004), plant traits (Kattge et al., 2011), productivity and carbon residence times (Thurner et al., 2016), disturbance and extreme events (Frank et al., 2015; Hansen et al., 2013), mortality rates (van Mantgem et al., 2009), and other key forest energy and carbon fluxes (Williams et al., 2009) and functional responses (Dukes et al., 2005; Reichstein et al., 2014).

Examination of the spin-up effect suggests that the uncertainty introduced at the beginning of the simulation in ESMs plays an important role in influencing the forest biomass estimates. Such spin-up issues have also been reported in soil carbon storage in CMIP5 outputs (Exbrayat et al., 2014). BNU-ESM and the IPSL ESMs simulate almost a unity *SR* value, demonstrating that the initial vegetation conditions from the spin-up processes in these models have substantial impact on present forest biomass estimates. As discussed above, the DGVM, land cover changes, and better representations and parameterizations of productivity, respiration and carbon turnover processes in the land models should be considered to improve model performance. Recent studies have shown that, in addition to mismatches in modeled compared to observed net primary production, carbon turnover processes are a major source of uncertainty in global vegetation models (Friend et al., 2014; Thurner et al., 2017). Simplified and not adequately represented turnover processes are contributing significantly to unrealistic magnitudes and spatial patterns of simulated biomass and to uncertainty in the response of vegetation carbon stocks to climate change (Friend et al., 2014; Thurner et al., 2017).

However, in addition to the uncertainties in the models, the observation-based product exhibits uncertainties as well. Sources of these uncertainties in the observation-based biomass estimate include the sensitivity of the radar signal to properties other than vegetation structure, the influence of non-forest vegetation on the signal, uncertainties in additional datasets (e.g. allometric databases, land cover, etc.) used for conversion of satellite measurements to biomass estimates, and the necromass component of vegetation in the observed growing stock volume. The application of allometric relationships derived on a leaf type level from a biomass compartment database has introduced relatively high uncertainties in observation-based estimates of leaf and root biomass compared to a moderate uncertainty in wood biomass. The uncertainty of the observation-based total biomass, however, is considered to be a conservative estimate and independent evaluations using upscaled forest inventory data have demonstrated the validity of the applied product at regional scales (Santoro et al., 2011, 2015; Thurner et al., 2014).

Since the uncertainty of extratropical forest biomass estimates in ESMs can be from more factors in addition to the causes mentioned in this study, we suggest that the community utilize software packages to evaluate the performance of coupled ESMs whenever there is an improvement or modification in models. These tools can benefit the community by informing future development of ESMs. For instance, the International Land Model Benchmarking (ILAMB) project (Forrest M Hoffman et al., 2017) provides a means to not only provide the statistics of model outputs but also quickly and easily evaluate how model performance changes with each modification in ESMs through skill score spreads. Because of uncertainties in observational data, ILAMB incorporated multiple observational data sets for the same variable to provide the user with some indication of that observational uncertainty. With an increasing or a decreasing score, researchers are able to determine whether a modification in ESMs will reduce the model uncertainty in forest biomass estimates.

Conclusion

We evaluated forest biomass from eight CMIP5 ESMs using a biomass dataset for the northern extratropical latitudes that was synthesized from radar remote sensing of stem

volume and ground-based observations of wood density and allometric relationships between biomass compartments. ESMs exhibited large biases in forest distribution, forest fraction, and carbon mass that contributed to the overall uncertainty in forest total biomass. We showed that forest total biomass is positively correlated with precipitation variations with temperature becoming equally important at higher latitudes. Finally, we showed that uncertainties in the pre-industrial forest biomass (spin-up) persisted into the contemporary period in most ESMs. To improve future analysis of vegetation biomass, we recommend saving and archiving PFT-level carbon stocks and fluxes, which can be used for analysis and benchmarking. Routine evaluation of model biomass in all compartments and of the spatial distribution of vegetation types is important for identifying sources of uncertainty in carbon cycle predictions.

Methods

Model outputs

Outputs of eight Earth system model (ESM) simulations from the CMIP5 archive with the historical experiment "r1i1p1" (Table 2-1) are selected based on the data availability of carbon density of individual plant functional types (PFTs) for all biomass compartments including leaf, wood, root, and the total biomass. The model outputs contain climatic variables as well as detailed information about forest biomass for various PFTs (Table 2-2). Two climatic variables, the precipitation rate (PR) and the surface temperature (TAS), are analyzed to investigate the spatial correlations of forest biomass and climate. The forest biomass in CMIP5 archive stores a single carbon density derived from the area-weighted carbon density of all vegetation types in each grid cell. Hence, forests and grasses have the same carbon density value as long as their area fractions are non-zero within a grid cell. In this study, forest carbon density (kg C m^{-2}) is converted into carbon mass (petagrams of carbon, Pg C). Data during 1982–2005 is averaged to represent the climatological mean status during the contemporary period, while that during the pre-industrial period is based on the climatological mean status during 1861–1885.

Observation-based data sets

The applied observation-based forest biomass product (Thurner et al., 2014) (available from http://www.bgc-jena.mpg.de/geodb/projects/Home.php) provides vegetation carbon density and its uncertainty covering northern boreal and temperate forests (30°N–80°N) at 0.01° resolution. First, forest biomass in stems was derived from a radar remote sensing growing stock volume (GSV) product (Santoro et al., 2011, 2015), which integrates observations between October 2009 and February 2011, and information on wood density. Subsequently, the other biomass compartments (branches, roots, foliage) have been estimated based on a database of allometric relationships to stems. Furthermore, precipitation flux and surface temperature from the Global Soil Wetness Project Phase 3 (GSWP3) forcing data products (0.5° × 0.5°) (Kim, 2018) serve as the observational climatic data. For land cover types, we adopt the land cover definitions from 1 km × 1 km global land cover classification for the year 2000 (GLC2000) database (Joint Research Centre, 2003) (Table 2-2). We reproject GLC2000 (applying nearest-neighbor interpolation) in order to match the resolution of the observation-based biomass product. To compare to each ESM's output, this product is further upscaled to eight data sets with coarser grid resolutions that are the same as the eight selected CMIP5 model simulations (Table 2-1) while retaining the PFT-level biomass distributions (i.e., different carbon densities instead of a single area-weighted carbon density for each PFT within a grid cell).

Common–grid land mask

We verify the data availability at each grid cell for the upscaled observational data sets and the ESM output. A grid cell is masked out when either observational or modeled forest biomass is unavailable at that grid cell. Due to different PFT distributions and grid resolutions, the available grid cells vary in each ESM. The total carbon stock estimated from the upscaled observational data sets, even though they are upscaled from the same product, are hence different. Therefore, we use relative errors, in addition to the total carbon stock, to evaluate the performance of each ESM output.

Land cover types and forest fractions

The forest fractions for observation-based data are determined by GLC2000. The GLC2000 data is upscaled to coarser resolutions, varying from 1.25° × 1.875° to 2.8125° × 2.8125° (Table 2-1), according to each model's setup. We classify four major forest types including broadleaf evergreen trees, needleleaf evergreen trees, broadleaf deciduous trees, and needleleaf deciduous trees (Table 2-5) when evaluating modeled forest distributions in Whittaker climate space. Alternatively, we combine the first ten classes in GLC2000 as the "lumped" forest type (Thurner et al., 2014) to quantify the uncertainty caused by spin-up processes in ESMs (Table 2-6). For each ESM output, modeled forest fractions are compared to that from those upscaled GLC2000 data at the same grid resolution. Uncertainty due to different forest definitions between GLC2000 and ESMs can be minimized by applying a common-grid land mask with various forest fraction thresholds (F_f). The common-grid land mask keeps only the grid cells where both model outputs and observations have non-zero forest fractions as well as valid biomass values of forest types. F_f ranges from 0 to 0.9 with an increment of 0.1. Grid cells with forest fractions lower than or equal to F_f are masked out in both model outputs and observations. A higher F_f means that the carbon pool in grid cells composed of a larger proportion of forest-only biomass, i.e., the uncertainty caused by assigning a fixed carbon density for all PFTs in the ESMs is reduced.

Spatial correlations and skill scores

Spatial differences between model outputs and observations are compared in terms of forest fractions and forest total carbon mass. We apply a 11 × 11 moving window to compute the spatial correlation between forest total carbon mass and precipitation rate as well as that between forest total carbon mass and surface temperature at the default forest fraction threshold ($F_f = 0$) over extratropical regions in the Northern Hemisphere. The spread of biomass in the precipitation–temperature space is lumped into two (broadleaf and needleleaf trees) and four categories (broadleaf evergreen, needleleaf evergreen, broadleaf deciduous, and needleleaf deciduous trees) depending on the PFT definitions in each model. A Taylor diagram (Taylor, 2001) is also produced to assess the spatial uncertainty

due to F_f through the correlation, the root-mean-square difference and the ratio of the variances of forest total carbon mass from observations and from model outputs. Due to different spatial resolutions in each model, we use standardized deviations from each model's variance normalized by the variance from the observations upscaled to its resolution. Model performance is evaluated through the skill scores (S) (Taylor, 2001):

$$S_i = \frac{4\times\ 1+R_i}{\left(\frac{\sigma_i}{\sigma_r}+\frac{\sigma_r}{\sigma_i}\right) 1+R_0}, \tag{2.1}$$

where R_i is the spatial pattern correlation of forest total carbon mass between model i and the upscaled observation at its resolution, σ_i the variance of modeled forest total carbon mass, σ_r the variance of observed forest total carbon mass. We compute ten different R_i values for each model i by varying F_f from 0 to 0.9 with an increment of 0.1. The maximum value of R_i among the ten F_f cases is assigned to R_0.

Relative error

To quantify the modeled forest biomass uncertainty, we measure the relative error (ER) with the common-grid land mask applied to evaluate the discrepancies of the magnitude of forest carbon amount between models and that from upscaled observational data:

$$ER = \frac{\sum_{i=1}^{n} y_i - \sum_{i=1}^{n} x_i}{\sum_{i=1}^{n} x_i}, \tag{2.2}$$

where n is the total available grid cells, y_i the global forest total biomass from model outputs and x_i the global forest total biomass upscaled from the observational MPI–BGIv3 data set at grid cell i. The magnitude of observed global forest total biomass depends on data availability in each model output with the common-grid land mask applied. The multi-model average of forest total biomass is calculated based on the average of modeled outputs and upscaled observations for all ESMs using Equation. (2.2). In addition to analyzing the

grid area-weighted results, we further examine the forest biomass with detailed carbon mass in individual PFTs at each grid cell from the HadGEM2-ES outputs. Grid cell-level uncertainty is computed by averaging *ER* over *n* available grid cells at each grid cell *i*:

$$ER_{grid} = \frac{1}{n}\sum_{i=1}^{n} y_i - x_i \tag{2.3}$$

In the present study, we evaluate *ER* for forest total biomass (ER_{total}) as well as biomass in leaves (ER_{leaf}), wood (ER_{wood}), and roots (ER_{root}). Because of the inconsistent definition of roots in ESMs, we also compute *ER* for the combined wood and roots biomass ($ER_{wood+root}$). A model has less uncertainty in forest carbon mass estimates when *ER* approaches zero.

Spin-up effects

The impact of the initial-to-equilibrium state from spin-up inputs on simulated forest biomass can be evaluated by the ratios of ER_{grid} values during the PI period and the modern time, i.e.,

$$SR = \frac{ER_{grid,PI}}{ER_{grid,contemporary}} \tag{2.4}$$

Note that we utilize the observations in contemporary years as the reference values for both $ER_{grid,PI}$ and $ER_{grid,contemporary}$ due to the absence of forest biomass information during the PI period. Nevertheless, it is suggested that higher possibilities of uncertainty in future carbon pool projections may be influenced by the inputs from spin-up results when *SR* values approach unity.

CHAPTER 3
INTERACTIONS AND BIOGEOCHEMICAL FEEDBACKS IN THE CLIMATE-WILDFIRE-TERRESTRIAL ECOSYSTEM UNDER GEOENGINEERING

A version of this chapter was originally submitted for peer-review and publication by Cheng-En Yang, Forrest M. Hoffman, Daniel M. Ricciuto, Simone Tilmes, Lili Xia, Douglas G. MacMartin, Jadwiga H. Richter, Michael Mills, Ben Kravitz, and Joshua S. Fu:

Cheng-En Yang, Forrest M. Hoffman, Daniel M. Ricciuto, Simone Tilmes, Lili Xia, Douglas G. MacMartin, Jadwiga H. Richter, Michael Mills, Ben Kravitz, and Joshua S. Fu (2019). Assessing Terrestrial Biogeochemical Feedbacks in A Strategically Geoengineered Climate. *Submitted.*

Discussions of biomass in individual compartments of plants as well as fire activities are added in this chapter. Tables and figures are re-numbered, and their captions are modified accordingly. Cheng-En Yang performed the analysis, generated graphical results, and prepared the manuscript in consultation with Forrest M. Hoffman, Joshua S. Fu, Daniel M. Ricciuto, and Lili Xia. Forrest M. Hoffman provided impulse response function calculations. Simone Tilmes, Douglas G. MacMartin, Jadwiga H. Richter, Michael Mills, Ben Kravitz are the core team conducting the model simulations in the Stratospheric Aerosol Geoengineering Large Ensemble project. All authors contributed to group discussions and manuscript revisions.

Abstract

Geoengineering by injecting sulfur dioxide into the lower stratosphere has been suggested to reduce anthropogenically induced warming. While impacts of such geoengineering on climate have been investigated in recent decades, few modeling studies have considered biogeochemical feedbacks resulting from such intervention. This study is the first to comprehensively characterize responses and feedbacks of terrestrial ecosystems from an ensemble of climate change simulations under a high greenhouse gas scenario. Carbon cycle feedbacks can alter the trajectory of atmospheric carbon dioxide levels by storing or releasing additional carbon on land and in the ocean, thus moderating or amplifying climate change. We assess terrestrial biogeochemical feedbacks to climate in response to geoengineering, using model output from the Stratospheric Aerosol Geoengineering Large Ensemble (GLENS) project. Results indicate terrestrial ecosystems become a stronger carbon sink globally because of lower ecosystem respiration and

diminished disturbance effects under geoengineering. An additional 79 Pg C would be stored on land by the end of the twenty-first century, yielding as much as a 4% reduction in atmospheric CO_2 mole fraction without marine biogeochemical feedbacks, compared to the high greenhouse gas scenario without geoengineering.

Main

Rising global mean surface temperature along with increasing anthropogenic greenhouse gas emissions have been observed since the last century (Pachauri & Meyer, 2014), and future projections of increasing global mean surface temperature remain even if anthropogenic emissions are reduced (Steffen et al., 2018). To prevent continued warming that could cause devastating damage to natural ecosystems and human socio-economic activities (Hoegh-Guldberg et al., 2018), various climate intervention strategies, such as solar radiation management, have been proposed to offset the risks of warming (Crutzen, 2006; Shepherd, 2009). Extensive analyses of Earth System Model (ESM) simulations have addressed climate impacts of stratospheric sulfur injection, including stratospheric ozone depletion (Tilmes et al., 2008), weakening of monsoons (Robock et al., 2008; Tilmes et al., 2013), acid deposition and ocean acidification (Kravitz et al., 2009; Moreno-Cruz & Keith, 2013), repartitioning of direct and diffuse radiation (Gu et al., 2003; Mercado et al., 2009), and suppressed precipitation (Bala et al., 2008). Terrestrial biogeochemical (BGC) responses have received limited attention in such simulations, particularly for optimized aerosol injection strategies or for high greenhouse gas forcing scenarios using fully coupled ESMs (Cao & Jiang, 2017; Dagon & Schrag, 2019; Keith et al., 2017; Keller et al., 2014; Tjiputra et al., 2016; Xia et al., 2016). A recent geoengineering activity known as the Stratospheric Aerosol Geoengineering Large Ensemble (GLENS) project (Tilmes et al., 2018) simulated the climate response to stratospheric sulfur aerosol injections designed to maintain three temperature goals at their 2020 levels: (1) the global mean surface temperature, (2) the interhemispheric surface temperature gradient, and (3) the equator-to-pole surface temperature gradient. The simulations were conducted with the Community Earth System Model (CESM) version 1 with the Whole Atmosphere Community Climate Model (WACCM) as its atmospheric component (0.9° latitude × 1.25°

longitude horizontal grid resolution) (Mills et al., 2017), the Community Land Model version 4.5 as the land component (Oleson et al., 2013), the Los Alamos Sea Ice Model (CICE version 4) as the sea ice component (Hunke & Lipscomb, 2008), and the Parallel Ocean Program version 2 as the ocean component (Danabasoglu et al., 2012).

The control experiment was designed to project future climate in a business-as-usual (Representative Concentration Pathway 8.5, RCP8.5) scenario (Riahi et al., 2011) from 2010 to 2099. The control experiment consisted of a 20-member ensemble of simulations from 2010 to 2030, with the first three ensembles continued at least until the year 2097. Each member started from the same ocean state and differed by small perturbations to their initial atmospheric states. Another experiment was conducted with the same experimental design except it included sulfur aerosol injections in the lower stratosphere at four optimized locations to achieve the three temperature goals (Kravitz et al., 2017) from 2020 to 2099 . The large number of ensemble members, a longer simulation period, higher model grid resolutions, effects of sulfate aerosols on stratospheric chemistry, and a high anthropogenic emission scenario through the coupled CESM simulations enable GLENS to serve the needs of a more comprehensive examination of geoengineering impacts, including effects on atmospheric chemistry and land biogeochemical feedbacks to the Earth system. Note that the marine biogeochemistry model was not enabled in these simulations. While GLENS results have been used to investigate a wide variety of physical climate responses to aerosol geoengineering (Cheng et al., 2019; Fasullo et al., 2018; Tilmes et al., 2018), this study is the first to comprehensively characterize the responses and feedbacks of terrestrial ecosystems in the GLENS simulations. Since the geoengineering experiment was branched from the control experiment at year 2020, simulation results from 2010 to 2019 serve as the baseline period, representing present climate (called "*BASE*" hereafter). The period 2020–2097 from the control experiment (called "*CTRL*" hereafter) and from the geoengineering experiment (called "*GEOENG*" hereafter) are compared with each other and with *CTRL* (see Methods in this chapter for more details).

Results

Global climate change

Global mean surface temperatures are projected higher in *CTRL* than in *BASE* due to rising greenhouse gas levels as previously reported (Pachauri & Meyer, 2014) (Figure 3-1a). In *GEOENG*, slightly higher global mean surface temperatures in the Sahara Desert and at mid-to-high latitudes compared to *BASE* (Figure 3-1b) are compensated by lower surface temperatures in the central US, parts of South America, Central Asia, southern India, and eastern Australia. The global mean surface temperatures in *GEOENG* are lower compared to *CTRL* despite their having the same greenhouse gas trajectories as a result of stratospheric aerosol injections (Figure 3-1c). Circulation changes due to higher surface temperatures in *CTRL* than in *BASE* result in higher precipitation rates in most regions, whereas lower precipitation rates are simulated in the Amazon Basin, southern Chile and Argentina, Uruguay, western Congo, southern Africa, some southern parts of Europe, and Indonesia (Figure 3-1d), consistent with known features of projected climate change (Pachauri & Meyer, 2014). The regions with lower precipitation rates in *CTRL* than in *BASE*, which include forests, croplands, and open shrublands (Figure 3-2), are influenced by changing atmospheric dynamics (Yoon & Zeng, 2010) and physiological responses (Langenbrunner et al., 2019) along with enhanced direct solar radiation but reduced diffuse solar radiation (Figures 3-1g,j). In *GEOENG*, cooler temperatures, reduced evapotranspiration, and aerosol-cloud interactions (suppressed precipitation due to the aerosol indirect effect (Albrecht, 1989)) lead to a drier climate compared to *BASE* over the southern Sahel and South Africa, India, Southeast Asia, and parts of the boreal zone across Eurasia and northeastern North America (Figure 3-1e). Global mean precipitation rates in *GEOENG* are generally smaller than that in *CTRL* (Figure 3-1f) due to lower temperatures and induced suppression of precipitation, with the exception of the southern Amazon (evergreen broadleaf forests) (Langenbrunner et al., 2019) and semi-arid and monsoon regions (Tilmes et al., 2013), including the western U.S. (open shrublands), southern Africa (open shrublands), eastern Australia (open shrublands), southern Europe/northern Africa/western Asia (open shrublands/sparsely vegetated lands).

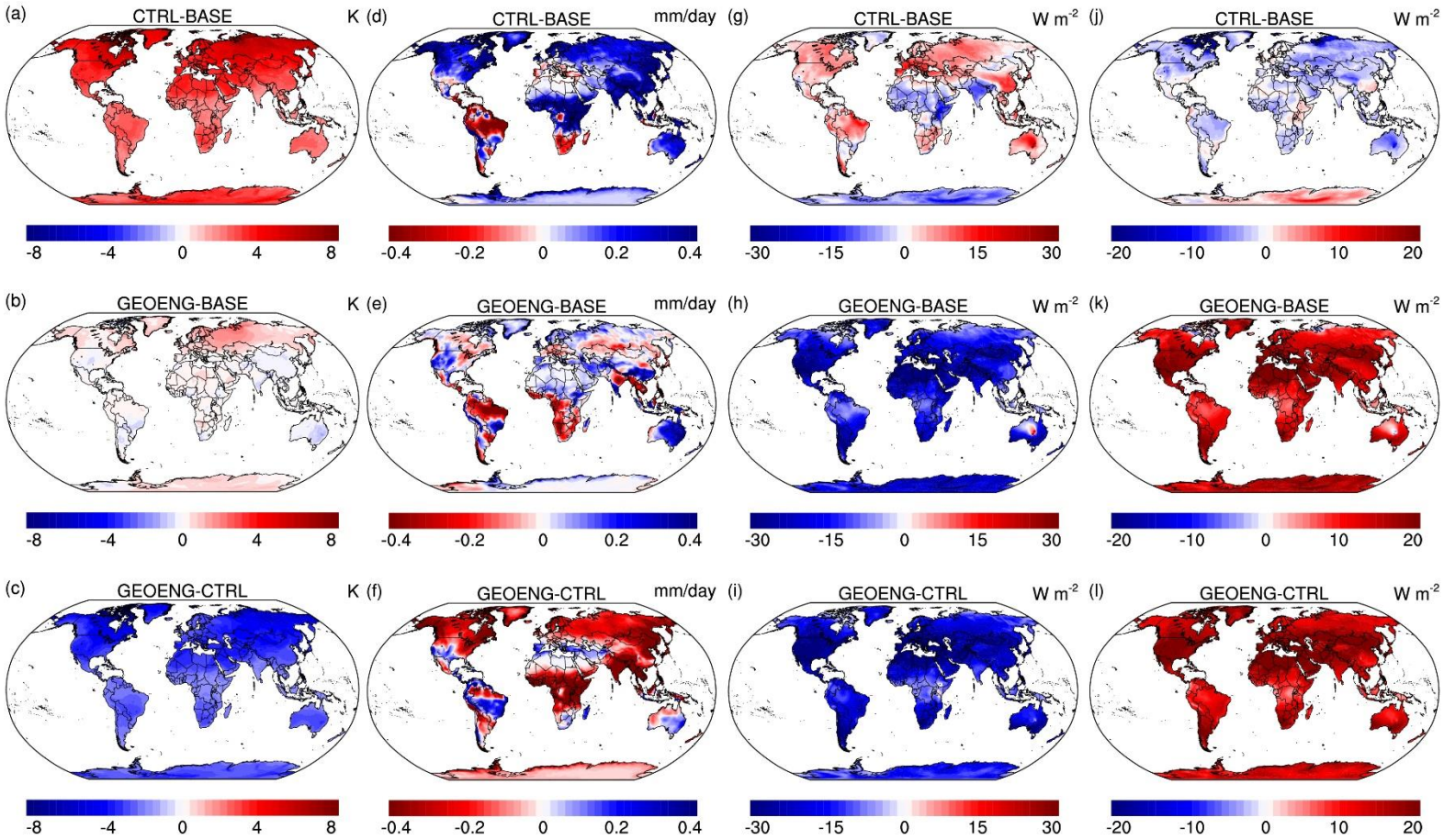


Figure 3-1. Changes of spatial distributions between *CTRL* and *BASE* (top row), between *GEOENG* and *BASE* (middle row), and between *GEOENG* and *CTRL* (bottom row) for surface temperature (K, (a)–(c)), precipitation (mm/day, (d)–(f)), total downward direct solar radiation (W/m^2, (g)–(i)), and total downward diffuse solar radiation (W/m^2, (j)–(l)). The spatial distribution of *CTRL* is from the 2020–2097 time-averaged results without geoengineering while that of *GEOENG* is from the 2020–2097 time-averaged results with geoengineering applied. The spatial distribution of *BASE* is from the 2010–2019 time-average results.

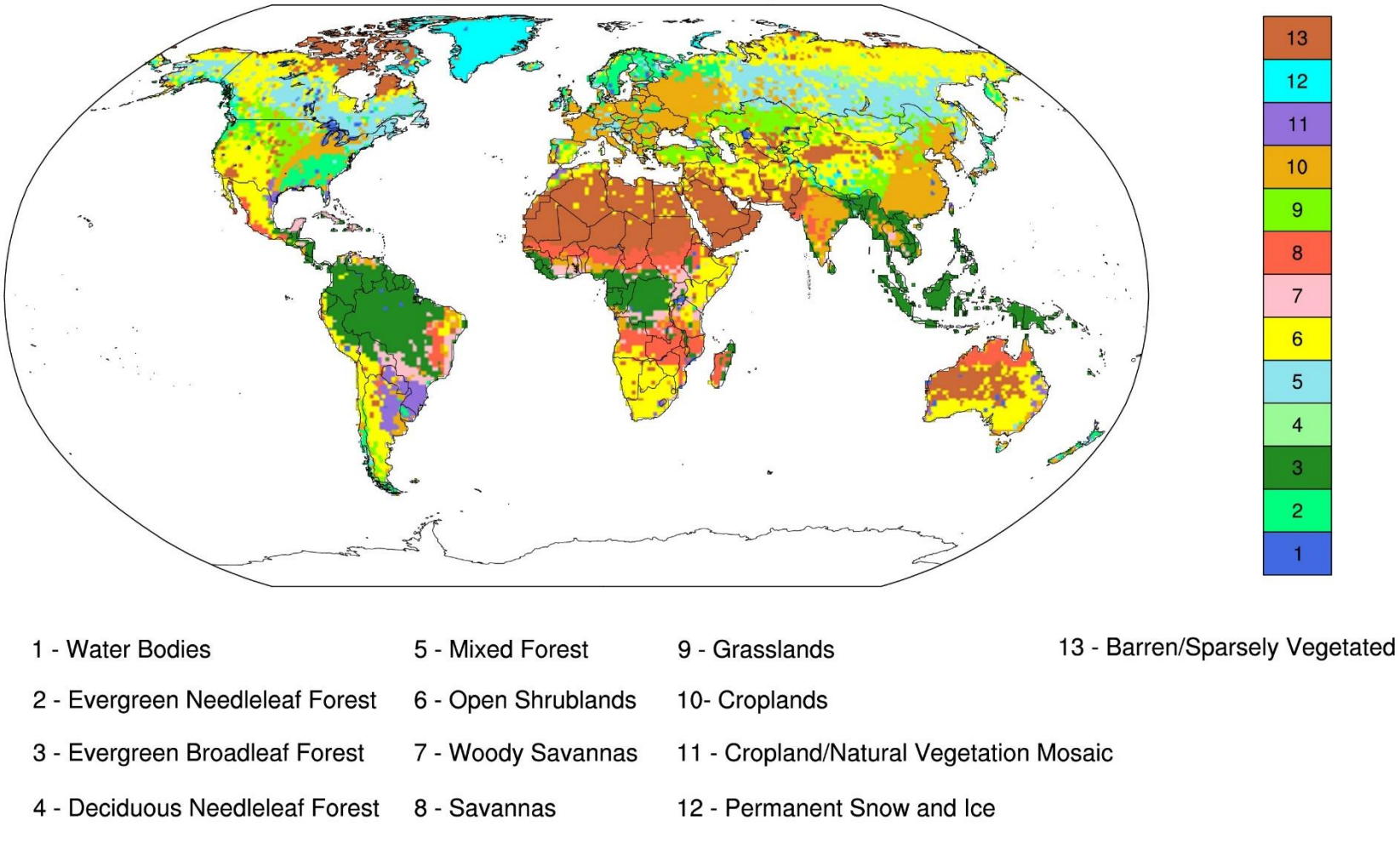


Figure 3-2. Ecoregions defined in this study.

In terms of downward solar radiation, increased direct radiation and reduced diffuse radiation is projected in *CTRL* than in *BASE* in most regions (Figures 3-1g,j) due to increased precipitation that washes out aerosols in the atmosphere (Figure 3-1d). Some regions, particularly Central Africa and India, experience reduced direct radiation because of increased aerosol amounts from anthropogenic emissions and land use change despite projected increases in precipitation rates. On the other hand, *GEOENG* shows decreased direct radiation and increased diffuse radiation with respect to *BASE* (Figures 3-1h,k). Such changes are attributed to the increased amounts of aerosols suspended in the atmosphere due to sulfur injections. An abnormal change in central Australia is simulated in *GEOENG* (Figure 3-1h) as a result of lower dust emission because of wetter climate conditions (not shown). Differences in downward solar radiation between *GEOENG* and *CTRL* are associated with higher aerosol amount due to sulfur injections, which block direct radiation and enhanced diffuse radiation (Figures 3-1i,l).

Global terrestrial biogeochemical responses

Photosynthesis rates (*FPSN*) and gross primary production (*GPP*) for both *CTRL* and *GEOENG* substantially increase in most of the world because of rising atmospheric CO_2 mole fractions with respect to *BASE* (Figures 3-3a,b,d,e). At high latitudes, *FPSN* and *GPP* were lower in *BASE* and in *GEOENG* than in *CTRL* because higher surface temperatures in *CTRL* (Figure 3-1c) thaw permafrost regions, lengthen growing seasons and enable enhanced photosynthesis (Figures 3-3a,c). At mid and low latitudes, lower precipitation and less diffuse radiation in the Amazon Basin and southern Africa produce lower *FPSN* and *GPP* in *CTRL* than in *BASE* (Figures 3-3a,d). In addition, lower *FPSN* and *GPP* in India and central Africa, where land cover is dominated by croplands and savannas, are subjected to lower precipitation in *BASE* and in *GEOENG* than in *CTRL* (Figures 3-1d,f). However, substantial *FPSN* and *GPP* increases in *GEOENG* with respect to *CTRL* are found in the southwestern U.S. (open shrublands), southern Amazon (woody savannas), France/Spain/northern Africa (croplands and open shrublands), southern Africa (open shrublands), central Russia (mixed forests), and eastern Australia (open shrublands) (Figure 3-3f). Such increases in *FPSN* and *GPP* are associated with increased precipitation

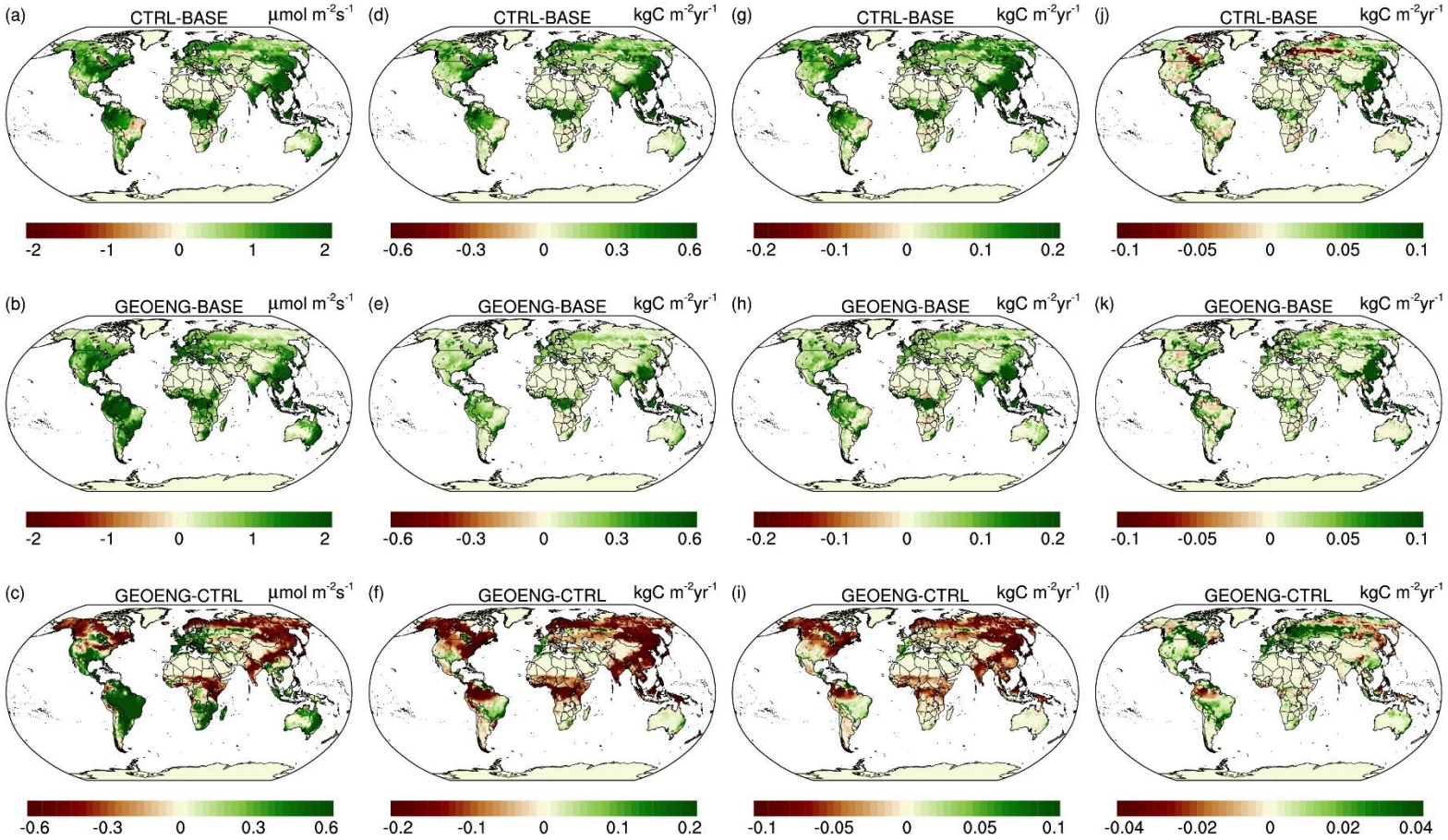


Figure 3-3. Same as Figure 3-1 except for photosynthesis rates (µmol m^{-2} s^{-1}, (a)–(c)), gross primary production (kg C m^{-2} yr^{-1}, (d)–(f)), net primary production (kg C m^{-2} yr^{-1}, (g)–(i)), and net biome production (kg C m^{-2} yr^{-1}, (j)–(l)).

and soil moisture (Figures 3-1f and 3-4). While the projected spatial *GPP* patterns are consistent with previous studies (Dagon & Schrag, 2019; Kalidindi et al., 2015; Tjiputra et al., 2016), different spatial patterns are found between *FPSN* and *GPP* across the Amazon Basin for changes between *GEOENG* and *CTRL* (Figures 3-3c,f). This is mainly because lower temperatures in *GEOENG* produce lower net nitrogen mineralization rates, reducing conversion of organic nitrogen to a plant-available inorganic form and hence downregulating photosynthesis (Figure 3-5).

The autotrophic respiration rate (R_a) is sensitive to changes in temperatures and *GPP* (see Equation (3.1)). Enhanced R_a in *CTRL* and in *GEOENG* with respect to *BASE* are caused by enhanced *GPP*, which is attributed to the CO_2 fertilization effect (Figure 3-6). Lower R_a in *GEOENG* than in *CTRL* is primarily caused by the cooler climate in *GEOENG*. The net primary production (*NPP*), which is determined by *GPP* and R_a, increases in both *CTRL* and *GEOENG* compared to *BASE* (Figures 3-3g,h). Stronger reductions in *GPP* than in R_a result in lower *NPP* in *GEOENG* with respect to *CTRL* (Figure 3-3i). Like R_a, the heterotrophic respiration rate (R_h) is also sensitive to changes in temperature and the carbon amounts in litter and soil. Higher rates of *GPP* in *CTRL* and *GEOENG* compared to *BASE* drive higher rates of R_h because of larger litter inputs that also increased soil pools (Figure 3-7). Therefore, higher R_h is simulated in both *CTRL* and *GEOENG* compared to *BASE* in most regions (Figure 3-8). Nevertheless, regions with reduced precipitation and lower temperatures in *GEOENG* than in *CTRL*, such as the northern Amazon, undergo lower R_h and evapotranspiration rates in *GEOENG*, which in turn retains more water in soil due to stomatal closure in plants (Swann et al., 2016) (Figures. 3-4 and 3-9).

The spatial patterns of net ecosystem production (*NEP*) are determined by *NPP* and R_h. Both *CTRL* and *GEOENG* demonstrate enhanced *NEP* compared to *BASE* with the exception of North America. Higher *NPP* induces higher *NEP* in *CTRL* and in *GEOENG* with respect to *BASE*; however, stronger increases of R_h due to land use change and accelerated litter input than the increases of *NPP* in North America cause reduced *NEP* in both *CTRL* and *GEOENG* when compared to *BASE* (Figure 3-10). Similar to *NPP*, the cooler climate in *GEOENG* leads to lower *NEP* than that of *CTRL*. The variations of *NEP*

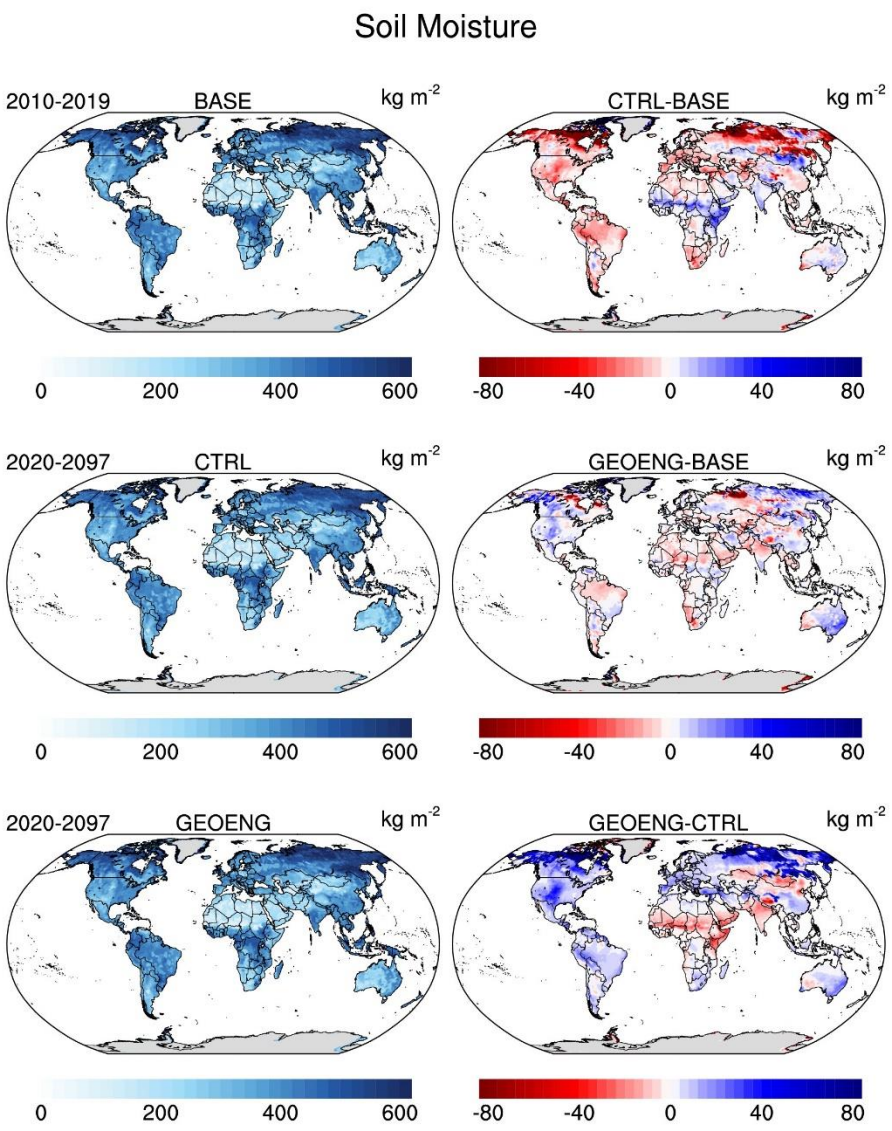


Figure 3-4. Spatial distributions of soil moisture (kg/m^2). Left column shows the averaged values for *BASE* (2010–2019, top), *CTRL* (2020–2097, middle), and *GEOENG* (2020–2097, bottom). Right column shows the differences of *CTRL−BASE* (top), *GEOENG−BASE* (middle), and *GEOENG−CTRL* (bottom).

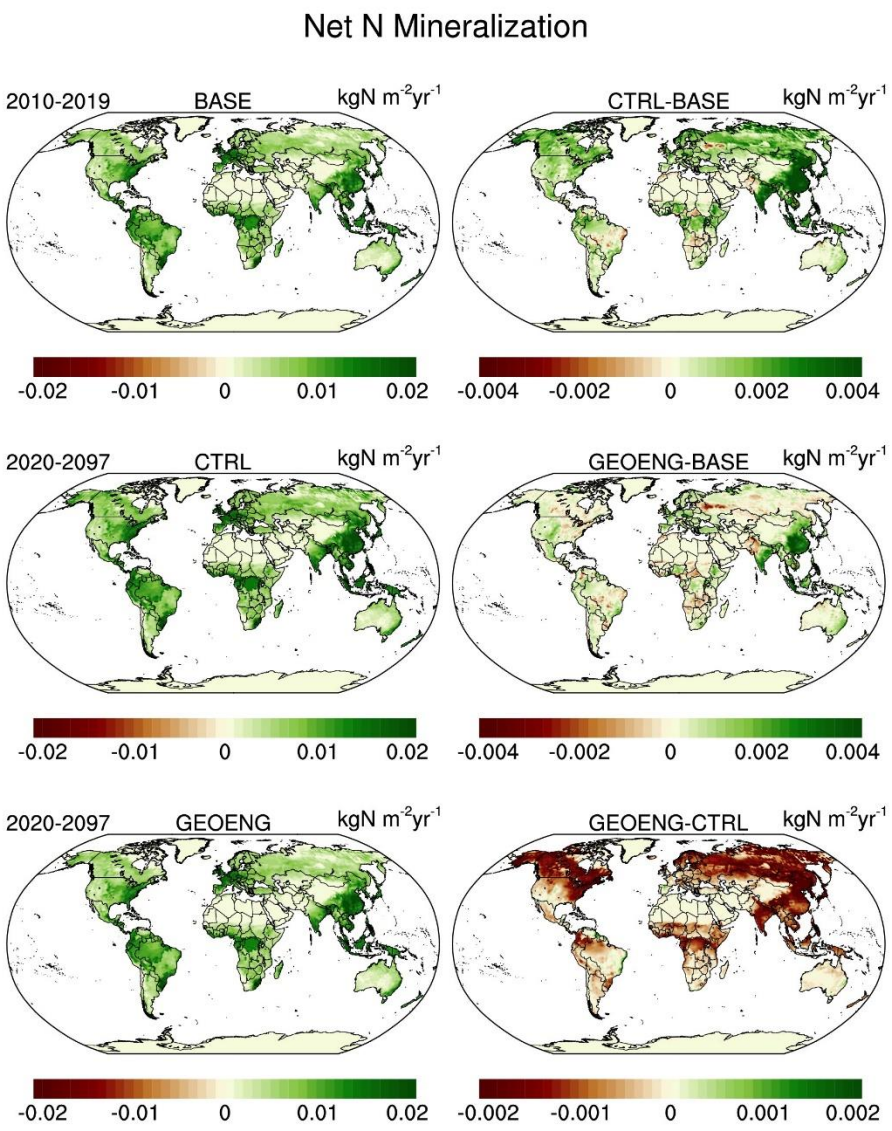


Figure 3-5. Same as Figure 3-4 except for net nitrogen mineralization rate (kg N m^{-2} yr^{-1}).

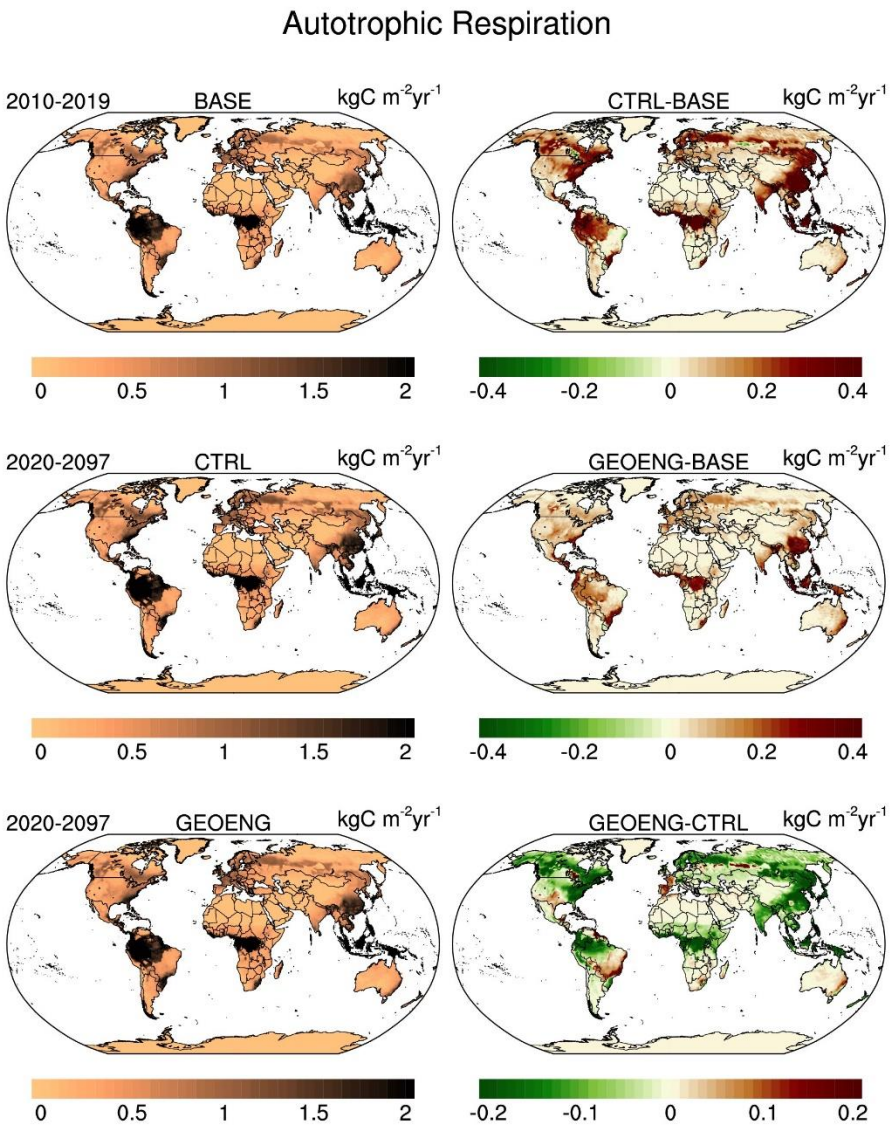


Figure 3-6. Same as Figure 3-4 except for autotrophic respiration (kg C m^{-2} yr^{-1}).

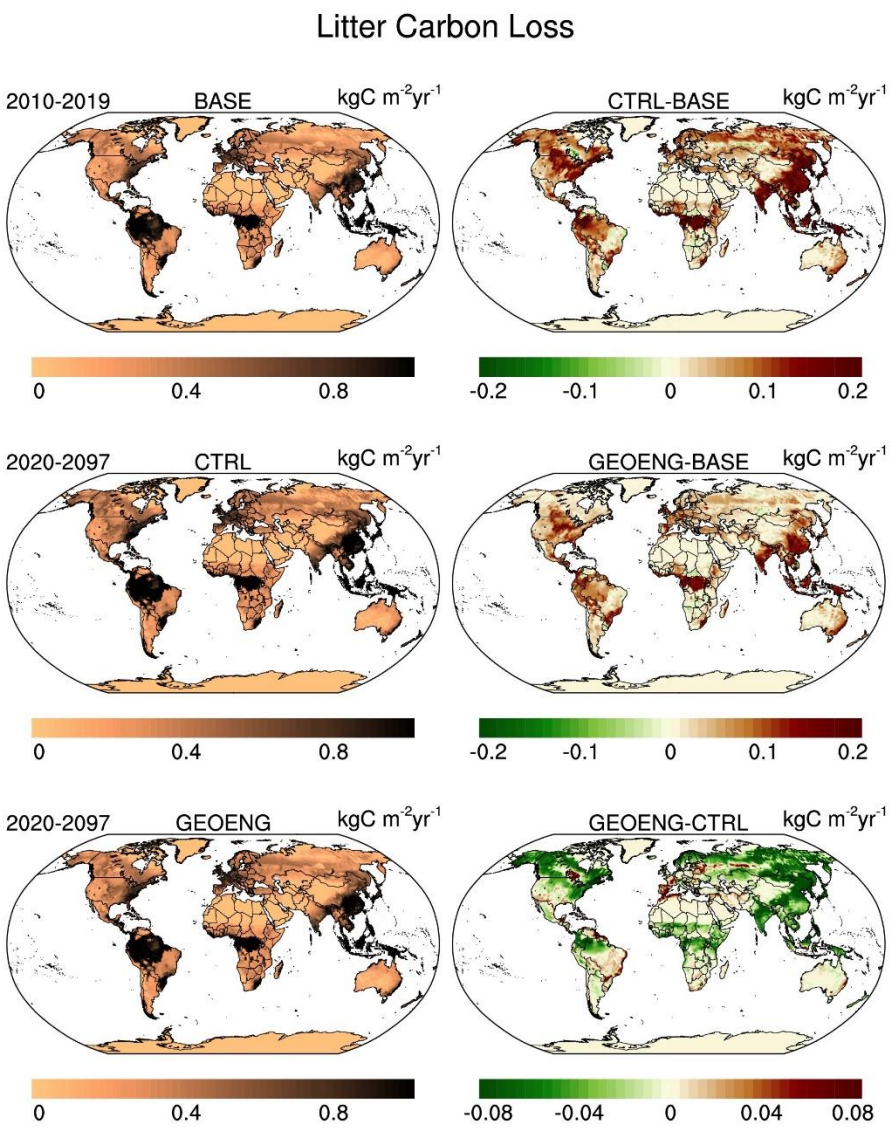


Figure 3-7. Same as Figure 3-4 except for carbon loss from litters (kg C m^{-2} yr^{-1}).

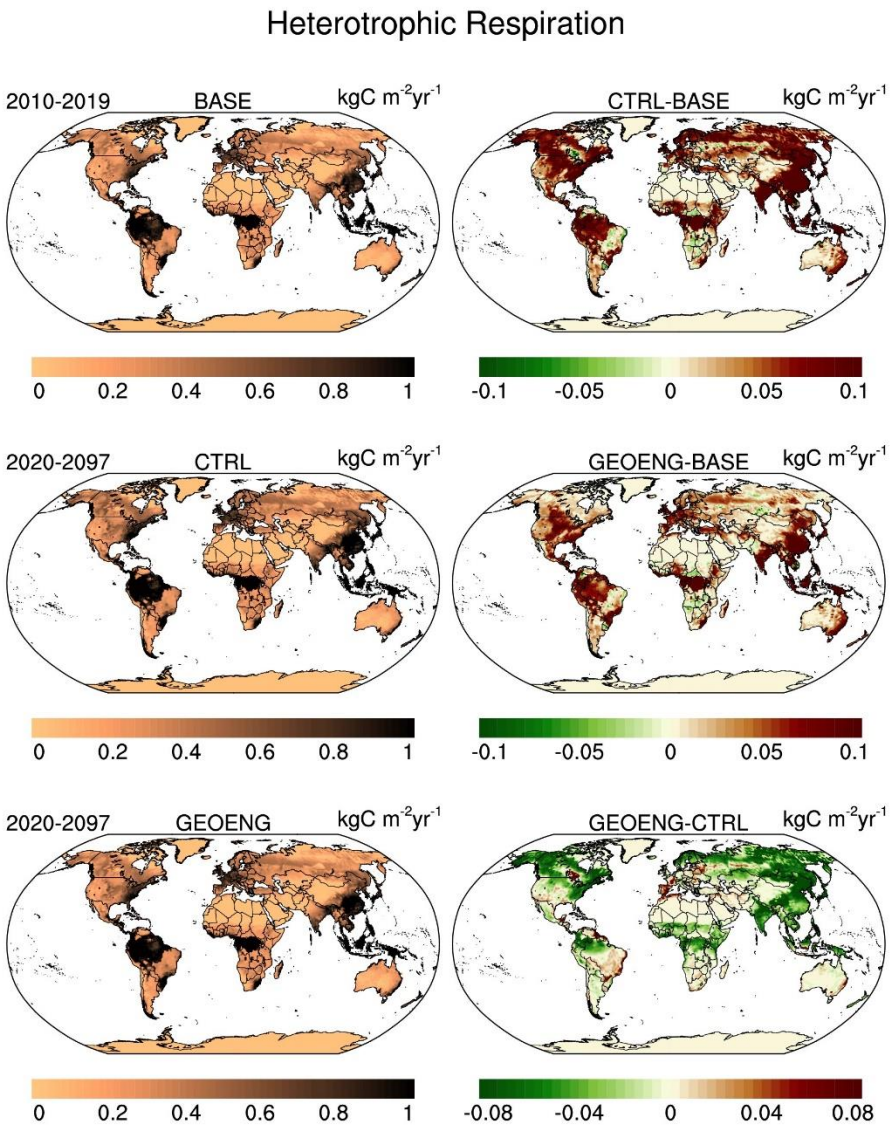


Figure 3-8. Same as Figure 3-4 except for heterotrophic respiration (kg C m^{-2} yr^{-1}).

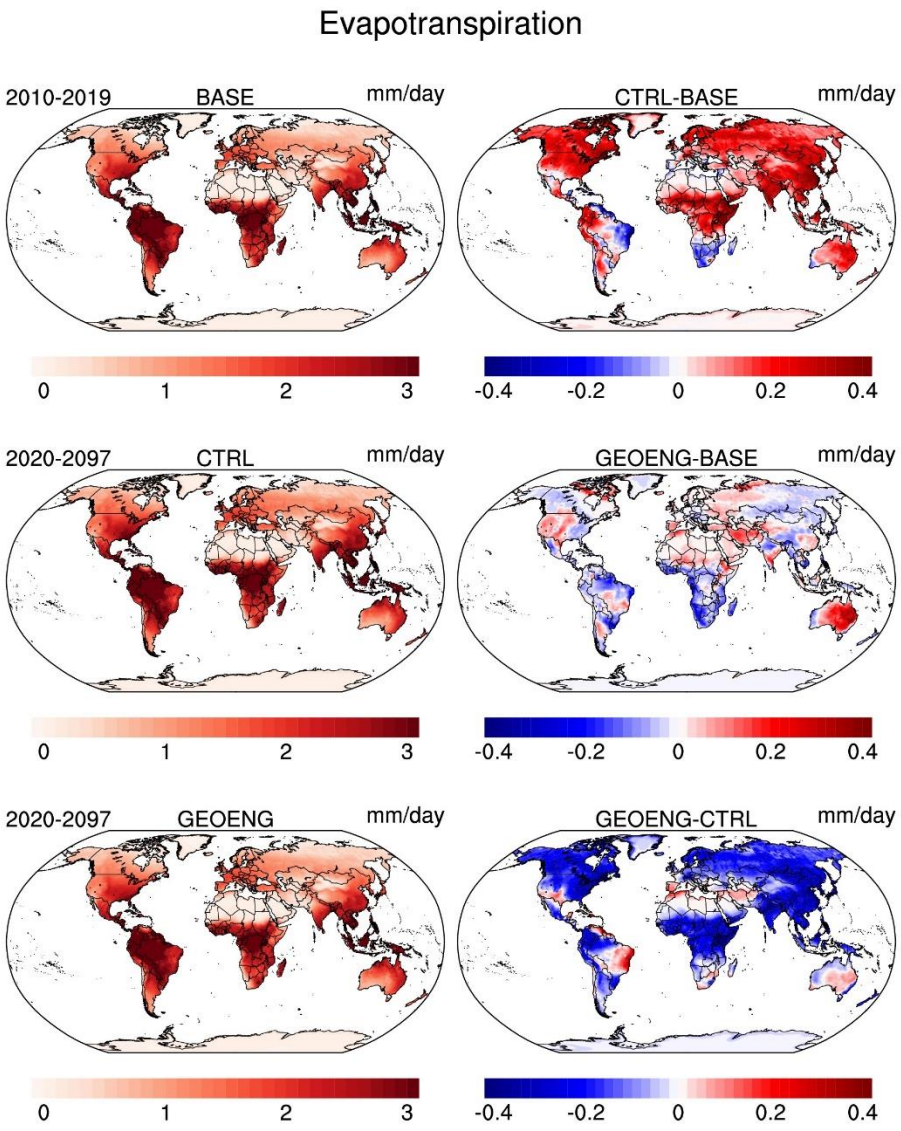


Figure 3-9. Same as Figure 3-4 except for evapotranspiration (mm/day).

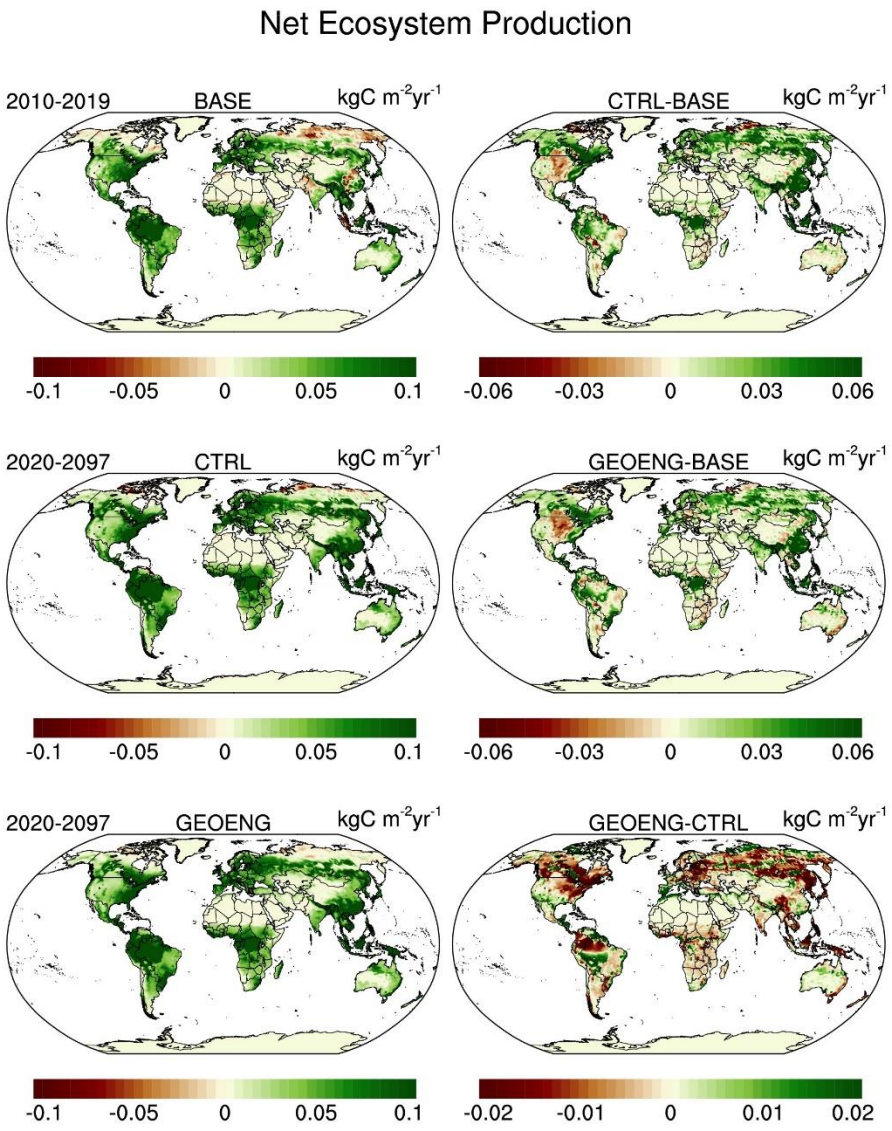


Figure 3-10. Same as Figure 3-4 except for net ecosystem production (kg C m^{-2} yr^{-1}).

and *disturbance* (e.g., fires, wood harvest, and land use changes) determine the changes of net biome production (*NBP*), which represents the long-term and large-scale carbon uptake by ecosystems (see Equation (3.1)). In GLENS outputs, *disturbance* is excluded in *NEP* but is included in *NBP*. Hence, differences in the spatial patterns between *NBP* and *NEP* illustrate the human and natural disturbances. In general, *CTRL* and *GEOENG* simulate enhanced *NBP* attributed to stronger *GPP* than in *BASE* (Figures 3-3j,k); smaller *NBP* over North America in *CTRL* than in *BASE* is caused by increased carbon loss due to fires (Figures 3-11 and 3-12). Similarly, smaller burned area and lower carbon loss due to fire in *GEOENG* explain the enhanced *NBP* in North America, the boreal region of Eurasia, and the southeast coast of Australia with respect to *CTRL*.

Carbon sink strength and atmospheric CO_2 trajectory adjustments

The carbon sink strength (CSS) is determined by the accumulated *NBP* over a period of time. The terrestrial ecosystem has higher global total *GPP* primarily due to elevated CO_2 mole fractions in both *CTRL* and *GEOENG* with respect to *BASE* (Table 3-1). All the other terrestrial carbon fluxes except *NBP* in the terrestrial carbon budget (see Equation (3.1)) are enhanced over time in both *CTRL* and *GEOENG*. Increases of *GPP*, *NPP*, *NEP*, R_a, and R_h in *GEOENG* are slower compared to *CTRL* because of lower temperatures and lower precipitation rates in *GEOENG* (Table 3-1). Differences of accumulated *NBP* between *GEOENG* and *CTRL* showed stronger CSS in *GEOENG* than in *CTRL* by 76±6 Pg C at year 2097, increased from 13±2 Pg C during 2020–2039 to 30±3 Pg C during 2078–2097. Such CSS enhancement is attributed primarily to reduced R_a and R_h, which leaves more carbon resident in land globally (Table 3-1). Additionally, smaller carbon losses due to natural or anthropogenic disturbances (estimated by *NEP*−*NBP*) in *GEOENG* also indicate a larger land carbon reservoir.

For individual ecoregions, about 63% (125±1 Pg C) of global *NBP* (198±4 Pg C) in *CTRL* and 47% (130±1 Pg C) of global *NBP* (277±3 Pg C) in *GEOENG* during 2020–2097 are contained in evergreen broadleaf forests in tropical regions, which have the largest CSS among all ecoregions (Table 3-2). Nevertheless, the largest differences of CSS (ΔCSS) between *GEOENG* and *BASE* are found in croplands and mixed forests

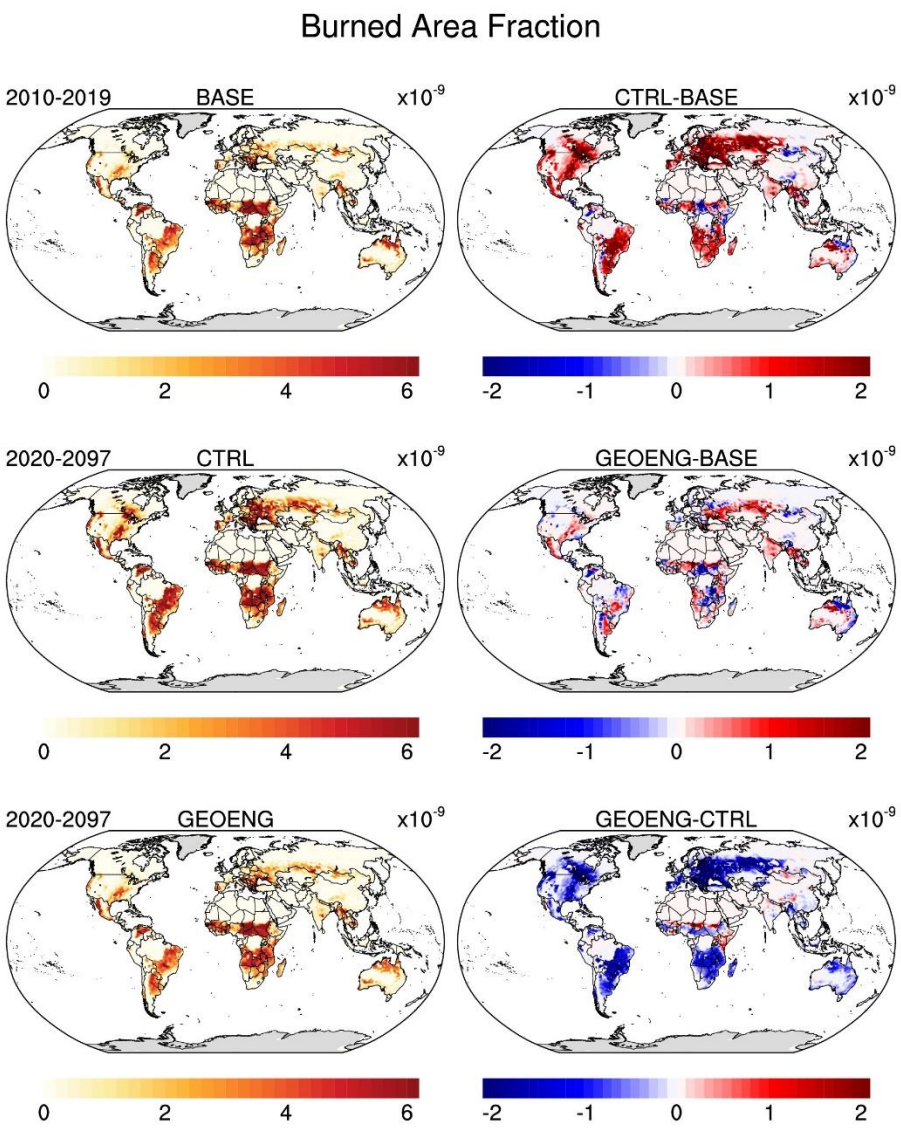


Figure 3-11. Same as Figure 3-4 except for burned area fractions by fires in each grid cell ($\times 10^{-9}$, unitless).

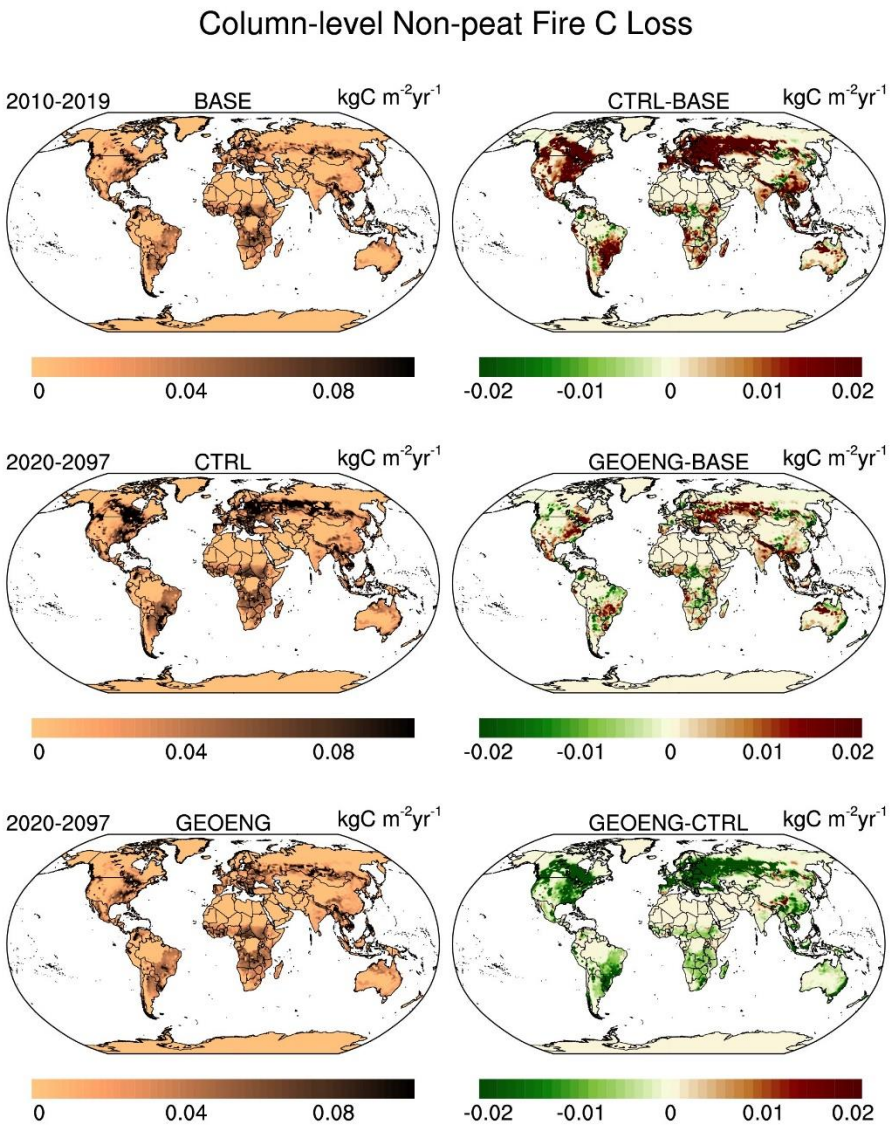


Figure 3-12. Same as Figure 3-4 except for column-level non-peatland carbon loss by fires (kg C m^{-2} yr^{-1}).

Table 3-1. Accumulated global climate change over various time periods. Numbers represent the mean and cross-ensemble standard deviation of the first three ensemble members for the *BASE*, *CTRL*, and *GEOENG* (abbreviated as *GEOG*). *PRECIP* and *ET* are precipitation and evapotranspiration (unit: mm/day), respectively, and the other variable annotations (unit: Pg C) are the same as shown in the Methods section. Positive values for *GPP*, *NPP*, *NEP*, and *NBP* indicate carbon gains in ecosystems while negative values represent carbon losses to the atmosphere; the opposite applies to R_a and R_h. Symbol "Δ" denotes the differences of *GEOENG*−*CTRL*. The asterisk sign indicates 2011–2019 cumulative sum of *NBP*.

Variable	2010–2019	2020–2097			2020–2039			2050–2069			2078–2097		
	BASE	***CTRL***	***GEOG***	**Δ**	***CTRL***	***GEOG***	**Δ**	***CTRL***	***GEOG***	**Δ**	***CTRL***	***GEOG***	**Δ**
GPP	1153±7	11085±27	10271±7	−813∓21	2497±15	2474±5	−23∓11	2863±5	2648±8	−215∓7	3176±9	2783±2	−393∓9
NPP	499±3	4700±8	4442±3	−258∓5	1072±4	1067±2	−5∓2	1216±2	1146±4	−69∓4	1329±3	1205±2	−124∓3
NEP	51±2	602±2	585±2	−17∓3	128±1	136±1	7±1	159±1	154±1	−4∓1	173±3	160±1	−14∓2
NBP	4±2*	198±4	277±3	79±6	50±1	62±1	13±2	56±1	77±1	20±2	43±4	73±0	30±3
R_a	654±4	6385±20	5830±4	−555∓16	1425±11	1407±3	−18∓8	1648±3	1502±5	−146∓4	1847±6	1579±0	−269∓6
R_h	448±2	4098±6	3856±2	−241∓4	944±4	931±1	−13∓3	1057±2	992±3	−65∓4	1155±1	1045±1	−110∓2
disturbance	42±1*	405±2	308±1	−96∓3	79±1	74±1	−5∓1	103±1	78±0	−25∓2	130±1	86±0	−44∓1
PRECIP	24±0	199±0	184±0	−15∓1	48±0	47±0	−1∓0	51±0	47±0	−4∓1	53±0	47±0	−7∓0
ET	14±0	120±0	110±0	−10∓0	29±0	29±0	−1∓0	31±0	28±0	−3∓0	32±0	28±0	−5∓0

Table 3-2. Accumulated net biome production (*NBP*) of individual ecoregions over different time periods. Numbers represent the mean and cross-ensemble standard deviation of the first three ensemble members in the *BASE*, *RCP85*, and *GEOENG* cases (abbreviated as *GEOG*). "Δ" symbol denotes the difference of *NBP* between *GEOENG* and *RCP85*. Positive values indicate carbon gains in land.

Ecoregion	**2010–2019**	**2020–2097**			**2020–2039**			**2050–2069**			**2078–2097**		
	BASE	***CTRL***	***GEOG***	**Δ**	***CTRL***	***GEOG***	**Δ**	***CTRL***	***GEOG***	**Δ**	***CTRL***	***GEOG***	**Δ**
Water bodies	0±0	1±0	2±0	1±0	0±0	0±0	0±0	0±0	1±0	0±0	0±0	1±0	0±0
Evergreen needleleaf forests	0±0	7±0	11±0	4±1	2±0	2±0	1±0	2±0	3±0	1±1	1±0	3±0	2±1
Evergreen broadleaf forests	5±1	125±1	130±1	6±2	31±0	35±0	4±0	33±1	33±1	1±2	32±1	33±1	1±1
Deciduous needleleaf forests	0±0	2±0	2±0	0±0	0±0	0±0	0±0	1±0	1±0	0±0	1±0	1±0	0±0
Mixed forests	1±0	4±1	23±0	19±0	2±0	5±0	2±0	2±1	7±0	5±1	-1±1	6±0	7±1
Open shrublands	1±0	16±0	27±1	11±0	4±0	5±1	1±0	5±1	8±0	3±1	3±0	8±0	5±1
Woody savannas	0±0	5±0	8±0	3±0	1±0	2±0	0±0	1±0	2±0	1±0	1±0	2±0	1±0

Table 3-2 (*continued*).

Ecoregion	2010–2019	2020–2097			2020–2039			2050–2069			2078–2097		
	BASE	*CTRL*	*GEOG*	Δ	*CTRL*	*GEOG*	Δ	*CTRL*	*GEOG*	Δ	*CTRL*	*GEOG*	Δ
Savannas	0±0	4±0	6±0	2±0	1±0	1±0	0±0	1±0	2±0	0±0	1±0	2±0	1±0
Grasslands	1±0	6±0	8±0	2±0	1±0	1±0	0±0	2±0	2±0	0±0	2±0	2±0	0±0
Croplands	−2∓1	12±2	34±1	22±2	3±1	5±1	2±0	5±1	11±1	6±1	0±1	9±0	9±1
Croplands / natural vegetation mosaics	0±0	2±0	6±0	3±0	1±0	1±0	0±0	1±0	2±0	1±1	1±0	2±0	1±0
Permanent snow and ice	0±0	0±0	0±0	0±0	0±0	0±0	0±0	0±0	0±0	0±0	0±0	0±0	0±0
Barren or sparsely vegetated	0±0	0±0	3±0	2±0	0±0	0±0	0±0	0±0	1±0	1±0	0±0	1±0	1±0
Global	4±2	198±4	277±3	79±6	50±1	62±1	13±2	56±1	77±1	20±2	43±4	73±0	30±3

(Figure 3-13). The former are responsible for 27% (22±2 Pg C) and the latter for 25% (19±0 Pg C) of the total ΔCSS (79±6 Pg C) by 2097. Less heat stress due to lower temperatures in *GEOENG* than in *CTRL* is the main factor that increases crop yields (i.e., more carbon gains on land) in spite of lower precipitation (Proctor et al., 2018). Increases in ΔCSS are also simulated in all other vegetated ecoregions during 2020–2097, primarily as a result of reduced respiration rates. Most ecoregions in both *CTRL* and *GEOENG* undergo increasing CSS from 2020–2039 to 2050–2069 but declined CSS from 2050–2069 to 2078–2097. Land use changes due to forest clearing and conversion to agriculture in the RCP8.5 emission scenario are likely the cause of these CSS changes (Hurtt et al., 2011).

Changes in ΔCSS provide information to reconstruct the atmospheric CO_2 trajectory in GLENS simulations. GLENS experiments were driven by the same CO_2 concentration based on the RCP8.5 emission scenario (Riahi et al., 2011). Even though carbon pools were simulated with an active terrestrial carbon cycle, terrestrial BGC feedbacks to the Earth system were not accounted for in the coupled modeling system. Such feedbacks can alter the carbon amount in the atmosphere, resulting in a different atmospheric CO_2 trajectory and hence climate change. Given the assumption that the land carbon fluxes in *CTRL* are consistent with the specified atmospheric CO_2 mole fraction trajectory, the accumulated differences in CSS between *GEOENG* and *CTRL* over time indicate a carbon gain on land as a result of aerosol geoengineering (Figure 3-14a). The global ΔCSS reaches 79±6 Pg C by 2097. That is, terrestrial ecosystems globally store additional carbon in *GEOENG* compared to *CTRL*, amounting to 37±3 ppm CO_2-equivalent, reducing the atmospheric CO_2 mole fraction by as much as 4% in 2097 (Figure 3-14b). The reduced airborne fraction of anthropogenic carbon due to terrestrial BGC feedbacks is within the range reported in previous studies by the year 2100 despite different models and aerosol geoengineering strategies compared with GLENS (Cao & Jiang, 2017; Keller et al., 2014; Tjiputra et al., 2016).

Implications of terrestrial biogeochemical responses to geoengineering

Terrestrial BGC feedbacks to the geoengineered climate in GLENS result in net carbon gains on land by sequestering a maximum of an additional 37 ppm of atmospheric

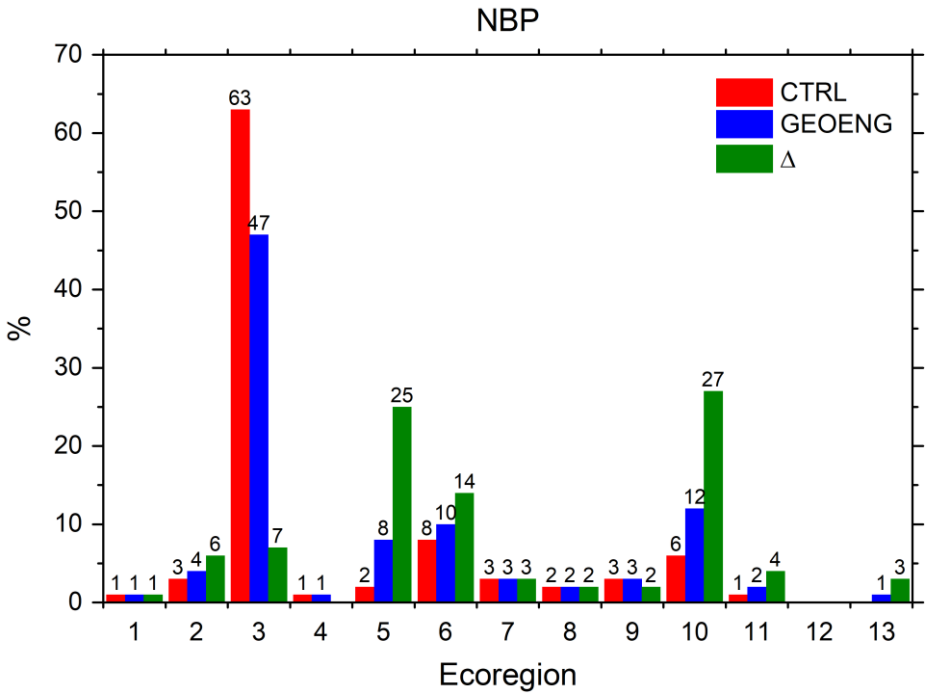


Figure 3-13. Percentages of ensemble mean of accumulated *NBP* for each ecoregion with respect to the accumulated global *NBP* from 2020 to 2097. Ecoregion labels are the same as those defined in Figure 3-2. Colored columns denote the cases *CTRL* (red), *GEOENG* (blue), and *GEOENG−CTRL* (Δ, green). The numbers above each column represent the percentages.

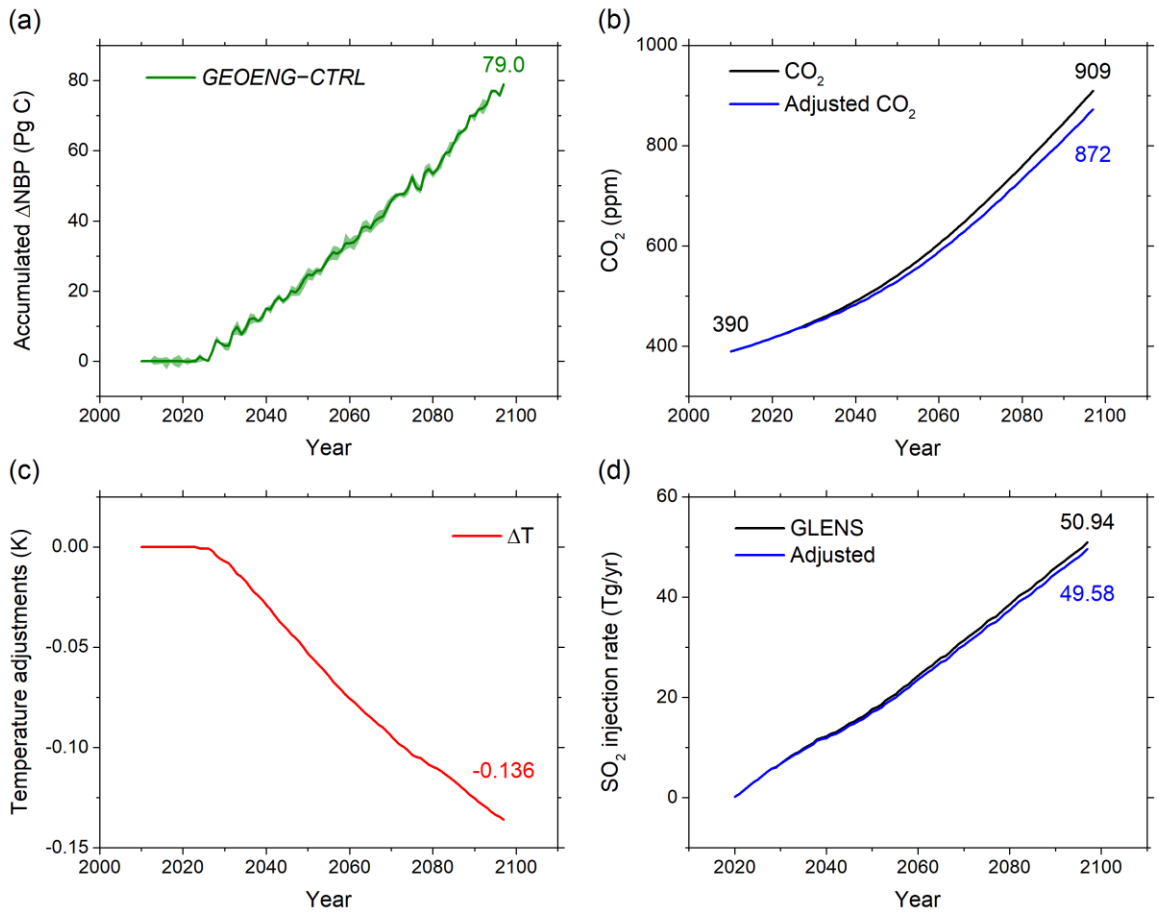


Figure 3-14. The trajectories of (a) accumulated global carbon sink strength changes (Pg C) due to geoengineering, (b) the atmospheric CO_2 mole fraction (ppm) during 2010–2097 for *CTRL* (Meinshausen et al., 2011) (black line) and the adjusted atmospheric CO_2 mole fraction due to the terrestrial BGC feedbacks (blue line), (c) surface temperature responses due to atmospheric CO_2 mole fraction adjustments, and (d) sulfur injection rates in GLENS (red) and adjusted injection rates due to terrestrial BGC feedbacks (blue). Shaded area in (a) represents the range of changes for the first three ensemble members between *GEOENG* and *CTRL*; solid green line is the ensemble mean. Adjusted values shown in (b) – (d) are calculated based on the ensemble mean values from (a).

CO_2 globally by 2097 (Figure 3-14b). By accounting for the terrestrial BGC feedback, lower atmospheric CO_2 mole fraction would induce a cooler global surface temperature in *GEOENG* compared to the prescribed CO_2 concentrations, differing by 0.136 K in 2097 (Figure 3-14c). Hence, in order to maintain the global surface temperature at 2020-levels, less sulfur aerosol would have needed to be injected had we used prescribed emissions rather than prescribed concentrations in GLENS (Figure 3-14d). As the ocean CO_2 sink is about 78% of the terrestrial CO_2 sink (Le Quéré et al., 2018) and the primary carbon cycle response to the geoengineered climate is determined mainly by terrestrial CSS rather than marine CSS (Matthews et al., 2009), only parts of the reductions in atmospheric CO_2 levels would be realized in GLENS because no marine BGC feedback was taken into consideration in the simulations. In general, marine CSS is enhanced in a cooler climate that maintains higher CO_2 solubility and stronger overturning circulation in oceans; however, increasing anthropogenic ocean acidification would likely mediate marine CSS due to its detrimental effects on calcifying biota (Doney et al., 2009; Fabry et al., 2008; Gattuso et al., 2015; Orr et al., 2005). While fully coupled emissions-forced simulations with interactive terrestrial and marine biogeochemistry are required to quantify competing feedback effects, we expect that temperature-induced reduction of the solubility pump in *CTRL* simulations would be responsible for stronger marine CSS in *GEOENG* simulations; however, over decadal timescales (out to 2100), we expect a smaller ocean feedback compared to the land feedback in *GEOENG*, consistent with other studies (Cao & Jiang, 2017; Keller et al., 2014). Conducting fully coupled emissions-forced ESM simulations with both marine and terrestrial BGC feedbacks enabled, as well as stratospheric and tropospheric chemistry, will be necessary to reduce the uncertainty in quantifying aerosol geoengineering impacts on the Earth system.

Biomass in individual compartments and fuel loads

Global vegetated lands gain more biomass in almost all regions for both *CTRL* and *GEOENG* compared to *BASE* (Figure 3-15). Enhanced CO_2 fertilization effect plays the key role in such vegetation biomass increases. However, regions (e.g., southeastern Canada and boreal region of Eurasia) with increased burned area and fire-induced carbon loss in

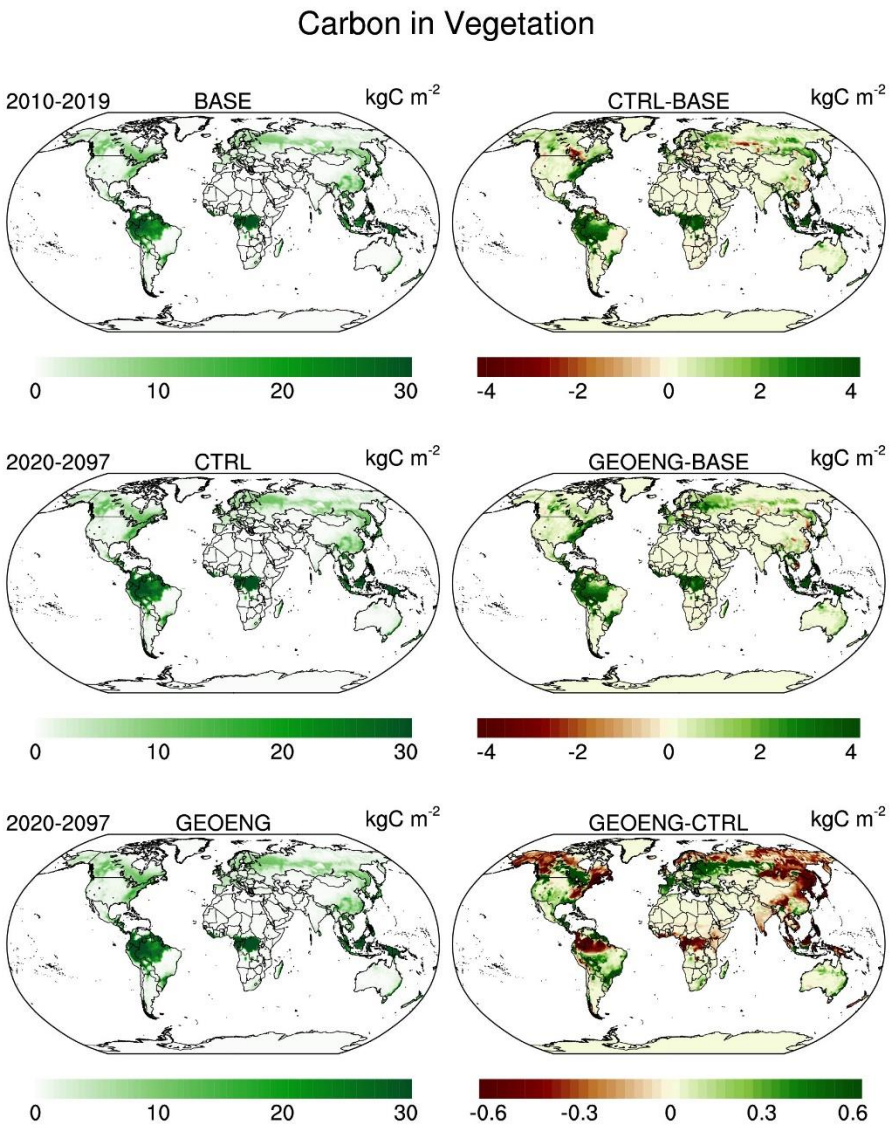


Figure 3-15. Same as Figure 3-4 except for biomass in vegetation (kg C m^{-2}).

CTRL would experience biomass loss (Figure 3-11 and 3-12) compared to *BASE*. This loss is found in all compartments with wood the largest (Figures 3-16, 3-17, and 3-18) in *CTRL* with respect to *BASE*. Biomass in individual compartments between *CTRL* and *GEOENG* illustrate substantial differences, especially in wood and in leaves (Figures 3-16 and 3-17). Similar to *NPP* and *NEP*, higher surface temperatures in *CTRL* at high latitudes thaw permafrost regions, lengthen growing seasons and enable more biomass in vegetation than that in *GEOENG*; at mid and low latitudes, reduced precipitation and lower temperatures induce lower biomass in *GEOENG* than in *CTRL* over northern Amazon and southern Africa.

Globally, *GEOENG* produces more vegetation biomass (*cVeg*) than *CTRL* during the first 50 years of geoengineering then less biomass would be produced in *GEOENG* (Table 3-3). The accumulated difference increases with the aerosol geoengineering over time, peaking at year 2076 (~0.14 Pg C) and gradually decreases until the end of the simulation (~0.11 Pg C in 2097) (Figure 3-19a). The dominate biomes that have the largest biomass increases are croplands and woody savannas; the largest biomass decreases shift from open shrublands and grasslands during the peaking year to evergreen broadleaf forests and open shrublands in the end of the simulation. Such biomass variations in biomes are also found in leaves (*cLeaf*), wood (*cWood*), and roots (*cRoot*) (Figures 3-19b,c,d), except that *cWood* increases over time during the whole geoengineering period while *cLeaf* and *cRoot* do not have the same increasing trends. Instead, there would be small increases before 2068 for *cLeaf* and before 2051 for *cRoot* then both compartments show reduced biomass in *GEOENG* compared to that in *CTRL*. In *GEOENG*, croplands and mixed forests are the major biomes that increase *cWood* compared to *CTRL*, with some losses of biomass in evergreen broadleaf forests, deciduous needleleaf forest, and grasslands; the decreases in *cLeaf* is attributed to the smaller biomass in leaves in evergreen broadleaf forests, grasslands, and open shrublands; lower root biomass in mixed forests, croplands and grasslands in *GEOENG* are the major biomes that cause the decreasing trend of *cRoot*. These biomass variations only induce small changes (< 1%) of global biomass allocations for individual compartments in both *CTRL* and *GEOENG* globally (Figure 3-20). Since CO_2 fertilization increases the total vegetation biomass, there would be a larger amount of

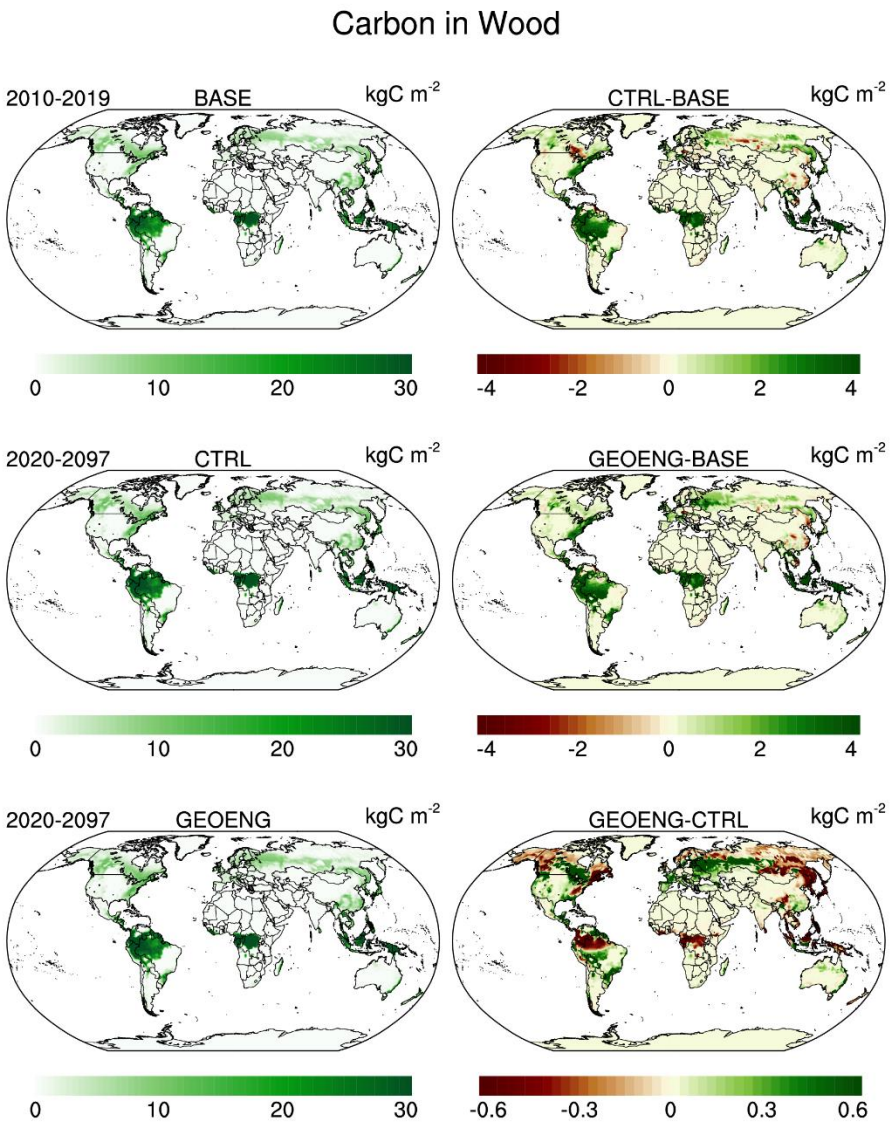


Figure 3-16. Same as Figure 3-4 except for biomass in wood (kg C m^{-2}).

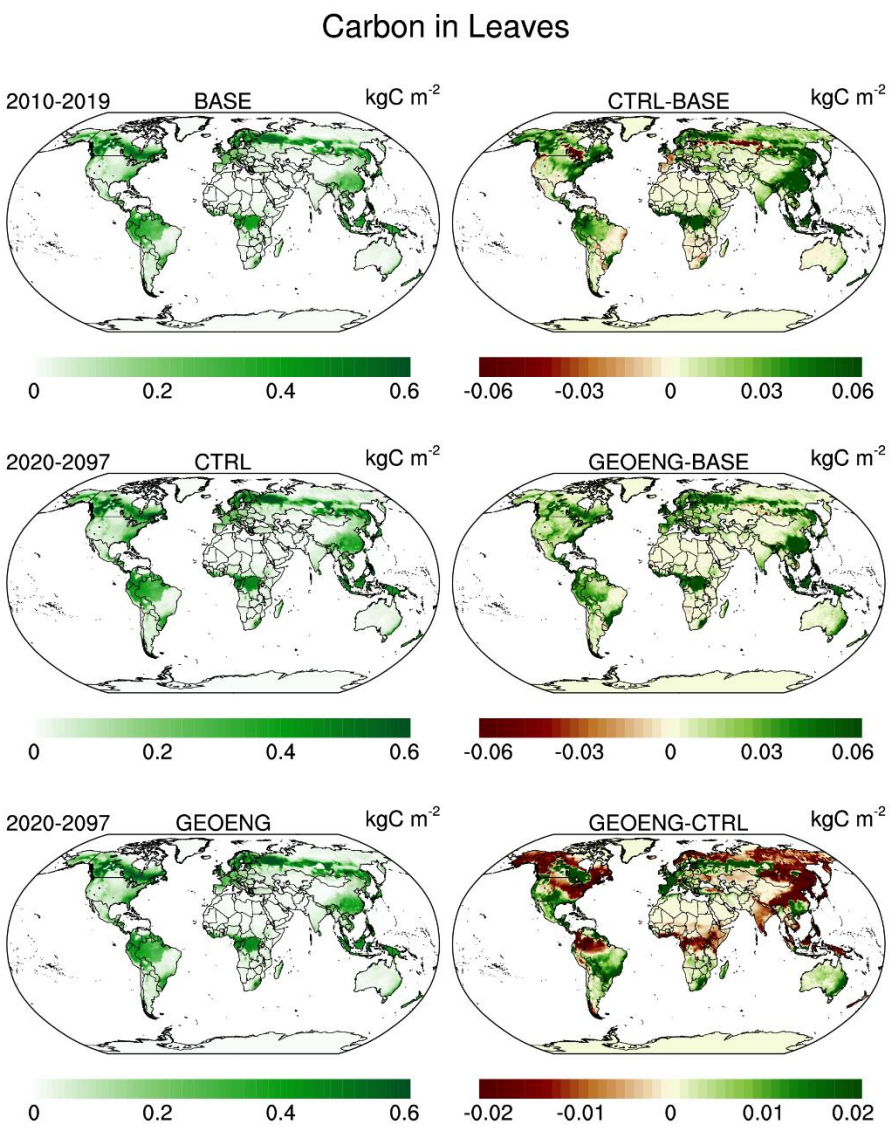


Figure 3-17. Same as Figure 3-4 except for biomass in leaves (kg C m^{-2}).

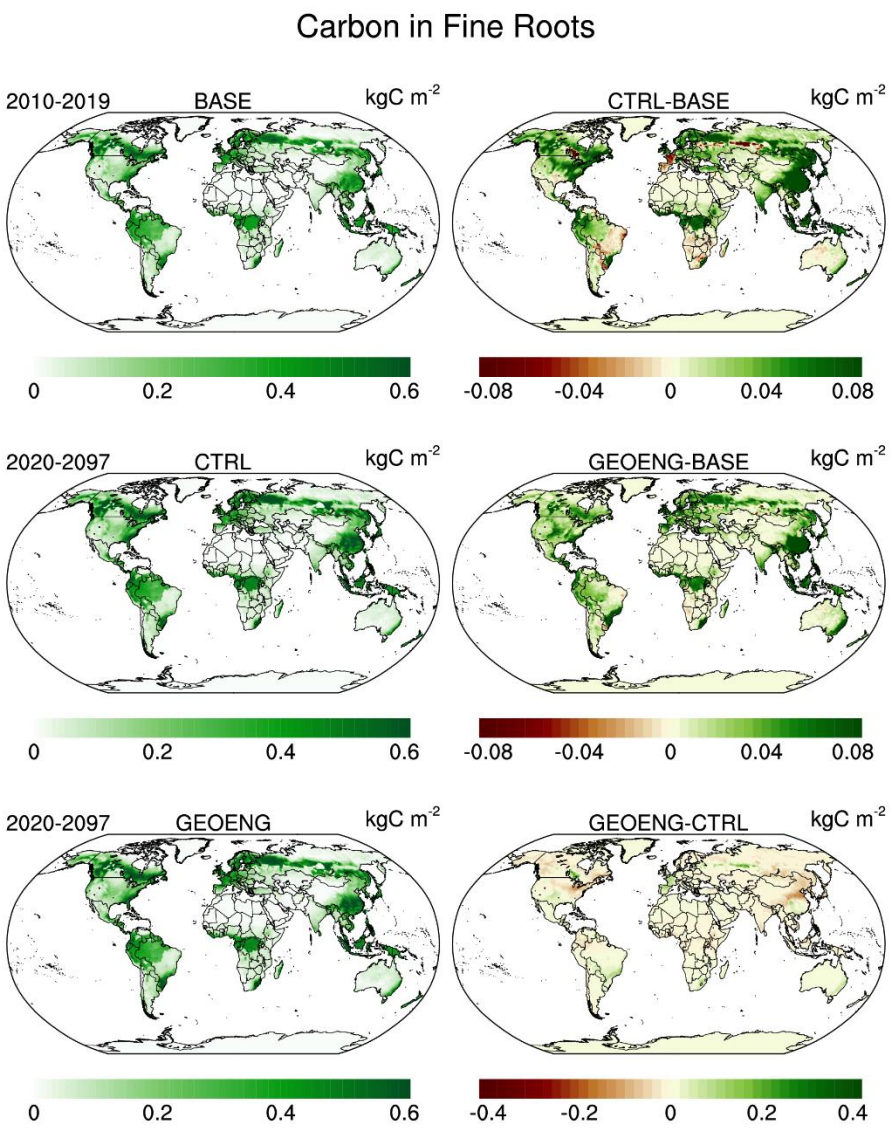


Figure 3-18. Same as Figure 3-4 except for biomass in fine roots (kg C m^{-2}).

Table 3-3. Same as Table 3-2 except for the carbon amount in total vegetation (Pg C).

Ecoregion	2010–2019	2020–2097			2020–2039			2050–2069			2078–2097		
	BASE	*CTRL*	*GEOG*	Δ	*CTRL*	*GEOG*	Δ	*CTRL*	*GEOG*	Δ	*CTRL*	*GEOG*	Δ
Water bodies	0±0	0±0	0±0	0.01±0.00	0±0	0±0	0.00±0.00	0±0	0±0	0.00±0.00	0±0	0±0	0.00±0.00
Evergreen needleleaf forests	0±0	2±0	2±0	0.00±0.01	0±0	0±0	0.00±0.00	1±0	1±0	0.00±0.01	1±0	1±0	0.00±0.01
Evergreen broadleaf forests	3±0	29±0	28±0	−0.14∓0.02	7±0	7±0	0.02±0.01	7±0	7±0	0.00±0.00	8±0	8±0	−0.15∓0.01
Deciduous needleleaf forests	0±0	0±0	0±0	−0.02∓0.00	0±0	0±0	0.00±0.00	0±0	0±0	0.00±0.00	0±0	0±0	−0.01∓0.00
Mixed forests	1±0	5±0	5±0	0.03±0.03	1±0	1±0	0.00±0.01	1±0	1±0	0.00±0.01	1±0	1±0	0.02±0.02
Open shrublands	0±0	4±0	4±0	−0.06∓0.00	1±0	1±0	0.00±0.00	1±0	1±0	−0.02∓0.00	1±0	1±0	−0.03∓0.00
Woody savannas	0±0	1±0	1±0	0.05±0.00	0±0	0±0	0.00±0.00	0±0	0±0	0.01±0.00	0±0	0±0	0.02±0.00
Savannas	0±0	1±0	1±0	0.01±0.01	0±0	0±0	0.00±0.00	0±0	0±0	0.00±0.00	0±0	0±0	0.01±0.00

Table 3-3 (*continued*).

Ecoregion	2010–2019	2020–2097			2020–2039			2050–2069			2078–2097		
	BASE	*CTRL*	*GEOG*	Δ	*CTRL*	*GEOG*	Δ	*CTRL*	*GEOG*	Δ	*CTRL*	*GEOG*	Δ
Grasslands	0±0	1±0	1±0	−0.03∓0.00	0±0	0±0	0.00±0.00	0±0	0±0	−0.01±0.00	0±0	0±0	−0.02∓0.00
Croplands	1±0	5±0	5±0	0.20±0.08	1±0	1±0	0.00±0.01	1±0	1±0	0.05±0.02	1±0	1±0	0.11±0.04
Croplands / natural vegetation mosaics	0±0	1±0	1±0	0.06±0.01	0±0	0±0	0.00±0.00	0±0	0±0	0.01±0.00	0±0	0±0	0.03±0.00
Permanent snow and ice	0±0	0±0	0±0	−0.01∓0.00	0±0	0±0	0.00±0.00	0±0	0±0	0.00±0.00	0±0	0±0	0.00±0.00
Barren or sparsely vegetated	0±0	0±0	0±0	−0.01∓0.00	0±0	0±0	0.00±0.00	0±0	0±0	0.00±0.00	0±0	0±0	0.00±0.00
Global	6±0	52±0	52±0	0.11±0.15	12±0	12±0	0.04±0.02	13±0	13±0	0.06±0.04	15±0	15±0	−0.03∓0.08

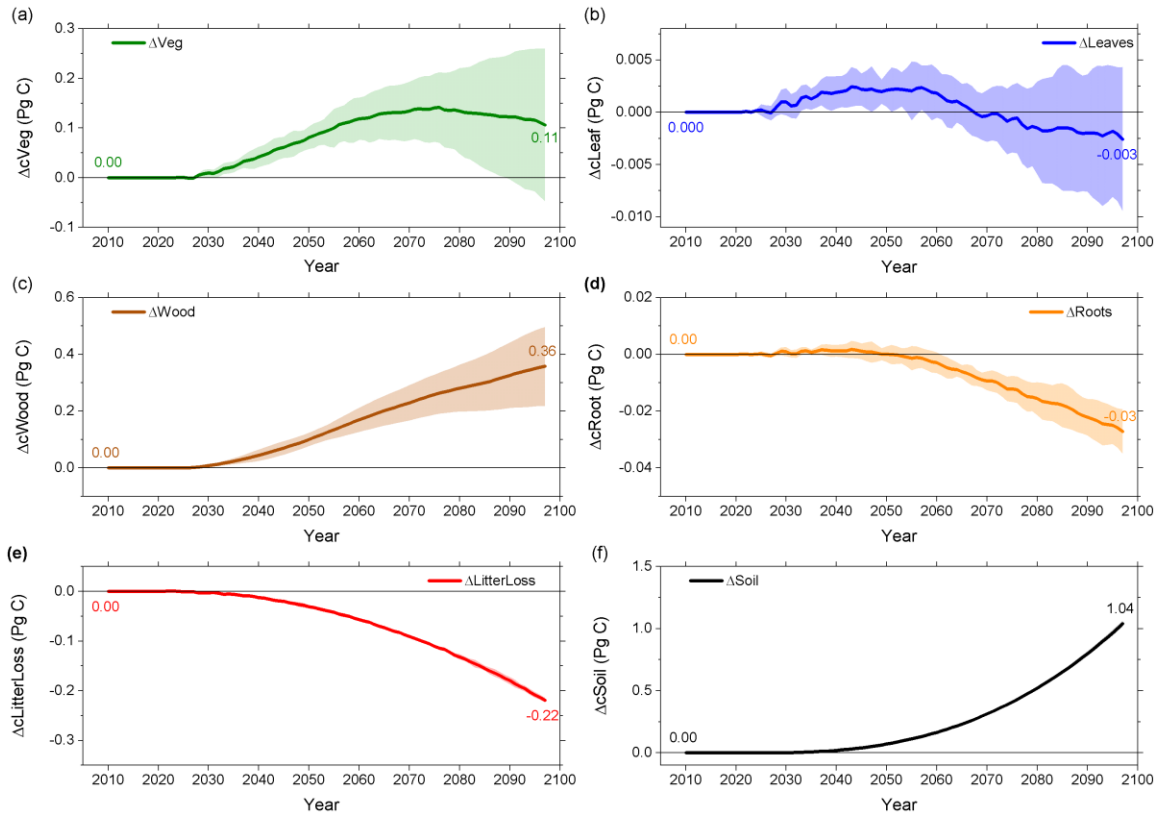


Figure 3-19. Accumulated global biomass changes (*GEOENG−CTRL*) in individual compartments and carbon pools (Pg C). (a) Carbon in total vegetation (green), (b) carbon in leaves (blue), (c) carbon in wood (light brown), (d) carbon in roots (orange), (e) litter carbon loss (red), and (f) carbon in soil (black). Solid lines represent the ensemble mean of the three ensemble members with the shaded area showing the standard deviation. Numbers in each panel along with the curves denote the starting and ending values of biomass change between *GEOENG* and *CTRL*.

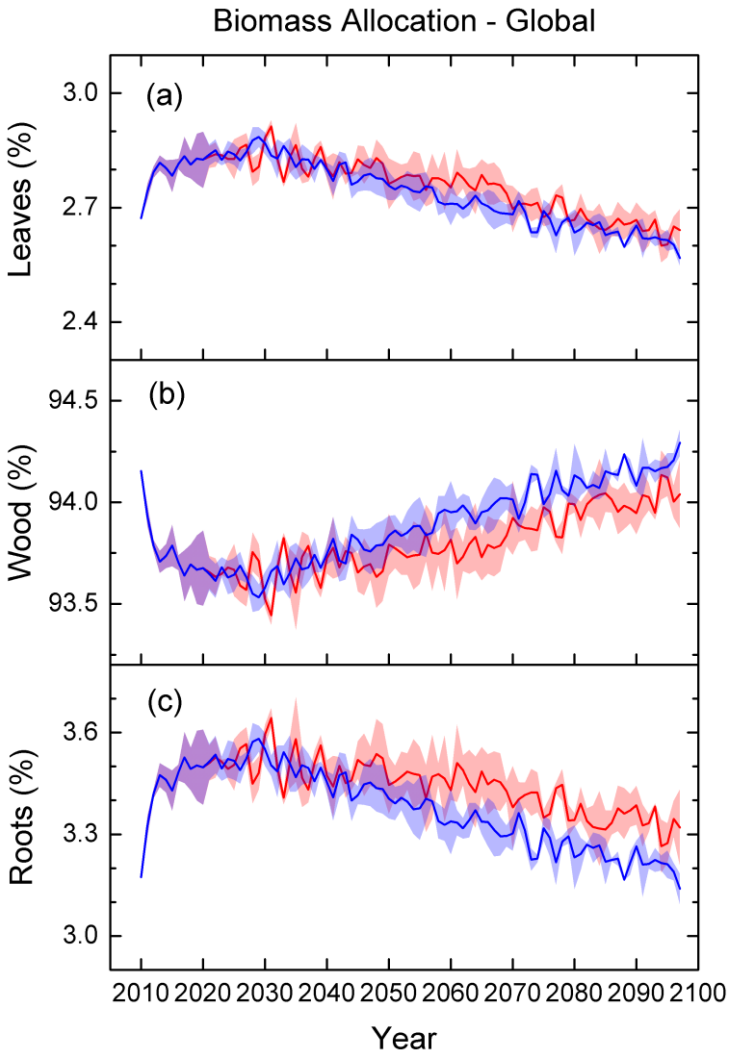


Figure 3-20. Annual global carbon allocation in individual compartments (%) for *CTRL* (red) and *GEOENG* (blue). (a) carbon allocation in leaves, (b) carbon allocation in wood, (c) carbon allocation in roots. Solid lines represent the ensemble mean of the three ensemble members with the shaded area showing the standard deviation. Values are computed based on accumulated biomass in each compartment.

carbon in litters for both *GEOENG* and *CTRL*. Nevertheless, higher temperatures induce higher R_h in *CTRL* compared to *GEOENG*, implying the carbon losses in litters are higher in *CTRL* than in *GEOENG* (Figure 3-19(e)). Therefore, the soil carbon is higher in *GEOENG* than in *CTRL* because more carbon is released from litter to the atmosphere in *CTRL* (Figure 3-19(f)).

Global fuel loads increase as a result of more vegetation biomass due to CO_2 fertilization in both *CTRL* and *GEOENG* with respect to *BASE* (Figure 3-21). While most fuel load increases take place at northern high latitudes, larger burned area and carbon loss due to fires (Figures 3-11 and 3-12) reduce the amount of available fuel loads in some boreal regions and eastern Asia in *CTRL* and *GEOENG* compared to *BASE*. Northern hemisphere, excluding the northeastern Asia where declined fuel loads are associated with lower surface temperature and precipitation (Figures 3-1a,b), would have more available fuel loads in *GEOENG* than in *CTRL*.

Methods

Stratospheric Aerosol Geoengineering Large Ensemble (GLENS) dataset

Two experiments from the GLENS project (Tilmes et al., 2018) are analyzed. Each experiment consists of 20-member ensemble runs performed with the Community Earth System Model using the Whole Atmosphere Community Climate Model (CESM1(WACCM)) as its atmospheric component (Mills et al., 2017). Both experiments were conducted under the same Representative Concentration Pathway 8.5 (RCP8.5) emission trajectory (Riahi et al., 2011) used in the Fifth Phase of the Coupled Modeling Intercomparison Project (CMIP5). Simulations were driven by specified CO_2 mole fractions rather than anthropogenic CO_2 emissions rates. The simulations were configured to use a simple tropospheric chemistry scheme, and active marine biogeochemistry was not enabled. The control experiment was simulated with the RCP8.5 emission trajectory over the reference period 2010–2030 and the first three ensemble members continued at least through 2097. The geoengineering experiment followed the same experimental design as the control one except for optimized SO_2 injections at four locations along 180°E at 30°N, 15°N, 15°S, and 30°S in the lower stratosphere (25 km for 15° and 22.8 km for 30°)

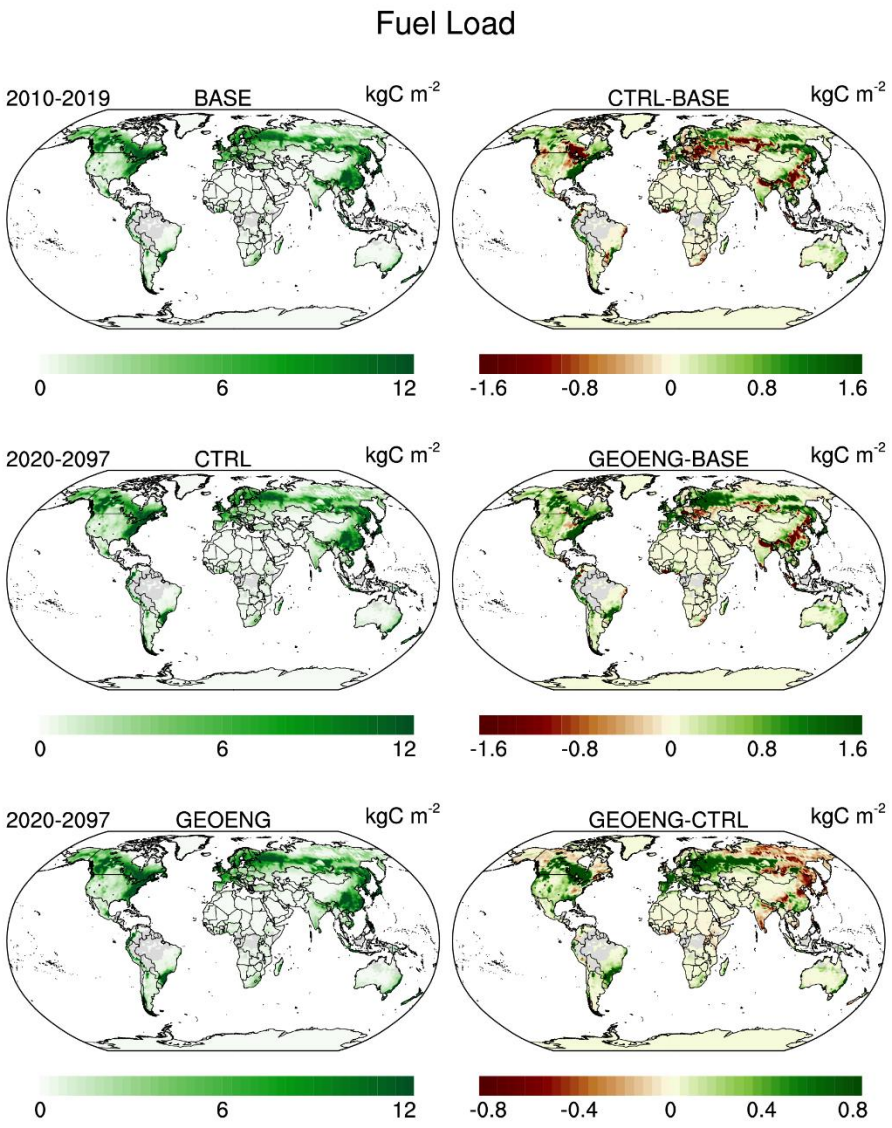


Figure 3-21. Same as Figure 3-4 except for carbon in fuel loads (kg C m^{-2}).

(Kravitz et al., 2017) starting at year 2020. The SO_2 injection rate was adjusted annually during 2020–2099, using a feedback algorithm that maintained global mean surface temperature, the interhemispheric surface temperature gradient, and the equator-to-pole surface temperature gradient at their 2020 values (Kravitz et al., 2016, 2017; MacMartin et al., 2014). Since only the first three (of 20) ensemble members in the baseline experiment were extended to at least year 2097, to fairly compare the differences in climate and terrestrial biogeochemical feedbacks between the baseline and geoengineering experiments, as well as those differences with respect to the present climate, we analyzed the first three ensemble members from the baseline period during 2010–2019 (defined as case "*BASE*") and during 2020–2097 (defined as case "*CTRL*"), and the first three ensemble members from the geoengineering experiment during 2020–2097 (defined as case "*GEOENG*").

Ecoregions

Thirteen ecoregions are defined in this study by clustering climate, soil, and topography information into regions that were fitted to the International Geosphere-Biosphere Programme (IGBP) ecoregion definitions (Hargrove et al., 2006; Hargrove & Hoffman, 2004; Townshend, 1992) (see Figure 3-2). Terrestrial BGC feedbacks to the climate with and without geoengineering are compared globally as well as over individual ecoregions.

Carbon sink strength

The carbon budget in the terrestrial ecosystem can be expressed, according to the Intergovernmental Panel on Climate Change (Watson et al., 2000), as

$$\begin{aligned} GPP &= NPP + R_a \\ &= NEP + R_h + R_a \\ &= NBP + R_h + R_a + disturbance \end{aligned} , \qquad (3.1)$$

where *GPP* is the gross primary production, R_a the autotrophic respiration, *NPP* the net primary production, R_h the heterotrophic respiration, *NEP* the net ecosystem production, *NBP* the net biome production, and *disturbance* includes anthropogenic emissions due to

land cover and land use changes (e.g., fires, deforestation, and crop harvest). Note that *disturbance* was combined into *NBP* in GLENS. Positive values for *GPP*, *NPP*, *NEP*, and *NBP* indicate carbon gains in land while negative values denote carbon losses to the atmosphere; contrarily, positive values for R_a and R_h represent carbon losses to the atmosphere and larger negative values imply more carbon remaining in land. We interpreted *NBP* as the carbon sink strength (CSS) that indicated carbon storage in terrestrial ecosystem. A positive CSS value indicates atmospheric CO_2 is stored in the terrestrial ecosystem while a negative value represents carbon releases from the terrestrial ecosystem to the atmosphere. A fixed ratio of 1:2.13 is used in this study to convert the amount of carbon (Pg C) released from or sequestered in the terrestrial ecosystem to the equivalent amount of airborne CO_2 mole fractions (ppm).

Adjusted atmospheric CO_2 and surface temperature trajectory

Simulations in GLENS were driven by the atmospheric CO_2 mole fraction specified in the RCP8.5 emission scenario (Meinshausen et al., 2011; Riahi et al., 2011). The simulations were conducted with an active global land carbon cycle, but terrestrial biogeochemical feedbacks were not incorporated into the coupled modeling system. In this analysis we assumed the *NBP* variations were consistent with the atmospheric CO_2 mole fraction for the *CTRL* case. Differences in simulated *NBP* between *GEOENG* and *CTRL* are attributed to ecosystem responses due to sulfur injections in the lower stratosphere. These differences are subtracted (if positive) or added (if negative) to the atmospheric CO_2 concentration to reconstruct atmospheric CO_2 trajectory according to the equation

$$C_{t+1} = C_t + F_{t+1} - F_t + B_{t,GEOENG} - B_{t,CTRL} \tag{3.2}$$

where t is the time step, C the adjusted atmospheric CO_2 airborne mole fractions, F the atmospheric CO_2 airborne mole fractions, and B the terrestrial BGC feedbacks from case *GEOENG* or *CTRL*. The changes of atmospheric CO_2 trajectory alter the radiative forcing, resulting in a different surface temperature trajectory. Adjusted surface temperatures due to atmospheric CO_2 adjustments are approximated through an impulse response function tuned to the mean of CMIP5 models (Boucher & Reddy, 2008; F. M. Hoffman et al., 2014).

We use this function to compute the CO_2-induced radiative forcing changes. These changes are then used to calculate the adjusted temperature trajectory. Differences between the simulated global mean surface temperature in GLENS and the adjusted one are compared to estimate a reduced amount of SO_2 injection (Tilmes et al., 2018).

CHAPTER 4
IMPACTS OF WILDFIRES ON AIR QUALITY CHANGES IN THE WESTERN UNITED STATES

Abstract

Wildfires emit smoke particles and pollutants that greatly affect the public health over the western United States (WUS) each fire season. With rising surface temperatures projected by climate models, increasing wildfire activities and severities are predicted because vegetated regions become more vulnerable to fires as a result of lower soil moisture and atmospheric humidity. In this study, I conducted model simulations with and without fire emissions during the present years (2003–2010) and the future years (2050–2059). Results demonstrated that wildfires would have negligible impacts on ozone concentration changes in WUS both in present and future years. On the contrary, increases of fine particulate matter ($PM_{2.5}$) concentration could be significant with the domain maximum increased by 194.92 μg/m^3 and the largest increase rate could be 61 times higher with fire emissions compared to without fire emissions during the present years. Such increases were also simulated in future years, which utilized projected emissions based on the 2005 emission dataset from U.S. EPA, with the domain maximum increased by 57.58 μg/m^3 and the largest increase rate could reach about 21 times higher with fire emission compared to without fire emissions.

Introduction

Wildfires emit large amounts of trace gases and particles (Alves et al., 2011; Andreae & Merlet, 2001; Ito & Penner, 2004; Michel et al., 2005; Na & Cocker, 2008; Urbanski et al., 2008; Wiedinmyer et al., 2006) that can substantially influence regional air quality. Greenhouse gases including carbon dioxide (CO_2), methane (CH_4), nitrogen oxides (NO_x) and nitrous oxide (N_2O) released to the atmosphere during the combustion processes enhance the temperature warming effect and worsen air quality. Wiedinmyer and Neff (2007) estimated the amount of CO_2 emitted from fires is equivalent to 4–6% of anthropogenic emissions and in some cases the fire emissions of CO_2 can even exceed the annual CO_2 emission from fossil fuel usage in the United States. Pfister et al. (2008) found that 17% of the exceedances of 8-hour ozone (O_3) concentrations in California exceeding the U.S. public health standards were attributed to wildfires. Di Carlo et al. (2015) suggested that 10% of surface O_3 concentration in central Italy was contributed by fire

emissions. Higher organic compounds concentrations after wildfires are also observed compared to that in typical urban air pollution (Alves et al., 2011; Na & Cocker, 2008). These compounds can form O_3 and particulate matter (PM) that degrade the air quality and induce adverse impacts on human health (Coates et al., 2016; Finlay et al., 2012; Haikerwal et al., 2015; J. C. Liu et al., 2015, 2017; Morris et al., 2006; Mühle et al., 2007; Sapkota et al., 2005; Wardle et al., 2003) and the ecosystem (Ainsworth et al., 2012; D. A. Jaffe & Wigder, 2012; Xu et al., 2012) through photochemical reactions in the atmosphere.

Since heightened wildland fire activities have been observed in the western United States (WUS) in recent decades (Littell et al., 2009; Y. Liu et al., 2013; Marlon et al., 2012; Miller et al., 2009; Running, 2006; Westerling et al., 2006; Wiedinmyer & Neff, 2007), the rising global temperatures, as well as reduced precipitation and soil moisture (Cayan et al., 2010; Chylek et al., 2017; A. Dai et al., 2004; Gao et al., 2014; Pachauri & Meyer, 2014) due to elevated anthropogenic emissions in the future suggest an environment that is more conducive for wildfire activities (Y. Liu et al., 2013). As a result, future wildfire activities are likely to become important sources of air pollutants altering regional air quality in WUS (Spracklen et al., 2009). While previous research had reported the increasing wildfire activities in WUS (Spracklen et al., 2009; Yue et al., 2013), these studies predicted future wildfire activities by applying the Special Report on Emissions Scenarios (SRES) in which no carbon emission controls were included. As the public awareness of the rapid climate change rises, it is important to consider the efforts of the climate change mitigation policies to limit anthropogenic emissions for projecting future wildfires. Hence, simulations with the Representative Concentration Pathways (RCPs) (Moss et al., 2008) that integrate socioeconomic, emissions, and climate scenarios altogether provide more convincing information to governments and policymakers for developing wildfires and air pollution management plans than SRES. In this study multiple global and regional climate and chemistry-transport models that have been widely used in the climate and air quality community were used to simulate hourly gas-phase and particulate species concentration. Through controlling wildfire emissions under the same meteorology as well as initial and boundary conditions, this study presents the fire-induced air pollutant concentration change in WUS during present years and in the future.

Methods

Model descriptions

This study employed multiple global and regional climate and chemistry-transport models to evaluate the variations of air pollutants induced by wildfires during present years (2003–2010) and future years (2050–2059). The global and regional climate and chemistry models were set up the same as Gao et al. (2013), with a newer regional chemistry-transport model and updated emission inputs. The global climate simulations were conducted with the Community Earth System Model (CESM) version 1 with the Community Atmosphere Model version 4 (CAM4) (Neale et al., 2010) as its atmospheric component (0.9° latitude × 1.25° longitude horizontal grid resolution and 26 vertical layers with the model top about 3 hPa), the Community Land Model (CLM4) (Oleson et al., 2010) as the land component, the Parallel Ocean Program version 2 (POP2) (Smith et al., 2010) as the ocean component, and the Los Alamos National Laboratory Sea Ice Model version 4 (CICE4) (Hunke & Lipscomb, 2008) as the sea ice component. The global climate-chemistry model was integrated with the CAM4 (CAM–Chem) (Lamarque et al., 2012) that adopted the Model for OZone And Related chemical Tracers (MOZART) version 4 and bulk aerosol model (Emmons et al., 2010; Lamarque et al., 2005). This global chemistry-transport model, CESM(CAM-Chem), only simulated how atmospheric gaseous and particulate constituents reacted and transported through chemical and dynamical processes in the atmosphere. Variations in the atmospheric gaseous and particulate constituents had no impact on altering the climate conditions in order to keep the simulated climate between CESM and CESM(CAM-Chem) identical. In addition, both CESM and CESM(CAM-Chem) stored the simulation results with a time step of three hours. All global climate simulations for the future years adopted the RCP8.5 emission scenario (Riahi et al., 2011), a scenario with very high greenhouse gases emissions without any specific climate mitigation target.

The CESM climate simulation results provided the boundary conditions for simulating regional climate by the Weather Research and Forecast (WRF) model (Skamarock & Klemp, 2008) through dynamical downscaling (Gao et al., 2012). This study

adopted WRF version 3.2.1 with the same scientific physics options used in Gao et al. (2012), which included Kain–Fritsch convective parameterization (Lam et al., 2011; Qian et al., 2010; Wong et al., 2012), the single-moment 6-class microphysical scheme (Hong & Lim, 2006; Qian et al., 2010; Wong et al., 2012), the Mellor–Yamada–Janjić planetary boundary layer scheme (Janjić, 1990; Lam et al., 2011; Mellor & Yamada, 1982), the Noah land surface model (Chen & Dudhia, 2001; Lam et al., 2011; Qian et al., 2010), and the rapid radiative transfer model for GCMs (RRTMG) as the shortwave and longwave radiation scheme (Iacono et al., 2008; Morcrette et al., 2008). The WRF outputs included hourly meteorological information over the contiguous United State (CONUS) with 12 km × 12 km horizontal grid resolution.

The CESM(CAM-Chem) simulation results served as the initial and boundary conditions of the gas-phase and particulate species concentration for the regional chemistry-transport model—the Community Multiscale Air Quality (CMAQ) modeling system—developed and improved by the U.S. EPA and the air quality modeling community (Byun & Schere, 2006; Wong et al., 2012). As a regulatory model, CMAQ is used to predict O_3, PM, air toxics, and acid deposition for air quality management as well as scientific studies such as health risks induced by O_3 and PM (Stowell et al., 2019; Weber et al., 2016). This study adopted CMAQ version 5.2 (Appel et al., 2018; U.S. EPA, 2017) with the Carbon Bond 05 (CB05) chemistry module (Appel et al., 2017) and the aerosol model (AE6) with non-volatile primary organic aerosols (nvPOA) option (Simon & Bhave, 2012). Other chemistry and physics options included the aqueous-phase chemistry module by Fahey et al. (2017) for the clouds and aqueous-phase chemistry, the vertical diffusion scheme from the updated Asymmetric Convective Method (Pleim, 2007), the horizontal advection scheme from Colella and Woodward (1984), inline photolysis rate calculations (Binkowski et al., 2007), inline lightning-induced nitrogen oxides (NO_x), and inline plume-rise modules for emissions (UNC Institute for the Environment, 2009). To conduct CMAQ simulations, three mandatory input information including (1) meteorological conditions, (2) initial and boundary conditions of gas-phase and particulate species concentration, and (3) emissions of gas-phase and particulate species is required.

Meteorological and initial and boundary inputs for CMAQ

In this study, meteorological variables from WRF were processed by the Meteorology-Chemistry Interface Processor (MCIP) (Otte & Pleim, 2010) and zoomed to the WUS domain (Figure 4-1) with the same 12 km × 12 km horizontal grid resolution as WRF. Although MCIP reduced WRF's 34 vertical layers to 25 vertical layers due to limited computational resources, the outputs from MCIP had the same top pressure at 50 hPa as the WRF output. Note that the required sea ice fraction information for CMAQ was not included in the MCIP outputs because of compatible issues between CESM, MCIP and CMAQ versions. Such information was extracted from the CESM results and added to each grid cell in MCIP output. The gas-phase and particulate species concentration from the CESM(CAM-Chem) output was extracted and regridded to the WUS domain as the CMAQ initial conditions (ICON) and boundary conditions (BCON) using the species mapping table from Gao et al. (2013). Since CMAQ v5.2 was a newer version than that used in Gao et al. (2013), additional species were re-mapped as shown in Table 4-1 (Pye & Pouliot, 2012). In addition, the mapping of secondary organic aerosols (SOA) from CESM(CAM-Chem) to CMAQ v5.2 used the ratios of concentration between SOA species in CMAQ simulations driven by clean air ICON and BCON suggested by Carlton et al. (2010) and Gao et al. (2013).

Emission inputs for present year CMAQ simulations

The present year emission data from U.S. EPA contained point sources and area sources during 2001–2010. The point sources included anthropogenic emissions from Electric Generating Units point sectors (*ptipm*), non-Electric Generating Units point sectors (*ptnonipm*), and other point source emissions outside the CONUS domain (*op*). The area sources included anthropogenic emission sectors (e.g. industrial processes, solvent, and agricultural production) and biogenic emissions with 36 km × 36 km horizontal grid resolution. The data was regridded and zoomed to the 12 km × 12 km WUS domain (Figure 4-1). Note that mobile emissions from vehicles and the emissions from prescribed and wildland fires were combined in the area source emissions. As fire-induced emissions should be distributed vertically according to the meteorological conditions and the sizes of

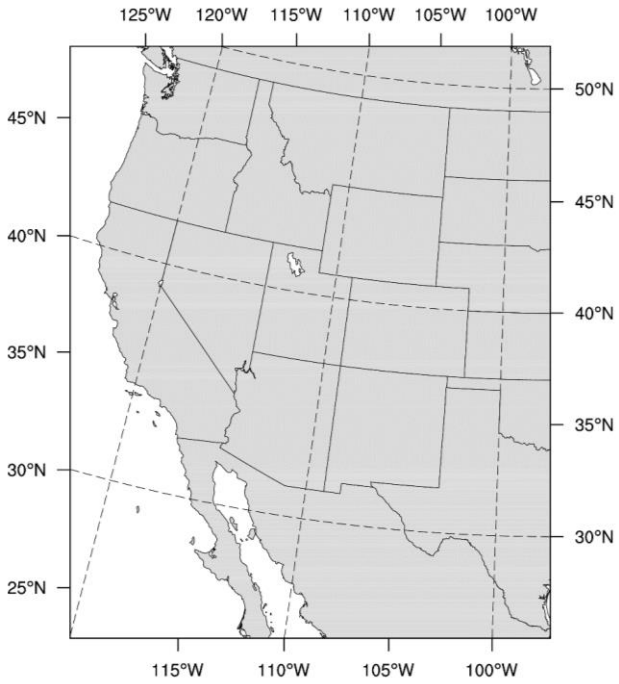


Figure 4-1. The simulation domain used in this study.

Table 4-1. Updated mapping table for gas-phase pollutant emissions (mole/s) based on Gao et al. (2013). XYL represents xylene.

New CMAQ Species	Species Name	Value
NAPH	Naphthalene	0.002*XYL
XYLMN	Xylene without naphthalene	0.998*XYL
PAR (new)	Paraffin carbon bond (C-C)	PAR−0.00001*NAPH
SOAALK	lumped SOA tracer species formed from alkanes	0.108*PAR

burned area, this study used the Fire INventory (FINN) version 1.5 from National Center for Atmospheric Research (NCAR) (Wiedinmyer et al., 2011) and the Global Fire Emissions Database version 4.1 with small fires (GFED4.1s) (Giglio et al., 2013) to re-allocate the wildfire emissions in the U.S. EPA emissions. FINN provided satellite retrievals of 40 fire-induced species emissions with a horizontal resolution about 1 km × 1 km. Table 4-2 illustrates the species mapping between FINN MOZART4 and CMAQ CB05 according to Tai et al. (2008) with updated species mapping shown in Table 4-1.

Daily FINN fire emissions were distributed hourly output based on the temporal profiles of GFED4.1s data. GFED4.1s stored fire activity information every three hours with 0.25° × 0.25° horizontal grid resolution. This study used the nearest neighbor method to re-allocate FINN fire emissions according to the GFED4.1s temporal profiles. Note that the fire emission rates were the same within three hours due to GFED4.1s three-hour output limitation. The resulting 2-D fire emissions were then distributed vertically following the method described in Fu et al. (2012):

$$P_{top,hour} = BE_{hour}^{\ 2} \times BE_{size}^{\ 2} \times P_{top,\max}, \tag{4.1}$$

$$P_{bot,hour} = BE_{hour}^{\ 2} \times BE_{size}^{\ 2} \times P_{bot,\max}, \tag{4.2}$$

where P_{top} and P_{bot} represent the top and bottom of fire plume heights, and *BE* denotes the buoyant efficiency looked up from the hourly or size class tables shown in Tables 4-3 and 4-4 (Air Sciences Inc., 2005). The U.S. EPA area source emissions were subtracted by the surface layer of the new processed three-dimensional hourly fire emissions (*FINN3D*) to obtain the U.S. EPA area source emissions without fire emissions, i.e.,

$$Emis_{USEPA,area,nofire} = Emis_{USEPA,area} - FINN3D_{surface}. \tag{4.3}$$

Negative values from Equation (4.3) were zeroed out and the U.S. EPA emissions were adjusted from 2003 to 2010 in this study as GFED4.1s data is available after 2003.The U.S. EPA area source emissions without fire emissions were then combined with *FINN3D* to obtain the adjusted three-dimensional hourly emissions including area sources and fires:

$$newEmis_{USEPA} = Emis_{USEPA,area,nofire} + FINN3D. \tag{4.4}$$

Table 4-2. Species mapping between CMAQ CB05 and FINN MOZART4.

CMAQ	FINN	Species Name
CH_4	CH_4	Methane
CO	CO	Carbon monoxide
NH_3	NH_3	Ammonia
NO	NO	Nitrogen monoxide
NO_2	NO_2	Nitrogen dioxide
SO_2	SO_2	Sulfur dioxide
FORM	CH_2O	Formaldehyde
ALD2	CH_3CHO	Acetaldehyde
ALDX	GLYALD	Propionaldehyde and higher aldehydes
ETOH	C_2H_5OH	Ethanol
ETH	C_2H_4	Ethene
ETHA	C_2H_6	Ethane
MEOH	CH_3OH	Methanol
ISOP	ISOP	Isoprene
TERP	$C_{10}H_{16}$	Terpene
OLE	C_3H_6 + BIGENE	Terminal olefin carbon bond (R-C=C)
TOL	0.3*TOLUENE	Toluene
XYL	0.1*TOLUENE	Xylene
BENZENE	0.6*TOLUENE	Benzene

Table 4-2 (*continued*).

CMAQ	FINN	Species Name
PAR	C_3H_6 + 1.7*BIGENE + 5.0*BIGALK + 1.5*C_3H_8 + 3.0*CH_3COCH_3 + 4.0*MEK + C_2H_2 + 3.0*HYAC	Paraffin carbon bond (C-C)
UNR	C_2H_2 + 1.5*C_3H_8 + 0.5*TOLUENE + 0.3*BIGENE	Unreactive compounds
POC	OC	Primary organic carbon
PEC	BC	Primary elemental carbon
PMC	$PM_{10} - PM_{25}$	Primary un-speciated coarse particulate matter
PMOTHR	$PM_{25} - OC - BC$	Primary un-speciated fine particulate matter

Table 4-3. Hourly buoyant efficiency.

Hour	1	2	3	4	5	6	7	8	9	10	11	12
$\boldsymbol{BE_{hour}}$	0.03	0.03	0.03	0.03	0.03	0.03	0.03	0.03	0.06	0.10	0.20	0.40
Hour	13	14	15	16	17	18	19	20	21	22	23	24
$\boldsymbol{BE_{hour}}$	0.70	0.80	0.90	0.95	0.99	0.80	0.70	0.40	0.06	0.03	0.03	0.03

Table 4-4. Parameters as a function of fire size classes based on burned area.

Class	**1**	**2**	**3**	**4**	**5**
Size (acres)	0–10	≥10–100	≥100–1000	≥1000–5000	≥5000
BE_{size}	0.40	0.60	0.75	0.85	0.90
$P_{top,\max}$ (meter)	160	2400	6400	7200	8000
$P_{bot,\max}$ (meter)	0	900	2200	3000	3000

Emission inputs for future year CMAQ simulations

Future anthropogenic emissions for the RCP8.5 scenario (Riahi et al., 2011) were retrieved from the International Institute for Applied Systems Analysis (IIASA) database (available at http://www.iiasa.ac.at/web-apps/tnt/RcpDb). Since the database provided 12 sectoral emissions on a monthly basis every decade, additional efforts were required to prepare the hourly emissions for CMAQ. The mapping table for emission sectors between RCP8.5 and CMAQ is shown in Table 4-5. The processing steps are described as follows:

(1) Calculated monthly RCP8.5 emissions during 2051–2059 through linear interpolations between 2050 and 2060.

(2) Computed ratios of each species in each emission sector for every year during 2050–2059 to 2005.

(3) Applied the monthly ratios of individual species in the emissions to the adjusted 2005 U.S. EPA area source emissions, the 2005 FINN3D fire emissions, and the 2005 U.S. EPA point source emissions based on the emission sectors listed in Table 4-5. Therefore, the hourly emission of individual species in each emission sector during 2050–2059 were projected by Equations (4.5) – (4.9):

$$Emis_{area,nofire,205x} = Emis_{USEPA,area,nofire,2005} \times \frac{IIASA_{area,nofire,205x}}{IIASA_{area,nofire,2005}}, \quad (4.5)$$

$$Emis_{ptipm,205x} = Emis_{USEPA,ptipm,2005} \times \frac{IIASA_{ptipm,205x}}{IIASA_{ptipm,2005}}, \quad (4.6)$$

$$Emis_{ptnonipm,205x} = Emis_{USEPA,ptnonipm,2005} \times \frac{IIASA_{ptnonipm,205x}}{IIASA_{ptnonipm,2005}}, \quad (4.7)$$

$$Emis_{op,205x} = Emis_{USEPA,op,2005} \times \frac{IIASA_{op,205x}}{IIASA_{op,2005}}, \quad (4.8)$$

$$Emis_{fire,205x} = Emis_{FINN3D,2005} \times \frac{IIASA_{fire,205x}}{IIASA_{fire,2005}}. \quad (4.9)$$

Note that $Emis_{205x}$ would have the same spatial and temporal distributions as $Emis_{2005}$ and the biogenic emissions were assumed to vary with the same ratios applied to anthropogenic

Table 4-5. Mapping of emission sectors from IIASA RCP8.5 to U.S. EPA.

IIASA	U.S. EPA
Power plants, energy conversion, extraction	*ptipm*
Industrial processes and combustion	*ptnonipm*
Agricultural waste burning	*ptnonipm*
Residential and commercial combustion	*ptnonipm*
Aviation	*ptnonipm*
International shipping	*op*
Land transport	*area*
Waste treatment and disposal	*area*
Agricultural activities (animals, rice, soil)	*area*
Solvent production and use	*area*
Grassland burning	*fire*
Forest burning	*fire*

emissions. The specie mapping table between IIASA and CMAQ can be found in Table 4-6. In addition, the PM species ($PM_{2.5}$ and PM_{10}) were estimated using the ratios between PM and CO for each emission sector from the Evaluating the CLimate and Air Quality ImPacts of Short-livEd Pollutants database (ECLIPSE) version 5a (Amann et al., 2015; International Energy Agency, 2012).

Another wildfire emission data set projected by an empirical fire model was also used in this study (Y. Liu et al., 2013; Urbanski, 2014). The projections of fire emissions were simulated based on the extreme value theory. The projected $PM_{2.5}$ emissions due to wildfires were primarily based on the meteorological conditions from WRF's future year simulation output including (1) daily precipitation, (2) daily and maximum temperature, (3) daily humidity, and (4) daily and maximum wind speed and direction. Emissions for other species due to wildfires were estimated using the ratios of emission factors (see Table 4-7) for each species to $PM_{2.5}$ (Urbanski, 2014). Fire emissions were projected to increase by more than 50% for total emissions of all fire size ranges (> 1,000 acres burned) as a result of increasing numbers of future wildfire activities, which were projected to increase by 10%–80% compared to the present years. Because the fire model provided monthly wildfire emissions with specific geospatial locations, all data within a 12 km × 12 km grid cell was aggregated. The temporal allocation of 2053–2059 wildfire emissions was based on 2003–2009 GFED4.1s data while that for 2050–2052 was based on 2010–2012 GFED4.1s data. Moreover, the projected wildfire emissions by this fire model would have different spatial patterns compared to that projected by IIASA since the baseline spatial profiles were different. The former was projected from historical large fires with burned area greater than 1,000 acres while the latter was projected using 2005 FINN dataset.

Experimental design

To evaluate how the pollutant concentration changes due to wildfires, this study conducted two sets of CMAQ simulations with five different emission scenarios (Figure 4-2). The first simulation set included two experiments during the present years (2003–2010) under the same climate conditions as well as the same initial and boundary conditions: (1) U.S. EPA point source emissions and adjusted U.S. EPA area source

Table 4-6. Species mapping between CMAQ CB05 and IIASA RCP8.5 database.

CMAQ	IIASA	Species Name
CH_4	CH_4	Methane
CO	CO	Carbon monoxide
NH_3	NH_3	Ammonia
NO	NO	Nitrogen monoxide
CH_4	CH_4	Nitrogen dioxide
SO_2	SO_2	Sulfur dioxide
POC	OC	Primary organic carbon
PEC	BC	Primary elemental carbon

Table 4-7. Emission factors (g/kg) for various species from fires. NMOC denotes non-methane volatile organic compounds and nNMOC is unidentified NMOC. Other abbreviated species names can be found in Table 4-2.

Species	$PM_{2.5}$	PM_{10}	CO_2	CO	CH_4	NMOC	nNMOC	NO_2	NH_3	SO_2
Emission factors	23.2	28.0	1600	135	7.32	33.87	25.68	2.0	1.5	1.06

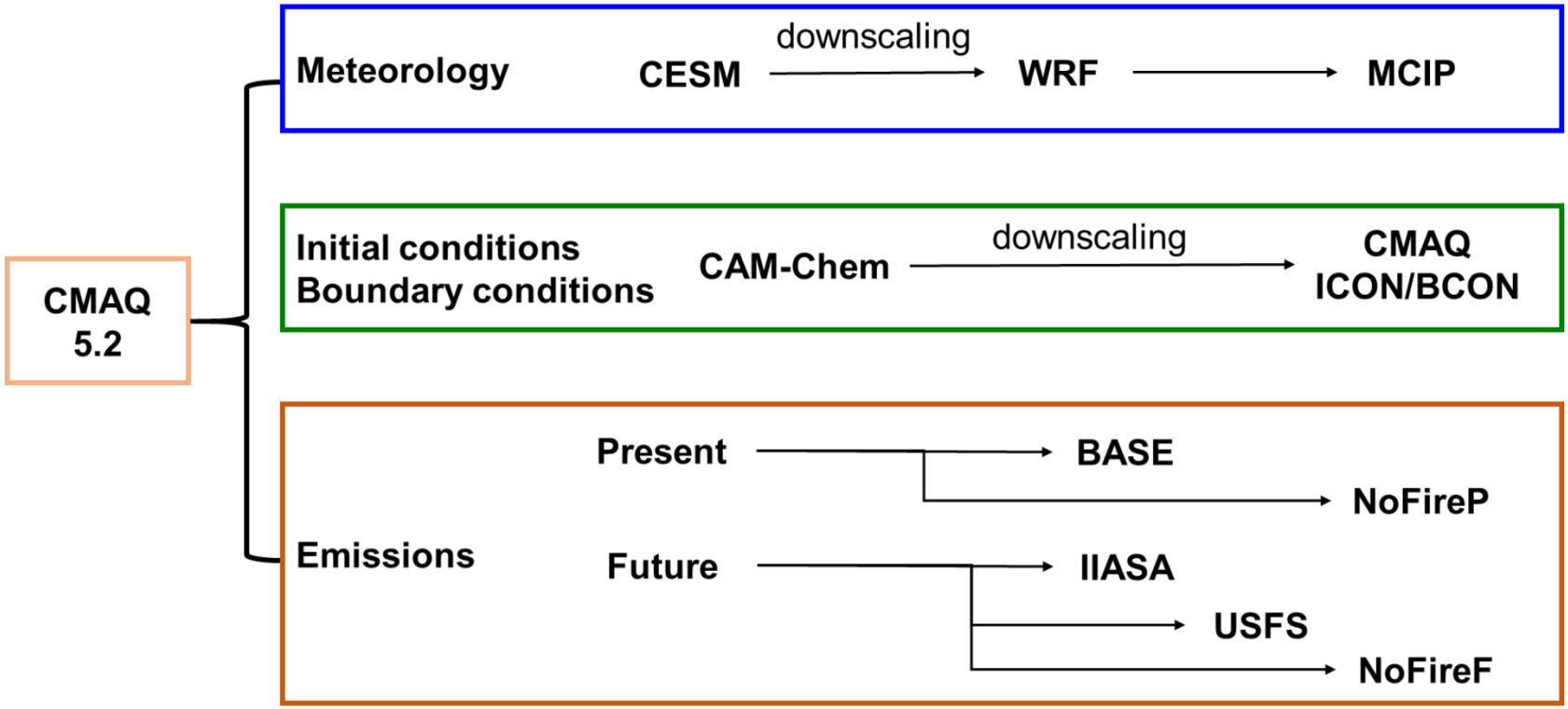


Figure 4-2. A schematic diagram of the experimental design in this study.

emissions with *FINN3D* fire emissions (called "*BASE*" hereafter in this chapter), and (2) U.S. EPA point source emissions and adjusted U.S. EPA emissions without fire emissions (called "*NoFireP*" hereafter in this chapter). The second simulation set consisted three experiments during the future years (2050–2059): (1) RCP8.5 emissions from IIASA (called "*IIASA*" hereafter in this chapter), (2) RCP8.5 emissions from IIASA excluding wildfire emissions (called "*NoFireF*" hereafter in this chapter) and (3) RCP8.5 emissions from IIASA with the wildfire emissions replaced by a fire model outputs (called "*USFS*" hereafter in this chapter). Differences between with and without fire emissions in each CMAQ simulation set were evaluated to estimate the contribution of wildfires to the changes in air pollutant concentration.

Model performance metrics

The CMAQ simulation results for present years were compared to the observational data from the U.S. EPA Air Quality System (AQS) stations within the WUS domain. The study applied the two metrics—the mean fractional error (MFE) and the mean fractional bias (MFB)—from Boylan and Russell (2006) to evaluate CMAQ model performance:

$$MFE = \frac{1}{N}\sum_{i=1}^{N}\frac{\left|C_m - C_o\right|}{\left(C_o + C_m/2\right)}, \tag{4.10}$$

$$MFB = \frac{1}{N}\sum_{i=1}^{N}\frac{\left(C_m - C_o\right)}{\left(C_o + C_m/2\right)}, \tag{4.11}$$

where C_m and C_o are the modeled and observed concentration at station i, respectively; N is the number of model-observation pairs from all valid monitoring station data during the time period of interest. Suggested model performance goal is met if MFE ≤ 50% and MFB ≤ ±30%, respectively; the model performance criteria is met if both MFE ≤ 75% and MFB ≤ ±60%. Performance goals indicate the best a model can simulate that is close enough to the observation; performance criteria are the level of accuracy that is acceptable for standard modeling applications (Boylan & Russell, 2006).

Results

Evaluations of CMAQ model performance

CMAQ simulations for the *BASE* experiment are compared to the U.S. EPA AQS data on a monthly mean basis. Figures 4-3 and 4-4 show that 50 of 64 months of the simulated O_3 concentration meet the performance goal while all months meet the performance criteria during 2003–2010. Compared to observations, CMAQ underestimates O_3 concentration during the summer season (June–August) but overestimates O_3 concentration during autumn (September–November), especially in November in WUS. The modeled $PM_{2.5}$ concentration has only about half of the months (34/64) that meet the performance goal while all months meet the performance criteria (Figures 4-5 and 4-6). Modeled $PM_{2.5}$ concentration is generally underestimated with a few months during summertime overestimated by CMAQ. In terms of seasons, both modeled O_3 and $PM_{2.5}$ concentration has the lowest MFB during summertime; substantial overestimates in O3 are found in autumn while large MFE and MFB in modeled $PM_{2.5}$ are observed during the springtime (Table 4-8).

Since the CESM-WRF downscaling results have been evaluated previously (Gao et al., 2012), meteorological conditions are expected to be a minor factor that cause the biases in simulated O_3 and $PM_{2.5}$. The initial and boundary conditions of species concentration as well as the emission input are likely the major reasons resulting in such biases. This study adopted the species mapping table from Gao et al. (2013) who used CMAQ v5.0 in their simulations. From CMAQ v5.0 to CAMQ v5.2, there have been major updates in both gas-phase chemistry, aerosol speciations, and secondary organic aerosol (SOA) formations. Although adjustments of mapping gas-phase species have been made (Table 4-1), uncertainty still exhibits during the species mapping processes, especially for sub-speciations of volatile organic compounds (VOCs). In addition, this study selected AE6nvPOA as the aerosol module in order to be compatible to the CESM(CAM-Chem) downscaling processes. Organic aerosols, which are parts of $PM_{2.5}$, would substantially be underestimated in CMAQ when choosing the nvPOA model rather than the semivolatile POA model (Murphy et al., 2017). Moreover, the large MFE and MFB in $PM_{2.5}$ during the

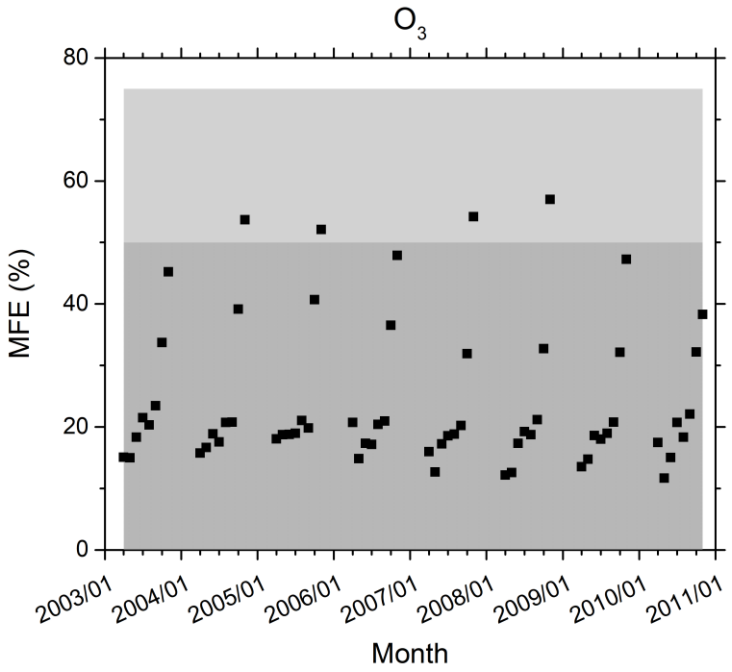


Figure 4-3. Model performance of monthly O_3 concentration (ppbv) in WUS. The vertical axis denotes the range of MFE (%) while the horizontal axis represents the fire months. Black markers within the shaded area denote the simulated O_3 values meet the model performance goal (dark gray) or the model performance criteria (light gray).

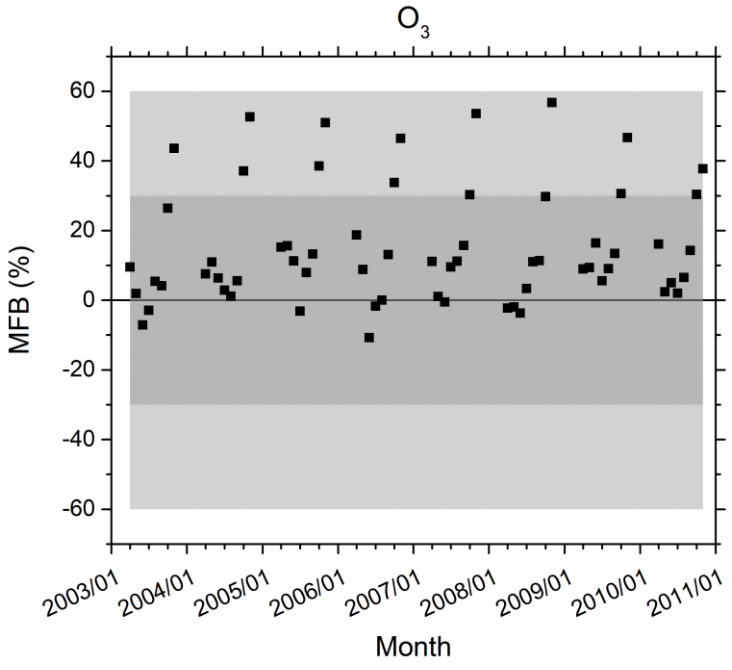


Figure 4-4. Same as Figure 4-3 except for MFB (%).

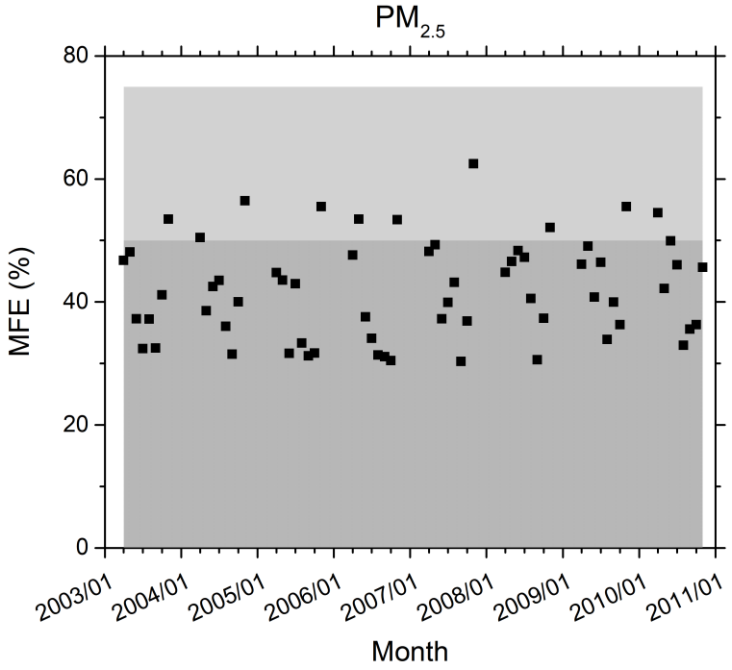


Figure 4-5. Model performance of monthly $PM_{2.5}$ concentration ($\mu g/m^3$) in WUS. The vertical axis denotes the range of MFE (%) while the horizontal axis represents the fire months. Black markers within the shaded area denote the simulated $PM_{2.5}$ values meet the model performance goal (dark gray) or the model performance criteria (light gray).

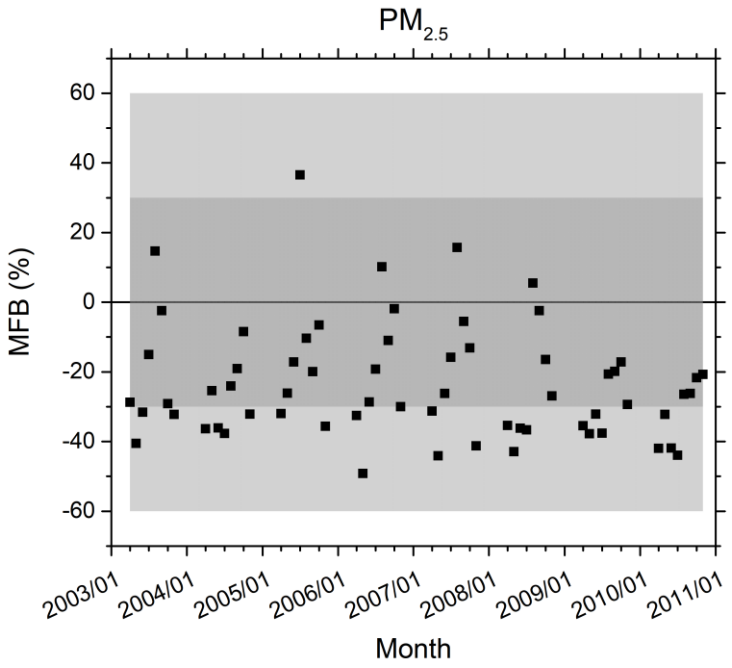


Figure 4-6. Same as Figure 4-5 except for MFB (%).

Table 4-8. Model performance of seasonal O_3 and $PM_{2.5}$ based on the monthly MFE and MFB values.

Season	O_3		$PM_{2.5}$	
	MFE	**MFB**	**MFE**	**MFB**
Spring	15.35±2.54	8.32±6.52	47.14±3.99	−35.76∓6.70
Summer	18.77±1.49	3.53±6.51	39.43±5.68	−18.95∓21.15
Autumn	35.16±12.43	30.67±16.23	41.14±10.33	−19.55∓11.35
All fire months	24.06±11.65	14.91±16.63	42.00±8.00	−23.38∓16.52

springtime could also be attributed to the wind-blown dust emission as a result of the different land cover classifications between CMAQ versions show in Table 4-9 (UNC Institute for the Environment, 2012; Wang et al., 2012).

Wildfire-induced ozone and $PM_{2.5}$ changes in present years

Changes of monthly O_3 concentration due to fires are small in present years according to the *BASE* and *NoFireP* experiments (Figure 4-7). The largest increase of domain averaged O_3 due to fires is only 0.64 ppb in July 2008. The maximum of fire-induced monthly O_3 increase (calculated by *BASE−NoFireP*) could be up to 10.32 ppb (or 41% increase) in July 2008. The decadal average of monthly mean O_3 shows that August and July are influenced by fires the most among all fire months. The domain mean values are 0.38 ppb for August and 0.26 ppb for July while the domain maximum increases are 3.48 ppb in August and 2.89 ppb in July (Figure 4-8a). The larger O_3 increases due to fires in July and August lead to higher fire-induced decadal seasonal O_3 increases in summer compared to that in spring and autumn seasons (Figure 4-8b). The domain mean O_3 increase is 0.27±0.15 ppb with 2.51±2.32 ppb for the seasonal domain maximum O_3 increase in summertime during 2003–2010. The decadal average of all fire months for fire-induced O_3 increase is 0.20±0.13 ppb for the domain mean and 1.41±1.72 ppb for the domain maximum.

Compared to the small impacts on O_3 changes, fire activities significantly increase $PM_{2.5}$ concentration during 2003–2010 (Figure 4-9). Although the largest domain-averaged $PM_{2.5}$ increase due to fires is only 1.63 μg/m^3 in August 2007, the maximum of fire-induced monthly $PM_{2.5}$ increase could reach 194.92 μg/m^3 (or 3481%) in July 2008 (Figure 4-9). For all fire months during 2003–2010, the percentages of domain maximum $PM_{2.5}$ increases (calculated by (*BASE−NoFireP*)/*NoFireP* ×*100%*) are all more than 125%, which implies the fire activities would worsen regional air quality in terms of $PM_{2.5}$ concentration in WUS. The greatest domain maximum $PM_{2.5}$ increase in percentage takes place in September 2006 with 6057% (177.2 μg/m^3) increase during the present years (Figure 4-9). The decadal average of monthly mean $PM_{2.5}$ demonstrates that July–September are influenced by fires the most among all fire months (Figure 4-10a). The

Table 4-9. Land use categories used in CMAQ v5.0 (USGS 20 land use categories) and CMAQ v5.2 (USGS 24 land use categories).

Category	CMAQ v5.0	CAMQ v5.2
1	Urban and Built-Up Land	Urban and Built-Up Land
2	Dryland Cropland and Pasture	Dryland Cropland and Pasture
3	Irrigated Cropland and Pasture	Irrigated Cropland and Pasture
4	—	Mixed Dryland/Irrigated Cropland and Pasture
5	Cropland/Grassland Mosaic	Cropland/Grassland Mosaic
6	Cropland/Woodland Mosaic	Cropland/Woodland Mosaic
7	Grassland	Grassland
8	Shrubland	Shrubland
9	Mixed Shrubland/Grassland	Mixed Shrubland/Grassland
10	Savanna	Savanna
11	Deciduous Forest	Deciduous Broadleaf Forest
12	Conifer Forest	Deciduous Needleleaf Forest
13	Evergreen Broadleaf	Evergreen Broadleaf
14	—	Evergreen Needleleaf
15	Mixed Forest	Mixed Forest
16	Water Bodies	Water Bodies
17	Herbaceous Wetland	Herbaceous Wetland
18	Wooden Wetland	Wooden Wetland
19	Barren or Sparsely Vegetated	Barren or Sparsely Vegetated
20	—	Herbaceous Tundra
21	Wooded Tundra	Wooded Tundra
22	Mixed Tundra	Mixed Tundra
23	—	Bare Ground Tundra
24	Snow or Ice	Snow or Ice

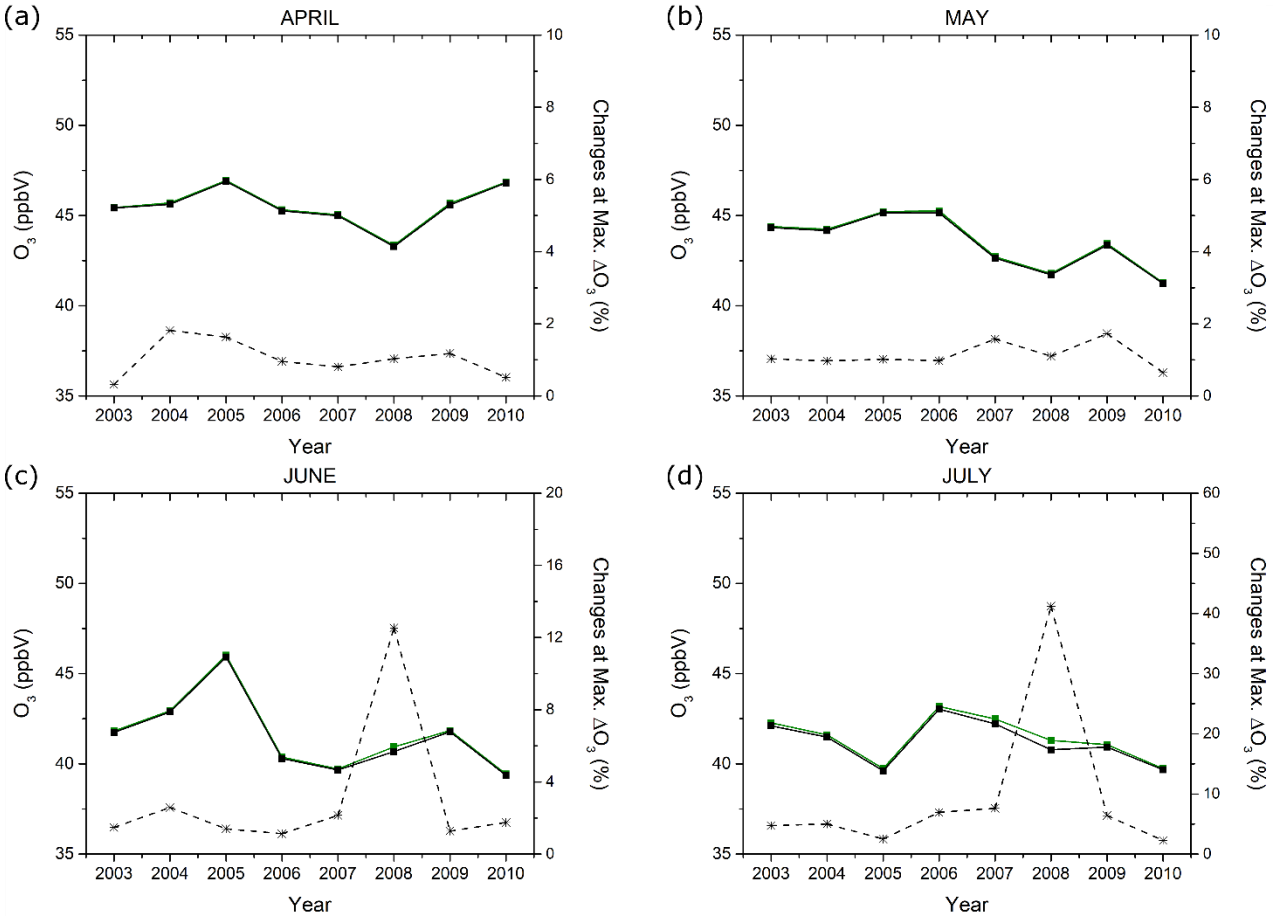


Figure 4-7. Simulated monthly O_3 domain mean concentration (ppb) and the maximum change (%) at grid-cell level during 2003–2010. Solid lines represent the domain averaged O_3 concentration for *BASE* (green) and *NoFireP* (black) while the dashed line denotes the maximum change (*(BASE−NoFireP)/NoFireP×100%*) at grid-cell level within the WUS domain. Months are (a) April, (b) May, (c) June, (d) July, (e) August, (f) September, (g) October, and (h) November.

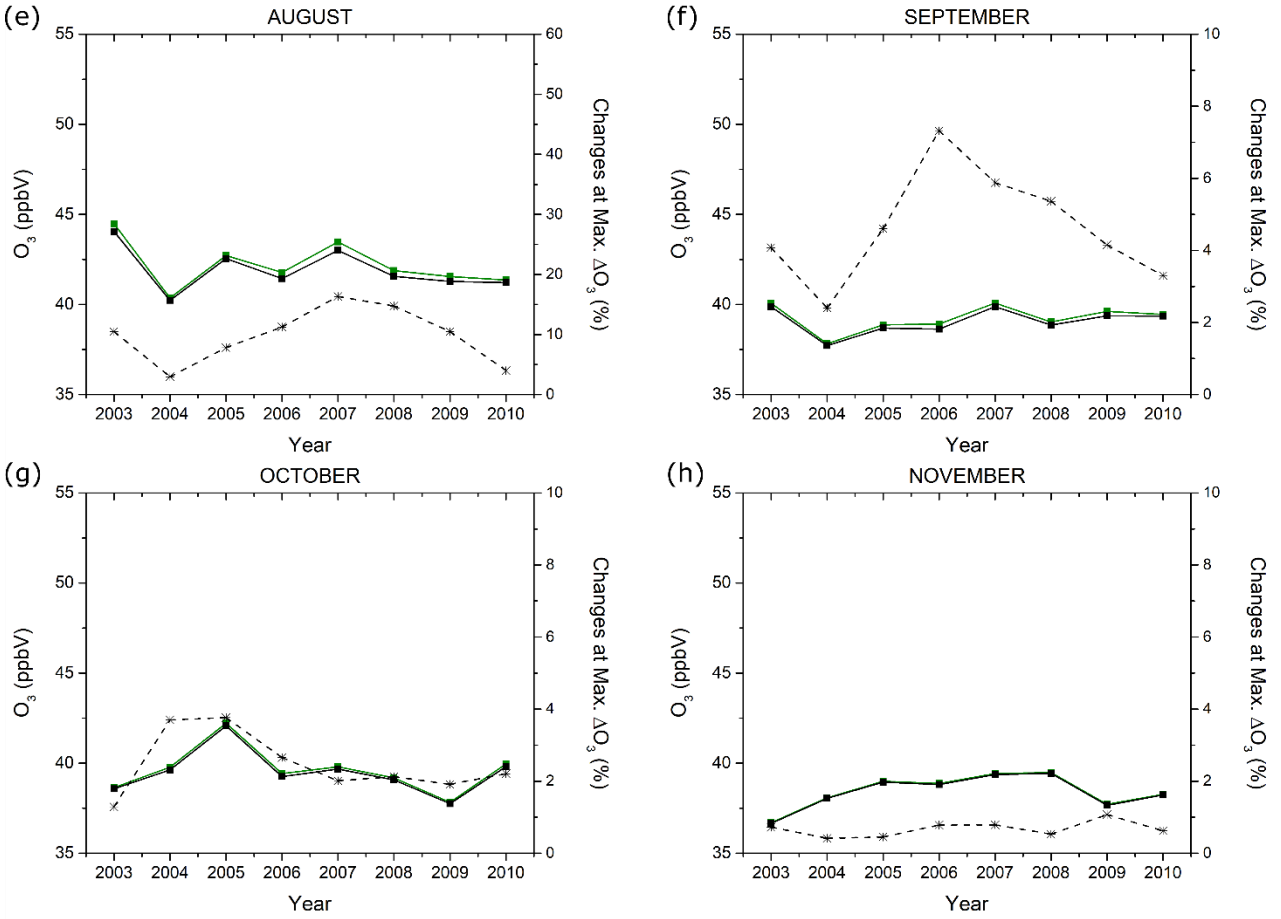


Figure 4-7 (*continued*).

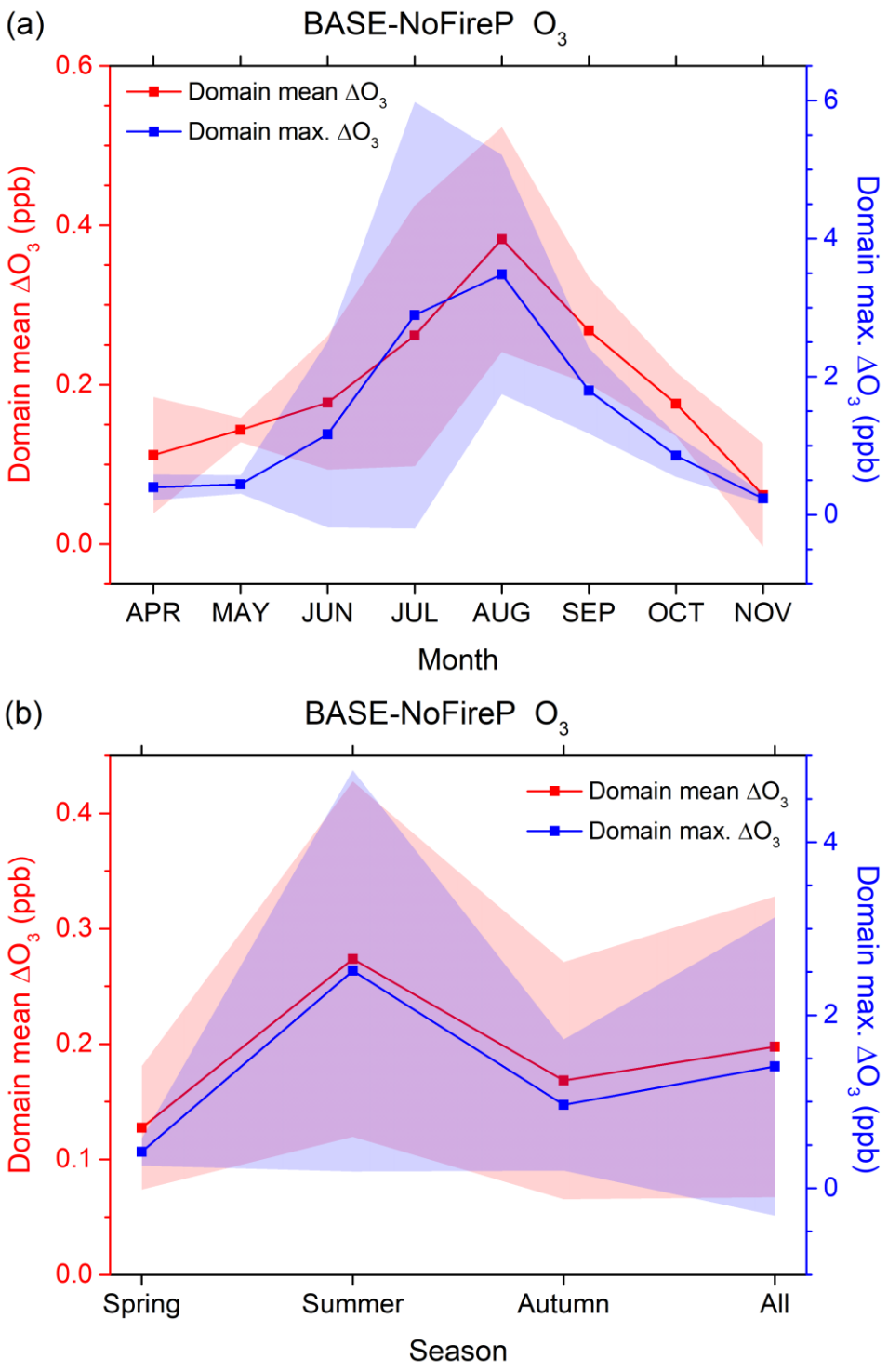


Figure 4-8. Decadal average of (a) monthly and (b) seasonal O_3 changes (ppb) due to fires during 2003–2010. Curves represent the domain mean (red) and the maximum within the domain (blue). Shaded area is the one standard deviation range. The "All" in seasonal O_3 changes represents all fire months during 2003–2010.

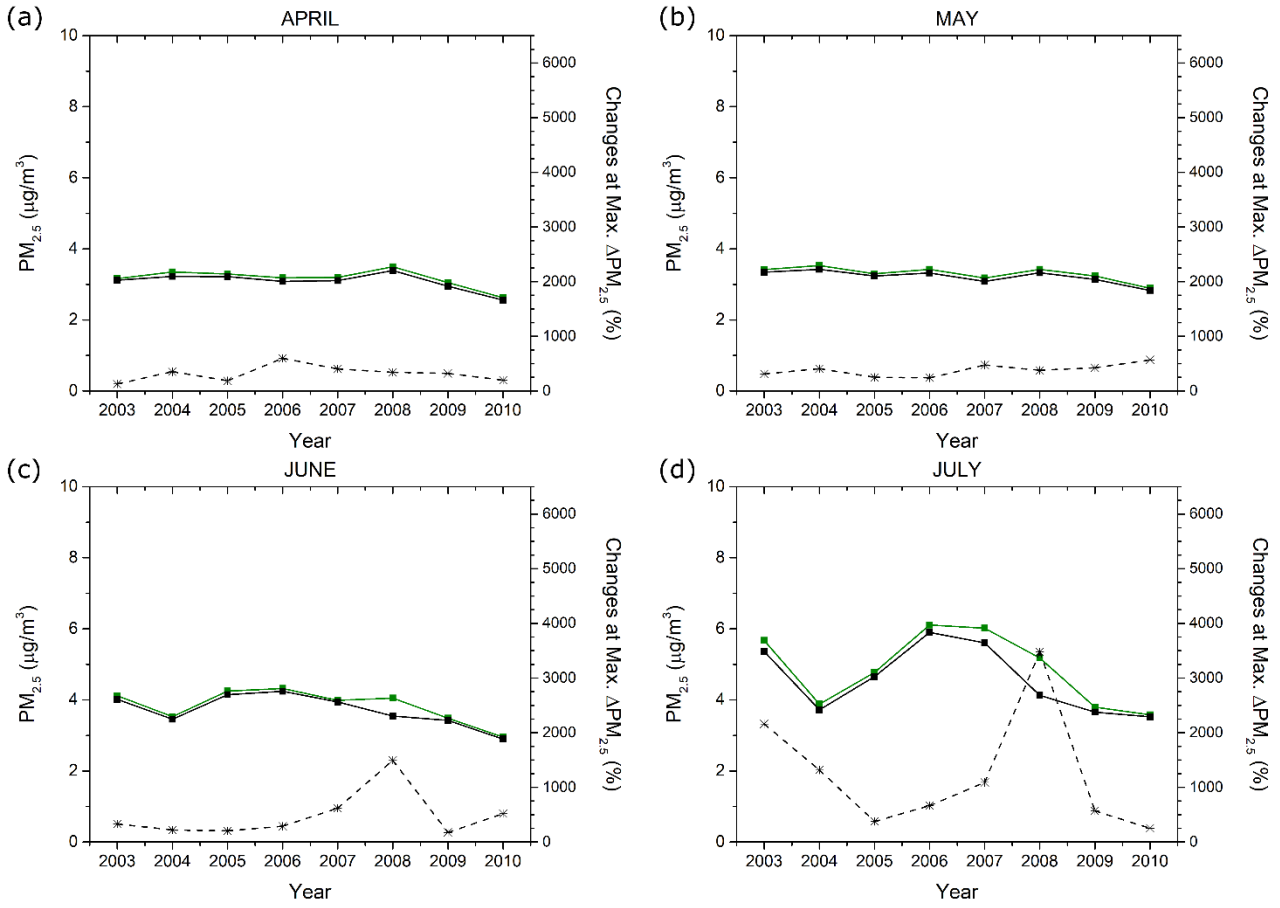


Figure 4-9. Same as Figure 4-7 except for $PM_{2.5}$ ($\mu g/m^3$).

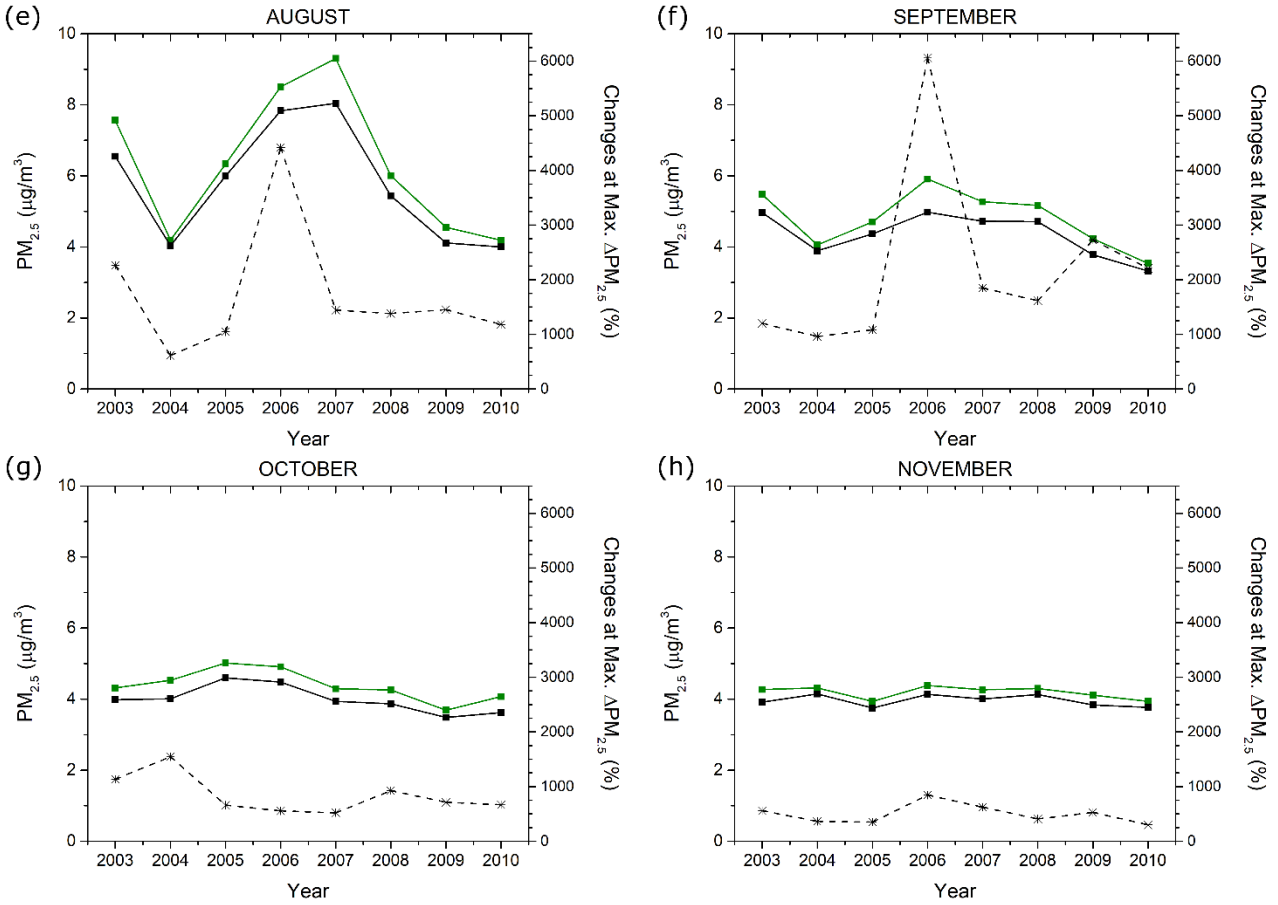


Figure 4-9. Same as Figure 4-7 except for $PM_{2.5}$ ($\mu g/m^3$).

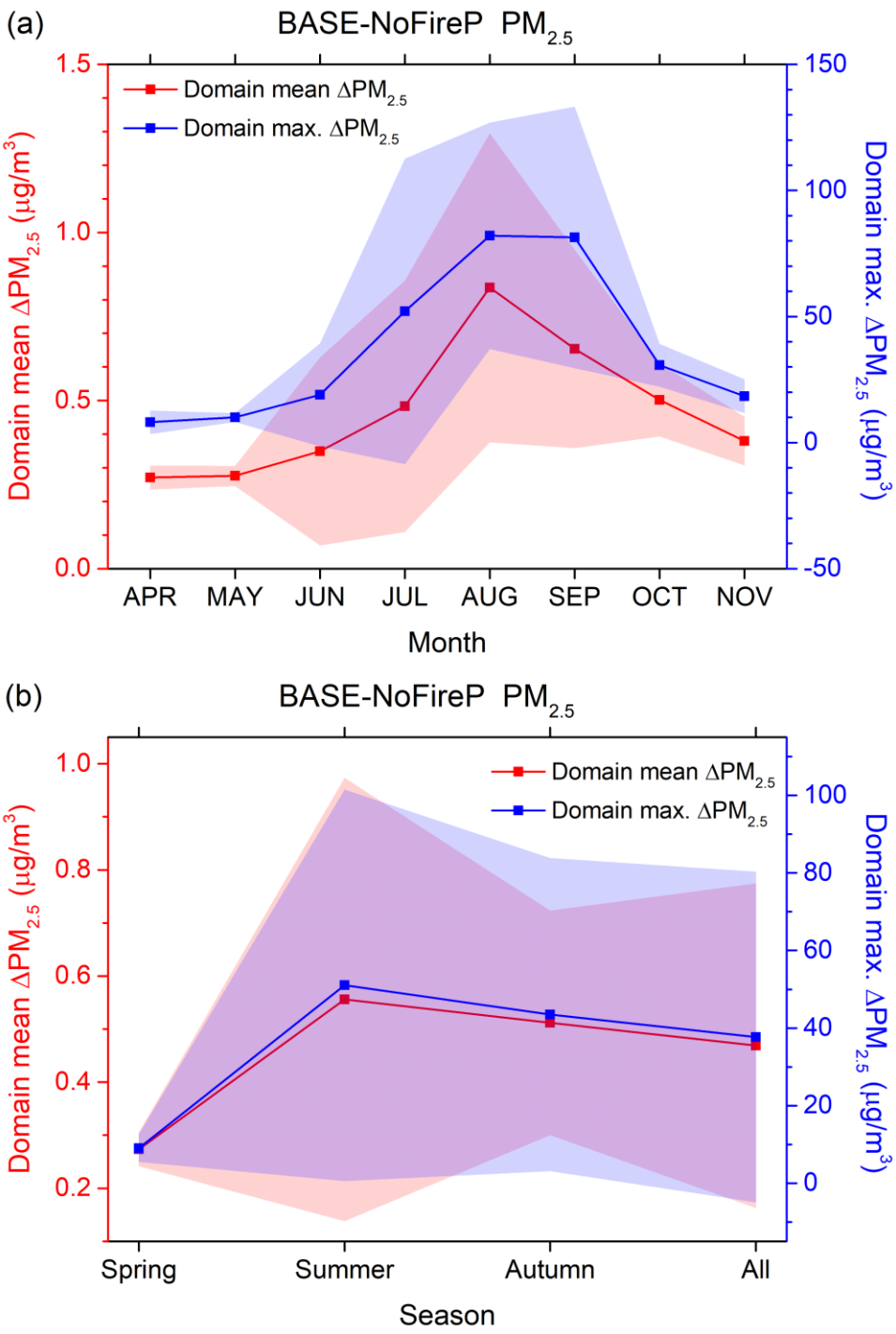


Figure 4-10. Same as Figure 4-8 except for $PM_{2.5}$ ($\mu g/m^3$).

domain mean $PM_{2.5}$ increases are 0.84±0.46 μg/m^3 in August and 0.65±0.30 μg/m^3 in September while the domain maximum $PM_{2.5}$ increases are 82.04±44.92 μg/m^3 in August and 81.43±51.89 μg/m^3 in September (Figure 4-10a). The higher $PM_{2.5}$ increases in August and September cause both decadal seasonal $PM_{2.5}$ increases higher in summer and autumn seasons. The domain mean $PM_{2.5}$ increases are 0.56±0.42 μg/m^3 in summer and 0.51±0.21 μg/m^3 in autumn during 2003–2010 (Figure 4-10b). The decadal average of all fire months for $PM_{2.5}$ increase from fires is 0.47±0.31 μg/m^3 for the domain mean and 37.72±42.65 μg/m^3 for the domain maximum.

Projections of wildfire-induced ozone and $PM_{2.5}$ changes

Similar to the present years, the monthly O_3 changes for the *IIASA* and *USFS* with respect to *NoFireF* are insignificant during 2050–2059 (Figure 4-11). The domain mean O_3 increases are all under 0.31 ppb and the domain maximum O_3 values have less than 2.50 ppb among all fire months for *IIASA* compared to *NoFireF*. The largest domain mean O_3 increase is 0.31 ppb in August 2055, which is also the largest domain maximum O_3 increase in percentage (6.38%). The decadal average of monthly mean O_3 from *IIASA* and *NoFireF* shows slight increases in domain mean O_3 levels due to fires for each fire month except November (Figure 4-12a). Both the decadal domain mean O_3 levels and the decadal domain maximum O_3 levels are the largest in August, with values of 0.28±0.02 ppb and 2.04±0.30 ppb, respectively. The decadal averages of seasonal domain mean O_3 level and domain maximum O_3 level are projected to have the highest increases in summer with 0.21±0.05 ppb and 1.23±0.63 ppb, respectively (Figure 4-12b).

For *USFS*, much smaller O_3 increases due to wildfires are simulated by CMAQ. There are only 10 of 80 fire months with the domain mean O_3 changes (either positive or negative) greater than ±0.1 ppb (Figure 4-11). The largest domain mean O_3 increase is 0.23 ppb in August 2055 while the largest domain maximum O_3 increase in percentage is 1.76% in July 2051. The decadal average of monthly mean O_3 from *USFS* and *NoFireF* demonstrates slight increases in domain mean O_3 levels due to wildfires from July to September but decreases in June and October (Figure 4-13a). The decadal domain mean O_3 level is the highest in July (0.15±0.02 ppb) while the decadal domain maximum O_3 in

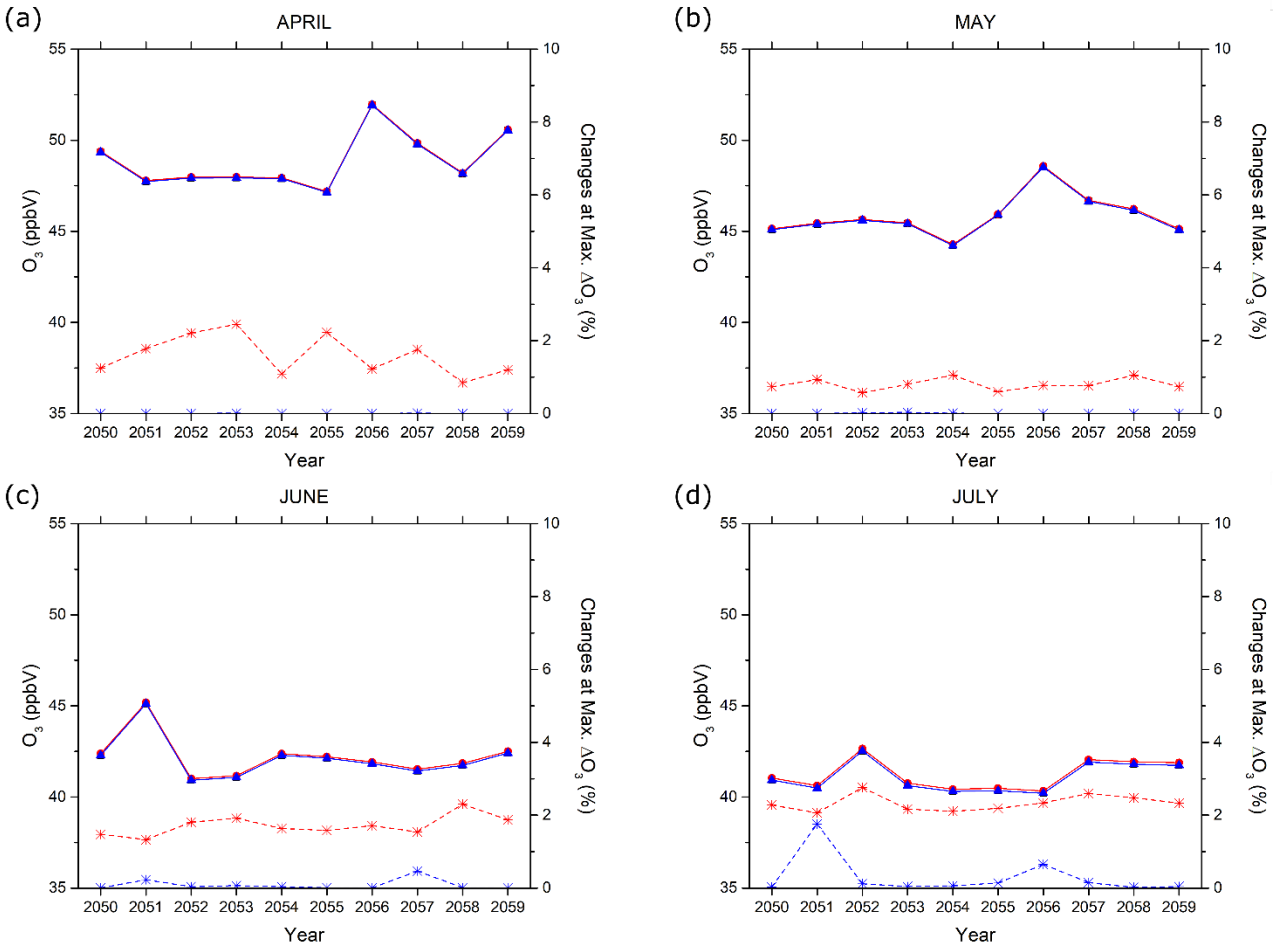


Figure 4-11. Simulated monthly O_3 domain mean concentration (ppb) and the maximum change (%) at grid-cell level during 2050–2059. Solid lines represent the domain averaged O_3 concentration for *IIASA* (red), *USFS* (blue), and *NoFireF* (black) while the dashed line denotes the maximum changes for *IIASA* (red, *(IIASA−NoFireP)/NoFireP×100%*) and *USFS* (blue, *(USFS−NoFireP)/NoFireP×100%*) at grid-cell level. Months are (a) April, (b) May, (c) June, (d) July, (e) August, (f) September, (g) October, and (h) November.

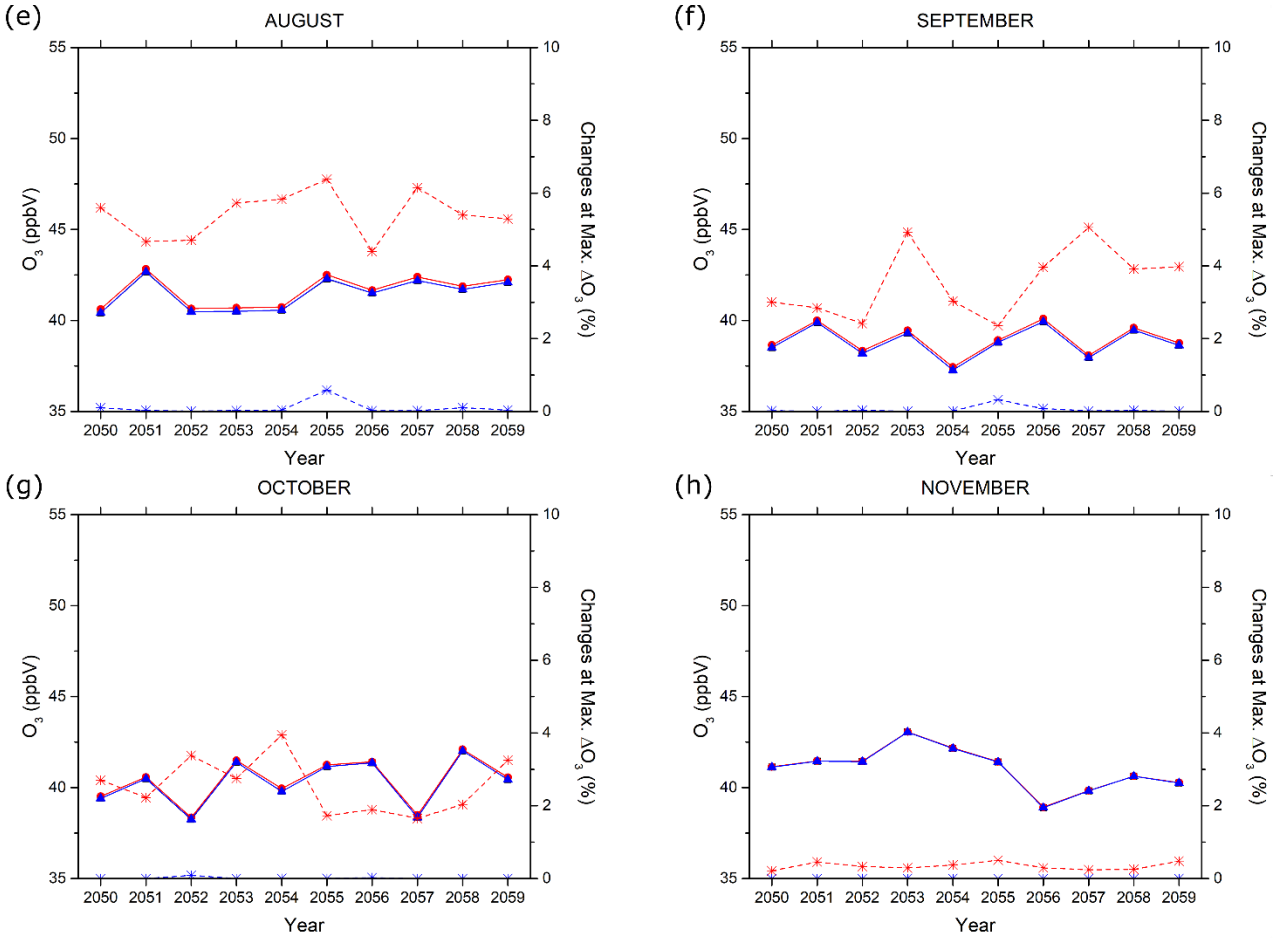


Figure 4-11 (*continued*).

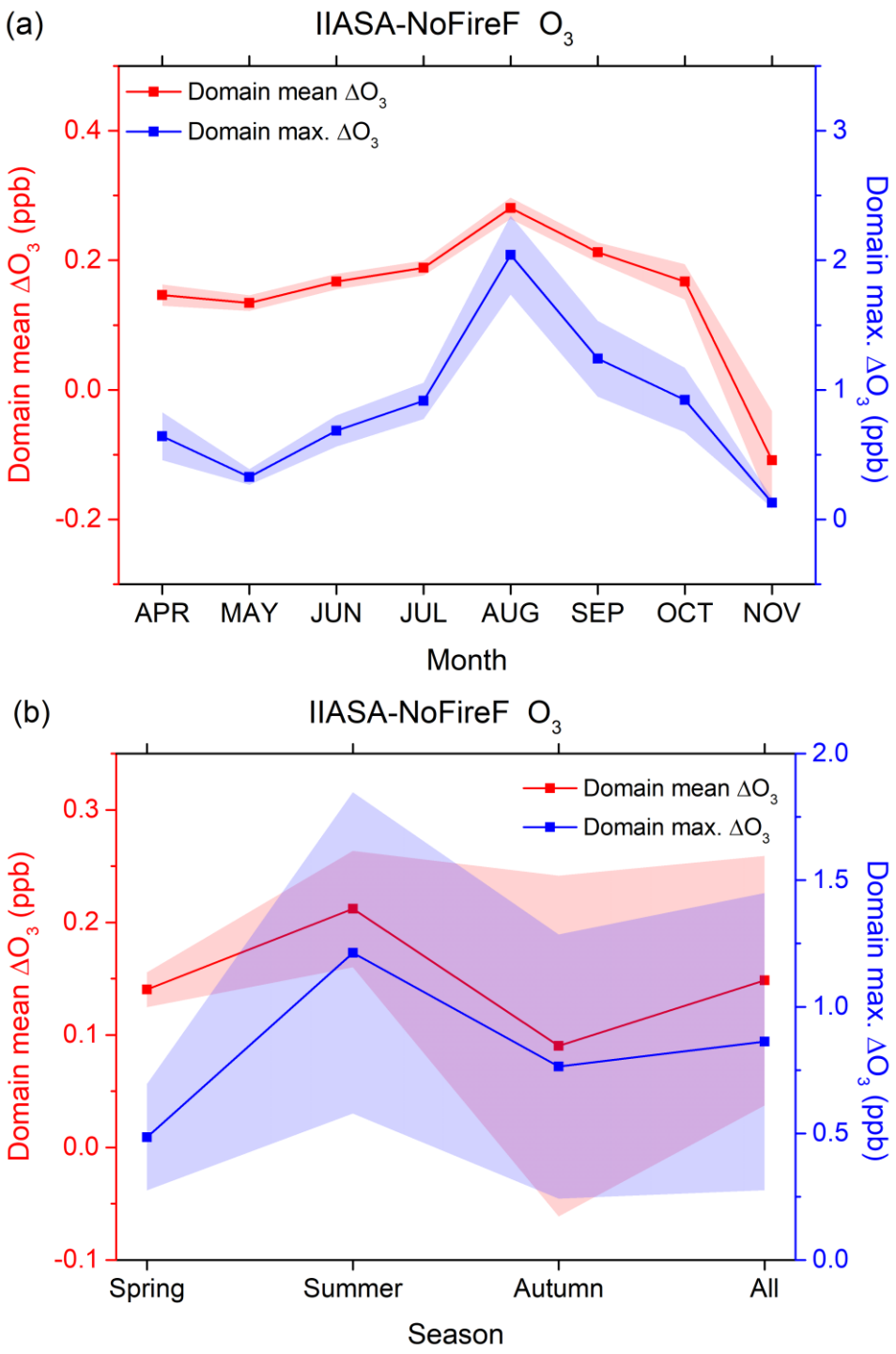


Figure 4-12. Decadal average of (a) monthly and (b) seasonal O_3 changes (ppb) between *IIASA* and *NoFireF* due to fires during 2050–2059. Curves represent the domain mean (red) and the maximum within the domain (blue). Shaded area is the one standard deviation range.

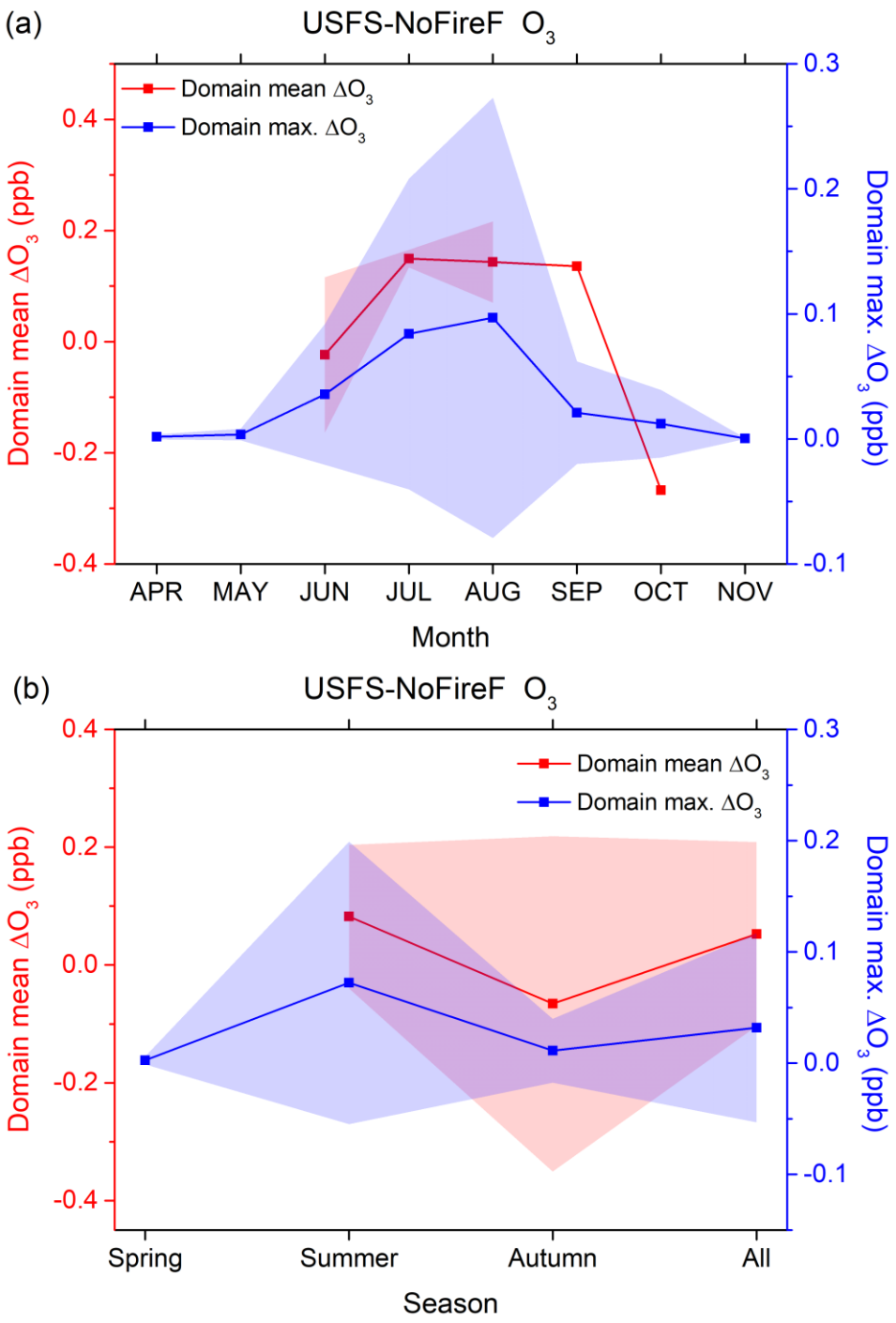


Figure 4-13. Same as Figure 4-12 except for the changes between *USFS* and *NoFireF*. Note that missing values are due to the values with monthly O_3 changes smaller than 0.1 ppb.

August has the largest increase (0.10±0.18 ppb). Summer is still the season influenced by wildfires the most (0.08±0.12 ppb for the decadal averages of seasonal domain mean O_3 and 0.07±0.13 ppb for the domain maximum O_3) (Figure 4-13b). The changes due to wildfires over the decade are 0.05±0.16 ppb for the domain mean O_3 and 0.03±0.08 ppb for the domain maximum O_3. These small changes either in domain mean O_3 level or in domain maximum O_3 level are likely caused by the meteorological conditions that were designed to be the same in *IIASA*, *USFS*, and *NoFireF* experiments. As there are no differences in meteorological conditions between the three experiments and NO_x emission in wildfires is relatively small compared to PM species (see Table 4-7), projected O_3 changes due to wildfires are thus negligible.

Variations of projected monthly $PM_{2.5}$ concentration for *IIASA*, *USFS*, and *NoFireF* experiments are displayed in Figure 4-14. The domain mean $PM_{2.5}$ would increase by up to 0.82 μg/m^3 in October 2054 in *IIASA* compared to *NoFireF* while the domain maximum $PM_{2.5}$ increases by up to 57.58 μg/m^3 (or 1217%) in August 2054. For all fire months during 2050–2059, the percentages of domain maximum $PM_{2.5}$ increases (calculated by (*IIASA*−*NoFireF*)/*NoFireF* ×*100%*) are all more than 200%, which implies projected wildfire activities would reduce regional air quality in WUS in the future. The greatest domain maximum $PM_{2.5}$ increase in percentage takes place in August 2051 with 2085% (54.75 μg/m^3) increase during 2050–2059 (Figure 4-14). The decadal average of monthly mean $PM_{2.5}$ increases in *IIASA* with respect to *NoFireF* demonstrates that August and October are influenced by fires the most among all fire months (Figure 4-15a). The domain mean $PM_{2.5}$ increases are 0.65±0.04 μg/m^3 in August and 0.58±0.14 μg/m^3 in October. The domain maximum $PM_{2.5}$ increase is projected the highest (50.94±4.01 μg/m^3) in August (Figure 4-15a). Despite the highest $PM_{2.5}$ increases projected in August, small $PM_{2.5}$ changes in June and in July cause that the decadal average of both the domain mean and the domain maximum $PM_{2.5}$ increases during the autumn season are higher (0.48±0.12 μg/m^3 and 23.66±8.20 μg/m^3, respectively) than that during summertime (Figure 4-15b).

The projected $PM_{2.5}$ concentration in *USFS* is smaller compared to *IIASA* and is close to *NoFireF* values (Figure 4-14). There are only 67 of 80 fire months with the domain mean $PM_{2.5}$ changes (either positive or negative) greater than ±0.1 μg/m^3 (Figure 4-14).

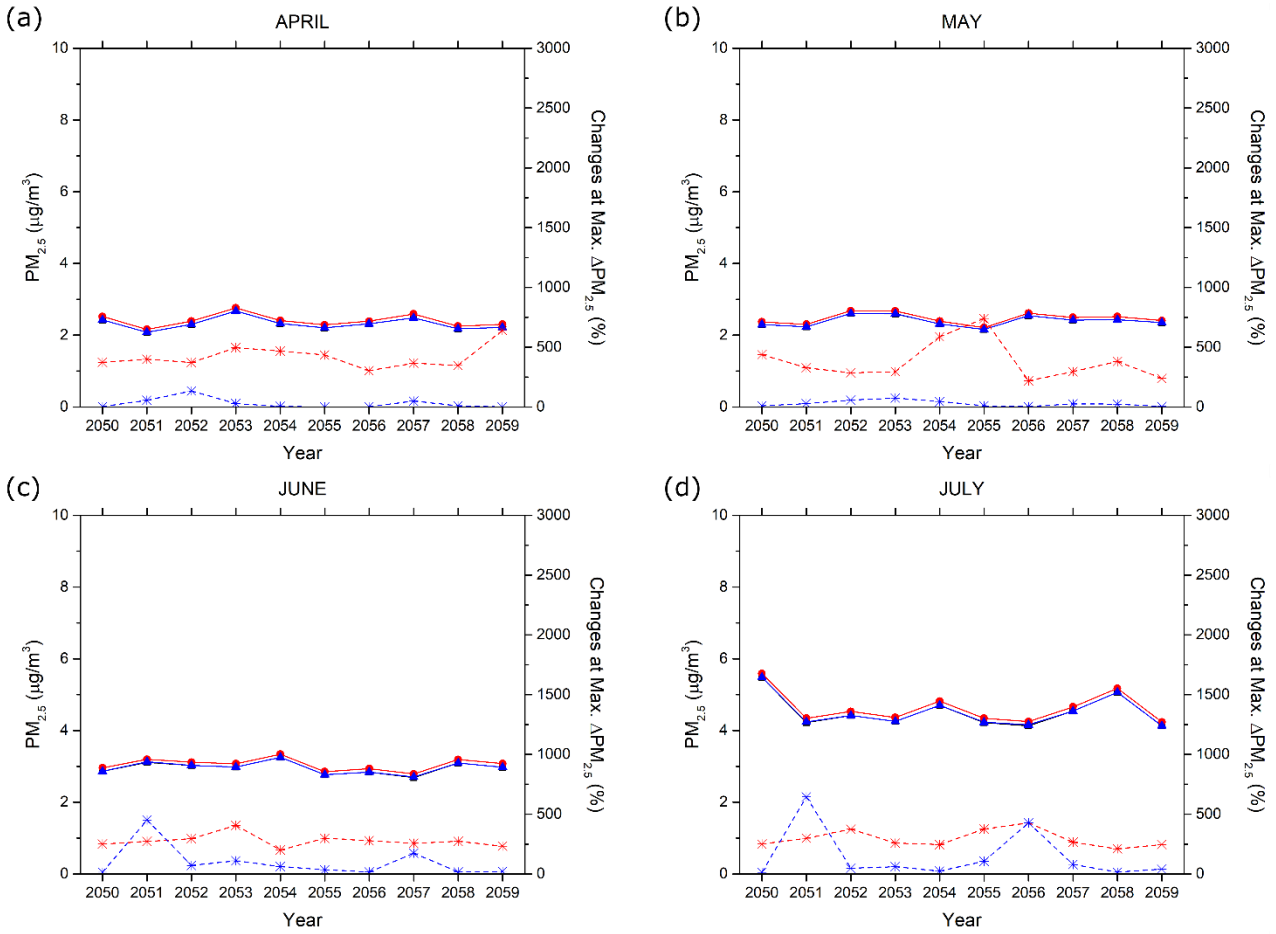


Figure 4-14. Same as Figure 4-11 except for $PM_{2.5}$ (μg/m^3).

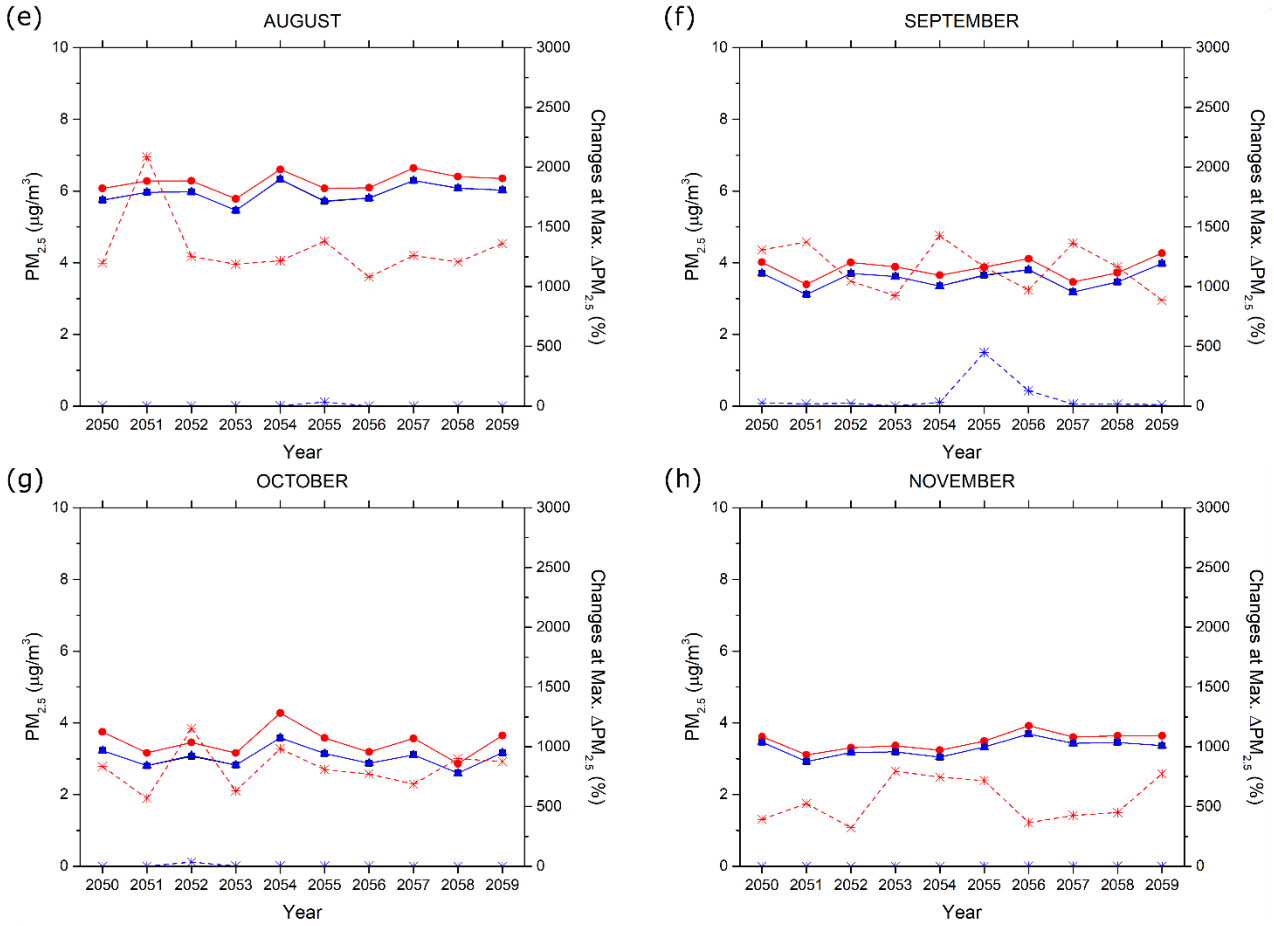


Figure 4-15 (*continued*).

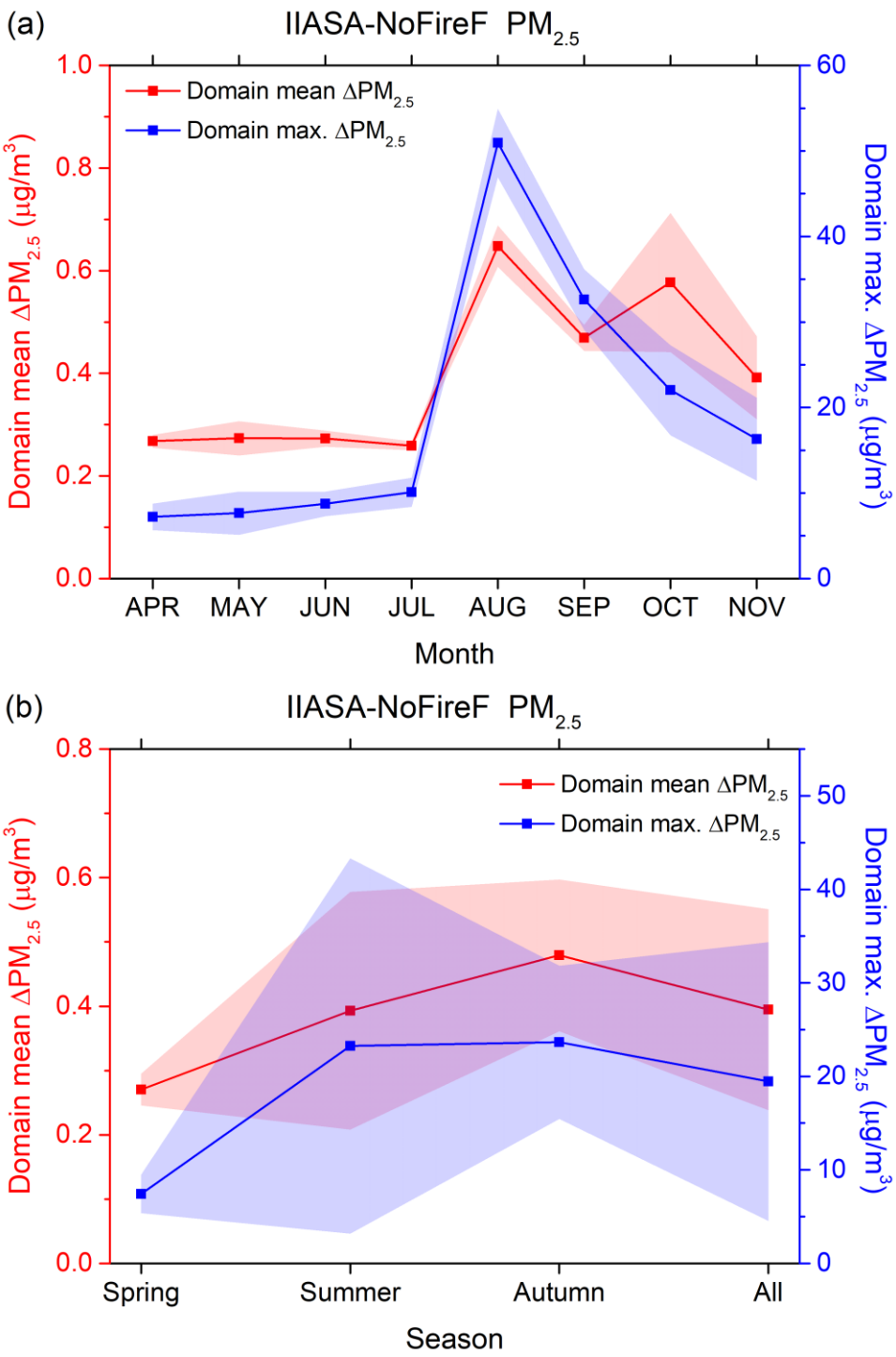


Figure 4-16. Same as Figure 4-12 except for $PM_{2.5}$ (μg/m^3).

This result implies that wildfires induce more changes in $PM_{2.5}$ than in O_3, which is reasonable as the wildfire emission factors for $PM_{2.5}$ is higher than NO_2 (a precursor of O_3) (Table 4-7). The largest domain mean $PM_{2.5}$ increase is 0.49 μg/m^3 in July 2051 and the largest domain maximum $PM_{2.5}$ increase is 35.98 μg/m^3 (or 1317%) in October 2052. For all fire months, about half the number of total months have 10%–75% increases of domain maximum $PM_{2.5}$ and there are only 12 of 80 fire months have more than 100% increases in domain maximum $PM_{2.5}$ concentration during 2050–2059 (Figure 4-14). The decadal average of monthly mean $PM_{2.5}$ increases in *USFS* with respect to *NoFireF* are projected with similar values for each fire month, ranging from 0.18±0.07 μg/m^3 in November to 0.29±0.09 μg/m^3 in July (Figure 4-16a). The decadal average of domain maximum $PM_{2.5}$ increase due to wildfires is projected the highest (5.32±10.02 μg/m^3) in August while wildfires only induce 0.13±0.09 μg/m^3 in November. In terms of seasons, the decadal average of the domain mean $PM_{2.5}$ increase is relatively higher in summer (0.28±0.08 μg/m^3) than in spring and autumn seasons; the domain maximum $PM_{2.5}$ increases due to wildfires are 4.24±6.79 μg/m^3 in summer (Figure 4-16b).

The differences of projected $PM_{2.5}$ increases due to wildfires between *USFS* and *IIASA* are mainly attributed to the different wildfire emissions (Figures 4-17 and 4-18). *USFS* simulations used the wildfire emissions projected by the empirical fire model that depends on the meteorological conditions while *IIASA* simulations used the wildfire emissions based on social-economical activities (Riahi et al., 2011). The differences in wildfire emissions result in (1) domain mean $PM_{2.5}$ increases are the largest at August and October in *IIASA* while *USFS* peaks at July, and (2) domain maximum $PM_{2.5}$ increases peak at August in *IIASA* but July, August, and October have the largest increases in domain maximum $PM_{2.5}$ values in *USFS* (Figures 4-15a and 4-16a).

Comparisons between the results from the present years (*BASE*) and from the future years (*IIASA*) illustrate that projected domain mean $PM_{2.5}$ concentration and domain maximum $PM_{2.5}$ increases caused by fires would be lower in the future years than that in present years in WUS (Figures 4-9 and 4-14). However, future wildfire emissions were projected using the 2005 data. By setting the 2005 domain mean and domain maximum increases as reference values, April and August both show higher $PM_{2.5}$ concentration

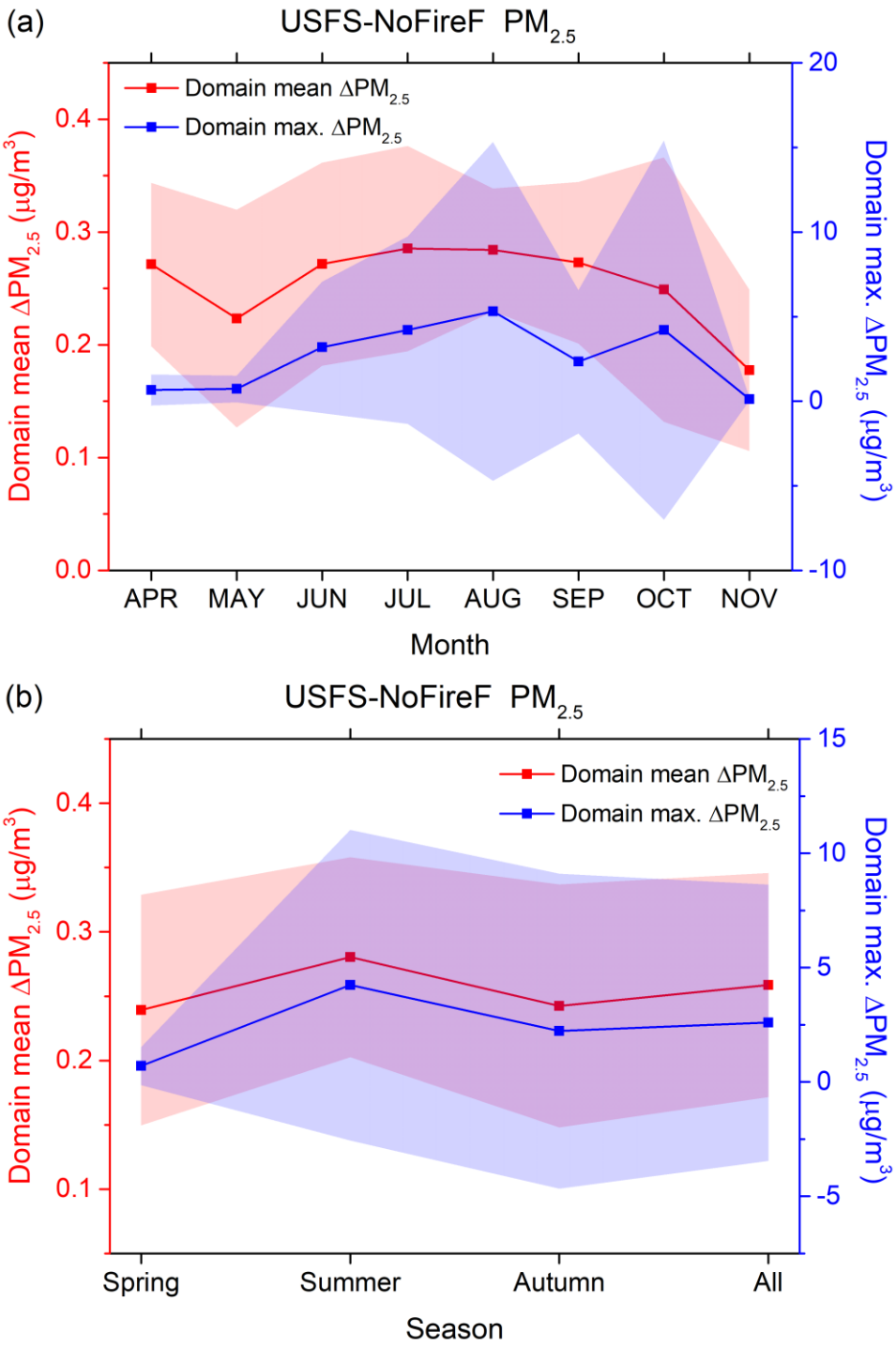


Figure 4-17. Same as Figure 4-13 except for $PM_{2.5}$ ($\mu g/m^3$).

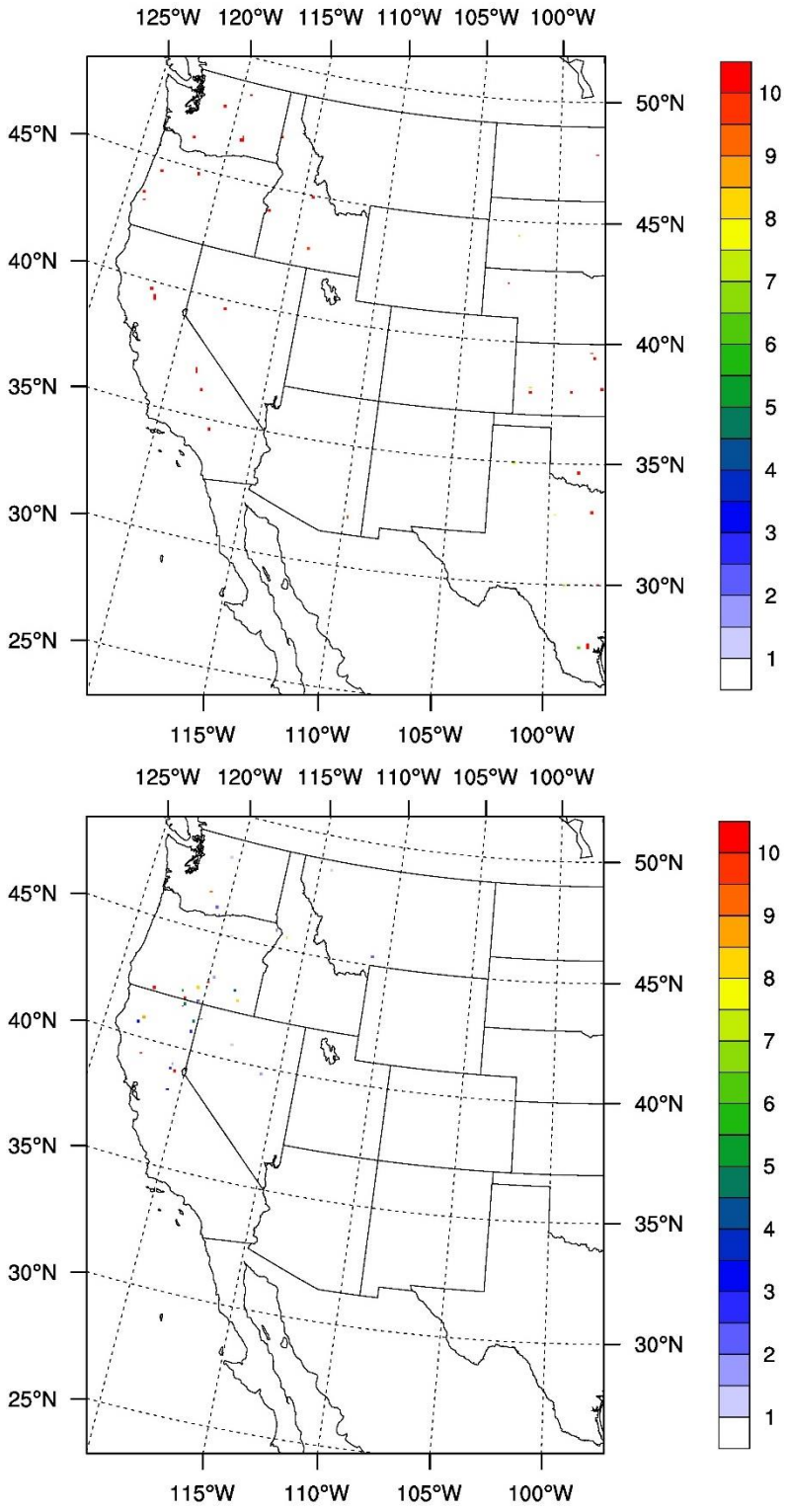


Figure 4-18. Projected $PM_{2.5}$ emission rates (g/s/grid) due to wildfires on August 2, 2050 used in *IIASA* (top) and in *USFS* (bottom) experiments.

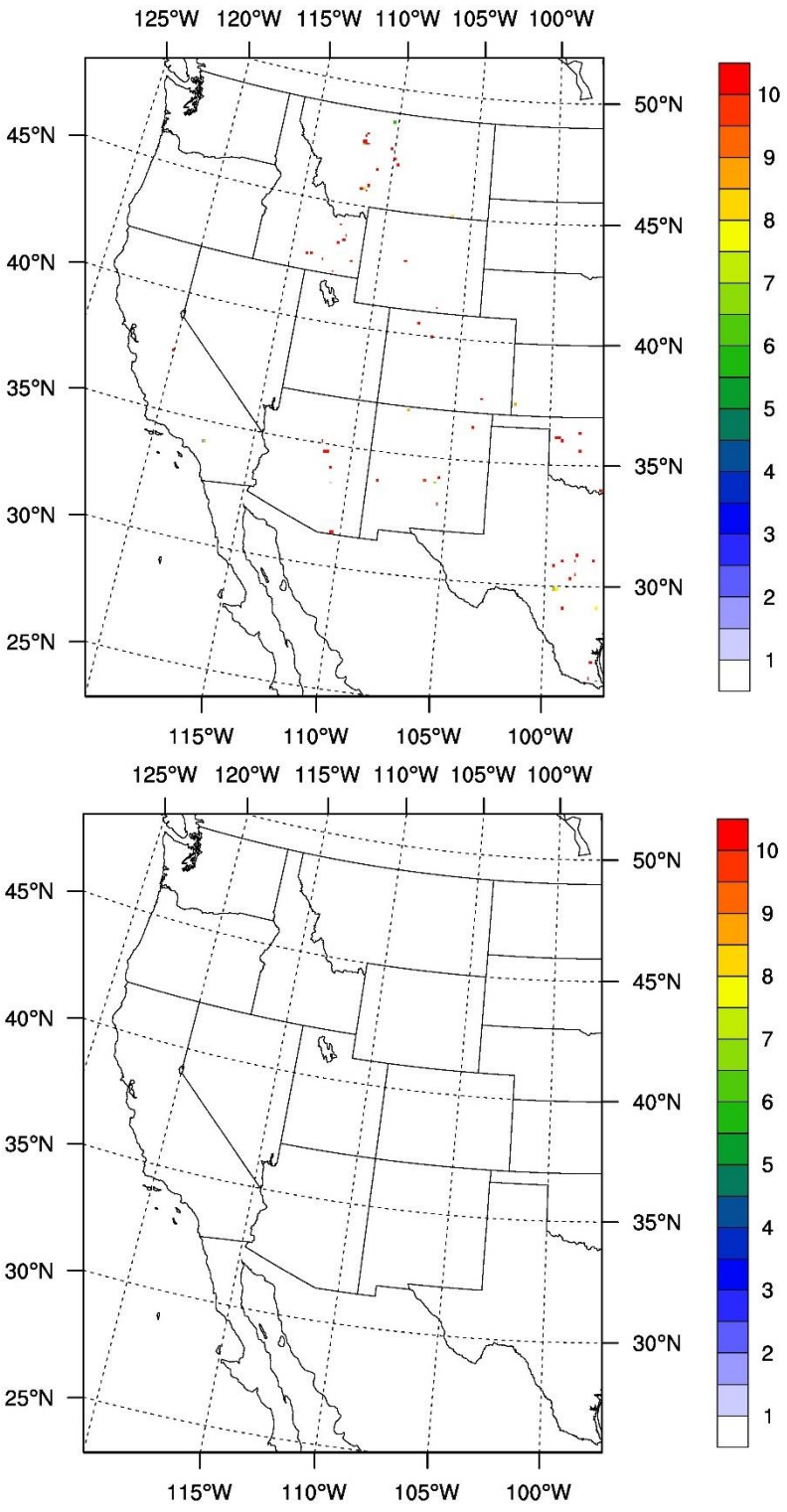


Figure 4-19. Same as Figure 4-18 except on April 13, 2056.

induced by fires in the future compared to the 2005 levels (Figure 4-19). Decadal average of the domain mean $PM_{2.5}$ increases are enhanced in all months except August while the domain maximum $PM_{2.5}$ increases are enhanced in April, June, August, and November (Figure 4-20a). The seasonal domain mean $PM_{2.5}$ increases become lower in summer but higher in spring and autumn seasons during 2050–2059 compared to 2005. The domain maximum $PM_{2.5}$ increases become larger in spring and summer but smaller in autumn (Figure 4-20b). There is no obvious change in decadal average for all fire months in the future compared to the 2005 results.

Conclusion

Five experiments were conducted to evaluate the air quality changes in WUS due to fire activities during the present years (2003–2010) as well as the future years (2050–2059). With the same meteorology, initial conditions, and boundary conditions, the fire-induced O_3 and $PM_{2.5}$ variations can be estimated through fire emission controls. Results show that wildfires have negligible impacts on O_3 concentration both in present and future years. However, substantial increases in $PM_{2.5}$ concentration due to wildfires are observed in WUS, with the domain maximum $PM_{2.5}$ could increase by more than 60 times of the value if there were no fires during the present years and by more than 20 times in the future. In addition, wildfires have the largest impacts on domain maximum $PM_{2.5}$ increases in WUS during summertime, especially in August, during 2003–2010. For future years, with wildfire emissions projected using either the 2005 temporal and spatial profiles (*IIASA*) or the future meteorological conditions (*USFS*), the largest domain maximum $PM_{2.5}$ increases would still be in summertime and in August. Since the results presented here are based on the domain averages and the domain maximum increase at a single grid cell, fire-induced $PM_{2.5}$ change may be underestimated in particular regions such as the California State where increasing frequency and severity of wildfires are observed in recent years. Further examinations on state- and city-level air pollutant concentration changes induced by wildfires would be necessary to quantify air quality changes for health impact research and to decision-making strategies for environmental management.

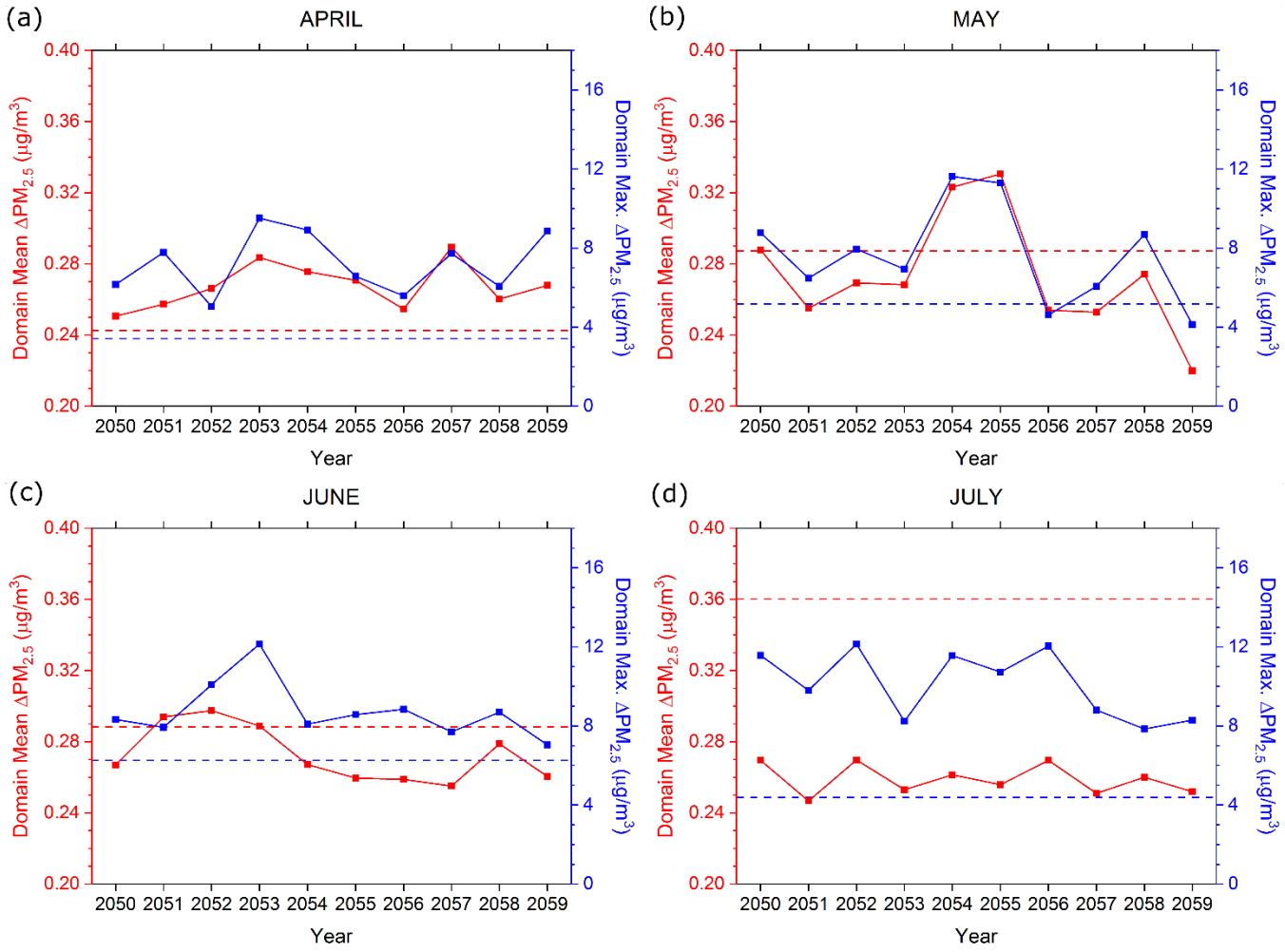


Figure 4-20. Simulated monthly domain mean (red) and domain maximum (blue) changes for $PM_{2.5}$ (μg/m^3). Solid lines show the *IIASA* results during 2050–2059. Dashed lines are the 2005 domain mean and domain maximum changes. Months are (a) April, (b) May, (c) June, (d) July, (e) August, (f) September, (g) October, and (h) November.

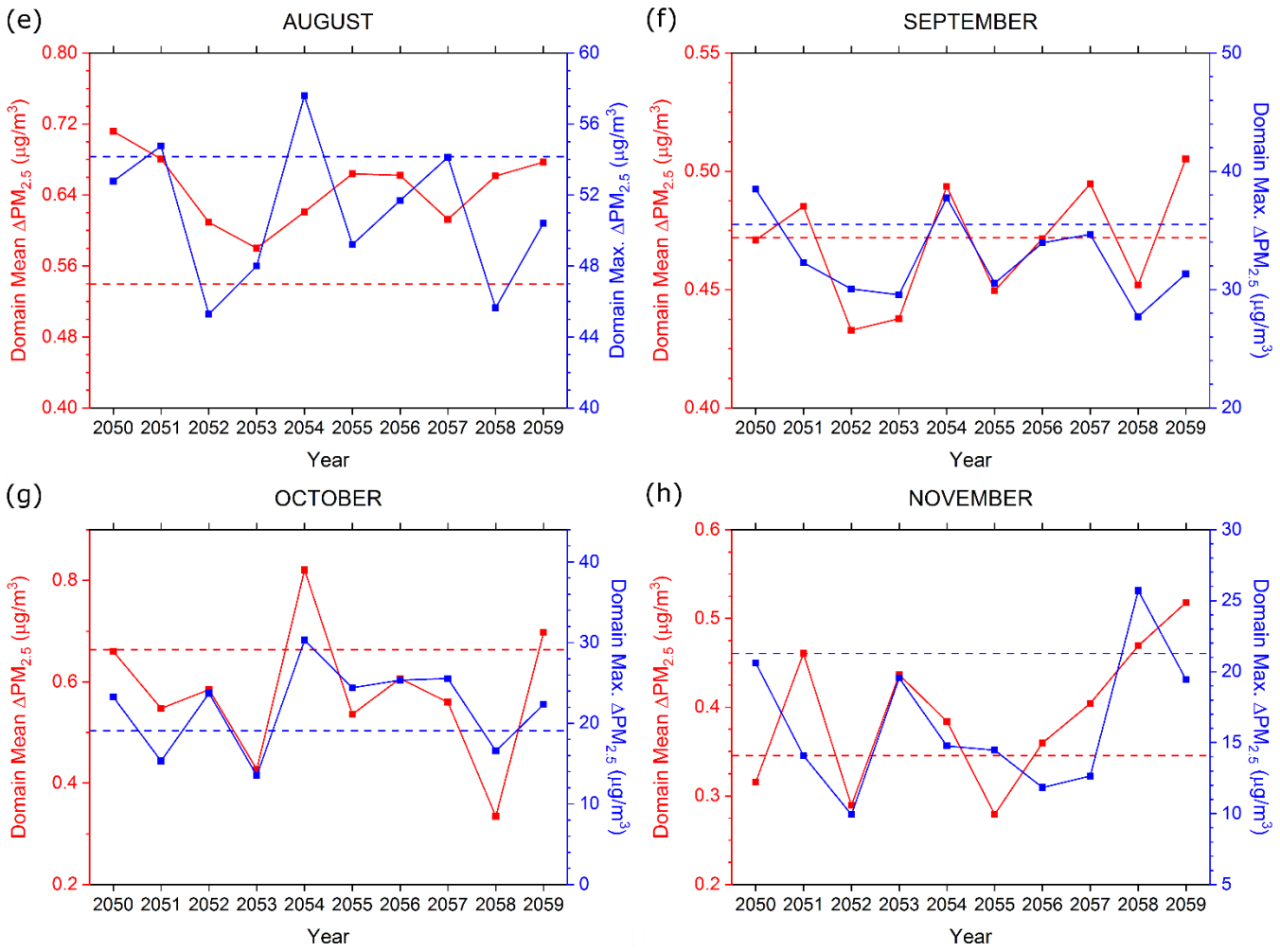


Figure 4-19 (*continued*).

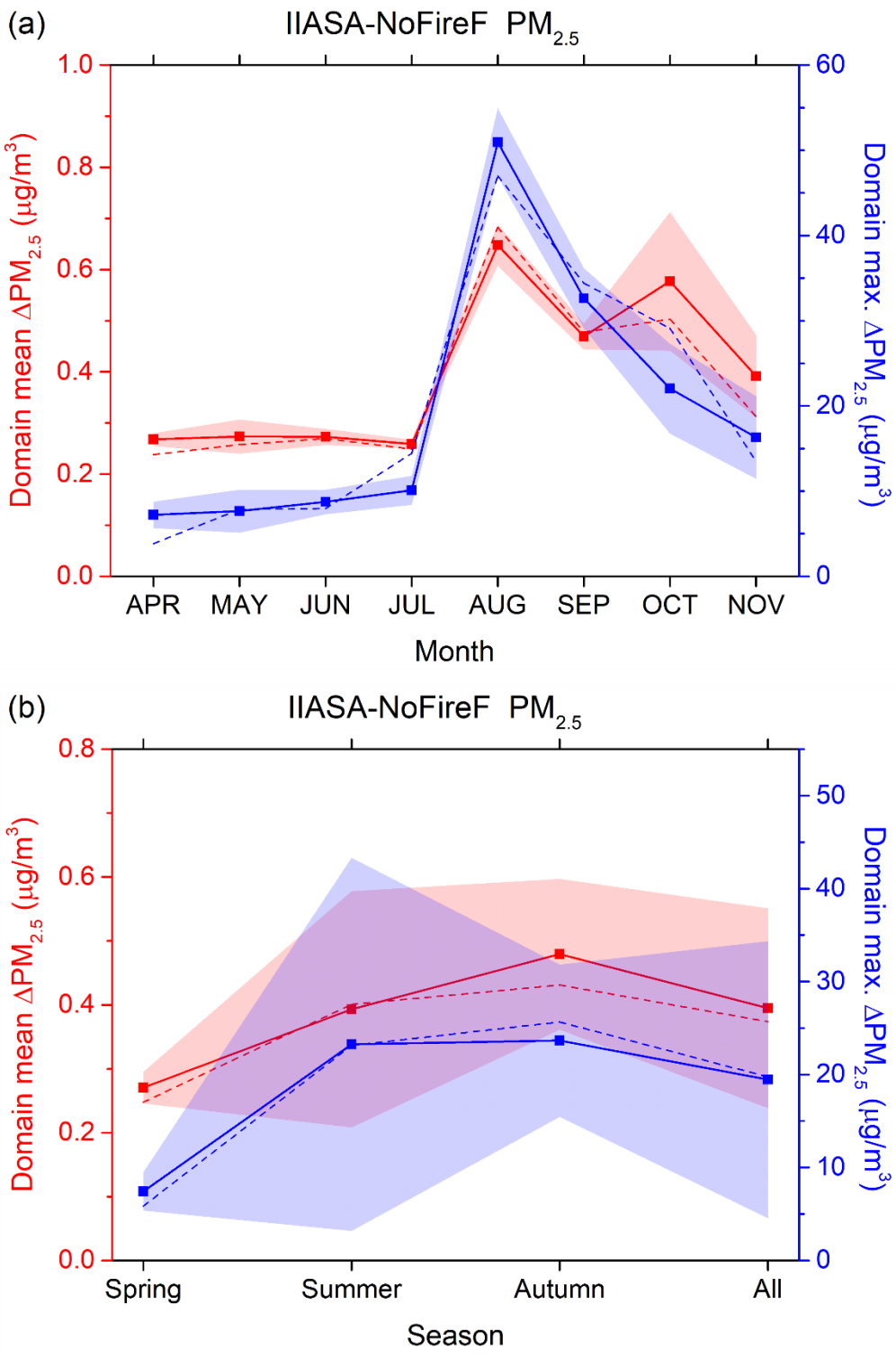


Figure 4-21. Same as Figure 4-15 with the dashed lines represent the 2005 domain mean and domain maximum $PM_{2.5}$ changes.

CHAPTER 5
CONCLUSION AND FUTURE STUDIES

The research presented here addresses important gaps in Earth system science through rigorous statistical analysis, model–data integration, and computational experiments designed to separate responses and feedbacks of terrestrial processes and land–atmosphere interactions. In particular, I showed that (1) we can reduce the uncertainty in projections of future forest biomass, and therefore carbon cycle feedbacks and fire risk, by improving dynamic carbon allocation schemes, better capturing the evolving distribution of vegetation types, and correctly initializing pre-industrial vegetation conditions; (2) geoengineering climate mitigation will have impacts on terrestrial ecosystems, and unaccounted for carbon cycle feedbacks will affect projected future atmospheric CO_2 mole fractions; and (3) increasing wildfire intensity is likely to substantially increase regional $PM_{2.5}$ concentration in a warming climate.

The biomass study used the ESM output from the CMIP5 archive. The new CMIP6 project (Eyring et al., 2016) is now underway and has been continuously accepting new ESM results, which offers the opportunity to explore whether biomass estimates are improved in the results from a new generation of ESMs with increased complexity. Simulations from land models employing the Ecosystem Demography concept (Moorcroft et al., 2001), such as the Functionally Assembled Terrestrial Ecosystem Simulator (FATES), may exhibit better representations of forest distribution, fraction, and biomass by integrating processes associated with vegetation demography. I would like to investigate if uncertainty in global biomass estimates is reduced in FATES compared to traditional "big-leaf" land models that fail to capture forest dynamics, age classes, and vegetation structure.

In the stratospheric aerosol geoengineering study, the data from the GLENS simulations contained an active terrestrial carbon cycle but the simulations did not consider terrestrial BGC feedbacks to the climate because the simulations were forced by atmospheric CO_2 mole fraction. To account for these feedbacks, as well as those from marine biogeochemistry, I would like to conduct new fully-coupled, emission-forced ESM

simulations with interactive terrestrial and marine BGC feedbacks taken into account in projections of prognostic atmospheric CO_2. From the new simulation results, evaluations of the interaction between climate change and ecosystems would be more representative. In particular, I would like to explore how future wildfires change with respect to soil moisture, burned area sizes, vegetation biomass, and fuel loads. Developing metrics for these variables will help identify the most influential factor for future wildfire disturbances in an unmitigated climate as well as a geoengineered climate.

From the study of wildfire-induced air quality changes in WUS, CMAQ simulated relatively smaller monthly increases in domain mean and domain maximum $PM_{2.5}$ concentration due to wildfires in the future compared to those in the present years. Further analyses are required to evaluate the wildfire contributions at State level and in major cities in WUS, especially in daily maximum $PM_{2.5}$ concentration that better capture the impacts of episodic wildfire events on $PM_{2.5}$ changes. In addition, large spatial and temporal uncertainty in future wildfire projections were found between RCP8.5 and that projected by an empirical fire model, even though both emission data sets demonstrated increased wildfire emissions compared to their own emission data sets in the present years. Additional effort in future wildfire emission development by disentangling emissions factors, for example fuel loads, climate conditions, and burned area sizes, would help quantify the uncertainty in each factor. Moreover, this wildfire study produced more than 2 PB of data that contains information from simulations both with and without wildfire emissions during the present and future years. This dataset can be used for new studies, such as estimating the impacts of wildfire-emitted $PM_{2.5}$ on human health. Since, as Stowell et al. (2019) suggested, asthma and combined respiratory disease were associated with wildfire smoke $PM_{2.5}$ concentration in Colorado during 2011–2014, future potential health risks can be assessed using this simulation dataset, which can inform constraints for decision-making strategies regarding future environmental management in a changing climate.

REFERENCES

Ainsworth, E. A., Yendrek, C. R., Sitch, S., Collins, W. J., & Emberson, L. D. (2012). The Effects of Tropospheric Ozone on Net Primary Productivity and Implications for Climate Change. *Annual Review of Plant Biology*, *63*(1), 637–661. https://doi.org/10.1146/annurev-arplant-042110-103829

Air Sciences Inc. (2005). *2002 Fire Emission Inventory for the WRAP Region – Phase II, Prepared for the Western Governors Association/Western Regional Aia Partnership*. Denver, CO.

Albrecht, B. A. (1989). Aerosols, Cloud Microphysics, and Fractional Cloudiness. *Science*, *245*(4923), 1227–1230. https://doi.org/10.1126/science.245.4923.1227

Alves, C. A., Vicente, A., Monteiro, C., Gonçalves, C., Evtyugina, M., & Pio, C. (2011). Emission of trace gases and organic components in smoke particles from a wildfire in a mixed-evergreen forest in Portugal. *Science of The Total Environment*, *409*(8), 1466–1475. https://doi.org/10.1016/j.scitotenv.2010.12.025

Amann, M., Bertok, I., Borken-Kleefeld, J., Cofala, J., Heyes, C., Hoglund-Isaksson, L., et al. (2015). *Adjusted historic emission data, projections, and optimized emission reduction targets for 2030 – A comparison with COM data 2013*. (M. Amann & International Institute for Applied Systems Analysis, Eds.). Laxenburg, Austria.

Andreae, M. O., & Merlet, P. (2001). Emission of trace gases and aerosols from biomass burning. *Global Biogeochemical Cycles*, *15*(4), 955–966. https://doi.org/10.1029/2000GB001382

Appel, K. W., Napelenok, S. L., Foley, K. M., Pye, H. O. T., Hogrefe, C., Luecken, D. J., et al. (2017). Description and evaluation of the Community Multiscale Air Quality (CMAQ) modeling system version 5.1. *Geoscientific Model Development*, *10*(4), 1703–1732. https://doi.org/10.5194/gmd-10-1703-2017

Appel, K. W., Napelenok, S., Hogrefe, C., Pouliot, G., Foley, K. M., Roselle, S. J., et al. (2018). Overview and Evaluation of the Community Multiscale Air Quality (CMAQ) Modeling System Version 5.2. In C. Mensink & G. Kallos (Eds.), *Air Pollution Modeling and its Application XXV* (pp. 69–73). Cham, Switzerland: Springer International Publishing. https://doi.org/10.1007/978-3-319-57645-9_11

Baccini, A., Goetz, S. J., Walker, W. S., Laporte, N. T., Sun, M., Sulla-Menashe, D., et al. (2012). Estimated carbon dioxide emissions from tropical deforestation improved by carbon-density maps. *Nature Climate Change*, *2*(3), 182–185. https://doi.org/10.1038/nclimate1354

Bala, G., Duffy, P. B., & Taylor, K. E. (2008). Impact of geoengineering schemes on the global hydrological cycle. *Proceedings of the National Academy of Sciences*, *105*(22), 7664–7669. https://doi.org/10.1073/pnas.0711648105

Bellouin, N., Collins, W. J., Culverwell, I. D., Halloran, P. R., Hardiman, S. C., Hinton, T. J., et al. (2011). The HadGEM2 family of Met Office Unified Model climate configurations. *Geoscientific Model Development*, *4*(3), 723–757. https://doi.org/10.5194/gmd-4-723-2011

Binkowski, F. S., Arunachalam, S., Adelman, Z., & Pinto, J. P. (2007). Examining Photolysis Rates with a Prototype Online Photolysis Module in CMAQ. *Journal of Applied Meteorology and Climatology*, *46*(8), 1252–1256. https://doi.org/10.1175/JAM2531.1

Bonan, G. B. (2008). Forests and Climate Change: Forcings, Feedbacks, and the Climate

Benefits of Forests. *Science*, *320*(5882), 1444–1449. https://doi.org/10.1126/science.1155121
Bonan, G. B., & Doney, S. C. (2018). Climate, ecosystems, and planetary futures: The challenge to predict life in Earth system models. *Science*, *359*(6375), eaam8328. https://doi.org/10.1126/science.aam8328
Boucher, O., & Reddy, M. S. (2008). Climate trade-off between black carbon and carbon dioxide emissions. *Energy Policy*, *36*(1), 193–200. https://doi.org/10.1016/j.enpol.2007.08.039
Boudreau, J., Nelson, R., Margolis, H., Beaddoin, A., Guidon, L., & Kimes, D. (2008). Regional aboveground forest biomass using airborne and spaceborne LiDAR in Québec. *Remote Sensing of Environment*, *112*(10), 3876–3890. https://doi.org/10.1016/j.rse.2008.06.003
Boylan, J. W., & Russell, A. G. (2006). PM and light extinction model performance metrics, goals, and criteria for three-dimensional air quality models. *Atmospheric Environment*, *40*(26), 4946–4959. https://doi.org/10.1016/j.atmosenv.2005.09.087
Bradley, B. A., Houghton, R. A., Mustard, J. F., & Hamburg, S. P. (2006). Invasive grass reduces aboveground carbon stocks in shrublands of the Western US. *Global Change Biology*, *12*(10), 1815–1822. https://doi.org/10.1111/j.1365-2486.2006.01232.x
Bradshaw, C. J. A., & Warkentin, I. G. (2015). Global estimates of boreal forest carbon stocks and flux. *Global and Planetary Change*, *128*, 24–30. https://doi.org/10.1016/j.gloplacha.2015.02.004
Byun, D., & Schere, K. L. (2006). Review of the Governing Equations, Computational Algorithms, and Other Components of the Models-3 Community Multiscale Air Quality (CMAQ) Modeling System. *Applied Mechanics Reviews*, *59*(2), 51. https://doi.org/10.1115/1.2128636
Cao, L. (2018). The Effects of Solar Radiation Management on the Carbon Cycle. *Current Climate Change Reports*, *4*(1), 41–50. https://doi.org/10.1007/s40641-018-0088-z
Cao, L., & Jiang, J. (2017). Simulated Effect of Carbon Cycle Feedback on Climate Response to Solar Geoengineering. *Geophysical Research Letters*, *44*(24), 12,484-12,491. https://doi.org/10.1002/2017GL076546
Di Carlo, P., Aruffo, E., Biancofiore, F., Busilacchio, M., Pitari, G., Dari-Salisburgo, C., et al. (2015). Wildfires impact on surface nitrogen oxides and ozone in Central Italy. *Atmospheric Pollution Research*, *6*(1), 29–35. https://doi.org/10.5094/APR.2015.004
Carlton, A. G., Bhave, P. V., Napelenok, S. L., Edney, E. O., Sarwar, G., Pinder, R. W., et al. (2010). Model Representation of Secondary Organic Aerosol in CMAQv4.7. *Environmental Science & Technology*, *44*(22), 8553–8560. https://doi.org/10.1021/es100636q
Cayan, D. R., Das, T., Pierce, D. W., Barnett, T. P., Tyree, M., & Gershunov, A. (2010). Future dryness in the southwest US and the hydrology of the early 21st century drought. *Proceedings of the National Academy of Sciences*, *107*(50), 21271–21276. https://doi.org/10.1073/pnas.0912391107
Chen, F., & Dudhia, J. (2001). Coupling an Advanced Land Surface–Hydrology Model

with the Penn State–NCAR MM5 Modeling System. Part I: Model Implementation and Sensitivity. *Monthly Weather Review*, *129*(4), 569–585. https://doi.org/10.1175/1520-0493(2001)129<0569:CAALSH>2.0.CO;2

Cheng, W., MacMartin, D. G., Dagon, K., Kravitz, B., Tilmes, S., Richter, J. H., et al. (2019). Soil moisture and other hydrological changes in a stratospheric aerosol geoengineering large ensemble. *Journal of Geophysical Research: Atmospheres*, 2018JD030237. https://doi.org/10.1029/2018JD030237

Chylek, P., Dubey, M., Hengartner, N., & Klett, J. (2017). Observed and Projected Precipitation Changes over the Nine US Climate Regions. *Atmosphere*, *8*(12), 207. https://doi.org/10.3390/atmos8110207

Coates, P. S., Ricca, M. A., Prochazka, B. G., Brooks, M. L., Doherty, K. E., Kroger, T., et al. (2016). Wildfire, climate, and invasive grass interactions negatively impact an indicator species by reshaping sagebrush ecosystems. *Proceedings of the National Academy of Sciences*, *113*(45), 12745–12750. https://doi.org/10.1073/pnas.1606898113

Colella, P., & Woodward, P. R. (1984). The Piecewise Parabolic Method (PPM) for gas-dynamical simulations. *Journal of Computational Physics*, *54*(1), 174–201. https://doi.org/10.1016/0021-9991(84)90143-8

Collins, W. J., Bellouin, N., Doutriaux-Boucher, M., Gedney, N., Halloran, P., Hinton, T., et al. (2011). Development and evaluation of an Earth-System model – HadGEM2. *Geoscientific Model Development*, *4*(4), 1051–1075. https://doi.org/10.5194/gmd-4-1051-2011

Cox, P. M. (2001). Description of the "TRIFFID" Dynamic Global Vegetation Model. In *Hadley Centre technical note*. Retrieved from http://climate.uvic.ca/model/common/HCTN_24.pdf

Cox, P. M., Betts, R. A., Bunton, C. B., Essery, R. L. H., Rowntree, P. R., & Smith, J. (1999). The impact of new land surface physics on the GCM simulation of climate and climate sensitivity. *Climate Dynamics*, *15*(3), 183–203. https://doi.org/10.1007/s003820050276

Crutzen, P. J. (2006). Albedo Enhancement by Stratospheric Sulfur Injections: A Contribution to Resolve a Policy Dilemma? *Climatic Change*, *77*(3–4), 211–220. https://doi.org/10.1007/s10584-006-9101-y

Dagon, K., & Schrag, D. P. (2019). Quantifying the effects of solar geoengineering on vegetation. *Climatic Change*, *153*(1–2), 235–251. https://doi.org/10.1007/s10584-019-02387-9

Dai, A., Trenberth, K. E., & Qian, T. (2004). A Global Dataset of Palmer Drought Severity Index for 1870–2002: Relationship with Soil Moisture and Effects of Surface Warming. *Journal of Hydrometeorology*, *5*(6), 1117–1130. https://doi.org/10.1175/JHM-386.1

Dai, Y., Zeng, X., Dickinson, R. E., Baker, I., Bonan, G. B., Bosilovich, M. G., et al. (2003). The Common Land Model. *Bulletin of the American Meteorological Society*, *84*(8), 1013–1023. https://doi.org/10.1175/BAMS-84-8-1013

Dai, Y., Dickinson, R. E., & Wang, Y.-P. (2004). A Two-Big-Leaf Model for Canopy Temperature, Photosynthesis, and Stomatal Conductance. *Journal of Climate*, *17*(12), 2281–2299. https://doi.org/10.1175/1520-

0442(2004)017<2281:ATMFCT>2.0.CO;2
Danabasoglu, G., Bates, S. C., Briegleb, B. P., Jayne, S. R., Jochum, M., Large, W. G., et al. (2012). The CCSM4 Ocean Component. *Journal of Climate*, *25*(5), 1361–1389. https://doi.org/10.1175/JCLI-D-11-00091.1
Davies-Barnard, T., Valdes, P. J., Singarayer, J. S., Wiltshire, A. J., & Jones, C. D. (2015). Quantifying the relative importance of land cover change from climate and land use in the representative concentration pathways. *Global Biogeochemical Cycles*, *29*(6), 842–853. https://doi.org/10.1002/2014GB004949
Doney, S. C., Fabry, V. J., Feely, R. A., & Kleypas, J. A. (2009). Ocean Acidification: The Other CO_2 Problem. *Annual Review of Marine Science*, *1*(1), 169–192. https://doi.org/10.1146/annurev.marine.010908.163834
Doughty, C. E., Malhi, Y., Araujo-Murakami, A., Metcalfe, D. B., Silva-Espejo, J. E., Arroyo, L., et al. (2014). Allocation trade-offs dominate the response of tropical forest growth to seasonal and interannual drought. *Ecology*, *95*(8), 2192–2201. https://doi.org/10.1890/13-1507.1
Doughty, C. E., Metcalfe, D. B., Girardin, C. A. J., Amézquita, F. F., Cabrera, D. G., Huasco, W. H., et al. (2015). Drought impact on forest carbon dynamics and fluxes in Amazonia. *Nature*, *519*(7541), 78–82. https://doi.org/10.1038/nature14213
Dufresne, J.-L., Foujols, M.-A., Denvil, S., Caubel, A., Marti, O., Aumont, O., et al. (2013). Climate change projections using the IPSL-CM5 Earth System Model: from CMIP3 to CMIP5. *Climate Dynamics*, *40*(9–10), 2123–2165. https://doi.org/10.1007/s00382-012-1636-1
Dukes, J. S., Chiariello, N. R., Cleland, E. E., Moore, L. A., Shaw, M. R., Thayer, S., et al. (2005). Responses of grassland production to single and multiple global environmental changes. *PLoS Biology*, *3*(10), e319. https://doi.org/10.1371/journal.pbio.0030319
Emmons, L. K., Walters, S., Hess, P. G., Lamarque, J.-F., Pfister, G. G., Fillmore, D., et al. (2010). Description and evaluation of the Model for Ozone and Related chemical Tracers, version 4 (MOZART-4). *Geoscientific Model Development*, *3*(1), 43–67. https://doi.org/10.5194/gmd-3-43-2010
Enoch, H. Z. (1984). Primary Plant Production during Increasing Global CO2 Concentration. In *Advances in Photosynthesis Research* (pp. 201–207). Dordrecht: Springer Netherlands. https://doi.org/10.1007/978-94-017-4971-8_43
Essery, R. L. H., Best, M. J., Betts, R. A., Cox, P. M., & Taylor, C. M. (2003). Explicit Representation of Subgrid Heterogeneity in a GCM Land Surface Scheme. *Journal of Hydrometeorology*, *4*(3), 530–543. https://doi.org/10.1175/1525-7541(2003)004<0530:EROSHI>2.0.CO;2
Exbrayat, J.-F., Pitman, A. J., & Abramowitz, G. (2014). Response of microbial decomposition to spin-up explains CMIP5 soil carbon range until 2100. *Geoscientific Model Development*, *7*(6), 2683–2692. https://doi.org/10.5194/gmd-7-2683-2014
Eyring, V., Bony, S., Meehl, G. A., Senior, C. A., Stevens, B., Stouffer, R. J., & Taylor, K. E. (2016). Overview of the Coupled Model Intercomparison Project Phase 6 (CMIP6) experimental design and organization. *Geoscientific Model Development*, *9*(5), 1937–1958. https://doi.org/10.5194/gmd-9-1937-2016

Fabry, V. J., Seibel, B. A., Feely, R. A., & Orr, J. C. (2008). Impacts of ocean acidification on marine fauna and ecosystem processes. *ICES Journal of Marine Science*, *65*(3), 414–432. https://doi.org/10.1093/icesjms/fsn048

Fahey, K. M., Carlton, A. G., Pye, H. O. T., Baek, J., Hutzell, W. T., Stanier, C. O., et al. (2017). A framework for expanding aqueous chemistry in the Community Multiscale Air Quality (CMAQ) model version 5.1. *Geoscientific Model Development*, *10*(4), 1587–1605. https://doi.org/10.5194/gmd-10-1587-2017

Fasullo, J. T., Tilmes, S., Richter, J. H., Kravitz, B., MacMartin, D. G., Mills, M. J., & Simpson, I. R. (2018). Persistent polar ocean warming in a strategically geoengineered climate. *Nature Geoscience*, *11*(12), 910–914. https://doi.org/10.1038/s41561-018-0249-7

Finlay, S. E., Moffat, A., Gazzard, R., Baker, D., & Murray, V. (2012). Health Impacts of Wildfires. *PLoS Currents Disasters*, (NOVEMBER 2012). https://doi.org/10.1371/4f959951cce2c

Fisher, R. A., Muszala, S., Verteinstein, M., Lawrence, P., Xu, C., McDowell, N. G., et al. (2015). Taking off the training wheels: the properties of a dynamic vegetation model without climate envelopes, CLM4.5(ED). *Geoscientific Model Development*, *8*(11), 3593–3619. https://doi.org/10.5194/gmd-8-3593-2015

Fisher, R. A., Koven, C. D., Anderegg, W. R. L., Christoffersen, B. O., Dietze, M. C., Farrior, C. E., et al. (2018). Vegetation demographics in Earth System Models: A review of progress and priorities. *Global Change Biology*, *24*(1), 35–54. https://doi.org/10.1111/gcb.13910

Frank, D., Reichstein, M., Bahn, M., Thonicke, K., Frank, D., Mahecha, M. D., et al. (2015). Effects of climate extremes on the terrestrial carbon cycle: concepts, processes and potential future impacts. *Global Change Biology*, *21*(8), 2861–2880. https://doi.org/10.1111/gcb.12916

Franklin, O., Johansson, J., Dewar, R. C., Dieckmann, U., McMurtrie, R. E., Brannstrom, A., & Dybzinski, R. (2012). Modeling carbon allocation in trees: a search for principles. *Tree Physiology*, *32*(6), 648–666. https://doi.org/10.1093/treephys/tpr138

Friedlingstein, P., Joel, G., Field, C. B., & Fung, I. Y. (1999). Toward an allocation scheme for global terrestrial carbon models. *Global Change Biology*, *5*(7), 755–770. https://doi.org/10.1046/j.1365-2486.1999.00269.x

Friend, A. D., Lucht, W., Rademacher, T. T., Keribin, R., Betts, R., Cadule, P., et al. (2014). Carbon residence time dominates uncertainty in terrestrial vegetation responses to future climate and atmospheric CO 2. *Proceedings of the National Academy of Sciences*, *111*(9), 3280–3285. https://doi.org/10.1073/pnas.1222477110

Fu, J. S., Hsu, N. C., Gao, Y., Huang, K., Li, C., Lin, N.-H., & Tsay, S.-C. (2012). Evaluating the influences of biomass burning during 2006 BASE-ASIA: a regional chemical transport modeling. *Atmospheric Chemistry and Physics*, *12*(9), 3837–3855. https://doi.org/10.5194/acp-12-3837-2012

Gao, Y., Fu, J. S., Drake, J. B., Liu, Y., & Lamarque, J.-F. (2012). Projected changes of extreme weather events in the eastern United States based on a high resolution climate modeling system. *Environmental Research Letters*, *7*(4), 044025. https://doi.org/10.1088/1748-9326/7/4/044025

Gao, Y., Fu, J. S., Drake, J. B., Lamarque, J.-F., & Liu, Y. (2013). The impact of

emission and climate change on ozone in the United States under representative concentration pathways (RCPs). *Atmospheric Chemistry and Physics*, *13*(18), 9607–9621. https://doi.org/10.5194/acp-13-9607-2013

Gao, Y., Leung, L. R., Lu, J., Liu, Y., Huang, M., & Qian, Y. (2014). Robust spring drying in the southwestern U.S. and seasonal migration of wet/dry patterns in a warmer climate. *Geophysical Research Letters*, *41*(5), 1745–1751. https://doi.org/10.1002/2014GL059562

Gattuso, J.-P., Magnan, A., Billé, R., Cheung, W. W. L., Howes, E. L., Joos, F., et al. (2015). Contrasting futures for ocean and society from different anthropogenic CO_2 emissions scenarios. *Science*, *349*(6243), aac4722. https://doi.org/10.1126/science.aac4722

Gibbs, H. K., Olsen, L., & Boden, T. (2006). Major world ecosystem complexes ranked by carbon in live vegetation: an updated database using the GLC2000 land cover product. *Oak Ridge National Laboratory, Oak Ridge, USA*. https://doi.org/10.3334/CDIAC/lue.ndp017.2006

Giglio, L., Randerson, J. T., & van der Werf, G. R. (2013). Analysis of daily, monthly, and annual burned area using the fourth-generation global fire emissions database (GFED4). *Journal of Geophysical Research: Biogeosciences*, *118*(1), 317–328. https://doi.org/10.1002/jgrg.20042

Gu, L., Baldocchi, D. D., Wofsy, S. C., Munger, J. W., Michalsky, J. J., Urbanski, S. P., & Boden, T. A. (2003). Response of a Deciduous Forest to the Mount Pinatubo Eruption: Enhanced Photosynthesis. *Science*, *299*(5615), 2035–2038. https://doi.org/10.1126/science.1078366

Haikerwal, A., Akram, M., Del Monaco, A., Smith, K., Sim, M. R., Meyer, M., et al. (2015). Impact of Fine Particulate Matter ($PM_{2.5}$) Exposure During Wildfires on Cardiovascular Health Outcomes. *Journal of the American Heart Association*, *4*(7). https://doi.org/10.1161/JAHA.114.001653

Hansen, M. C., Potapov, P. V., Moore, R., Hancher, M., Turubanova, S. A., Tyukavina, A., et al. (2013). High-Resolution Global Maps of 21st-Century Forest Cover Change. *Science*, *342*(6160), 850–853. https://doi.org/10.1126/science.1244693

Hantson, S., Arneth, A., Harrison, S. P., Kelley, D. I., Colin Prentice, I., Rabin, S. S., et al. (2016). The status and challenge of global fire modelling. *Biogeosciences*, *13*(11), 3359–3375. https://doi.org/10.5194/bg-13-3359-2016

Hargrove, W. W., & Hoffman, F. M. (2004). Potential of Multivariate Quantitative Methods for Delineation and Visualization of Ecoregions. *Environmental Management*, *34*(S1), S39–S60. https://doi.org/10.1007/s00267-003-1084-0

Hargrove, W. W., Hoffman, F. M., & Hessburg, P. F. (2006). Mapcurves: a quantitative method for comparing categorical maps. *Journal of Geographical Systems*, *8*(2), 187–208. https://doi.org/10.1007/s10109-006-0025-x

Heimann, M., & Reichstein, M. (2008). Terrestrial ecosystem carbon dynamics and climate feedbacks. *Nature*, *451*(7176), 289–292. https://doi.org/10.1038/nature06591

Hicke, J. A., Allen, C. D., Desai, A. R., Dietze, M. C., Hall, R. J., Ted Hogg, E. H., et al. (2012). Effects of biotic disturbances on forest carbon cycling in the United States and Canada. *Global Change Biology*, *18*(1), 7–34. https://doi.org/10.1111/j.1365-

2486.2011.02543.x
Hoegh-Guldberg, O., Jacob, D., Taylor, M., Bindi, M., Brown, S., Camilloni, I., et al. (2018). Chapter 3: Impacts of 1.5ºC global warming on natural and human systems. In *Global Warming of 1.5ºC an IPCC special report on the impacts of global warming of 1.5ºC above pre-industrial levels and related global greenhouse gas emission pathways, in the context of strengthening the global response to the threat of climate change*. Intergovernmental Panel on Climate Change.
Hoffman, F. M., Randerson, J. T., Arora, V. K., Bao, Q., Cadule, P., Ji, D., et al. (2014). Causes and implications of persistent atmospheric carbon dioxide biases in Earth System Models. *Journal of Geophysical Research: Biogeosciences*, *119*(2), 141–162. https://doi.org/10.1002/2013JG002381
Hoffman, Forrest M, Koven, C. D., Keppel-Aleks, G., Lawrence, D. M., Riley, W. J., Randerson, J. T., et al. (2017). *2016 International Land Model Benchmarking (ILAMB) Workshop Report*. https://doi.org/10.2172/1330803
Hong, S.-Y., & Lim, J.-O. J. (2006). The WRF single-moment 6-class microphysics scheme (WSM6). *J. Korean Meteorol. Soc.*, *42*, 129–151.
Houghton, R. A., Lawrence, K. T., Hackler, J. L., & Brown, S. (2008). The spatial distribution of forest biomass in the Brazilian Amazon: a comparison of estimates. *Global Change Biology*, *7*(7), 731–746. https://doi.org/10.1111/j.1365-2486.2001.00426.x
Hunke, E. C., & Lipscomb, W. H. (2008). *CICE: The Los Alamos sea ice model documentation and software user's manual version 4.0*. *Los Alamos National Laboratory Tech. Rep. LA-CC-06-012*. Los Alamos, NM, USA: Los Alamos National Laboratory.
Hurtt, G. C., Fisk, J., Thomas, R. Q., Dubayah, R., Moorcroft, P. R., & Shugart, H. H. (2010). Linking models and data on vegetation structure. *Journal of Geophysical Research: Biogeosciences*, *115*(G2). https://doi.org/10.1029/2009JG000937
Hurtt, G. C., Chini, L. P., Frolking, S., Betts, R. A., Feddema, J., Fischer, G., et al. (2011). Harmonization of land-use scenarios for the period 1500–2100: 600 years of global gridded annual land-use transitions, wood harvest, and resulting secondary lands. *Climatic Change*, *109*(1–2), 117–161. https://doi.org/10.1007/s10584-011-0153-2
Iacono, M. J., Delamere, J. S., Mlawer, E. J., Shephard, M. W., Clough, S. A., & Collins, W. D. (2008). Radiative forcing by long-lived greenhouse gases: Calculations with the AER radiative transfer models. *Journal of Geophysical Research*, *113*(D13), D13103. https://doi.org/10.1029/2008JD009944
International Energy Agency. (2012). *Energy Technology Perspectives 2012: Pathways to a Clean Energy System*. *International Energy Agency* (2nd ed.). Paris. France: OECD/IEA.
Irvine, P. J., Kravitz, B., Lawrence, M. G., & Muri, H. (2016). An overview of the Earth system science of solar geoengineering. *Wiley Interdisciplinary Reviews: Climate Change*, *7*(6), 815–833. https://doi.org/10.1002/wcc.423
Ito, A., & Penner, J. E. (2004). Global estimates of biomass burning emissions based on satellite imagery for the year 2000. *Journal of Geophysical Research D: Atmospheres*, *109*(14), D14S05. https://doi.org/10.1029/2003JD004423

Jackson, R. B., Banner, J. L., Jobbágy, E. G., Pockman, W. T., & Wall, D. H. (2002). Ecosystem carbon loss with woody plant invasion of grasslands. *Nature*, *418*(6898), 623–626. https://doi.org/10.1038/nature00910

Jaffe, D., Hafner, W., Chand, D., Westerling, A., & Spracklen, D. (2008). Interannual Variations in $PM_{2.5}$ due to Wildfires in the Western United States. *Environmental Science & Technology*, *42*(8), 2812–2818. https://doi.org/10.1021/es702755v

Jaffe, D. A., & Wigder, N. L. (2012). Ozone production from wildfires: A critical review. *Atmospheric Environment*, *51*, 1–10. https://doi.org/10.1016/j.atmosenv.2011.11.063

Janjić, Z. I. (1990). The step-mountain coordinate: physical package. *Monthly Weather Review*, *118*(7), 1429–1443. https://doi.org/10.1175/1520-0493(1990)118<1429:TSMCPP>2.0.CO;2

Ji, D., Wang, L., Feng, J., Wu, Q., Cheng, H., Zhang, Q., et al. (2014). Description and basic evaluation of Beijing Normal University Earth System Model (BNU-ESM) version 1. *Geoscientific Model Development*, *7*(5), 2039–2064. https://doi.org/10.5194/gmd-7-2039-2014

Jiang, L., Yan, Y., Hararuk, O., Mikle, N., Xia, J., Shi, Z., et al. (2015). Scale-Dependent Performance of CMIP5 Earth System Models in Simulating Terrestrial Vegetation Carbon. *Journal of Climate*, *28*(13), 5217–5232. https://doi.org/10.1175/JCLI-D-14-00270.1

Jobbágy, E. G., & Jackson, R. B. (2000). The vertical distribution of soil organic carbon and its relation to climate and vegetation. *Ecological Applications*, *10*(2), 423–436. https://doi.org/10.1890/1051-0761(2000)010[0423:TVDOSO]2.0.CO;2

Joint Research Centre, E. C. (2003). Global Land Cover 2000 database. Retrieved from http://forobs.jrc.ec.europa.eu/products/glc2000/glc2000.php

Jolly, W. M., Cochrane, M. A., Freeborn, P. H., Holden, Z. A., Brown, T. J., Williamson, G. J., & Bowman, D. M. J. S. (2015). Climate-induced variations in global wildfire danger from 1979 to 2013. *Nature Communications*, *6*(1), 7537. https://doi.org/10.1038/ncomms8537

Jones, C. D., Hughes, J. K., Bellouin, N., Hardiman, S. C., Jones, G. S., Knight, J., et al. (2011). The HadGEM2-ES implementation of CMIP5 centennial simulations. *Geoscientific Model Development*, *4*(3), 543–570. https://doi.org/10.5194/gmd-4-543-2011

Kalidindi, S., Bala, G., Modak, A., & Caldeira, K. (2015). Modeling of solar radiation management: a comparison of simulations using reduced solar constant and stratospheric sulphate aerosols. *Climate Dynamics*, *44*(9–10), 2909–2925. https://doi.org/10.1007/s00382-014-2240-3

Kattge, J., Díaz, S., Lavorel, S., Prentice, I. C., Leadley, P., Bönisch, G., et al. (2011). TRY - a global database of plant traits. *Global Change Biology*, *17*(9), 2905–2935. https://doi.org/10.1111/j.1365-2486.2011.02451.x

De Kauwe, M. G., Medlyn, B. E., Zaehle, S., Walker, A. P., Dietze, M. C., Wang, Y.-P., et al. (2014). Where does the carbon go? A model-data intercomparison of vegetation carbon allocation and turnover processes at two temperate forest free-air CO_2 enrichment sites. *The New Phytologist*, *203*(3), 883–99. https://doi.org/10.1111/nph.12847

Keith, D. W., Wagner, G., & Zabel, C. L. (2017). Solar geoengineering reduces atmospheric carbon burden. *Nature Climate Change*, *7*(9), 617–619. https://doi.org/10.1038/nclimate3376

Keller, D. P., Feng, E. Y., & Oschlies, A. (2014). Potential climate engineering effectiveness and side effects during a high carbon dioxide-emission scenario. *Nature Communications*, *5*(1), 3304. https://doi.org/10.1038/ncomms4304

Kim, H. (2018, July 25). Global Soil Wetness Project Phase 3 Atmospheric Boundary Conditions (Experiment 1). Data Integration and Analysis System (DIAS). https://doi.org/10.20783/DIAS.501

Kottek, M., Grieser, J., Beck, C., Rudolf, B., & Rubel, F. (2006). World Map of the Köppen-Geiger climate classification updated. *Meteorologische Zeitschrift*, *15*(3), 259–263. https://doi.org/10.1127/0941-2948/2006/0130

Kravitz, B., Robock, A., Oman, L., Stenchikov, G., & Marquardt, A. B. (2009). Sulfuric acid deposition from stratospheric geoengineering with sulfate aerosols. *Journal of Geophysical Research*, *114*(D14), D14109. https://doi.org/10.1029/2009JD011918

Kravitz, B., Caldeira, K., Boucher, O., Robock, A., Rasch, P. J., Alterskjaer, K., et al. (2013). Climate model response from the Geoengineering Model Intercomparison Project (GeoMIP). *Journal of Geophysical Research: Atmospheres*, *118*(15), 8320–8332. https://doi.org/10.1002/jgrd.50646

Kravitz, B., MacMartin, D. G., Wang, H., & Rasch, P. J. (2016). Geoengineering as a design problem. *Earth System Dynamics*, *7*(2), 469–497. https://doi.org/10.5194/esd-7-469-2016

Kravitz, B., MacMartin, D. G., Mills, M. J., Richter, J. H., Tilmes, S., Lamarque, J., et al. (2017). First Simulations of Designing Stratospheric Sulfate Aerosol Geoengineering to Meet Multiple Simultaneous Climate Objectives. *Journal of Geophysical Research: Atmospheres*, *122*(23), 12,616-12,634. https://doi.org/10.1002/2017JD026874

Krinner, G., Viovy, N., de Noblet-Ducoudré, N., Ogée, J., Polcher, J., Friedlingstein, P., et al. (2005). A dynamic global vegetation model for studies of the coupled atmosphere-biosphere system. *Global Biogeochemical Cycles*, *19*(1), GB1015. https://doi.org/10.1029/2003GB002199

Lam, Y. F., Fu, J. S., Wu, S., & Mickley, L. J. (2011). Impacts of future climate change and effects of biogenic emissions on surface ozone and particulate matter concentrations in the United States. *Atmospheric Chemistry and Physics*, *11*(10), 4789–4806. https://doi.org/10.5194/acp-11-4789-2011

Lamarque, J.-F., Kiehl, J. T., Hess, P. G., Collins, W. D., Emmons, L. K., Ginoux, P., et al. (2005). Response of a coupled chemistry-climate model to changes in aerosol emissions: Global impact on the hydrological cycle and the tropospheric burdens of OH, ozone, and NO x. *Geophysical Research Letters*, *32*(16), L16809. https://doi.org/10.1029/2005GL023419

Lamarque, J.-F., Emmons, L. K., Hess, P. G., Kinnison, D. E., Tilmes, S., Vitt, F., et al. (2012). CAM-chem: description and evaluation of interactive atmospheric chemistry in the Community Earth System Model. *Geoscientific Model Development*, *5*(2), 369–411. https://doi.org/10.5194/gmd-5-369-2012

Langenbrunner, B., Pritchard, M. S., Kooperman, G. J., & Randerson, J. T. (2019). Why

Does Amazon Precipitation Decrease When Tropical Forests Respond to Increasing CO_2? *Earth's Future*, *7*(4), 450–468. https://doi.org/10.1029/2018EF001026
Lawrence, M. G., Schäfer, S., Muri, H., Scott, V., Oschlies, A., Vaughan, N. E., et al. (2018). Evaluating climate geoengineering proposals in the context of the Paris Agreement temperature goals. *Nature Communications*, *9*(1), 3734. https://doi.org/10.1038/s41467-018-05938-3
Littell, J. S., McKenzie, D., Peterson, D. L., & Westerling, A. L. (2009). Climate and wildfire area burned in western U.S. ecoprovinces, 1916–2003. *Ecological Applications*, *19*(4), 1003–1021. https://doi.org/10.1890/07-1183.1
Litton, C. M., Raich, J. W., & Ryan, M. G. (2007). Carbon allocation in forest ecosystems. *Global Change Biology*, *13*(10), 2089–2109. https://doi.org/10.1111/j.1365-2486.2007.01420.x
Liu, J. C., Pereira, G., Uhl, S. A., Bravo, M. A., & Bell, M. L. (2015). A systematic review of the physical health impacts from non-occupational exposure to wildfire smoke. *Environmental Research*, *136*, 120–132. https://doi.org/10.1016/j.envres.2014.10.015
Liu, J. C., Mickley, L. J., Sulprizio, M. P., Dominici, F., Yue, X., Ebisu, K., et al. (2016). Particulate air pollution from wildfires in the Western US under climate change. *Climatic Change*, *138*(3–4), 655–666. https://doi.org/10.1007/s10584-016-1762-6
Liu, J. C., Wilson, A., Mickley, L. J., Dominici, F., Ebisu, K., Wang, Y., et al. (2017). Wildfire-specific Fine Particulate Matter and Risk of Hospital Admissions in Urban and Rural Counties. *Epidemiology*, *28*(1), 77–85. https://doi.org/10.1097/EDE.0000000000000556
Liu, Y., L. Goodrick, S., & A. Stanturf, J. (2013). Future U.S. wildfire potential trends projected using a dynamically downscaled climate change scenario. *Forest Ecology and Management*, *294*, 120–135. https://doi.org/10.1016/j.foreco.2012.06.049
Lloyd, J. (1999). The CO_2 dependence of photosynthesis, plant growth responses to elevated CO_2 concentrations and their interaction with soil nutrient status, II. Temperate and boreal forest productivity and the combined effects of increasing CO<sub>2. *Functional Ecology*, *13*(4), 439–459. https://doi.org/10.1046/j.1365-2435.1999.00350.x
Luo, Y. Q., Randerson, J. T., Abramowitz, G., Bacour, C., Blyth, E., Carvalhais, N., et al. (2012). A framework for benchmarking land models. *Biogeosciences*, *9*(10), 3857–3874. https://doi.org/10.5194/bg-9-3857-2012
MacMartin, D. G., Kravitz, B., Keith, D. W., & Jarvis, A. (2014). Dynamics of the coupled human–climate system resulting from closed-loop control of solar geoengineering. *Climate Dynamics*, *43*(1–2), 243–258. https://doi.org/10.1007/s00382-013-1822-9
Malhi, Y., Meir, P., & Brown, S. (2002). Forests, carbon and global climate. *Philosophical Transactions of the Royal Society of London. Series A: Mathematical, Physical and Engineering Sciences*, *360*(1797), 1567–1591. https://doi.org/10.1098/rsta.2002.1020
van Mantgem, P. J., Stephenson, N. L., Byrne, J. C., Daniels, L. D., Franklin, J. F., Fule, P. Z., et al. (2009). Widespread Increase of Tree Mortality Rates in the Western United States. *Science*, *323*(5913), 521–524.

https://doi.org/10.1126/science.1165000
Mao, J., Ricciuto, D. M., Thornton, P. E., Warren, J. M., King, A. W., Shi, X., et al. (2016). Evaluating the Community Land Model in a pine stand with shading manipulations and $^{13}CO_2$ labeling. *Biogeosciences*, *13*(3), 641–657. https://doi.org/10.5194/bg-13-641-2016
Marlon, J. R., Bartlein, P. J., Gavin, D. G., Long, C. J., Anderson, R. S., Briles, C. E., et al. (2012). Long-term perspective on wildfires in the western USA. *Proceedings of the National Academy of Sciences*, *109*(9), E535–E543. https://doi.org/10.1073/pnas.1112839109
Matthews, H. D., Cao, L., & Caldeira, K. (2009). Sensitivity of ocean acidification to geoengineered climate stabilization. *Geophysical Research Letters*, *36*(10), L10706. https://doi.org/10.1029/2009GL037488
Medvigy, D., Wofsy, S. C., Munger, J. W., Hollinger, D. Y., & Moorcroft, P. R. (2009). Mechanistic scaling of ecosystem function and dynamics in space and time: Ecosystem Demography model version 2. *Journal of Geophysical Research*, *114*(G1), G01002. https://doi.org/10.1029/2008JG000812
Meinshausen, M., Smith, S. J., Calvin, K., Daniel, J. S., Kainuma, M. L. T., Lamarque, J.-F., et al. (2011). The RCP greenhouse gas concentrations and their extensions from 1765 to 2300. *Climatic Change*, *109*(1–2), 213–241. https://doi.org/10.1007/s10584-011-0156-z
Mellor, G. L., & Yamada, T. (1982). Development of a turbulence closure model for geophysical fluid problems. *Reviews of Geophysics*, *20*(4), 851. https://doi.org/10.1029/RG020i004p00851
Mercado, L. M., Bellouin, N., Sitch, S., Boucher, O., Huntingford, C., Wild, M., & Cox, P. M. (2009). Impact of changes in diffuse radiation on the global land carbon sink. *Nature*, *458*(7241), 1014–1017. https://doi.org/10.1038/nature07949
Michel, C., Liousse, C., Grégoire, J.-M., Tansey, K., Carmichael, G. R., & Woo, J.-H. (2005). Biomass burning emission inventory from burnt area data given by the SPOT-VEGETATION system in the frame of TRACE-P and ACE-Asia campaigns. *Journal of Geophysical Research*, *110*(D9), D09304. https://doi.org/10.1029/2004JD005461
Miller, J. D., Safford, H. D., Crimmins, M., & Thode, A. E. (2009). Quantitative Evidence for Increasing Forest Fire Severity in the Sierra Nevada and Southern Cascade Mountains, California and Nevada, USA. *Ecosystems*, *12*(1), 16–32. https://doi.org/10.1007/s10021-008-9201-9
Mills, M. J., Richter, J. H., Tilmes, S., Kravitz, B., MacMartin, D. G., Glanville, A. A., et al. (2017). Radiative and Chemical Response to Interactive Stratospheric Sulfate Aerosols in Fully Coupled CESM1(WACCM). *Journal of Geophysical Research: Atmospheres*, *122*(23), 13,061-13,078. https://doi.org/10.1002/2017JD027006
Moorcroft, P. R., Hurtt, G. C., & Pacala, S. W. (2001). A method for scaling vegetation dynamics: The ecosystem demography model (ED). *Ecological Monographs*, *71*(4), 557–586. https://doi.org/10.1890/0012-9615(2001)071[0557:AMFSVD]2.0.CO;2
Moore, D., Copes, R., Fisk, R., Joy, R., Chan, K., & Brauer, M. (2006). Population Health Effects of Air Quality Changes Due to Forest Fires in British Columbia in 2003. *Canadian Journal of Public Health*, *97*(2), 105–108.

https://doi.org/10.1007/BF03405325
Morcrette, J.-J., Barker, H. W., Cole, J. N. S., Iacono, M. J., & Pincus, R. (2008). Impact of a New Radiation Package, McRad, in the ECMWF Integrated Forecasting System. *Monthly Weather Review*, *136*(12), 4773–4798. https://doi.org/10.1175/2008MWR2363.1
Moreno-Cruz, J. B., & Keith, D. W. (2013). Climate policy under uncertainty: a case for solar geoengineering. *Climatic Change*, *121*(3), 431–444. https://doi.org/10.1007/s10584-012-0487-4
Morris, G. A., Hersey, S., Thompson, A. M., Pawson, S., Nielsen, J. E., Colarco, P. R., et al. (2006). Alaskan and Canadian forest fires exacerbate ozone pollution over Houston, Texas, on 19 and 20 July 2004. *Journal of Geophysical Research*, *111*(D24), D24S03. https://doi.org/10.1029/2006JD007090
Moss, R. H., Nakicenovic, N., & O'Neill, B. C. (2008). *Towards New Scenarios for Analysis of Emissions, Climate Change, Impacts, and Response Strategies*. Geneva: IPCC. Retrieved from http://pure.iiasa.ac.at/id/eprint/8659/
Mühle, J., Lueker, T. J., Su, Y., Miller, B. R., Prather, K. A., & Weiss, R. F. (2007). Trace gas and particulate emissions from the 2003 southern California wildfires. *Journal of Geophysical Research*, *112*(D3), D03307. https://doi.org/10.1029/2006JD007350
Murphy, B. N., Woody, M. C., Jimenez, J. L., Carlton, A. M. G., Hayes, P. L., Liu, S., et al. (2017). Semivolatile POA and parameterized total combustion SOA in CMAQv5.2: impacts on source strength and partitioning. *Atmospheric Chemistry and Physics*, *17*(18), 11107–11133. https://doi.org/10.5194/acp-17-11107-2017
Na, K., & Cocker, D. R. (2008). Fine organic particle, formaldehyde, acetaldehyde concentrations under and after the influence of fire activity in the atmosphere of Riverside, California. *Environmental Research*, *108*(1), 7–14. https://doi.org/10.1016/j.envres.2008.04.004
Neale, R. B., Richter, J. H., Conley, A. J., Park, S., Lauritzen, P. H., Gettelman, A., et al. (2010). *Description of the NCAR Community Atmosphere Model (CAM4.0)*. *Tech. Rep. NCAR/TN-485+STR*. Boulder, CO, USA: National Center for Atmospheric Research.
Negrón-Juárez, R. I., Koven, C. D., Riley, W. J., Knox, R. G., & Chambers, J. Q. (2015). Observed allocations of productivity and biomass, and turnover times in tropical forests are not accurately represented in CMIP5 Earth system models. *Environmental Research Letters*, *10*(6), 064017. https://doi.org/10.1088/1748-9326/10/6/064017
O'Connell, B. M., LaPoint, E. B., Turner, J. A., Ridley, T., Pugh, S. A., Wilson, A. M., et al. (2014). *The Forest Inventory and Analysis Database: Database description and user guide version 6.0.1 for Phase 2*. U.S. Department of Agriculture, Forest Service, Washington, DC. Retrieved from https://www.fia.fs.fed.us/library/database-documentation/current/ver80/FIADB User Guide P2_8-0.pdf
O'Dell, K., Ford, B., Fischer, E. V., & Pierce, J. R. (2019). Contribution of Wildland-Fire Smoke to US PM 2.5 and Its Influence on Recent Trends. *Environmental Science & Technology*, *53*(4), 1797–1804. https://doi.org/10.1021/acs.est.8b05430
Oleson, K. W., Lawrence, D. M., Bonan, G. B., Flanner, M. G., Kluzek, E., Lawrence, P.

J., et al. (2010). *Technical Description of version 4.0 of the Community Land Model (CLM). Tech. Rep. NCAR/TN-478+STR*. Boulder, CO, USA: National Center for Atmospheric Research. https://doi.org/10.5065/D6FB50WZ

Oleson, K. W., Lawrence, D. M., Bonan, G. B., Drewniak, B., Huang, M., Koven, C. D., et al. (2013). *Technical Description of version 4.5 of the Community Land Model (CLM). Tech. Rep. NCAR/TN-503+STR*. Boulder, CO, USA: National Center for Atmospheric Research. https://doi.org/10.5065/D6RR1W7M

Orr, J. C., Fabry, V. J., Aumont, O., Bopp, L., Doney, S. C., Feely, R. A., et al. (2005). Anthropogenic ocean acidification over the twenty-first century and its impact on calcifying organisms. *Nature*, *437*(7059), 681–686. https://doi.org/10.1038/nature04095

Otte, T. L., & Pleim, J. E. (2010). The Meteorology-Chemistry Interface Processor (MCIP) for the CMAQ modeling system: updates through MCIPv3.4.1. *Geoscientific Model Development*, *3*(1), 243–256. https://doi.org/10.5194/gmd-3-243-2010

Pacala, S. W., Hurtt, G. C., Baker, D., Peylin, P., Houghton, R. A., Birdsey, R. A., et al. (2001). Consistent Land- and Atmosphere-Based U.S. Carbon Sink Estimates. *Science*, *292*(5525), 2316–2320. https://doi.org/10.1126/science.1057320

Pachauri, R. K., & Meyer, L. A. (Eds.). (2014). *IPCC, 2014: Climate Change 2014: Synthesis Report. Contribution of Working Groups I, II and III to the Fifth Assessment Report of the Intergovernmental Panel on Climate Change*. Geneva, Switzerland: IPCC. Retrieved from https://www.ipcc.ch/report/ar5/syr/

Pan, Y., Birdsey, R. A., Fang, J., Houghton, R., Kauppi, P. E., Kurz, W. A., et al. (2011). A Large and Persistent Carbon Sink in the World's Forests. *Science*, *333*(6045), 988–993. https://doi.org/10.1126/science.1201609

Pfister, G. G., Wiedinmyer, C., & Emmons, L. K. (2008). Impacts of the fall 2007 California wildfires on surface ozone: Integrating local observations with global model simulations. *Geophysical Research Letters*, *35*(19), L19814. https://doi.org/10.1029/2008GL034747

Pleim, J. E. (2007). A Combined Local and Nonlocal Closure Model for the Atmospheric Boundary Layer. Part I: Model Description and Testing. *Journal of Applied Meteorology and Climatology*, *46*(9), 1383–1395. https://doi.org/10.1175/JAM2539.1

Poulter, B., Ciais, P., Hodson, E., Lischke, H., Maignan, F., Plummer, S., & Zimmermann, N. E. (2011). Plant functional type mapping for earth system models. *Geoscientific Model Development*, *4*(4), 993–1010. https://doi.org/10.5194/gmd-4-993-2011

Proctor, J., Hsiang, S., Burney, J., Burke, M., & Schlenker, W. (2018). Estimating global agricultural effects of geoengineering using volcanic eruptions. *Nature*, *560*(7719), 480–483. https://doi.org/10.1038/s41586-018-0417-3

Pye, H. O. T., & Pouliot, G. A. (2012). Modeling the Role of Alkanes, Polycyclic Aromatic Hydrocarbons, and Their Oligomers in Secondary Organic Aerosol Formation. *Environmental Science & Technology*, *46*(11), 6041–6047. https://doi.org/10.1021/es300409w

Qian, Y., Ghan, S. J., & Leung, L. R. (2010). Downscaling hydroclimatic changes over

the Western US based on CAM subgrid scheme and WRF regional climate simulations. *International Journal of Climatology*, *30*, 675–693. https://doi.org/10.1002/joc.1928

Le Quéré, C., Andrew, R. M., Canadell, J. G., Sitch, S., Korsbakken, J. I., Peters, G. P., et al. (2016). Global Carbon Budget 2016. *Earth System Science Data*, *8*(2), 605–649. https://doi.org/10.5194/essd-8-605-2016

Le Quéré, C., Andrew, R. M., Friedlingstein, P., Sitch, S., Hauck, J., Pongratz, J., et al. (2018). Global Carbon Budget 2018. *Earth System Science Data*, *10*(4), 2141–2194. https://doi.org/10.5194/essd-10-2141-2018

Randerson, J. T., Hoffman, F. M., Thornton, P. E., Mahowald, N. M., Lindsay, K., Lee, Y.-H., et al. (2009). Systematic assessment of terrestrial biogeochemistry in coupled climate–carbon models. *Global Change Biology*, *15*(10), 2462–2484. https://doi.org/10.1111/j.1365-2486.2009.01912.x

Reichstein, M., Bahn, M., Mahecha, M. D., Kattge, J., & Baldocchi, D. D. (2014). Linking plant and ecosystem functional biogeography. *Proceedings of the National Academy of Sciences*, *111*(38), 13697–13702. https://doi.org/10.1073/pnas.1216065111

Riahi, K., Rao, S., Krey, V., Cho, C., Chirkov, V., Fischer, G., et al. (2011). RCP 8.5—A scenario of comparatively high greenhouse gas emissions. *Climatic Change*, *109*(1–2), 33–57. https://doi.org/10.1007/s10584-011-0149-y

Robock, A. (2008). 20 reasons why geoengineering may be a bad idea. *Bulletin of the Atomic Scientists*, *64*(2), 14–18. https://doi.org/10.2968/064002006

Robock, A., Oman, L., & Stenchikov, G. L. (2008). Regional climate responses to geoengineering with tropical and Arctic SO_2 injections. *Journal of Geophysical Research*, *113*(D16), D16101. https://doi.org/10.1029/2008JD010050

Running, S. W. (2006). CLIMATE CHANGE: Is Global Warming Causing More, Larger Wildfires? *Science*, *313*(5789), 927–928. https://doi.org/10.1126/science.1130370

Running, S. W., Nemani, R. R., Heinsch, F. A., Zhao, M., Reeves, M., & Hashimoto, H. (2004). A continuos satellite-derived maesure of global terrestrial primary production. *BioScience*, *54*(6), 547–560. https://doi.org/10.1641/0006-3568(2004)054[0547:ACSMOG]2.0.CO;2

Russell, L. M., Rasch, P. J., Mace, G. M., Jackson, R. B., Shepherd, J., Liss, P., et al. (2012). Ecosystem Impacts of Geoengineering: A Review for Developing a Science Plan. *AMBIO*, *41*(4), 350–369. https://doi.org/10.1007/s13280-012-0258-5

Saatchi, S. S., Houghton, R. A., Dos Santos Alvalá, R. C., Soares, J. V., & Yu, Y. (2007). Distribution of aboveground live biomass in the Amazon basin. *Global Change Biology*, *13*(4), 816–837. https://doi.org/10.1111/j.1365-2486.2007.01323.x

Saatchi, S. S., Harris, N. L., Brown, S., Lefsky, M., Mitchard, E. T. A., Salas, W., et al. (2011). Benchmark map of forest carbon stocks in tropical regions across three continents. *Proceedings of the National Academy of Sciences*, *108*(24), 9899–9904. https://doi.org/10.1073/pnas.1019576108

Santoro, M., Beer, C., Cartus, O., Schmullius, C., Shvidenko, A., McCallum, I., et al. (2011). Retrieval of growing stock volume in boreal forest using hyper-temporal series of Envisat ASAR ScanSAR backscatter measurements. *Remote Sensing of Environment*, *115*(2), 490–507. https://doi.org/10.1016/j.rse.2010.09.018

Santoro, M., Beaudoin, A., Beer, C., Cartus, O., Fransson, J. E. S., Hall, R. J., et al. (2015). Forest growing stock volume of the northern hemisphere: Spatially explicit estimates for 2010 derived from Envisat ASAR. *Remote Sensing of Environment*, *168*, 316–334. https://doi.org/10.1016/j.rse.2015.07.005

Sapkota, A., Symons, J. M., Kleissl, J., Wang, L., Parlange, M. B., Ondov, J., et al. (2005). Impact of the 2002 Canadian Forest Fires on Particulate Matter Air Quality in Baltimore City. *Environmental Science & Technology*, *39*(1), 24–32. https://doi.org/10.1021/es035311z

Sato, H., Itoh, A., & Kohyama, T. (2007). SEIB–DGVM: A new Dynamic Global Vegetation Model using a spatially explicit individual-based approach. *Ecological Modelling*, *200*(3–4), 279–307. https://doi.org/10.1016/j.ecolmodel.2006.09.006

Schimel, D., Pavlick, R., Fisher, J. B., Asner, G. P., Saatchi, S., Townsend, P., et al. (2015). Observing terrestrial ecosystems and the carbon cycle from space. *Global Change Biology*, *21*(5), 1762–1776. https://doi.org/10.1111/gcb.12822

Sedjo, R., & Sohngen, B. (2012). Carbon Sequestration in Forests and Soils. *Annual Review of Resource Economics*, *4*(1), 127–144. https://doi.org/10.1146/annurev-resource-083110-115941

Shaver, G. R., Canadell, J., Chapin, F. S., Gurevitch, J., Harte, J., Henry, G., et al. (2000). Global Warming and Terrestrial Ecosystems: A Conceptual Framework for Analysis: Ecosystem responses to global warming will be complex and varied. Ecosystem warming experiments hold great potential for providing insights on ways terrestrial ecosystems will. *BioScience*, *50*(10), 871–882. https://doi.org/10.1641/0006-3568(2000)050[0871:GWATEA]2.0.CO;2

Shepherd, J. G. (2009). *Geoengineering the climate: science, governance and uncertainty* (10/29). Royal Society. Retrieved from https://eprints.soton.ac.uk/156647/

Shvidenko, A., Schepaschenko, D., McCallum, I., & Nilsson, S. (2010). Can the uncertainty of full carbon accounting of forest ecosystems be made acceptable to policymakers? *Climatic Change*, *103*(1–2), 137–157. https://doi.org/10.1007/s10584-010-9918-2

Simon, H., & Bhave, P. V. (2012). Simulating the Degree of Oxidation in Atmospheric Organic Particles. *Environmental Science & Technology*, *46*(1), 331–339. https://doi.org/10.1021/es202361w

Sitch, S., Huntingford, C., Gedney, N., Levy, P. E., Lomas, M., Piao, S. L., et al. (2008). Evaluation of the terrestrial carbon cycle, future plant geography and climate-carbon cycle feedbacks using five Dynamic Global Vegetation Models (DGVMs). *Global Change Biology*, *14*(9), 2015–2039. https://doi.org/10.1111/j.1365-2486.2008.01626.x

Skamarock, W. C., & Klemp, J. B. (2008). A time-split nonhydrostatic atmospheric model for weather research and forecasting applications. *Journal of Computational Physics*, *227*(7), 3465–3485. https://doi.org/10.1016/j.jcp.2007.01.037

Smith, R., Jones, P., Briegleb, B., Bryan2, F., Danabasoglu, G., Dennis, J., et al. (2010). *The Parallel Ocean Program (POP) Reference Manual: ocean component of the Community Climate System Model (CCSM) and Community Earth System Model (CESM). Los Alamos National Laboratory Tech. Rep. LAUR-10-01853*. Los Alamos, NM, USA: Los Alamos National Laboratory.

Spracklen, D. V., Mickley, L. J., Logan, J. A., Hudman, R. C., Yevich, R., Flannigan, M. D., & Westerling, A. L. (2009). Impacts of climate change from 2000 to 2050 on wildfire activity and carbonaceous aerosol concentrations in the western United States. *Journal of Geophysical Research*, *114*(D20), D20301. https://doi.org/10.1029/2008JD010966

Steffen, W., Rockström, J., Richardson, K., Lenton, T. M., Folke, C., Liverman, D., et al. (2018). Trajectories of the Earth System in the Anthropocene. *Proceedings of the National Academy of Sciences*, *115*(33), 8252–8259. https://doi.org/10.1073/pnas.1810141115

Stevens-Rumann, C. S., Kemp, K. B., Higuera, P. E., Harvey, B. J., Rother, M. T., Donato, D. C., et al. (2018). Evidence for declining forest resilience to wildfires under climate change. *Ecology Letters*, *21*(2), 243–252. https://doi.org/10.1111/ele.12889

Stowell, J. D., Geng, G., Saikawa, E., Chang, H. H., Fu, J., Yang, C.-E., et al. (2019). Associations of wildfire smoke $PM_{2.5}$ exposure with cardiorespiratory events in Colorado 2011–2014. *Environment International*, *133*, 105151. https://doi.org/10.1016/j.envint.2019.105151

Swann, A. L. S., Hoffman, F. M., Koven, C. D., & Randerson, J. T. (2016). Plant responses to increasing CO_2 reduce estimates of climate impacts on drought severity. *Proceedings of the National Academy of Sciences*, *113*(36), 10019–10024. https://doi.org/10.1073/pnas.1604581113

Tai, E., Jimenez, M., Nopmongcol, O., Wilson, G., Mansell, G., Koo, B., & Yarwood, G. (2008). *Boundary conditions and fire emissions modeling*. Novato, CA, USA: ENVIRON International Corporation.

Taylor, K. E. (2001). Summarizing multiple aspects of model performance in a single diagram. *Journal of Geophysical Research: Atmospheres*, *106*(D7), 7183–7192. https://doi.org/10.1029/2000JD900719

Taylor, K. E., Stouffer, R. J., & Meehl, G. A. (2012). An Overview of CMIP5 and the Experiment Design. *Bulletin of the American Meteorological Society*, *93*(4), 485–498. https://doi.org/10.1175/BAMS-D-11-00094.1

Thurner, M., Beer, C., Santoro, M., Carvalhais, N., Wutzler, T., Schepaschenko, D., et al. (2014). Carbon stock and density of northern boreal and temperate forests. *Global Ecology and Biogeography*, *23*(3), 297–310. https://doi.org/10.1111/geb.12125

Thurner, M., Beer, C., Carvalhais, N., Forkel, M., Santoro, M., Tum, M., & Schmullius, C. (2016). Large-scale variation in boreal and temperate forest carbon turnover rate related to climate. *Geophysical Research Letters*, *43*(9), 4576–4585. https://doi.org/10.1002/2016GL068794

Thurner, M., Beer, C., Ciais, P., Friend, A. D., Ito, A., Kleidon, A., et al. (2017). Evaluation of climate-related carbon turnover processes in global vegetation models for boreal and temperate forests. *Global Change Biology*, *23*(8), 3076–3091. https://doi.org/10.1111/gcb.13660

Tian, H., Lu, C., Ciais, P., Michalak, A. M., Canadell, J. G., Saikawa, E., et al. (2016). The terrestrial biosphere as a net source of greenhouse gases to the atmosphere. *Nature*, *531*(7593), 225–228. https://doi.org/10.1038/nature16946

Tilmes, S., Muller, R., & Salawitch, R. (2008). The Sensitivity of Polar Ozone Depletion

to Proposed Geoengineering Schemes. *Science*, *320*(5880), 1201–1204. https://doi.org/10.1126/science.1153966

Tilmes, S., Fasullo, J., Lamarque, J.-F., Marsh, D. R., Mills, M., Alterskjaer, K., et al. (2013). The hydrological impact of geoengineering in the Geoengineering Model Intercomparison Project (GeoMIP). *Journal of Geophysical Research: Atmospheres*, *118*(19), 11,036-11,058. https://doi.org/10.1002/jgrd.50868

Tilmes, S., Richter, J. H., Kravitz, B., MacMartin, D. G., Mills, M. J., Simpson, I. R., et al. (2018). CESM1(WACCM) Stratospheric Aerosol Geoengineering Large Ensemble Project. *Bulletin of the American Meteorological Society*, *99*(11), 2361–2371. https://doi.org/10.1175/BAMS-D-17-0267.1

Tjiputra, J. F., Grini, A., & Lee, H. (2016). Impact of idealized future stratospheric aerosol injection on the large-scale ocean and land carbon cycles. *Journal of Geophysical Research: Biogeosciences*, *121*(1), 2–27. https://doi.org/10.1002/2015JG003045

Townshend, J. R. G. (1992). *Improved Global Data for Land Applications: A Proposal for a New High Resolution Data Set: Report of the Land Cover Working Group of IGBP-DIS* (Global change report). IGBP Secretariat, the Royal Swedish Academy of Science.

Turner, M. G. (2010). Disturbance and landscape dynamics in a changing world. *Ecology*, *91*(10), 2833–2849. https://doi.org/10.1890/10-0097.1

U.S. EPA. (2016). *Inventory of US greenhouse gas emissions and sinks: 1990–2014*. U.S. EPA. Retrieved from https://www.epa.gov/ghgemissions/inventory-us-greenhouse-gas-emissions-and-sinks-1990-2014

U.S. EPA. (2017). Community Multiscale Air Quality Model version 5.2. Research Triangle Park, NC, USA: US EPA Office of Research and Development. https://doi.org/10.5281/zenodo.1167892

UNC Institute for the Environment. (2009). *SMOKE v2.6 User's Manual*. Chapel Hill, NC, USA: The University of North Carolina at Chapel.

UNC Institute for the Environment. (2012). *Operational Guidance for the Community Multiscale Air Quality (CMAQ) Modeling System Version 5.0*. Chapel Hill, NC, USA: The University of North Carolina at Chapel.

United Nations Environment Programme. (2011). *Drought , Fire and Deforestation in the Amazon : Feedbacks , Uncertainty and the Precautionary Approach*.

Urbanski, S. P. (2014). Wildland fire emissions, carbon, and climate: Emission factors. *Forest Ecology and Management*, *317*, 51–60. https://doi.org/10.1016/j.foreco.2013.05.045

Urbanski, S. P., Hao, W. M., & Baker, S. (2008). Chapter 4 Chemical Composition of Wildland Fire Emissions. In A. Bytnerowicz, M. Arbaugh, A. Riebau, & C. Andersen (Eds.), *Developments in Environmental Science* (Vol. 8, pp. 79–107). Elservier. https://doi.org/10.1016/S1474-8177(08)00004-1

Wang, W., Bruyère, C., Duda, M., Dudhia, J., Gill, D., Lin, H.-C., et al. (2012). *Weather Research and Forecasting: ARW Version 3 Modeling System User's Guide*. National Center for Atmospheric Research.

Wardle, D. A., Hörnberg, G., Zackrisson, O., Kalela-Brundin, M., & Coomes, D. A. (2003). Long-Term Effects of Wildfire on Ecosystem Properties Across an Island

Area Gradient. *Science*, *300*(5621), 972–975. https://doi.org/10.1126/science.1082709

Watanabe, S., Hajima, T., Sudo, K., Nagashima, T., Takemura, T., Okajima, H., et al. (2011). MIROC-ESM 2010: model description and basic results of CMIP5-20c3m experiments. *Geoscientific Model Development*, *4*(4), 845–872. https://doi.org/10.5194/gmd-4-845-2011

Watson, R. T., Noble, I., Bolin, B., Ravindranath, N. H., Verardo, D., Andrasko, K., et al. (2000). *IPCC Special Report: Land Use, Land-Use Change, and Forestry*. Cambridge Univ. Press, UK. Retrieved from https://www.ipcc.ch/report/land-use-land-use-change-and-forestry/

Weber, S. A., Insaf, T. Z., Hall, E. S., Talbot, T. O., & Huff, A. K. (2016). Assessing the impact of fine particulate matter ($PM_{2.5}$) on respiratory-cardiovascular chronic diseases in the New York City Metropolitan area using Hierarchical Bayesian Model estimates. *Environmental Research*, *151*, 399–409. https://doi.org/10.1016/j.envres.2016.07.012

Westerling, A. L., Hidalgo, H. G., Cayan, D. R., & Swetnam, T. W. (2006). Warming and earlier spring increase Western U.S. forest wildfire activity. *Science*, *313*(5789), 940–943. https://doi.org/10.1126/science.1128834

Whittaker, R. H. (1975). *Communities and ecosystems*. Macmillan.

Wiedinmyer, C., & Neff, J. C. (2007). Estimates of CO_2 from fires in the United States: implications for carbon management. *Carbon Balance and Management*, *2*(1), 10. https://doi.org/10.1186/1750-0680-2-10

Wiedinmyer, C., Quayle, B., Geron, C., Belote, A., McKenzie, D., Zhang, X., et al. (2006). Estimating emissions from fires in North America for air quality modeling. *Atmospheric Environment*, *40*(19), 3419–3432. https://doi.org/10.1016/j.atmosenv.2006.02.010

Wiedinmyer, C., Akagi, S. K., Yokelson, R. J., Emmons, L. K., Al-Saadi, J. A., Orlando, J. J., & Soja, A. J. (2011). The Fire INventory from NCAR (FINN): a high resolution global model to estimate the emissions from open burning. *Geoscientific Model Development*, *4*(3), 625–641. https://doi.org/10.5194/gmd-4-625-2011

Williams, M., Richardson, A. D., Reichstein, M., Stoy, P. C., Peylin, P., Verbeeck, H., et al. (2009). Improving land surface models with FLUXNET data. *Biogeosciences*, *6*(7), 1341–1359. https://doi.org/10.5194/bg-6-1341-2009

Wong, D. C., Pleim, J., Mathur, R., Binkowski, F., Otte, T., Gilliam, R., et al. (2012). WRF-CMAQ two-way coupled system with aerosol feedback: software development and preliminary results. *Geoscientific Model Development*, *5*(2), 299–312. https://doi.org/10.5194/gmd-5-299-2012

Xia, L., Robock, A., Tilmes, S., & Neely III, R. R. (2016). Stratospheric sulfate geoengineering could enhance the terrestrial photosynthesis rate. *Atmospheric Chemistry and Physics*, *16*(3), 1479–1489. https://doi.org/10.5194/acp-16-1479-2016

Xu, S., Chen, W., Huang, Y., & He, X. (2012). Responses of Growth, Photosynthesis and VOC Emissions of Pinus tabulaeformis Carr. Exposure to Elevated CO_2 and/or Elevated O_3 in an Urban Area. *Bulletin of Environmental Contamination and Toxicology*, *88*(3), 443–448. https://doi.org/10.1007/s00128-011-0462-1

Yoon, J.-H., & Zeng, N. (2010). An Atlantic influence on Amazon rainfall. *Climate Dynamics*, *34*(2–3), 249–264. https://doi.org/10.1007/s00382-009-0551-6

Yue, X., Mickley, L. J., Logan, J. A., & Kaplan, J. O. (2013). Ensemble projections of wildfire activity and carbonaceous aerosol concentrations over the western United States in the mid-21st century. *Atmospheric Environment*, *77*, 767–780. https://doi.org/10.1016/j.atmosenv.2013.06.003

Ziska, L. H., & Bunce, J. A. (1997). Influence of increasing carbon dioxide concentration on the photosynthetic and growth stimulation of selected C4 crops and weeds. *Photosynthesis Research*, *54*(3), 199–208. https://doi.org/10.1023/A:1005947802161

VITA

Cheng-En Yang was born in Taipei, Taiwan. He received his bachelor's and master's degrees in Atmospheric Sciences from the National Taiwan University in 2002 and 2007, respectively. He served one year in the Republic of China Army Aviation 601 Brigade as a weather officer providing weather forecast services. He came to the U.S. to pursue graduate studies and received his master's degree in Marine and Atmosphere Science in 2011 at the State University of New York at Stony Brook. He joined the Department of Civil and Environmental Engineering at the University of Tennessee in May 2012. In December 2019, he graduated with a Ph.D. degree in Civil Engineering and a minor in Computational Science.